

รายงานวิจัยฉบับสมบูรณ์

โครงการการจำลองปัญหาทางด้านกลศาสตร์วิศวกรรม โดยรวมอิทธิพลในระดับนาโน

โดย ศ.คร. ธีรพงศ์ เสนจันทร์ฒิใชย และคณะ

กันยายน 2561

รายงานวิจัยฉบับสมบูรณ์

โครงการการจำลองปัญหาทางด้านกลศาสตร์วิศวกรรม โดยรวมอิทธิพลในระดับนาโน

โดย ศ.ดร. ธีรพงศ์ เสนจันทร์ฒิไชย และ รศ.ดร. จรูญ รุ่งอมรรัตน์ ภาควิชาวิศวกรรมโยธา คณะวิศวกรรมศาสตร์ จุฬาลงกรณ์มหาวิทยาลัย

สนับสนุนโดยสำนักงานกองทุนสนับสนุนการวิจัย
(ความเห็นในรายงานนี้เป็นของผู้วิจัย สกว. ไม่จำเป็นต้องเห็นด้วยเสมอไป)

ACKNOWLEDGEMENTS

The principal investigator and co-researcher gratefully acknowledge the financial support provided

by the Thailand Research Fund (Grant No. BRG 5880017). They would also like to thank Professor

Dr. Nimal Rajapakse, School of Engineering Science, Simon Fraser University, Canada; and

Professor Mark E. Mear, Department of Aerospace Engineering and Engineering Mechanics,

University of Texas at Austin, USA for their useful comments during the course of this

investigation. In addition, thanks are conveyed to Dr. Pong-In Intarit, Dr. Bin Thai Nguyen, Dr.

Supakorn Tirapat, Mr. Rawiphas Plangmal, Mr. Suraparb Keawsawasvong, Ms. Jintara

Lawongkerd and Mr. Kanin Tarntira for their assistance in the development of solution schemes

and the preparation of this manuscript.

TEERAPONG SENJUNTICHAI

JAROON RUNGAMORNRAT

Department of Civil Engineering

Faculty of Engineering

Chulalongkorn University

September 2018

ii

ABSTRACT

Project Code: BRG5880017

Project Title: Modeling of engineering mechanics problems by integrating nano-scale influences

Investigators: Teerapong Senjuntichai and Jaroon Rungamornrat, Department of Civil

Engineering, Faculty of Engineering, Chulalongkorn University

Email Address: Teerapong.S@chula.ac.th and Jaroon.r@chula.ac.th

Project Period: 3 years

Abstract: This research project presents accurate and efficient techniques for solving various engineering mechanics with consideration of nano-scale influence by employing a complete Gurtin-Murdoch model for surface elasticity. The concept of surface elasticity is adopted to take into account the influence of surface energy that has been considered essential for nano-sized elements and soft elastic solids. Existing mathematical models obtained from the previous project (BRG5480006) are refined and extended for solving various nano-scaled problems, which include multi-layered elastic media under surface loading, nano-beams, non-planar nano-sized cracks, and nano-indentation with adhesive contact. In each problem, the governing equations for both surface and bulk are properly formulated, and appropriate solution schemes are then implemented to efficiently and accurately determine the solutions of the fully coupled governing equations. A computer code is developed to obtain numerical solutions for each problem, and its accuracy is verified with available benchmark solutions. Selected numerical results from extensive parametric studies are presented to portray the influence of surface energy effects on elastic fields of nanomechanic problems under consideration. Presented results confirm the fact that the presence of surface stresses renders elastic media stiffer, and size-dependent behavior is also observed. Thus, the surface energy effects cannot be ignored in the analysis of engineering mechanics problems involving nano-scale influence and soft elastic materials.

Keywords: Boundary element method, finite element method, nano-sized cracks, Gurtin-Murdoch, multi-layered elastic media, nano-beams, nano-indentation, nonlocal elasticity, surface stresses

บทคัดย่อ

รหัสโครงการ: BRG5880017

ชื่อโครงการ: การจำลองปัญหาทางด้านกลศาสตร์วิศวกรรมโดยรวมอิทธิพลในระดับนาโน

ชื่อนักวิจัย: ศ.คร. ธีรพงศ์ เสนจันทร์ฒิไชย และ รศ.คร.จรูญ รุ่งอมรรัตน์ ภาควิชาวิศวกรรมโยธา คณะวิศวกรรมศาสตร์ จุฬาลงกรณ์มหาวิทยาลัย

อีเมล์: Teerapong.S@chula.ac.th และ Jaroon.r@chula.ac.th

ระยะเวลาโครงการ: 3 ปี

บทคัดย่อ: โครงการวิจัยนี้นำเสนอระเบียบวิธีที่มีประสิทธิภาพสำหรับการวิเคราะห์ปัญหากลสาสตร์ของแข็งที่ พิจารณาผลกระทบในระดับนาโน โดยใช้สมการรูปแบบสมบูรณ์ตามทฤษฎีความยืดหยุ่นของเกอร์ตินและเมอร์ดอก เพื่อจำลองพฤติกรรมของหน่วยแรงที่ผิวซึ่งมีอิทธิพลอย่างสูงในปัญหากลสาสตร์ของแข็งในระดับนาโนและปัญหาที่ เกี่ยวข้องกับวัสดุยืคหยุ่นอ่อน แบบจำลองในโครงการวิจัยนี้ได้พัฒนาเพิ่มเติมจากโครงการวิจัยในอดีต (BRG5480006) เพื่อทำการวิเคราะห์ปัญหากลสาสตร์ของแข็งในระดับนาโนได้แก่ ปัญหาแรงกระทำบนตัวกลางยืดหยุ่นหลายชั้น ปัญหา คานขนาดนาโน ปัญหารอยแตกร้าวในระดับนาโนที่ไม่อยู่ในระนาบ และปัญหาการกดแบบแข็งเกร็งในระดับนาโน ใน การวิเคราะห์ปัญหาเหล่านี้ สมการกำกับของวัสดุบัลก์และพื้นผิวที่มีความหนาเป็นสูนย์และยึดแน่นกับวัสดุบัลก์ถูก สร้างขึ้นในรูปแบบที่เหมาะสม และระเบียบวิธีต่างๆได้ถูกพัฒนาขึ้นเพื่อแก้ปัญหาอย่างมีประสิทธิภาพ หลังจากสอบ เทียบกับผลเฉลยอ้างอิงแล้ว ระเบียบวิธีที่พัฒนาขึ้นถูกนำมาใช้ในการศึกษาอิทธิพลของหน่วยแรงที่ผิวที่มีต่อหน่วยแรง และการเคลื่อนที่ที่เกิดขึ้นในแต่ละปัญหา จากผลการศึกษาสามารถสรุปได้ว่าหน่วยแรงที่ผิวส่งผลให้วัสดุมีความแข็ง มากขึ้นและทำให้เกิดพฤติกรรมที่ขึ้นอยู่กับขนาดของวัสดุ ดังนั้นในการวิเคราะห์ปัญหาทางกลสาสตร์วิสวกรรมใน ระดับนาโนและปัญหาที่เกี่ยวข้องกับวัสดุยืดหยุ่นอ่อนจะต้องพิจารณาอิทธิพลของหน่วยแรงที่ผิวด้วย

คำสำคัญ: ระเบียบวิธีบาวดารีเอลิเมนต์, รอยร้าวในระดับนาโน, ระเบียบวิธีไฟในต์เอลิเมนต์, เกอร์ติน-เมอร์ดอก, คาน นาโน, ตัวกลางยืดหยุ่นหลายชั้น, การกดระดับนาโน, ทฤษฎียืดหยุ่นไม่เฉพาะที่, หน่วยแรงที่ผิว

TABLE OF CONTENSTS

Acknowledgements	ii
Abstract (English)	iii
Abstract (Thai)	iv
Table of Contents	v
List of Figures	ix
List of Tables	xvii
CHAPTER I INTRODUCTION	1
1.1 Motivation and Significance	1
1.2 Objectives	2
1.3 Scope of Work	2
1.4 Methodology and Procedure	3
1.5 Contribution	4
1.6 Organization of Report	5
CHAPTER II LAYERED ELASTIC MEDIA UNDER SURFACE LOADING	6
2.1 Background and Review	6
2.2 Basic Equations	8
2.3 General solution for bulk	9
2.4 Solution for layered elastic half-space	10
2.5 Exact Stiffness Matrix Method for Multi-Layered Elastic Medium	15
2.6 Numerical results	19
2.6.1 Numerical scheme	19

2.6	6.2 Y	Verification	20
2.6		Numerical solution for layered elastic half-space under surface loading	21
2.6		Numerical solution for multi-layered medium over rigid base under vertical surface loading	22
2.6		Numerical solution for functionally graded layer on a homogeneous elastic layer under uniform vertical surface loading	24
CHAPTER I	III I	MODELING OF NANO-BEAMS	42
3.1 B	Backg	round and Review	42
3.2 P	Proble	em Formulation	4 4
3.2	2.1 I	Problem Description	4 4
3.2	2.2 I	Basic Equations	45
3.2	2.3 I	Linearized Equations for Buckling Load Analysis	50
3.3 K	Key G	doverning Equations	50
3.3	3.1 I	Fixed-free Nano-Beams	51
3.3	3.2 I	Fixed-roller supported Nano-Beams	52
3.4 S	Solutio	on Methodology	54
3.4	4.1 I	Determination of Buckling Load	54
3.4	4.2	Nonlinear Solver	55
3.4	4.3	Quadrature for Involved Weakly Singular Integrals	55
3.5 R	Result	s and Discussion	56
3.5	5.1 I	Modified Flexural Rigidity and Nonlocal Parameter	56
3.5	5.2 I	Buckling Load of Nano-beams	57
3.5	53 I	Post-buckling of Nano-beams	58

3.5.4	Bending of Nano-beams	59
CHAPTER IV	MODELING OF NANO-CRACKS	73
4.1 Per	ny-shaped Crack	73
4.1.1	Background and Review	73
4.1.2	Governing Equations and General Solutions	74
4.1.3	Solution of Boundary Value Problem	76
4.1.4	Numerical Results and Discussion	78
4.2 No	n-planar Cracks	87
4.2.1	Background and Review	87
4.2.2	Problem Description	88
4.2.3	Problem Formulation and Solution Technique	88
4.2.4	Preliminary Results and Discussion	90
CHAPTER V	NANO-INDENTATION	94
5.1 Bac	ekground and Review	94
5.2 For	mulation of Nano-Indentation Problems	96
5.2.1	Nano-Indentation on Elastic Layer	96
5.2.2	Nano-Indentation on Layered Elastic Medium	98
5.3 Nu	merical results	101
5.3.1	Verification	101
5.3.2	Numerical solution for nano-indentation on elastic layer	102
5.3.3	Numerical solution for nano-indentation on layered elastic half-space	105
CHAPTER VI	CONCLUSIONS AND REMARKS	123

	6.1	Layered Media under Surface Loading	123
	6.2	Bending and Post-buckling of Nano-beams	123
	6.3	Nano-size Cracks	124
	6.4	Nano-indentation on Layered Media	125
REFE	REN	ICE	126
Apper	ndix A	A OUTPUT	A-1
Apper	ndix I	B REPRINTS/MANUSCRIPTS	B-1

LIST OF FIGURES

Figure 2.1	Layered elastic half-space subjected to axisymmetric surface loading	26
Figure 2.2	Multi-layered elastic medium over rigid base under axisymmetric surface loading	26
Figure 2.3	Comparisons of (a) normalized vertical displacement profiles at the interface; and (b) normalized normal stress profiles along the <i>z</i> -axis of a FG layer over an elastic half-space	27
Figure 2.4	Radial variations of elastic fields under the vertical loading for different values of layer thickness (h/a) : (a) surface displacements $(z = 0)$ and (b) stresses at the interface $(z = h)$	28
Figure 2.5	Radial variations of elastic fields under the vertical loading for $h/a = 1$ and different magnitudes of residual surface stress (τ^{s}_{2}): (a) surface displacements ($z = 0$) and (b) stresses at the interface ($z = h$)	29
Figure 2.6	Radial variations of elastic fields under the vertical loading for $h/a = 1$ and different values of loading radius (\bar{a}): (a) surface displacements ($z = 0$) and (b) stresses at the interface ($z = h$)	30
Figure 2.7	Radial variations of elastic fields under the radial loading for different values of layer thickness (h/a) : (a) surface displacements $(z = 0)$ and (b) stresses at the interface $(z = h)$	31
Figure 2.8	Multi-layered medium consisting of Si [100] and Al [111] under vertical surface loading	32
Figure 2.9	Radial profiles of elastic fields of the Si/Al multi-layered medium at defferent depths: (a) normalized vertical displacement; and (b) normalized normal stress	33
Figure 2.10	Radial profiles of elastic fields of the Si/Al multi-layered medium with different τ_R ratios: (a) normalized vertical surface displacement; (b) normalized radial surface displacement; (c) normalized normal stress at $z=0.1$ nm; (d) normalized shear stress at $z=0.1$ nm	34
Figure 2.11	Variation of elastic fields of the Si/Al multi-layered medium with normalized loading radius \bar{a} at different depths: (a) normalized vertical displacement; (b) normal stress	35

Figure 2.12	Radial profiles of elastic fields of the Si/Al multi-layered medium under different types of surface loading: (a) normalized vertical surface displacement; and (b) normalized normal stress at $z = 0.1$ nm	36
Figure 2.13	FG layer over an elastic medium under uniform vertical surface loading	37
Figure 2.14	Radial profiles of normalized vertical surface displacement of the FG elastic medium with different \bar{h}_2/\bar{h}_1 ratios	37
Figure 2.15	Radial profiles of normalized vertical surface displacement of the FG elastic medium with different \bar{H}/\bar{a} ratios	38
Figure 2.16	Radial profiles of normalized vertical displacement of the FG elastic medium at different depths	38
Figure 2.17	Radial profiles of elastic fields of the FG elastic medium with different τ_R ratios: (a) normalized vertical surface displacement, (b) normalized radial surface displacement; (c) normalized normal stress at the interface, (d) shear stress at the interface	39
Figure 2.18	Radial profiles of elastic fields of the FG elastic medium with different grading functions: (a) normalized vertical surface displacement; and (b) normalized normal stress at the interface	40
Figure 3.1	Schematic of (a) perfectly straight nano-beam clamped at the left end and subjected to longitudinal force P and transverse force Q at the right end and (b) perfectly straight nano-beam clamped at the left end, roller-supported at the right end and subjected to longitudinal force P and moment M at the right end	61
Figure 3.2	(a) Schematic of deformed and undeformed configurations of centroidal axis of nano-beam and (b) free body diagram of infinitesimal deformed element	61
Figure 3.3	Schematic of beam element treated as composite consisting of bulk material and material surface in unstrained state	62
Figure 3.4	Relationship between normalized flexural rigidity η and surface modulus of elasticity E^s for $E=76$ GPa, $v=0.3$, $h_0=10$ nm: (a) $\tau^s=0$ and (b) $\tau^s=0.89$ N/m	62
Figure 3.5	(a) Relationship between normalized flexural rigidity η and the residual surface tension τ^s of nano-beam with different slenderness	63

ratio $l_0 / h_0 \in \{5,10\}$	0,15} and	different	aspect	ratio	of cros	s sec	tion
$h_0 / b_0 \in \{2,1,0.5\}$	for $E =$	76 <i>GPa</i> ,	v = 0.3	, h ₀	=10nm	and	(b)
relationship between	een nonlo	cal parame	eter μ a	nd len	gth of n	ano-b	eam
$l \text{ for } (e_0 a)_{ref} = 10 r$	nm with d	ifferent α					

- **Figure 3.6** Relationship between normalized buckling load P_{cr}/P_{cr}^c and proportional ratio β of the nano-beam with different slenderness ratio $l_0/h_0 \in \{5,10,15\}$ for E=76GPa, v=0.3, $E^s=1.22N/m$, $\tau^s=0.89N/m$, $e_0a=10nm$, $h_0/b_0=1$, $h_0=10nm$: (a) fixed-free nanobeam and (b) fixed-roller supported nano-beam
- **Figure 3.7** Relationship between normalized buckling load P_{cr}/P_{cr}^c and surface modulus of elasticity E^s with different slenderness ratio $l_0/h_0 \in \{5,10,15\}$ for E=76 GPa, v=0.3, $\tau^s=0.89$ N/m, $e_0a=10$ nm, $h_0/h_0=1$, $l_0=100$ nm, $\beta=5$: (a) fixed-free nano-beam and (b) fixed-roller supported nano-beam
- **Figure 3.8** Relationship between normalized buckling load P_{cr}/P_{cr}^c and residual surface tension τ^s with different slenderness ratio $l_0/h_0 = \{5,10,15\}$ for E = 76 GPa , v = 0.3 , $E^s = 1.22$ N/m , $e_0a = 10$ nm , $h_0/h_0 = 1$, $l_0 = 100$ nm , $\beta = 5$: (a) fixed-free nano-beam and (b) for fixed-roller supported nano-beam
- **Figure 3.9** Relationship between normalized buckling load P_{cr}/P_{cr}^c and nonlocal parameter μ with different slenderness ratio $l_0/h_0=\{5,10,15\}$ for E=76GPa , v=0.3 , $E^s=1.22$ N/m , $\tau^s=0.89$ N/m , $h_0/h_0=1$, $l_0=100$ nm , $\beta=5$: (a) fixed-free nano-beam and (b) fixed-roller supported nano-beam
- **Figure 3.10** Relationship between normalized tip load p and tip rotation θ_2 for (a) fixed-free beam and (b) fixed-roller supported beam. Obtained results are compared with the available benchmark solution
- **Figure 3.11** Relationship between proportional ratio β and normalized maximum longitudinal displacement \overline{u}_{max} for E = 76 GPa, v = 0.3, $E^s = 1.22$ N/m, $\tau^s = 0.89$ N/m, $e_0a = 10$ nm, $h_0/b_0 = 1$, $l_0/h_0 = 10$, $l_0 = 100$ nm: (a) fixed-free nano-beam under normalized compression force $p = \{2.5, 5\}$ and (b) fixed-roller supported nano-beam under normalized compression force $p = \{20.5, 21.5\}$

Figure 3.12 Post-buckling shape of fixed-free nano-beam for E = 76GPa, v = 0.3, 66 $E^{s} = 1.22 N/m$, $\tau^{s} = 0.89 N/m$, $e_{0}a = 10 nm$, $h_{0}/h_{0} = 1$, $l_{0}/h_{0} = 10$, $l_0 = 100 nm$ with two values of proportional ratio $\beta = \{0.5, 5\}$ and two values of normalized compression force: (a) p = 2.5 and (b) p = 5**Figure 3.13** Post-buckling shape of fixed-roller supported nano-beam for 67 $E = 76 \, GPa$, v = 0.3 , $E^s = 1.22 \, N \, / \, m$, $\tau^s = 0.89 \, N \, / \, m$, $e_0 a = 10 \, nm$, $h_0 / b_0 = 1$, $l_0 / h_0 = 10$, $l_0 = 100 nm$ with two values of proportional ratio $\beta = \{5,15\}$ and two values of normalized compression force: (a) p = 20.5 and (b) p = 21.5**Figure 3.14** Relationship between normalized maximum longitudinal displacement 67 \bar{u}_{max} and surface modulus of elasticity E^{s} with different slenderness ratio $l_0 / h_0 = \{5,10,15\}$ for E = 76 GPa, v = 0.3, $\tau^s = 0.89$ N/m, $e_0 a = 10 nm$, $h_0 / b_0 = 1$, $l_0 = 100 nm$: (a) fixed-free nano-beam with $\beta = 5$, p = 2.5 and (b) fixed-roller supported nano-beam with $\beta = 15$, p = 20.5Relationship between normalized maximum longitudinal displacement 68 **Figure 3.15** $\bar{u}_{\rm max}$ and residual surface tension $\tau^{\rm s}$ with different slenderness ratio $l_0 / h_0 = \{5,10,15\}$ for $E = 76\,GPa$, v = 0.3, $E^s = 1.22\,N/m$, $e_0 a = 10\,nm$, $h_0/b_0 = 1$, $l_0 = 100 nm$: (a) fixed-free nano-beam with $\beta = 5$, p = 2.5and (b) fixed-roller supported nano-beam with $\beta = 15$, p = 20.5**Figure 3.16** Relationship between normalized maximum longitudinal displacement 68 $\overline{u}_{\mathrm{max}}$ and the nonlocal parameter μ with different slenderness ratio $l_0 / h_0 = \{5,10,15\}$ for $E = 76\,GPa$, v = 0.3 , $E^s = 1.22\,N/m$, $\tau^{s} = 0.89 \, N \, / \, m$, $h_0 \, / \, b_0 = 1$, $l_0 = 100 \, nm$: (a) fixed-free nano-beam with $\beta = 5$, p = 2.5 and (b) fixed-roller supported nano-beam with $\beta = 15$, p = 20.5**Figure 3.17** Deformed shape of nano-beams obtained from Model-1 for (a) fixed-69 free nano-beam subjected to normalized transverse force q = 2 and (b) fixed-roller supported nano-beam subjected to normalized end moment $\bar{m}_0 = 1/3$ 69 **Figure 3.18** Relationship between proportional ratio β and normalized maximum transverse displacement \overline{v}_{max} for E = 76 GPa, v = 0.3, $E^s = 1.22 N/m$, $\tau^{s} = 0.89 \, N \, / \, m$, $e_{0} a = 10 \, nm$, $h_{0} \, / \, b_{0} = 1$, $l_{0} \, / \, h_{0} = 10$, $l_{0} = 100 \, nm$: (a) fixed-free nano-beam under normalized end transverse load $q = \{2,4\}$

	moment $\bar{m}_0 = \{2, 2.5\}$	
Figure 3.19	Deformed shape of fixed-free nano-beam for $E=76GPa$, $v=0.3$, $E^s=1.22N/m$, $\tau^s=0.89N/m$, $e_0a=10nm$, $h_0/b_0=1$, $l_0/h_0=10$, $l_0=100nm$ with two values of proportional ratio $\beta=\{0.5,5\}$ and two values of normalized end transverse force (a) $q=2$ and (b) $q=4$	70
Figure 3.20	Deformed shape of fixed-roller supported nano-beam for $E=76GPa$, $v=0.3$, $E^s=1.22N/m$, $\tau^s=0.89N/m$, $e_0a=10nm$, $h_0/b_0=1$, $l_0/h_0=10$, $l_0=100nm$ with two values of proportional ratio $\beta=\{0.5,5\}$ and two values of normalized end moment (a) $\overline{m}_0=2$ and (b) $\overline{m}_0=2.5$	70
Figure 3.21	Relationship between normalized maximum transverse displacement $\overline{v}_{\rm max}$ and surface modulus of elasticity E^s with different slenderness ratio $l_0/h_0=\{5,10,15\}$ for $E=76$ GPa , $v=0.3$, $\tau^s=0.89$ N/m , $e_0a=10$ nm , $h_0/b_0=1$, $l_0=100$ nm , $\beta=5$: (a) fixed-free nano-beam with $q=2$ and (b) fixed-roller supported nano-beam with $\overline{m}_0=2.5$	71
Figure 3.22	Relationship between normalized maximum transverse displacement $\overline{v}_{\text{max}}$ and residual surface tension τ^s with different slenderness ratio $l_0/h_0=\{5,10,15\}$ for $E=76$ GPa, $v=0.3$, $E^s=1.22$ N/m, $e_0a=10$ nm, $h_0/b_0=1$, $l_0=100$ nm, $\beta=5$: (a) fixed-free nano-beam with $q=2$ and (b) fixed-roller supported nano-beam with $\overline{m}_0=2.5$	71
Figure 3.23	Relationship between normalized maximum transverse displacement $\overline{v}_{\rm max}$ and nonlocal parameter μ with different slenderness ratio $l_0/h_0 \in \{5,10,15\}$ for $E=76GPa$, $v=0.3$, $E^s=1.22N/m$, $\tau^s=0.89N/m$, $h_0/b_0=1$, $l_0=100nm$, $\beta=5$: (a) fixed-free nano-beam with $q=2$ and (b) fixed-roller supported nano-beam with $\overline{m}_0=2.5$	72
Figure 4.1	Penny-shaped crack in infinite elastic medium under vertical loading	80
Figure 4.2	Convergence of vertical stress solution in the vicinity of crack tip	80
Figure 4.3	Comparison with existing solutions: (a) Vertical stress; (b) Crack opening displacement	81
Figure 4.4	Variation of elastic field for different magnitudes of surface residual stress (τ ^s): (a) Vertical stress; (b) Crack opening displacement	82

and (b) fixed-rolle supported nano-beam under normalized end

Figure 4.5	Variation of elastic fields for different magnitudes of surface material constant (κ^s): (a) Vertical stress; (b) Crack opening displacement	83
Figure 4.6	Variation of elastic fields for different crack sizes (a_0) : (a) Vertical stress; (b) Crack opening displacement	84
Figure 4.7	Non-dimensional elastic fields under vertical loading against residual surface stresses (τ^s) for difference crack sizes (a_0): (a) Vertical stresses in the vicinity of crack tip; (b) Crack opening displacements at the center of crack	85
Figure 4.8	Size-dependency of non-dimensional (a) crack tip stress at $r/a = 1.01$; and (b) central crack opening displacement for different magnitudes of surface residual stress (τ^s)	86
Figure 4.9	Schematics of (a) non-planar crack embedded in three-dimensional, linear elastic, infinite medium, (b) prescribed general tractions on crack surfaces, (c) bulk cracked medium, (d) zero-thickness layers S_C^+ and S_C^-	91
Figure 4.10	(a) Schematic of circular crack of radius a embedded in linear elastic unbounded media; (b) crack surface subjected to uniform normal traction $t_3^+ = -t_3^- = \sigma_0^-$; (c) crack surface subjected to uniform shear traction $t_1^+ = -t_1^- = \tau_0^-$; and (d) meshes adopted in analysis	91
Figure 4.11	Results for (a) normalized crack opening displacements and (b) normalized vertical stresses in the vicinity of the crack-front	92
Figure 4.12	Results for (a) normalized crack sliding displacements and (b) normalized near-tip shear stress along the x_1 -direction	93
Figure 5.1	Elastic layer with finite thickness under frictionless axisymmetric: (a) <i>smooth-contact</i> profile; (b) <i>non-smooth-contact</i> profile	108
Figure 5.2	Indentation on a layered elastic half-space under rigid flat-ended cylindrical punch of radius a with adhesive contact	108
Figure 5.3	Validation of Green's functions for an elastic layer under surface energy effects: (a) without out-of-plane contribution of τ^s ; (b) with complete Gurtin-Murdoch model	109
Figure 5.4	Comparison with existing nanoindentation solutions: (a) flat-ended cylindrical indenter; (b) paraboloidal indenter	110

Figure 5.5	Comparison of elastic fields in an elastic half-space under indentation with adhesive contact (no surface energy effect): (a) normalized contact pressure and (b) normalized surface displacements	111
Figure 5.6	Radial profiles of contact pressure and surface vertical displacement under flat-ended cylindrical indenter for: (a) a_0 = 0.5 and different layer thicknesses; (b) t/a = 5 and different contact radii	112
Figure 5.7	Radial profiles of contact pressure under flat-ended cylindrical indenter with a_0 = 0.5 for: (a) different residual surface stresses; (b) different surface material parameters	113
Figure 5.8	Radial profiles of elastic fields at different depths under flat-ended cylindrical indenter with $t/a=5$ and $a_0=0.5$: (a) normalized displacements (b) normalized stresses	114
Figure 5.9	Radial profiles of contact pressure and surface vertical displacement under paraboloidal indenter for: (a) a_0 = 0.5 with different layer thicknesses; (b) t/a = 5 with different contact radii	115
Figure 5.10	Radial profiles of contact pressure under paraboloidal indenter with a_0 = 0.5 for: (a) different residual surface stresses; (b) different surface material parameters	116
Figure 5.11	Radial profiles of elastic fields at different depths under paraboloidal indenter with $t/a=5$ and $a_0=0.5$: (a) normalized displacements (b) normalized stresses	117
Figure 5.12	Variations of normalized indentation force with a_0 for different layer thicknesses: (a) flat-ended cylindrical indenter (b) paraboloidal indenter	118
Figure 5.13	Radial variations of elastic fields for different contact conditions with $h/a=1$ and $\overline{a}=1$: (a) normalized contact pressure and (b) normalized vertical surface displacement	118
Figure 5.14	Radial variations of elastic fields at different depths with $h/a=1$ and $\overline{a}=1$: (a) normalized displacements and (b) normalized stresses	119
Figure 5.15	Radial variations of elastic fields for different contact radii \bar{a} with h/a = 1: (a) normalized contact pressure and (b) normalized surface displacement	120

Figure 5.16	Radial variations of elastic fields for different values of τ_1^s/τ_2^s with h/a = 1 and \bar{a} = 1: (a) normalized contact pressure and (b) normalized surface displacement	121
Figure 5.17	Radial variations of elastic fields for different values of μ_1/μ_2 with $h/a=1$ and $\bar{a}=1$: (a) normalized contact pressure and (b) normalized surface displacement	121
Figure 5.18	Variations of normalized indentation force with \bar{a} for different layer thicknesses and contact conditions	122

LIST OF TABLES

Table 2.1	Comparison of normalized surface displacements and stresses at the interface of a layered elastic half-space under uniformly distributed normal traction for $\mu_1/\mu_2 = 5$ and $h/a = 1$		
Table 2.2	Comparison of normalized surface displacements and stresses at the interfaces of a layered elastic half-space under linearly distributed tangential traction for $\mu_1/\mu_2 = 5$ and $h/a = 1$	41	
Table 2.3	Material properties employed in numerical study	41	

CHAPTER I

INTRODUCTION

This chapter briefly summarizes the key motivation and significance of the current investigation. The objectives, scope of work, and the methodology and research procedures are then clearly addressed. Finally, the contribution of the present study is summarized.

1.1 Motivation and Significance

Nowadays, nanotechnology has become one of the most interesting research areas in various fields such as biology, chemistry, physics, medicine and engineering. Although nanotechnology deals with extremely tiny objects with their length scale of few nanometers (where one nanometer is approximately about 50,000 times smaller than the average of a human hair), its applications tend to be substantial. In the field of material science and engineering, advanced researches related to nano-science and nanotechnology such as nano-tubes, nano-wires, nano-composites and nanofilms have grown rapidly and continuously. The physical modeling and corresponding comprehensive analysis to gain an insight into the complex behavior of nano-sized devices and nano-structured materials become crucial aspects in the optimal design of nano-scale products. Besides the fundamental understanding of mechanical properties in the nano-scale level, failure/damage analysis and assessment has been found to be an essential step that must be properly considered to ensure their safety and integrity in the design procedure.

In the past three decades, various techniques have been applied to investigate mechanical properties and characteristics of nano-sized structures. It is generally acknowledged that experimental methods yield results reflecting actual response. However, it is still found highly dependent on experimental environments and, more importantly, expensive due to the requirement of sophisticated equipment and high-precision testing procedures. As a result, mathematical modeling and simulations has become an attractive alternative, and been widely employed to develop fundamental understanding to further investigate complex phenomena. In addition, once integrating essential features and properly calibrated with data from basic experiments, mathematical models are found capable of simulating responses under various practical conditions.

Within the context of modeling nano-scale influence on solids, two predominant mathematical models, one known as the molecular or atomistic models whereas the other corresponding to the modified or enhanced continuum-based models, have been commonly employed in the literature. The molecular-based simulations have been verified to yield accurate prediction of responses of interest due to their effectiveness in detailing with bonds and atoms. However, such simulations require enormous computational effort and resources to treat billions of atoms at nano-scale. This therefore renders the discrete atomic-scale models impractical in various applications. As a result, modified or enhanced continuum-based models have become attractive due to their advantages in saving computational resources. Unlike macro-structures, the surface to volume ratio in the case of nano-sized objects (e.g., thin films, quantum dots, nano-wires, nano-tubes and nano-composites) is much higher and, as a direct consequence, the surface free energy often plays a crucial role in the mechanical behavior. Therefore, the classical theory of continuum mechanics commonly used in the modeling of macroscopic bodies is not directly

applicable to accurately treat problems related to nano-scale structures and nano-sized cracks. While a conventional theory of linear elasticity has been well established and employed in the modeling of a variety of problems involving linear elastic uncracked and cracked bodies, the enhancement of classical continuum mechanics models to incorporate the nano-scale influence is essentially required. To be capable of capturing the surface free energy effect, a model that properly takes into account the influence of surface stresses must be utilized.

The present research project aims to extend the work carried out in the previous TRF project (Grant BRG5480006) to treat more general class of boundary value problems in nanomechanics. Existing mathematical models are to be refined and adjusted as necessary to be well-suited for modeling various nano-scale problems (e.g., nano-indentations and nano-cracks). In addition, an extensive numerical study is to be carried out to fully investigate the size dependent behavior and gain an insight into nano-scale influence on predicted solutions.

1.2 objectives

The main objectives of the present study are

- 1. to refine and necessarily adjust the modified continuum model that takes into account influence of surface stresses, established in the previous TRF project, to enhance modeling capability to treat more general boundary value problems,
- 2. to investigate more complex nano-indentation problems such as those associated with non-smooth contact and interfaces, and indentation on thin layer substrates, and
- 3. to investigate more complicated nano-size crack problems such as those involving non-planar.

1.3 Scope of Work

Scope of the present study and assumptions relevant to the development are summarized as follows:

- 1. The boundary value problem considered in this investigation is linear and governed by the theory of linear elasticity;
- 2. A body associated with the boundary value problem is three-dimensional with applications to layered elastic media;
- 3. A body is assumed to be free of a body force;
- 4. The influence of nano-scale in the local region near the boundary is modeled by properly incorporating the surface elasticity model (proposed by Gurtin and Murdoch (1975) into classical continuum theory for solid mechanics;
- 5. Analytical and semi-analytical solutions are constructed for boundary value problems involving simple geometry, loading conditions and boundary conditions (e.g., surface axisymmetric loadings on layered elastic media, and indentation problems with consideration of frictionless and adhesive contacts, etc.); and
- 6. A framework of numerical techniques (e.g., FEM, SGBEM, Coupling of FEM and SGBEM) capable of solving relatively complex boundary value problems induced by the presence of surface elasticity, embedded singularity such as cracks, complicated geometries, loadings and boundary conditions is developed. In house computer codes using FORTRAN 90 are implemented to demonstrate accuracy and capabilities of the proposed technique.

1.4 Methodology and Procedure

The fundamental theories, key methodology and research procedure adopted and developed in the previous TRF project are used as the basis for the proposed study. Additional theories (e.g., a theory of non-local linear elasticity, a theory of curvature-dependent and curvature-independent residual surface tension, a dilute theory in micromechanics, etc.) and solution techniques (e.g., a potential-function-based approaches, solution representations, singular boundary integral equation techniques, etc.) are also integrated to enhance the modeling capability. The procedure and methodology can be briefly summarized below.

- 1. A literature survey is conducted in addition to that reported in the previous TRF project to identify the most recent advances and state of the art in the relevant area and properly refine the scope of the current work.
- 2. An enhanced continuum-based mathematical model is utilized to establish basic governing equations and formulate the associated boundary value problems. Similar to the previous project, the classical theory of linear elasticity is still employed to efficiently model the majority of the domain whereas the nano-scale influence due to the presence of the surface/boundary is captured by a well-established and extensively verified Gurtin-Murdoch surface elasticity theory. For certain class of problems when the inherent nonlocal effect for tiny-scale objects becomes significant, the theory of nonlocal elasticity is utilized to formulate the nonlocal constitutive relations.
- 3. A singular boundary integral equation method will be developed to determine numerical solutions of general nano-indentation problems such as nano-indentors with axisymmetric profiles, nano-indentors with presence of friction, fully bonded nano-indentors, nano-indentation on thin elastic substrates, etc. Required fundamental solutions derived in the previous TRF project are utilized in the formulation of the key governing integral equations, and both collocation technique and standard Galerkin method are adopted in the discretization.
- 4. A two-dimensional asymptotic analysis will be conducted to investigate the behavior of near-tip fields of nano-size cracks. A conventional technique of separation of variables, series representation, and existing fundamental results for classical crack problems are proposed to achieve this particular task.
- 5. An existing coupling technique between a standard finite element method and a weakly singular Symmetric Galerkin boundary element method (developed in the previous project) will be generalized to solve non-planar cracks. The extension from planar to non-planar cracks is non-trivial and requires the modification of the governing equations for the curved crack surface. For the case where the residual surface tension does not vanish in the initial state, the residual stress within the bulk material is properly treated in the constitutive relations. In addition, results from the asymptotic analysis (performed in the procedure 4) will be used to develop the local basis functions near the crack front to enhance the accuracy of the approximation.
- 6. Beside the development of solution techniques, an extensive numerical study will be carried out to fully investigate the influence of surface stresses and nonlocal parameters on predicted solutions and size-dependency for various boundary value problems.

1.5 Contribution

The present study proposes the complete analytical solution of displacement and stresses corresponding to the boundary value problems involving layered elastic media under axisymmtric surface loading with consideration of surface energy effects. The influence of surface stresses in the mathematical model is considered by employing a complate Gurtin-Murdoch continuum model for surface elasticity. The present fundamental solution is useful in the development of boundary integral equation methods for the investigation of more complicated problems such as nanoindentation and contact problems involving a layered elastic half-space and a multi-layered elastic medium. In addition, the present analytical solutions can also be employed as a benchmark solution in the development of numerical techniques such as finite element and boundary element methods for analysis of a variety of problems with the influence of surface energy such as nano-scale systems and soft elastic solids.

The present investigation also offers a continuum-based mathematical model together with an efficient and accurate solution procedure for simulating bending, buckling, and post-buckling responses of nano-beams with consideration of the nano-scale influence such as the surface free energy and nonlocal effects. The former effect is simulated using Gurtin-Murdoch surface elasticity theory whereas the last one is modeled by the differential Eringen nonlocal theory. Due to the vast capability of the proposed technique, it should provide an attractive alternative tool, in addition to experimental methods and atomistic and molecular dynamic simulations, to explore the mechanical behavior of slender nano-scale elements. In addition, results and findings from the current parametric study should also enhance the fundamental understanding of the nano-scale influence on the size-dependent characteristics of predicted results.

Within the context of modeling and analysis of fracture problems, the present research should enhance or strengthen the capability in the modeling of nano-sized crack problems using an alternative, computationally cheap continuum-based model along with the proper treatment of surface stress effects via Gurtin-Murdoch surface elasticity model. The developed mathematical model and the implemented numerical procedure allow more practical nano-sized fracture problems to be investigated, e.g. cracks of arbitrary shapes (including both planar and non-planar geometries) under general loading conditions. Availability of a computational tool of such high capability should be very significant in the parametric study to investigate and gain an insight into various crucial responses of interest in the nano-scale level such as the size-dependent behavior of all field quantities.

The analysis of axisymmetric rigid indentation on a layered media with consideration of frictionless and adhesive contacts is investigated based on a complete Gurtin-Murdoch theory of surface elasticity. The fundamental solutions of a layered elastic medium with presence of surface stresses derived in this study are employed in the formulation of axisymmetric indentation problems as a mixed-boundary value problem. The displacement boundary condition is expressed in terms of a displacement Green's function, which is constructed from the fundamental solutions of an elastic layer and a layered elastic half-space with consideration of surface stresses presented by Intarit (2012) and Tirapat et al. (2017). The unknown contact pressure distribution under an indenter of axisymmetric profiles is determined by employing either collocation or discretization method. Numerical results indicate that the surface stresses have a significant influence on elastic fields of the layer especially in the vicinity of the top surface, and the material behavior becomes size-dependent when the surface stresses are accounted. The developed numerical technique is an alternative for studying the mechanical properties such as hardness and elastic modulus for nano-

indentation applications. In addition, the present solution can be used as a benchmark for assessing the accuracy of numerical models based on the finite element and boundary element methods to analyze more complicated indentation problems in the presence of surface energy effects.

1.6 Organization of Report

The remaining part of this report is organized into five chapters. Chapter 2 presents the modeling and analysis of layered elastic media under surface loading and the influence of surface energy effect via Gurtin-Murdoch surface elasticity theory. Next, Chapter 3 summarizes the development of an efficient numerical technique capable of simulating bending, buckling and post-buckling responses of nano-scale elements with the consideration of both surface and nonlocal effects. The modeling and analysis of nano-sized cracks with the integration of surface stress effects is also reported in Chapter 4. In this chapter, a solution procedure adopted specifically for solving a penny-shaped crack under axisymetric loading conditions and that implemented for cracks of arbitrary geometry and under general loading conditions are presented. Next, the modeling and analysis of nano-indentation problems with the incorporation of surface energy effects together with a set of extensive results is presented in Chapter 5. Finally, all significant findings and conluding remarks are addressed in Chapter 6.

CHAPTER II

LAYERED ELASTIC MEDIA UNDER SURFACE LOADING

In this chapter, the complete solution of displacements and stresses corresponding to the boundary value problems involving layered elastic media under axisymmetric surface loading with consideration of surface energy effects is presented. The basic equations are formulated based on classical elasticity theory for the bulk and complete Gurtin-Murdoch constitutive relation for the surface. The standard Love's representation and Hankel integral transform are employed to obtain the general solutions of the bulk material. An efficient numerical quadrature is then applied to accurately evaluate all involved integrals. Selected numerical results are presented to portray the influence of various parameters and size-dependency on elastic fields for a layered elastic half-space and a multi-layered elastic medium. In addition, the obtained fundamental solution is useful in the development of numerical solution scheme for the investigation of more complicated problems under the influence of surface energy effects such as nano-indentation and contact problems involving an elastic nanoplate.

2.1 Background and Review

Nanotechnology has received wide attention in recent years due to its vast applications in various disciplines such as biology, chemistry, physics, medicines, material sciences, and engineering. In the fields of material sciences and engineering, studies related to mechanical behavior of nanostructured materials have also become a subject of numerous investigations due to the fact that understanding fundamental aspects of their behaviors at nano-scale level is important for optimum design of nano-sized devices and structures. There are two approaches that have commonly been employed to theoretically investigate mechanical behaviors of materials at nanoscale, namely, atomistic simulation and modified continuum-based model. Atomistic modeling techniques require a very large computational effort, although they are considered very accurate. A modified continuum-based model then becomes an attractive alternative in obtaining firstapproximation to predict mechanical behaviors of nanostructured materials. Due to their high surface to volume ratio, nano-scale elements, usually exhibit high influence of surface/interface free energy, which is the energy associated with atoms at or near a free surface (e.g., see Yakobson, 2003), consequently, their mechanical behavior becomes size-dependent (Wong et al., 1997). Thus, surface energy effects, which are generally ignored in conventional continuum mechanics problems, need to be taken into account in modified continuum-based simulation for nano-scale systems. A theoretical framework based on continuum mechanics concepts was proposed by Gurtin and Murdoch (1975, 1978) to take into consideration the influence of surface energy effects. In their model, an elastic surface was formed as a mathematical layer of zero thickness perfectly bonded to the underlying bulk material without slipping. Several studies were carried out to verify that modified continuum-based simulations with surface energy effects and size-dependency can be employed to model nanostructured elements with acceptable accuracy. For instance, Miller and Shenoy (2000) examined the size-dependent behavior of nanostructured elements (i.e. bar, beam and plate) by adopting the Gurtin-Murdoch model, and found that their results were in a good

agreement with those obtained from direct atomistic simulations. Dingreville et al. (2005) developed a continuum framework to incorporate the surface free energy in the framework of continuum mechanics, and demonstrated that overall mechanical behaviors of nanostructured elements such as particles, wires, films were found to be size-dependent. There also exist other continuum-based theories that have been developed to take into account the size-dependent material behaviors at the nano-scale level such as the strain gradient elasticity theory by Mindlin (1964). The theory proposed by Mindlin has not been widely adopted in the modeling of nanoscale systems since it involves several additional material parameters and higher-order governing equations. Simplified versions of Mindlin's theory have then been proposed, and analytical solutions to various continuum mechanics problems were presented based on its simplified versions (e.g., see Georgiadis and Anagnostou, 2008; Gao and Liu, 2012; Gao and Zhou, 2013).

Over the last two decades, several researchers have investigated a variety of continuum mechanics problems by adopting the Gurtin-Murdoch theory of surface elasticity. For example, Huang and Yu (2007) studied an elastic half-plane under surface loading with consideration of surface energy effects. An elastic layer with finite thickness, subjected to surface loading under plane-strain and axisymmetric conditions, was also considered by Zhao and Rajapakse (2009). Intarit et al. (2010) derived fundamental solutions of an elastic half-plane under internal loading and dislocations. An elastic half-plane under surface shear loading was also investigated by Lei et al. (2012). Recently, nanocontact problem of layered viscoelastic solids with surface energy effects was presented by Abdel Rahman and Mahmoud (2016). All these studies, however, considered the surface stress tensor as a 2D quantity with its out-of-plane components being neglected. Wang et al. (2010) showed that the out-of-plane terms of the surface displacement gradient could be significant even in the case of small deformations particularly for curved and rotated surfaces. The complete version of Gurtin-Murdoch model, with consideration of the out-of-plane term, has later been employed to examine various continuum mechanics problems, for example, problems related to internally loaded elastic layer under plane strain condition (Intarit et al., 2011) and axisymmetric loading (Rungamornrat et al., 2016) respectively; contact problem (Zhou and Gao, 2013); nanoindentation (Pinyochotiwong et al., 2013; Attia and Mahmoud, 2015); nanobeams (Azizi et al., 2015); nanoplate (Sapsathiarn and Rajapakse, 2013); and nanosized cracks (Nguyen et al., 2016; Intarit et al., 2017). In addition, the influence of surface energy effects is also significant in problems related to soft elastic solids (He and Lim, 2006).

Stress analysis of a layered elastic medium under applied surface loading has a rich history (e.g. see Gerrard, 1969; Burmister, 1945; Gupta and Walowit, 1974; Perriot and Barthel, 2004) due to its close relevance to various engineering applications, such as characterization of mechanical properties of layered materials: for example, protective coatings, multilayer capacitors and layered composite materials; analysis and design of pavement and foundations; and in-situ testing of soils and rocks and so forth. A review of literature indicates that studies related to a layered elastic medium with consideration of surface energy effects based on the Gurtin-Murdoch theory are very limited. This class of problems has extensive applications in the study of nanocoatings and nanoscale surface layers that are used in electronic devices, tribological and biomaterial applications, advanced industrial materials, communication devices, etc. The main objective of this study is to present analytical solutions to a layered elastic half-space and a multilayered elastic medium under axisymmetric surface loading by adopting the complete Gurtin-Murdoch theory of surface elasticity. The boundary value problems of a layered elastic media under axisymmetric surface loading involving non-classical boundary conditions due to surface

stress influence are formulated by employing the standard Love's representation and Hankel integral transform. Selected numerical results for displacements and stresses due to applied vertical and radial loading are presented to portray the influence of various parameters and size-dependency on elastic fields. The present fundamental solution is useful in the development of boundary integral equation methods for the investigation of more complicated problems such as nano-indentation and contact problems involving a layered elastic medium. In addition, the present numerical results can also be employed as a benchmark solution in the development of numerical techniques such as finite element and boundary element methods for analysis of a variety of problems with the influence of surface energy such as nano-scale problems and soft elastic solids.

2.2 Basic Equations

Consider an elastic medium under the influence of surface energy effects. According to Gurtin-Murdoch surface elasticity theory, the medium consists of two different parts, i.e. the bulk material and the surface, which is a zero-thickness layer perfectly bonded to the bulk material without slipping. In the absence of body forces, the equilibrium equations, the constitutive equations, and the strain-displacement relationship of the bulk material under axisymmetric deformations are the same as those in the classical elasticity theory, which are given respectively by

$$\frac{\partial \sigma_{rr}}{\partial r} + \frac{\partial \sigma_{rz}}{\partial z} + \frac{\sigma_{rr} - \sigma_{\theta\theta}}{r} = 0; \quad \frac{\partial \sigma_{rz}}{\partial r} + \frac{\partial \sigma_{zz}}{\partial z} + \frac{\sigma_{rz}}{r} = 0$$
(2.1)

$$\sigma_{rr} = (\lambda + 2\mu)\varepsilon_{rr} + \lambda\varepsilon_{\theta\theta} + \lambda\varepsilon_{zz}; \quad \sigma_{\theta\theta} = \lambda\varepsilon_{rr} + (\lambda + 2\mu)\varepsilon_{\theta\theta} + \lambda\varepsilon_{zz}$$
(2.2)

$$\sigma_{zz} = \lambda \varepsilon_{rr} + \lambda \varepsilon_{\theta\theta} + (\lambda + 2\mu) \varepsilon_{zz}; \quad \sigma_{rz} = 2\mu \varepsilon_{rz}$$
(2.3)

$$\varepsilon_{rr} = \frac{\partial u_r}{\partial r}; \quad \varepsilon_{\theta\theta} = \frac{u_r}{r}; \quad \varepsilon_{zz} = \frac{\partial u_z}{\partial z}; \quad \varepsilon_{rz} = \frac{1}{2} \left(\frac{\partial u_r}{\partial z} + \frac{\partial u_z}{\partial r} \right)$$
 (2.4)

where $\{\sigma_{rr}, \sigma_{\theta\theta}, \sigma_{zz}, \sigma_{rz}\}$ denote the components of stress tensors; $\{\varepsilon_{rr}, \varepsilon_{\theta\theta}, \varepsilon_{zz}, \varepsilon_{rz}\}$ denote the components of strain tensors; and $\{u_r, u_z\}$ denote the components of displacement tensors respectively. In addition, μ and λ are Lamé constants of a bulk material.

On the surface, the equilibrium conditions in terms of the generalized Young-Laplace equation (Povstenko, 1993), the surface constitutive relations, and the strain-displacement relationship can be expressed, respectively, as (Gurtin and Murdoch, 1975; Gurtin and Murdoch, 1978; Gurtin et al., 1998)

$$\frac{\partial \sigma_{rr}^{s}}{\partial r} + \frac{\sigma_{rr}^{s} - \sigma_{\theta\theta}^{s}}{r} + \sigma_{zr}\big|_{z=0} + t_{r}^{0} = 0; \quad \frac{\partial \sigma_{zr}^{s}}{\partial r} + \frac{\sigma_{zr}^{s}}{r} + \sigma_{zz}\big|_{z=0} + t_{z}^{0} = 0$$

$$(2.5)$$

$$\sigma_{rr}^{s} = \tau^{s} + \left(2\mu^{s} + \lambda^{s}\right)\varepsilon_{rr}^{s} + \left(\lambda^{s} + \tau^{s}\right)\varepsilon_{\theta\theta}^{s}; \ \sigma_{\theta\theta}^{s} = \tau^{s} + \left(2\mu^{s} + \lambda^{s}\right)\varepsilon_{\theta\theta}^{s} + \left(\lambda^{s} + \tau^{s}\right)\varepsilon_{rr}^{s}$$

$$(2.6)$$

$$\sigma_{zr}^s = \tau^s \frac{du_z^s}{dr} \tag{2.7}$$

$$\varepsilon_{rr}^s = \frac{du_r^s}{dr}; \quad \varepsilon_{\theta\theta}^s = \frac{u_r^s}{r}$$
 (2.8)

where the superscript "s" is used to denote the quantities corresponding to the surface; λ^s and μ^s are surface Lamé constants; τ^s is the residual surface stress (or surface tension) under unstrained conditions. In addition, t_r^0 and t_z^0 denote the prescribed traction on the surface in the radial and vertical directions respectively. Equation (2.7) can be viewed as the out-of-plane contribution of the pre-existing surface tension τ^s in the deformed configuration whereas the surface gradient of the displacement du_z^s/dr acts as the out-of-plane component of the unit vector tangent to the surface in the deformed state. This term has been ignored in several previous studies even though the contribution of τ^s could be significant even in the case of small deformations (e.g. see Intarit et al., 2011; Pinyochotiwong et al., 2013; Rungamornrat et al., 2016).

2.3 General solution for bulk

For the axisymmetric case, the corresponding elastic fields can be obtained by solving the following biharmonic equation (Sneddon, 1951) in a cylindrical coordinate system (r, θ, z)

$$\nabla^2 \nabla^2 \Phi(r, z) = 0 \tag{2.9}$$

where $\nabla^2 = \frac{\partial^2}{\partial r^2} + \frac{1}{r} \frac{\partial}{\partial r} + \frac{\partial^2}{\partial z^2}$ denotes the Laplacian operator in a cylindrical coordinate and $\Phi(r,z)$ is Love's strain potential.

By applying Hankel integral transform into equation (2.9), we obtain,

$$\left(\frac{d^2}{dz^2} - \xi^2\right)^2 G(\xi, z) = 0 \tag{2.10}$$

where $G(\xi, z) = \int_0^\infty r \Phi J_0(\xi r) dr$ and $J_n(\xi)$ denotes the Bessel functions of the first kind of order n. The general solution of above equation may be written in the form

$$G(\xi,z) = (A+Bz)e^{-\xi z} + (C+Dz)e^{\xi z}$$
(2.11)

where A, B, C and D are arbitrary functions that can be determined from the boundary conditions.

Thereafter, the general solutions for bulk stresses and displacements of an elastic solid can be expressed in the forms of Hankel integral transform as (Sneddon, 1951; Selvadurai, 2000)

$$u_r = \frac{\lambda + \mu}{\mu} \int_0^\infty \xi^2 \frac{dG}{dz} J_1(\xi r) d\xi \tag{2.12}$$

$$u_z = \int_0^\infty \xi \left[\frac{d^2 G}{dz^2} - \frac{\lambda + 2\mu}{\mu} \xi^2 G \right] J_0(\xi r) d\xi$$
 (2.13)

$$\sigma_{rr} = \int_{0}^{\infty} \xi \left[\lambda \frac{d^{3}G}{dz^{3}} + (\lambda + 2\mu) \xi^{2} \frac{dG}{dz} \right] J_{0}(\xi r) d\xi - \frac{2(\lambda + \mu)}{r} \int_{0}^{\infty} \xi^{2} \frac{dG}{dz} J_{1}(\xi r) d\xi$$

$$(2.14)$$

$$\sigma_{\theta\theta} = \lambda \int_{0}^{\infty} \xi \left[\frac{d^{3}G}{dz^{3}} - \xi^{2} \frac{dG}{dz} \right] J_{0}(\xi r) d\xi + \frac{2(\lambda + \mu)}{r} \int_{0}^{\infty} \xi^{2} \frac{dG}{dz} J_{1}(\xi r) d\xi$$
(2.15)

$$\sigma_{zz} = \int_{0}^{\infty} \xi \left[\left(\lambda + 2\mu \right) \frac{d^{3}G}{dz^{3}} - \left(3\lambda + 4\mu \right) \xi^{2} \frac{dG}{dz} \right] J_{0}(\xi r) d\xi \tag{2.16}$$

$$\sigma_{rz} = \int_{0}^{\infty} \xi^{2} \left[\lambda \frac{d^{2}G}{dz^{2}} + (\lambda + 2\mu) \xi^{2}G \right] J_{1}(\xi r) d\xi$$
(2.17)

Finally, the substitution of the function G, given by Eq. (2.11), results in the stresses and displacements, expressed in terms of the arbitrary functions A, B, C and D as,

$$u_{r} = \frac{\lambda + \mu}{\mu} \int_{0}^{\infty} \xi^{2} \left\{ \left[-A\xi + \left(1 - z\xi \right) B \right] e^{-\xi z} + \left[C\xi + \left(1 + z\xi \right) D \right] e^{\xi z} \right\} J_{1}(\xi r) d\xi \tag{2.18}$$

$$u_{z} = -\frac{\lambda + \mu}{\mu} \int_{0}^{\infty} \xi^{2} \left\{ \left[A\xi + \left(\frac{2\mu}{\lambda + \mu} + z\xi \right) B \right] e^{-\xi z} + \left[C\xi - \left(\frac{2\mu}{\lambda + \mu} - z\xi \right) D \right] e^{\xi z} \right\} J_{0}(\xi r) d\xi$$
(2.19)

$$\frac{\sigma_{rr}}{\mu} = \frac{2(\lambda + 2\mu)}{\mu} \int_{0}^{\infty} \xi^{3} \left\{ \left[-A\xi + \left(\frac{2\lambda + \mu}{\lambda + \mu} - z\xi \right) B \right] e^{-\xi z} + \left[C\xi + \left(\frac{2\lambda + \mu}{\lambda + \mu} + z\xi \right) D \right] e^{\xi z} \right\} J_{0}(\xi r) d\xi
- \frac{2(\lambda + \mu)}{r\mu} \int_{0}^{\infty} \xi^{2} \left\{ \left[-A\xi + (1 - z\xi) B \right] e^{-\xi z} + \left[C\xi + (1 + z\xi) D \right] e^{\xi z} \right\} J_{1}(\xi r) d\xi$$
(2.20)

$$\frac{\sigma_{\theta\theta}}{\mu} = \frac{2\lambda}{\mu} \int_{0}^{\infty} \xi^{3} \left\{ Be^{-\xi z} + De^{\xi z} \right\} J_{0}(\xi r) d\xi
+ \frac{2(\lambda + \mu)}{r\mu} \int_{0}^{\infty} \xi^{2} \left\{ \left[-A\xi + (1 - z\xi)B \right] e^{-\xi z} + \left[C\xi + (1 + z\xi)D \right] e^{\xi z} \right\} J_{1}(\xi r) d\xi$$
(2.21)

$$\frac{\sigma_{zz}}{\mu} = \frac{2(\lambda + \mu)}{\mu} \int_{0}^{\infty} \xi^{3} \left\{ \left[A\xi + \left(\frac{\mu}{\lambda + \mu} + z\xi \right) B \right] e^{-\xi z} + \left[-C\xi + \left(\frac{\mu}{\lambda + \mu} - z\xi \right) D \right] e^{\xi z} \right\} J_{0}(\xi r) d\xi$$
(2.22)

$$\frac{\sigma_{rz}}{\mu} = \frac{2(\lambda + \mu)}{\mu} \int_{0}^{\infty} \xi^{3} \left\{ \left[A\xi - \left(\frac{\lambda}{\lambda + \mu} - z\xi \right) B \right] e^{-\xi z} + \left[C\xi + \left(\frac{\lambda}{\lambda + \mu} + z\xi \right) D \right] e^{\xi z} \right\} J_{1}(\xi r) d\xi$$
(2.23)

2.4 Solution for layered elastic half-space

Consider a layered elastic half-space consisting of two elastic materials with different properties perfectly bonded together, in which the upper material is an elastic layer of finite thickness h and subjected to axisymmetric vertical and radial surface loads denoted by p(r) and q(r) respectively, as shown in Figure 2.1. To solve this problem, the layered half-space is divided into two domains. The domain '1' represents the upper layer and the domain '2' represents the underlying half-space. The general solutions of the bulk material in the domain '1', are given by Eqs. (2.18) to (2.23) whereas those of the domain '2' can also be obtained from Eqs. (2.18) to (2.23) by replacing the arbitrary functions A to D with the arbitrary functions E to E to the domain '2'. In addition, the subscript E is used to denote the quantities corresponding to the domains '1' and '2',

respectively. The solutions of A to F can be determined by solving the following boundary and continuity conditions.

$$\sigma_{zz1}\big|_{z=0} + \tau_1^s \left(\frac{d^2 u_{z1}}{dr^2} + \frac{1}{r} \frac{du_{z1}}{dr}\right)_{z=0} = -p(r)$$
(2.24)

$$\sigma_{rz1}\Big|_{z=0} + \kappa_1^s \left(\frac{d^2 u_{r1}}{dr^2} + \frac{1}{r} \frac{du_{r1}}{dr} - \frac{u_{r1}}{r^2} \right)_{z=0} = -q(r)$$
(2.25)

$$\sigma_{zz1}\big|_{z=h} - \sigma_{zz2}\big|_{z=h} + \tau_2^s \left(\frac{d^2 u_{z2}}{dr^2} + \frac{1}{r}\frac{du_{z2}}{dr}\right)_{z=h} = 0$$
(2.26)

$$\sigma_{rz1}\big|_{z=h} - \sigma_{rz2}\big|_{z=h} + \kappa_2^s \left(\frac{d^2 u_{r2}}{dr^2} + \frac{1}{r}\frac{du_{r2}}{dr} - \frac{u_{r2}}{r^2}\right)_{z=h} = 0$$
(2.27)

$$u_{z1}\Big|_{z=h} - u_{z2}\Big|_{z=h} = 0 (2.28)$$

$$u_{r1}\big|_{z=h} - u_{r2}\big|_{z=h} = 0 (2.29)$$

where $\kappa_i^s = 2\mu_i^s + \lambda_i^s$ is a surface material constant. It should be noted that Eqs. (2.24) to (2.27) are non-classical boundary conditions obtained from Eqs. (2.5) to (2.8). In view of Eqs. (2.18) to (2.23) together with the assumption that the surface residual stress τ^s is constant, the following six linear algebraic equations are established to solve for the arbitrary functions A to F.

$$\left(\lambda_{1}' + \frac{\lambda_{1}'\overline{\tau}_{1}^{s}\xi}{2}\right)A\xi + \left(1 + \overline{\tau}_{1}^{s}\xi\right)B + \left(-\lambda_{1}' + \frac{\lambda_{1}'\overline{\tau}_{1}^{s}\xi}{2}\right)C\xi + \left(1 - \overline{\tau}_{1}^{s}\xi\right)D = -\frac{\overline{P}(\xi)}{2\xi^{2}}$$
(2.30)

$$\left(\lambda_{1}' + \frac{\lambda_{1}'\overline{\kappa}_{1}^{s}\xi}{2}\right)A\xi + \left(-\lambda_{1}' + 1 - \frac{\lambda_{1}'\overline{\kappa}_{1}^{s}\xi}{2}\right)B + \left(\lambda_{1}' - \frac{\lambda_{1}'\overline{\kappa}_{1}^{s}\xi}{2}\right)C\xi + \left(\lambda_{1}' - 1 - \frac{\lambda_{1}'\overline{\kappa}_{1}^{s}\xi}{2}\right)D = -\frac{\overline{Q}(\xi)}{2\xi^{2}}$$
(2.31)

$$\lambda_{1}'e^{-\bar{h}\xi}A\xi + \left(1 + \lambda_{1}'\bar{h}\xi\right)e^{-\bar{h}\xi}B - \lambda_{1}'e^{\bar{h}\xi}C\xi + \left(1 - \lambda_{1}'\bar{h}\xi\right)e^{\bar{h}\xi}D \\
+ \left(-\lambda_{2}' + \frac{\lambda_{2}'\bar{\tau}_{2}^{s}\xi}{2\bar{\mu}_{2}}\right)e^{-\bar{h}\xi}E\xi + \left(-\bar{\mu}_{2} - \lambda_{2}'\bar{h}\xi + \left(\frac{2\bar{\mu}_{2}}{\lambda_{2}'} + \bar{h}\xi\right)\frac{\lambda_{2}'\bar{\tau}_{2}^{s}\xi}{2\bar{\mu}_{2}}\right)e^{-\bar{h}\xi}F = 0$$
(2.32)

$$\lambda_{1}'e^{-\bar{h}\xi}A\xi + \left(-\lambda_{1}' + 1 + \lambda_{1}'\bar{h}\xi\right)e^{-\bar{h}\xi}B + \lambda_{1}'e^{\bar{h}\xi}C\xi + \left(\lambda_{1}' - 1 + \lambda_{1}'\bar{h}\xi\right)e^{\bar{h}\xi}D$$

$$+ \left(-\lambda_{2}' + \frac{\lambda_{2}'\bar{\kappa}_{2}^{s}\xi}{2\bar{\mu}_{2}}\right)e^{-\bar{h}\xi}E\xi + \left(\lambda_{2}' - \bar{\mu}_{2} - \lambda_{2}'\bar{h}\xi - \left(1 - \bar{h}\xi\right)\frac{\lambda_{2}'\bar{\kappa}_{2}^{s}\xi}{2\bar{\mu}_{2}}\right)e^{-\bar{h}\xi}F = 0$$

$$(2.33)$$

$$-\lambda_{1}'e^{-\bar{h}\xi}A\xi + \left(-2 - \lambda_{1}'\bar{h}\xi\right)e^{-\bar{h}\xi}B - \lambda_{1}'e^{\bar{h}\xi}C\xi + \left(2 - \lambda_{1}'\bar{h}\xi\right)e^{\bar{h}\xi}D + \left(\frac{\lambda_{2}'}{\bar{\mu}_{2}}\right)e^{-\bar{h}\xi}E\xi$$

$$+ \left(2 + \left(\frac{\lambda_{2}'}{\bar{\mu}_{2}}\right)\bar{h}\xi\right)e^{-\bar{h}\xi}F = 0$$

$$(2.34)$$

$$-\lambda_{1}'e^{-\bar{h}\xi}A\xi + \lambda_{1}'\left(1 - \bar{h}\xi\right)e^{-\bar{h}\xi}B + \lambda_{1}'e^{\bar{h}\xi}C\xi + \lambda_{1}'\left(1 + \bar{h}\xi\right)e^{\bar{h}\xi}D + \left(\frac{\lambda_{2}'}{\bar{\mu}_{2}}\right)e^{-\bar{h}\xi}E\xi$$

$$+\left(\frac{\lambda_{2}'}{\bar{\mu}_{2}}\right)\left(-1 + \bar{h}\xi\right)e^{-\bar{h}\xi}F = 0$$

$$(2.35)$$

where the following non-dimensional quantities in the above equations are defined as: $\bar{h}=h/\Lambda_1$; $\lambda_1'=\bar{\lambda}_1+1$; $\lambda_2'=\bar{\lambda}_2+\bar{\mu}_2$; $\bar{\lambda}_1=\lambda_1/\mu_1$; $\bar{\lambda}_2=\lambda_2/\mu_1$; $\bar{\mu}_2=\mu_2/\mu_1$; $\bar{\tau}_1^s=\tau_1^s/\mu_1\Lambda_1$; $\bar{\tau}_2^s=\tau_2^s/\mu_1\Lambda_1$; $\bar{\kappa}_1^s=\kappa_1^s/\mu_1\Lambda_1$; $\bar{\kappa}_2^s=\kappa_2^s/\mu_1\Lambda_1$; and $\Lambda_1=\kappa_1^s(\lambda_1+2\mu_1)/2\mu_1(\lambda_1+\mu_1)$. In addition, the functions $\bar{P}(\xi)$ and $\bar{Q}(\xi)$ are obtained from the surface loads p(r) and q(r) respectively as

$$\overline{P}(\xi) = \int_{0}^{\infty} \overline{p}(\overline{r}) J_{0}(\xi \overline{r}) \overline{r} d\overline{r}$$
(2.36)

$$\bar{Q}(\xi) = \int_{0}^{\infty} \bar{q}(\bar{r}) J_{1}(\xi \bar{r}) \bar{r} d\bar{r}$$
(2.37)

in which $\bar{p} = p/\mu_1$; $\bar{q} = q/\mu_1$; and $\bar{r} = r/\Lambda_1$. The arbitrary functions A to F for given functions of the applied surface loads p(r) and q(r) can then be obtained separately by solving the linear equation system, Eqs. (2.30) to (2.35), and they are given by

$$A\xi = A_N \xi + A_R \xi \tag{2.38}$$

$$B = B_N + B_R \tag{2.39}$$

$$C\xi = C_N \xi + C_R \xi \tag{2.40}$$

$$D = D_N + D_R \tag{2.41}$$

$$\begin{cases}
E\xi \\
F
\end{cases} = \begin{bmatrix}
b_{11} & b_{12} & b_{13} & b_{14} \\
b_{21} & b_{22} & b_{23} & b_{24}
\end{bmatrix} \begin{cases}
A\xi \\
B \\
C\xi \\
D
\end{cases}$$
(2.42)

$$\begin{cases} A_{N}\xi \\ B_{N} \\ C_{N}\xi \\ D_{N} \end{cases} = -\frac{\bar{P}(\xi)}{2\xi^{2} \cdot |a_{ij}|} \begin{cases} a_{22}(a_{33}a_{44} - a_{34}a_{43}) + a_{23}(a_{34}a_{42} - a_{32}a_{44}) + a_{24}(a_{32}a_{43} - a_{33}a_{42}) \\ a_{21}(a_{34}a_{43} - a_{33}a_{44}) + a_{23}(a_{31}a_{44} - a_{34}a_{41}) + a_{24}(a_{33}a_{41} - a_{31}a_{43}) \\ a_{21}(a_{32}a_{44} - a_{34}a_{42}) + a_{22}(a_{34}a_{41} - a_{31}a_{44}) + a_{24}(a_{31}a_{42} - a_{32}a_{41}) \\ a_{21}(a_{33}a_{42} - a_{32}a_{43}) + a_{22}(a_{31}a_{43} - a_{33}a_{41}) + a_{23}(a_{32}a_{41} - a_{31}a_{42}) \end{cases}$$

$$\begin{cases} A_{R}\xi \\ B_{R} \\ C_{R}\xi \\ D_{R} \end{cases} = -\frac{\bar{Q}(\xi)}{2\xi^{2} \cdot |a_{ij}|} \begin{cases} a_{12}(a_{34}a_{43} - a_{33}a_{44}) + a_{13}(a_{32}a_{44} - a_{34}a_{42}) + a_{14}(a_{33}a_{42} - a_{32}a_{43}) \\ a_{11}(a_{33}a_{44} - a_{34}a_{43}) + a_{13}(a_{34}a_{41} - a_{31}a_{44}) + a_{14}(a_{31}a_{43} - a_{33}a_{41}) \\ a_{11}(a_{34}a_{42} - a_{32}a_{44}) + a_{12}(a_{31}a_{44} - a_{34}a_{41}) + a_{14}(a_{32}a_{41} - a_{31}a_{42}) \\ a_{11}(a_{32}a_{43} - a_{33}a_{42}) + a_{12}(a_{33}a_{41} - a_{31}a_{43}) + a_{13}(a_{31}a_{42} - a_{32}a_{41}) \end{cases}$$
 (2.44)

$$\begin{vmatrix} a_{ij} | = \begin{vmatrix} a_{11} & a_{12} & a_{13} & a_{14} \\ a_{21} & a_{22} & a_{23} & a_{24} \\ a_{31} & a_{32} & a_{33} & a_{34} \\ a_{41} & a_{42} & a_{43} & a_{44} \end{vmatrix}$$

$$(2.45)$$

$$a_{11} = \lambda_1' + \frac{\lambda_1' \overline{\tau}_1^s \xi}{2} \tag{2.46}$$

$$a_{12} = 1 + \bar{\tau}_1^s \xi \tag{2.47}$$

$$a_{13} = -\lambda_1' + \frac{\lambda_1' \overline{\tau}_1^s \xi}{2} \tag{2.48}$$

$$a_{14} = 1 - \bar{\tau}_1^s \xi \tag{2.49}$$

$$a_{21} = \lambda_1' + \frac{\lambda_1' \overline{\kappa}_1^s \xi}{2} \tag{2.50}$$

$$a_{22} = 1 - \lambda_1' - \frac{\lambda_1' \bar{\kappa}_1^s \xi}{2} \tag{2.51}$$

$$a_{23} = \lambda_1' - \frac{\lambda_1' \bar{\kappa}_1^s \xi}{2} \tag{2.52}$$

$$a_{24} = -1 + \lambda_1' - \frac{\lambda_1' \bar{\kappa}_1^s \xi}{2}$$
 (2.53)

$$a_{31} = \frac{\lambda_1' e^{-2\bar{h}\xi}}{2} \left(\bar{\tau}_2^s \xi - 2\bar{\mu}_2 + 2 \right) \tag{2.54}$$

$$a_{32} = \frac{e^{-2\bar{h}\xi}}{2} \left(\left(2 + \lambda_1' \bar{h} \xi \right) \left(\bar{\tau}_2^s \xi - 2\bar{\mu}_2 \right) + \left(2 + 2\lambda_1' \bar{h} \xi \right) \right) + \bar{\mu}_2^2 e^{-2\bar{h}\xi} \frac{\lambda_1' + 2}{\lambda_2' + 2\bar{\mu}_2}$$
(2.55)

$$a_{33} = -\lambda_1' - \frac{\lambda_1' \lambda_2' \bar{\mu}_2}{\lambda_2' + 2\bar{\mu}_2} + \frac{\lambda_1' \bar{\tau}_2^s \xi}{2}$$
 (2.56)

$$a_{34} = -\overline{\tau}_{2}^{s} \xi \left(1 - \frac{\lambda_{1}' \overline{h} \xi}{2} \right) + \overline{\mu}_{2} \left(2 - \lambda_{1}' \overline{h} \xi \right) + \left(1 - \lambda_{1}' \overline{h} \xi \right) + \overline{\mu}_{2}^{2} \left(\frac{\lambda_{1}' + 2\lambda_{1}' \overline{h} \xi - 2}{\lambda_{2}' + 2\overline{\mu}_{2}} \right)$$

$$(2.57)$$

$$a_{41} = \frac{\lambda_1' e^{-2\bar{h}\xi}}{2} \left(\bar{\kappa}_2^s \xi - 2\bar{\mu}_2 + 2 \right) \tag{2.58}$$

$$a_{42} = \frac{e^{-2\bar{h}\xi}}{2} \left(\lambda_1' \left(\bar{h}\xi - 1 \right) \left(2 - 2\bar{\mu}_2 + \bar{\kappa}_2^s \xi \right) + 2 \right) - \bar{\mu}_2^2 e^{-2\bar{h}\xi} \frac{\lambda_1' + 2}{\lambda_2' + 2\bar{\mu}_2}$$
(2.59)

$$a_{43} = \lambda_1' - \frac{\lambda_1' \bar{\kappa}_2^s \xi}{2} + \frac{\lambda_1' \lambda_2' \bar{\mu}_2}{\lambda_2' + 2\bar{\mu}_2}$$
 (2.60)

$$a_{44} = \left(1 + \overline{h}\,\xi\right) \left(\lambda_1' + \lambda_1'\,\overline{\mu}_2 - \frac{\lambda_1'\,\overline{\kappa}_2^s\,\xi}{2}\right) - 1 - \overline{\mu}_2^2 \left(\frac{\lambda_1' + 2\lambda_1'\,\overline{h}\,\xi - 2}{\lambda_2' + 2\overline{\mu}_2}\right) \tag{2.61}$$

$$b_{11} = \frac{\lambda_1' \,\overline{\mu}_2}{\lambda_2'} \tag{2.62}$$

$$b_{12} = -\frac{2\bar{\mu}_2 (\bar{h}\xi - 1)(\lambda_2' - \lambda_1'\bar{\mu}_2)}{\lambda_2' (\lambda_2' + 2\bar{\mu}_2)}$$
(2.63)

$$b_{13} = -e^{2\bar{h}\xi} \frac{\lambda_1' \bar{\mu}_2 \left(2\bar{\mu}_2 - \lambda_2' + 2\lambda_2' \bar{h}\xi \right)}{\lambda_2' \left(\lambda_2' + 2\bar{\mu}_2 \right)}$$
(2.64)

$$b_{14} = -e^{2\bar{h}\xi} \frac{2\bar{\mu}_2 \left(\lambda_2' + \lambda_1' \bar{\mu}_2 - \lambda_2' \bar{h} \xi + \lambda_1' \lambda_2' \left(\bar{h} \xi\right)^2 + \lambda_1' \bar{\mu}_2 \bar{h} \xi\right)}{\lambda_2' \left(\lambda_2' + 2\bar{\mu}_2\right)}$$
(2.65)

$$b_{21} = 0 (2.66)$$

$$b_{22} = \overline{\mu}_2 \frac{\lambda_1' + 2}{\lambda_2' + 2\overline{\mu}_2} \tag{2.67}$$

$$b_{23} = e^{2\bar{h}\xi} \frac{2\lambda_1' \bar{\mu}_2}{\lambda_2' + 2\bar{\mu}_2} \tag{2.68}$$

$$b_{24} = \overline{\mu}_2 e^{2\overline{h}\xi} \frac{\lambda_1' + 2\lambda_1' \overline{h}\xi - 2}{\lambda_2' + 2\overline{\mu}_2}$$
 (2.69)

Substitution of the arbitrary functions A to F into Eqs. (2.18) to (2.23) yields the displacement and stress fields at an arbitrary point of the layered elastic half-space under axisymmetric surface loading as shown in Figure 2.1.

2.5 Exact Stiffness Matrix Method for Multi-Layered Elastic Medium

Consider a multi-layered elastic medium subjected to axisymmetric vertical and radial surface loads denoted by p(r) and q(r), respectively, as shown in Figure 2.2. The layers and the surfaces of the multi-layered medium are illustrated where the 2^{nd} surface to the N^{th} surface could be called "interface". The stress boundary conditions at the top surface and the displacement boundary conditions at the rigid base of the multi-layered medium are given below.

$$-\left\{\sigma_{zz}^{(1)} + T_{z}^{s}\right\}\Big|_{z=z_{1}} = p(r) \tag{2.70}$$

$$-\left\{\sigma_{zr}^{(1)} + T_r^s\right\}\Big|_{z=z_1} = q(r) \tag{2.71}$$

$$u_{\alpha}\big|_{z=z_{N+1}}=0\tag{2.72}$$

where $\alpha = r, z$ and

$$T_{z}^{s}\Big|_{z=z_{1}} = \left[\frac{d\tau_{1}^{s}}{dr}\left(\frac{du_{z}^{s}}{dr}\right)_{z=z_{1}} + \tau_{1}^{s}\left(\frac{d^{2}u_{z}^{s}}{dr^{2}} + \frac{1}{r}\frac{du_{z}^{s}}{dr}\right)_{z=z_{1}}\right]$$
(2.73)

$$T_r^s \Big|_{z=z_1} = \left[\frac{d\tau_1^s}{dr} \left(1 + \frac{u_r^s}{r} \right)_{z=z_1} + \kappa_1^s \left(\frac{d^2 u_r^s}{dr^2} + \frac{1}{r} \frac{du_r^s}{dr} - \frac{u_r^s}{r^2} \right)_{z=z_1} \right]$$
(2.74)

where $\kappa_1^s = 2\mu_1^s + \lambda_1^s$ is a surface material constant corresponding to the 1st surface and u_z^s and u_r^s are the displacements of the surface in the *n*-direction (n = r, z). In addition, the terms T_z^s and T_r^s represent the contribution from the surface energy effects in the normal and tangential directions respectively. These terms are normally ignored in the macro-scale problems but for nano-scale problems, these effects have to be considered at the top surface and every interface. Thus, the traction and displacement continuity conditions at the n^{th} surface, where n = 2,3,...,N, can be written as follows:

$$\left. \left\{ \sigma_{zz}^{(n-1)} - \sigma_{zz}^{(n)} - T_z^s \right\} \right|_{z=z_n} = 0 \tag{2.75}$$

$$\left. \left\{ \sigma_{zr}^{(n-1)} - \sigma_{zr}^{(n)} - T_r^s \right\} \right|_{z=z_n} = 0$$
 (2.76)

$$u_{\alpha}^{(n)}\Big|_{z=z_{n}} = u_{\alpha}^{s}\Big|_{z=z_{n}} = u_{\alpha}^{(n-1)}\Big|_{z=z_{n}}$$
(2.77)

The terms on the right-hand side of Eqs. (2.75) and (2.76) can be condsidered as the continuity of traction at the n^{th} surface. If there is traction applied at a layer interface, the right-hand side term at that interface is non-zero and this calculation scheme is still viable.

To solve this boundary value problem, the continuity condition of traction and displacements at each surface, Eqs. (2.75) to (2.77) have to be considered with the boundary conditions, Eqs. (2.70) to (2.72). For the problem shown in Figure 2.2, the condition number of the equation system is extremely large when using the high value of ξ for the equation system to be solved conventionally due to the presence of mis-matching exponential terms in the equations

system (Senjuntichai and Rajapakse, 1995). The large condition number indicates the ill-conditioning of the system, which results in the low numerical stability of the system. To avoid the low numerical stability, the exact stiffness matrix scheme, (Senjuntichai and Rajapakse, 1995; Wang and Rajapakse, 1994), is adopted to solve this boundary value problem related to a multi-layered medium with surface energy effects.

An exact stiffness matrix method is established to examine the behaviors of a multi-layered elastic medium from the relationship between displacements and traction at each layer. A multi-layered medium consisting of N layers of different properties and thicknesses over a rigid base is considered as shown in Figure 2.2. The general solutions given by Eqs. (2.18) to (2.23), can be expressed in the Hankel transform space in the following matrix form.

$$\left[u_z(\overline{\xi}, \overline{z}) \quad u_r(\overline{\xi}, \overline{z}) \right]^T = \mathbf{R}(\overline{\xi}, \overline{z}) \mathbf{c}(\overline{\xi})$$
 (2.78)

$$\begin{bmatrix} \sigma_{zz}(\bar{\xi},\bar{z}) & \sigma_{zz}(\bar{\xi},\bar{z}) \end{bmatrix}^T = \mathbf{S}(\bar{\xi},\bar{z})\mathbf{c}(\bar{\xi})$$
(2.79)

where

$$\mathbf{c}^{(n)}(\overline{\xi}) = \begin{bmatrix} A^{(n)} & B^{(n)} & C^{(n)} & D^{(n)} \end{bmatrix}^T$$
 (2.80)

$$\mathbf{R}^{(n)}(\overline{\xi},\overline{z}) = \left(\frac{\omega^{(n)}\overline{\xi}}{\overline{\mu}^{(n)}}\right) \begin{bmatrix} -e^{-\overline{\xi}\overline{z}} & \left(-\overline{z} - \frac{2\overline{\mu}^{(n)}}{\omega^{(n)}\overline{\xi}}\right) e^{-\overline{\xi}\overline{z}} & -e^{\overline{\xi}\overline{z}} & \left(-\overline{z} + \frac{2\overline{\mu}^{(n)}}{\omega^{(n)}\overline{\xi}}\right) e^{\overline{\xi}\overline{z}} \\ -e^{-\overline{\xi}\overline{z}} & \left(-\overline{z} + \frac{1}{\overline{\xi}}\right) e^{-\overline{\xi}\overline{z}} & e^{\overline{\xi}\overline{z}} & \left(\overline{z} + \frac{1}{\overline{\xi}}\right) e^{\overline{\xi}\overline{z}} \end{bmatrix}$$

$$(2.81)$$

$$\mathbf{S}^{(n)}(\overline{\xi}, \overline{z}) = \left(\omega^{(n)}\overline{\xi}\right) \begin{bmatrix} e^{-\overline{\xi}\overline{z}} & \left[\overline{z} + \frac{\overline{\mu}^{(n)}}{\omega^{(n)}\overline{\xi}}\right] e^{-\overline{\xi}\overline{z}} & -e^{\overline{\xi}\overline{z}} & \left[-\overline{z} + \frac{\overline{\mu}^{(n)}}{\omega^{(n)}\overline{\xi}}\right] e^{\overline{\xi}\overline{z}} \\ e^{-\overline{\xi}\overline{z}} & \left[\overline{z} - \frac{\overline{\lambda}^{(n)}}{\omega^{(n)}\overline{\xi}}\right] e^{-\overline{\xi}\overline{z}} & e^{\overline{\xi}\overline{z}} & \left[\overline{z} + \frac{\overline{\lambda}^{(n)}}{\omega^{(n)}\overline{\xi}}\right] e^{\overline{\xi}\overline{z}} \end{bmatrix}$$

$$(2.82)$$

In addition, the dimensionless quantities from the above equations are defined by

$$\kappa_n^s = 2\mu_n^s + \lambda_n^s \tag{2.83}$$

$$\Lambda = \frac{\kappa_1^s \left(\lambda^{(1)} + 2\mu^{(1)}\right)}{2\mu^{(1)} \left(\lambda^{(1)} + \mu^{(1)}\right)} \tag{2.84}$$

$$\overline{\mu}^{(n)} = \frac{\mu^{(n)}}{\mu^{(1)}} \tag{2.85}$$

$$\overline{\lambda}^{(n)} = \frac{\lambda^{(n)}}{\mu^{(1)}} \tag{2.86}$$

$$\omega^{(n)} = \overline{\lambda}^{(n)} + \overline{\mu}^{(n)} \tag{2.87}$$

$$\overline{\kappa}_n^s = \frac{\kappa_n^s}{\mu^{(1)}\Lambda} \tag{2.88}$$

$$\bar{\tau}_n^s = \frac{\tau_n^s}{\mu^{(1)}\Lambda} \tag{2.89}$$

$$\gamma_n = \frac{\omega^{(n)} \overline{\kappa_n}^s}{2\overline{u}^{(n)}} \tag{2.90}$$

$$\delta_n = \frac{\omega^{(n)} \overline{\tau}_n^s}{2\overline{\mu}^{(n)}} \tag{2.91}$$

$$\overline{z} = z / \Lambda \tag{2.92}$$

$$\bar{r} = r/\Lambda \tag{2.93}$$

$$\overline{\xi} = \xi \Lambda \tag{2.94}$$

in which the superscript letter "T" represents the transpose of a vector or a matrix. The superposed bar symbol, " $\bar{}$ ", denotes the non-dimensional quantities with respect to the properties of the first layer, Eqs. (2.83) to (2.94), where the tilde symbol, " $\bar{}$ ", denote the non-dimensional quantities in their Hankel transform space.

For the n^{th} layer, the displacements and traction at the top and bottom surfaces of the bulk can be formulated by using Eqs. (2.78) and (2.79) as follows:

$$\begin{cases}
 u_{z}(\overline{\xi},\overline{z}_{n}) \\
 u_{r}(\overline{\xi},\overline{z}_{n}) \\
 u_{z}(\overline{\xi},\overline{z}_{n+1}) \\
 u_{r}(\overline{\xi},\overline{z}_{n+1})
\end{cases} = \begin{bmatrix}
 \mathbf{R}^{(n)}(\overline{\xi},\overline{z}_{n}) \\
 \dots \dots \\
 \mathbf{R}^{(n)}(\overline{\xi},\overline{z}_{n+1})
\end{bmatrix} \mathbf{c}^{(n)}(\overline{\xi})$$
(2.95)

$$\begin{cases}
-\sigma_{zz}(\overline{\xi},\overline{z}_{n}) \\
-\sigma_{zr}(\overline{\xi},\overline{z}_{n}) \\
\sigma_{zz}(\overline{\xi},\overline{z}_{n+1}) \\
\sigma_{zz}(\overline{\xi},\overline{z}_{n+1})
\end{cases} = \begin{bmatrix}
-\mathbf{S}^{(n)}(\overline{\xi},\overline{z}_{n}) \\
\dots \\
\mathbf{S}^{(n)}(\overline{\xi},\overline{z}_{n+1})
\end{bmatrix} \mathbf{c}^{(n)}(\overline{\xi})$$
(2.96)

In addition to the stresses in the bulk, due to the presence of the surface energy effects, the terms corresponded to the surface effects, T_z^s and T_r^s , need to be considered in the same manner as the stresses. By considering the displacements continuity condition, Eq. (2.77), together with the

general solutions of normal displacement, radial displacement and their derivatives, Eqs. (2.18) and (2.19), the surface stresses can be represented as shown in the following equation:

$$\begin{cases}
-T_{z}^{s}(\overline{\xi},\overline{z}_{n}) \\
-T_{r}^{s}(\overline{\xi},\overline{z}_{n}) \\
0 \\
0
\end{cases} = \begin{bmatrix}
-\mathbf{Z}_{n}(\overline{\xi},\overline{z}_{n}) \\
.....
\\
0
\end{bmatrix} \mathbf{c}^{(n)}(\overline{\xi}) \tag{2.97}$$

where $T_z^s(\overline{\xi},\overline{z_n})$ and $T_r^s(\overline{\xi},\overline{z_n})$ are the Hankel transform of T_z^s and T_r^s , respectively, and the matrix \mathbf{Z}_n is given by

$$\mathbf{Z}_{n}(\overline{\xi},\overline{z}) = \left(\overline{\xi}^{2}\right) \begin{bmatrix} -\delta_{n}e^{-\overline{\xi}\overline{z}} & -\left(\overline{z} + \frac{2\overline{\mu}^{(n)}}{\omega^{(n)}\overline{\xi}}\right)\delta_{n}e^{-\overline{\xi}\overline{z}} & -\delta_{n}e^{\overline{\xi}\overline{z}} & -\left(\overline{z} - \frac{2\overline{\mu}^{(n)}}{\omega^{(n)}\overline{\xi}}\right)\delta_{n}e^{\overline{\xi}\overline{z}} \\ -\gamma_{n}e^{-\overline{\xi}\overline{z}} & \left(-\overline{z} + \frac{1}{\overline{\xi}}\right)\gamma_{n}e^{-\overline{\xi}\overline{z}} & \gamma_{n}e^{\overline{\xi}\overline{z}} & \left(\overline{z} + \frac{1}{\overline{\xi}}\right)\gamma_{n}e^{\overline{\xi}\overline{z}} \end{bmatrix}$$

$$(2.98)$$

Thereafter, the relationship between the displacements and traction at each layer is formulated. The stresses expressed in this relationship are the stresses in the bulk combining with the surface stresses of the interface between the layers. From Eqs. (2.96) and (2.97), the stresses terms can be merged as shown below.

$$\begin{cases}
-\sigma_{zz}(\overline{\xi},\overline{z}_{n}) \\
-\sigma_{zr}(\overline{\xi},\overline{z}_{n}) \\
\sigma_{zz}(\overline{\xi},\overline{z}_{n+1}) \\
\sigma_{zr}(\overline{\xi},\overline{z}_{n+1})
\end{cases} + \begin{cases}
-T_{z}^{s}(\overline{\xi},\overline{z}_{n}) \\
-T_{r}^{s}(\overline{\xi},\overline{z}_{n}) \\
0 \\
0
\end{cases} = \begin{bmatrix}
-\mathbf{S}^{(n)}(\overline{\xi},\overline{z}_{n}) - \mathbf{Z}_{n}(\overline{\xi},\overline{z}_{n}) \\
\mathbf{S}^{(n)}(\overline{\xi},\overline{z}_{n+1})
\end{bmatrix} \mathbf{c}^{(n)}(\overline{\xi})$$
(2.99)

In view of Eqs. (2.95) and (2.99), the following relationships can be established for the n^{th} layer:

$$\mathbf{\sigma}^{(n)} = \mathbf{K}^{(n)} \mathbf{u}^{(n)} \tag{2.100}$$

where

$$\boldsymbol{\sigma}^{(n)} = \begin{cases} -\left[\sigma_{zz}(\overline{\xi}, \overline{z}_n) + T_z^s(\overline{\xi}, \overline{z}_n)\right] \\ -\left[\sigma_{zr}(\overline{\xi}, \overline{z}_n) + T_r^s(\overline{\xi}, \overline{z}_n)\right] \\ \sigma_{zz}(\overline{\xi}, \overline{z}_{n+1}) \\ \sigma_{zr}(\overline{\xi}, \overline{z}_{n+1}) \end{cases}$$

$$(2.101)$$

$$\mathbf{u}^{(n)} = \begin{cases} u_z(\overline{\xi}, \overline{z}_n) \\ u_r(\overline{\xi}, \overline{z}_n) \\ u_z(\overline{\xi}, \overline{z}_{n+1}) \\ u_r(\overline{\xi}, \overline{z}_{n+1}) \end{cases}$$

$$(2.102)$$

$$\mathbf{K}^{(n)} = \begin{bmatrix} -\mathbf{S}^{(n)}(\overline{\xi}, \overline{z}_n) - \mathbf{Z}_n(\overline{\xi}, \overline{z}_n) \\ \dots \\ \mathbf{S}^{(n)}(\overline{\xi}, \overline{z}_{n+1}) \end{bmatrix} \begin{bmatrix} \mathbf{R}^{(n)}(\overline{\xi}, \overline{z}_n) \\ \dots \\ \mathbf{R}^{(n)}(\overline{\xi}, \overline{z}_{n+1}) \end{bmatrix}^{-1}$$
(2.103)

The advantage of using the exact stiffness matrix scheme is that the condition number of the equation system is relatively low compared to the conventional technique (Senjuntichai and Rajapakse, 1995). To assemble the global stiffness matrix of the multi-layered elastic medium, the continuity conditions of traction and displacements at each surface are imposed. From the continuity conditions in Eqs. (2.75) to (2.77) and the relationship between the displacements and traction at each layer in Eq. (2.100), the global equation system can then be established as

$$\mathbf{K}^*\mathbf{U}^* = \mathbf{F}^* \tag{2.104}$$

in which

$$\mathbf{F}^* = \frac{1}{2\overline{\xi}^2} \left[P(\overline{\xi}) \quad Q(\overline{\xi}) \quad 0 \quad 0 \quad \cdots \quad 0 \quad 0 \right]^T \tag{2.105}$$

$$\mathbf{U}^* = \begin{bmatrix} u_z(\overline{\xi}, \overline{z}_1) & u_r(\overline{\xi}, \overline{z}_1) & u_z(\overline{\xi}, \overline{z}_2) & u_r(\overline{\xi}, \overline{z}_2) & \cdots & u_z(\overline{\xi}, \overline{z}_{N+1}) & u_r(\overline{\xi}, \overline{z}_{N+1}) \end{bmatrix}^T$$
(2.106)

and the matrix \mathbf{K}^* is the global stiffness matrix established by assembling the matrix $\mathbf{K}^{(n)}$ from Eq. (2.103) with the consideration of the continuity conditions of traction and displacements from Eqs. (2.75) to (2.77) at each surface. The functions $P(\bar{\xi})$ and $Q(\bar{\xi})$ are the Hankel transform of the normalized surface loading, i.e. $p(r)/\mu^{(1)}$ and $q(r)/\mu^{(1)}$ respectively. The solution to the above global equation system yields the Hankel transforms of the displacements at each layer interface. Hankel transforms of the stresses at the layer interfaces can then be obtained by substituting the solution to the displacements into Eq. (2.100). Finally, the displacement and stress fields can be determined by applying an accurate numerical quadrature scheme. In the next chapter, the procedure and the details of the numerical quadrature scheme are provided followed by the verification of the scheme on existing solutions. Thereafter, parametric studies investigation are conducted based on practical models to study the influence of various parameters on elastic fields of the layered medium.

2.6 Numerical results

The numerical solutions of displacements and stresses for a layered elastic half-space and a multi-layered elastic medium under axisymmetric surface loading as shown in Figure 2.1 and 2.2 respectively are presented to illustrate the nano-scale influence through the surface stress effects and size dependent behaviors.

2.6.1 Numerical scheme

A computer code based on the boundary value problem described in the previous section has been developed to evaluate all elastic fields of a layered elastic half-space and a multi-layered elastic medium under axisymmetric surface loading. A closed-form solution to the displacement and stress fields cannot be obtained in Eqs. (2.18) to (2.23). Therefore it is essential to determine all elastic fields by numerically evaluating the semi-infinite integrals appearing in Eqs. (2.18) to

(2.23). It is found that those semi-infinite integrals with respect to ξ can be accurately evaluated by employing an adaptive numerical quadrature scheme. This scheme subdivides the interval of integration and employs a 21-point Gauss–Kronrod rule (Piessens et al., 1983) to estimate the integral over each subinterval. The error for each subinterval is estimated by comparing the obtained results with those from a 10-point Gauss-Kronrod rule. The subdivision continues until the error from the approximation is reached a specified tolerance.

2.6.2 Verification

The accuracy of the proposed solution scheme is first verified by comparing with the existing solution given by Gerrard (1969), who presented the classical solutions (without the influence of surface energy effects) of a layered elastic half-space subjected to axisymmetric surface loading. Table 2.1 presents a comparison of normalized displacements at the surface (z = 0) and normalized stresses at the interface (z = h) along the radial direction of a layered elastic half-space under uniformly distributed normal traction p_0 , acting over a circular area of radius a at the surface. The comparison of surface displacements and stresses at the interface of the layered half-space under linearly distributed shear traction $\bar{q}(\bar{r}) = -q_0 r/\mu_1 a$ applied over a circular area of radius a at the surface is also presented in Table 2.2. In addition, $\mu_1/\mu_2 = 5$ with Poisson's ratio $\nu_1 = \nu_2 = 0.2$, and h/a = 1 are considered for the numerical results given in both tables. The solutions for normalized displacements and stresses from the present study are obtained by setting the parameters associated with the surface energy effects to be zero, i.e., $\tau^s \cong 0$ and $\kappa^s \cong 0$. It is evident that excellent agreement between the two solutions is observed for both displacements and stresses shown in Tables 2.1 and 2.2.

The proposed exact stiffness matrix scheme for a multi-layered medium is validated by comparing with the solution by Katebi and Selvadurai (2013) for an elastic functionally graded layer, called FG layer, over an underlying half-space subjected to uniformly distributed loading. The FG layer is modelled as a multi-layered medium with their elastic material properties vary through the layer thickness by the grading exponential function $\mu(\bar{z}) = \mu_0 e^{\bar{m}\mu_0\bar{z}}$ where \bar{m} is the grading constant and μ_0 is the shear modulus corresponding to the material of the top surface with the constant Poisson's ratio of 0.5. The FG layer is divided into a number of sublayers where each layer has the same thickness, the shear modulus within each layer is constant and it is computed at the mid-height of the layer. The appropriate number of sublayers to represent the FG layer is studied and as the normalized thickness of the layer is 1.0, ten sublayers are acceptable, in which the error occurred from this model is less than 0.01%. To improve the accuracy, the FG layer can be divided where the thickness of each layer is different corresponding to the gradient of the grading function. The properties of the remaining half-space are the same as the properties of the material at the lower surface of the layer. The half-space is modelled as 10 sublayers of elastic layers with uniform thickness of 0.1 on a relatively large elastic layer over rigid base. The medium is subjected to the internal axisymmetric uniform vertical loading applied at the interface between FG layer and homogeneous half-space. The internal loading function is expressed in the following equation:

$$p(r) = p_0 H(a - r) \tag{2.107}$$

where H(a-r) is the Heaviside step function, a is the loading radius and p_0 is the loading magnitude. The ratio of the layer thickness to the radius of the loading H/a is set to 1.0. The verification of the vertical displacement at the interface along the radial direction is illustrated in Figure 2.3(a) for the case where $\bar{m}=0.25$, 1.0 and 1.5, and the normal stress along the vertical direction when H/a ratio is set to 2.0 for the case when $\bar{m}=0.0$, 0.5 and 1.0 is presented in Figure 2.3(b). Both solutions show excellent agreement with the corresponding existing solutions given by Katebi and Selvadurai (2013).

2.6.3 Numerical solution for layered elastic half-space under surface loading

Numerical results for vertical and radial displacements, and vertical and shear stresses corresponding to a layered elastic half-space with the influence of surface energy effects subjected to axisymmetric surface loading as shown in Figure 2.1 are presented next. Two cases of axisymmetric surface loading, namely, the *vertical* loading and the *radial* loading are considered in the numerical study. The *vertical* loading denotes the case where uniformly distributed normal traction p_0 applied over a circular area of normalized radius $a/\Lambda_1 = \overline{a} = 10$. The *radial* loading represents the case where the layered half-space is subjected to linearly distributed tangential traction $\overline{q}(\overline{r}) = q_0 \overline{r}/\mu_1 \overline{a}$ over a circular area of normalized radius $\overline{a} = 10$, where q_0 is the maximum traction at the edge of the loading region. The functions defined as shown in Eqs. (2.36) and (2.37) are given respectively for the *vertical* loading and the *radial* loading as follows,

$$\bar{P}(\xi) = \frac{p_0 \bar{a}}{\xi} J_1(\xi \bar{a}) \text{ and } \bar{Q} = 0$$
(2.108)

$$\overline{P} = 0 \text{ and } \overline{Q}(\xi) = \frac{2q_0}{\xi^2} J_1(\xi \overline{a}) - \frac{q_0 \overline{a}}{\xi} J_0(\xi \overline{a})$$
 (2.109)

In addition, the numerical results presented hereafter correspond to the case where the material for the upper layer (the domain '1') is Si [100] whereas Al [111] is chosen for the underlying half-space (the domain '2') respectively. The material properties for both domains are given in Table 2.3 (Miller and Shenoy, 2000).

Figures 2.4 presents radial variations of non-dimensional displacements at the top surface (z=0) and non-dimensional stresses at the interface (z=h) of a layered elastic half-space under the vertical loading for different values of normalized thickness of the top layer (h/a). Note that the stress profiles in all figures presented in this section are computed at the interface (z=h) at the bulk material of the underlying half-space. Figure 2.4(a) shows radial profiles of vertical and radial surface displacements for various values of h/a whereas the profiles of normal and shear stresses at the interface are illustrated in Figure 2.4(b). The classical solutions also presented in these figures for comparison are obtained by setting the parameters associated with the surface energy effects to be zero, i.e., $\tau^s = 0$ and $\kappa^s = 0$. It is evident from Figure 2.4 that although the results from the present study and the classical solution display similar trends for both displacements and stresses at all values of h/a, the surface energy effects renders the layered medium stiffer. The present solution yields lower surface displacements and stresses at the interface. The influence of surface energy is however less significant in the interface stresses, especially in the case of the shear stress. It is also found that the magnitude of all displacements and stresses decrease with increasing the normalized thickness of the layer (h/a) since the upper layer is stiffer than the

underlying half-space (Lamé constants of Si [100] are higher than those of Al [111]). In addition, as the layer thickness increases both vertical and radial surface displacements move towards the homogeneous half-space solutions presented by Intarit (2012), and both solutions are virtually identical when $h/a \ge 100$.

Radial profiles of normalized surface displacements (z=0) and normalized stress at the interface (z=h) of the layered elastic medium under the vertical loading are shown in Figure 2.5 to demonstrate the influence of the residual surface stress (τ^s) on elastic fields. The values of the residual surface stress in the underlying half-space are varied (i.e. $\tau_2^s=0.1$, 1, 5, 10 N/m) whereas other material parameters associated with both upper layer and underlying half-space given in Table 2.3 remain unchanged. In addition, the normalized thickness of h/a=1 is considered in the numerical results shown in this figure. Once again, the influence of the surface stress is clearly observed from the displacement and stress solutions presented in Figure 2.5. The values of all displacements and stresses from the present study are substantially reduced from their classical elasticity counterparts as the value of the residual surface stress increases.

The next numerical results are presented to demonstrate the size-dependent behavior of the present solution when the influence of surface energy effects is considered. Figure 2.6 shows radial variations of vertical and radial surface displacements, and the vertical and shear stresses at the interface of the layered half-space under the vertical loading for different values of the normalized radius of loading area \bar{a} (i.e. $\bar{a} = a/\Lambda_1 = 1, 5, 10$). In addition, the thickness of the top layer and the circular loading area are varied while their ratio is maintained at h/a = 1. Note that the solution when $\bar{a} = 1$ corresponds to the case where the thickness of the layer is equal to the characteristic length (Λ_1) . The corresponding non-dimensional solution for the classical elasticity case is also shown, and it is size-independent. The size-dependency of the present solution is clearly observed in all displacement and stress profiles. It is evident from the numerical results presented in Figure 2.6 that the present solution accounting for surface energy effects approaches the classical solution as the loading radius increases. This is consistent with the fact that a larger loading area would produce higher displacements and stresses.

The final set of the numerical results corresponds to the case where the layered elastic half-space is subjected to the radial loading, in which the tangential traction is applied linearly distributed over a circular area of normalized radius $\bar{a}=10$. Figure 2.7 presents radial profiles of non-dimensional displacements at the top surface (z=0) and non-dimensional stresses at the interface (z=h) for different values of h/a. It is evident from Figure 2.7 that both displacements and stresses of the layered half-space under radial loading depend more significantly on surface energy effects for all values of h/a when compared to the results presented in Figure 2.4 under the vertical loading case. The presence of surface stresses significantly lowers the magnitude of all displacements and stresses shown in Figure 2.7. In addition, all displacements and stresses are reduced as the normalized thickness of the layer (h/a) increases. Once again, both vertical and radial surface displacements are practically the same as the half-space solutions given by Intarit (2012) when $h/a \ge 100$ similar to what observed in the vertical loading case.

2.6.4 Numerical solution for multi-layered medium over rigid base under vertical surface loading

A model of Si/Al multi-layered medium resting on a rigid base is selected since Si/Al multi-layered structure is one of the most well-known systems for micro- and nano-electronic materials

(Nakayama et al., 1995). The multi-layered medium consists of two different materials stacking alternately throughout the total thickness, H. The odd layers are Si [100] and the even layers are Al [111] where the thicknesses of both layers, h_1 and h_2 , are both equal to 0.2 nm. The thickness of the medium is equal to 1 μ m and subjected to top surface axisymmetric loading with the loading function as shown in Eq. (2.107) where the normalized thickness \bar{a} , a/Λ , equal to 1.0. The boundary value problem is illustrated in Figure 2.8. The material properties of Si [100] and Al [111] are shown in Table 2.3 where the surface properties of Si [100] are selected as the properties of the top surface and the surface properties of Al [111] are hypothetically selected as the properties of other interfaces. From Table 2.3, the material length scale Λ of Si [100] is equal to 0.16739 nm which is used as the structure length scale to normalize every dimensional parameter. Therefore, the normalized thickness of each layer is equal to 1.195 and the loading radius is equal to 0.16739 nm. In addition, the superposed bar symbol "" implies that the parameter below the symbol is normalized with the material length scale.

Figure 2.9 shows the vertical displacement and the normal stress of the Si/Al multi-layered medium at different profiles along the radial direction for the cases where the surface energy effects are considered and ignored. The monitoring profiles for the displacement are the top surface where z=0 nm, the second surface where z=0.2 nm and the third surface where z=0.4 nm while for the stress, the same set of monitoring profiles are used except for the first profile, the profile at the middle of the first layer where z=0.1 nm is used instead. It can be implied from the results that the influence of the surface energy effects is significant to the vertical displacement and normal stress at all profiles shown in Figure 2.9, especially the profile close to the top surface where the loading is applied.

The influence of the surface energy effects at the interface is investigated next by varying the surface elastic properties at each interface. The residual surface stress of the interfaces τ_2^s is varied whereas the residual surface stress of the top surface τ_1^s remain the same. The results, displacements at the top surface and stresses at the profile z=0.1 nm, are obtained with the ratio of the residual surface stress of the interface to the top surface, τ_R , being -0.5, 1.0, 2.0 and 5.0 while the value of κ^s remains the same for all cases. The similar trends can be observed in all the results shown in Figure 2.10, i.e. the value at every points of all the results converged to zero when the ratio increases. This means that the increment of the effects renders the medium stiffer than those with lesser value of the τ_R ratio, and the residual surface stress at every interface contributes significantly to the results in this model. Note that the surface elastic constant κ^s shows negligible influence on the results compared to the residual surface stress τ^s (Intarit, 2012).

Although the size dependency effect has been studied by various researchers, the effect on a multi-layered medium is the topic that has not been discussed yet. The numerical experiments have been conducted on a default model to obtain vertical displacement and normal stress at the depth of z=0.0 nm for the displacement, z=0.1 nm for the stress and $\overline{r}/\overline{a}=0.5$ for both fields while varying the parameter \overline{a} . The ratio $\overline{H}/\overline{a}$ is kept constant for every \overline{a} . The influence of the size dependency effect is illustrated in Figure 2.11, which indicates the trend of the elastic fields when the parameter \overline{a} is changed. The differences between the elastic fields, with and without the surface energy effects, are reduced when \overline{a} is increased. However, the differences are significant

when the value of \bar{a} is small, approximately below 2.0. Additionally, the results of the present study agree well with the work from Rungamornrat et al. (2016).

The capability of the numerical scheme in terms of applied loading cases is also investigated in this study. Three different types of axisymmetric loading cases are chosen with the same amount of total force, namely, uniformly distributed vertical loading as shown in Eq. (2.107), the contact pressure from the flat-ended rigid punch and the contact pressure from the paraboloid revolutionary rigid punch. The second and third loading cases are the assumed forms of loading function, which provides the similar contact pressure to flat-ended rigid punch and paraboloid revolutionary rigid punch indentation problem respectively, when applied to the homogeneous half-space medium. The assumed form of loading function of the flat-ended rigid punch is expressed in the following equation (Sneddon, 1965):

$$\overline{p}(\overline{r}) = \left(p_0/\mu^{(1)}\overline{a}\right) / \sqrt{\left(1 - \left(\overline{r}/\overline{a}\right)^2\right)} \cdot H(\overline{a} - \overline{r})$$
(2.110)

and the assumed form of loading function for paraboloid revolutionary case (Sneddon, 1965) is

$$\overline{p}(\overline{r}) = \left(p_0/\mu^{(1)}\overline{a}\right)\sqrt{\left(1-\left(\overline{r}/\overline{a}\right)^2\right)} \cdot H(\overline{a}-\overline{r}) \tag{2.111}$$

where $H(\bar{a}-\bar{r})$ is the Heaviside step function. The vertical displacement of the top surface and the normal stress at the profile z=0.1 nm are plotted in Figure 2.12. The vertical displacements of the flat ended and paraboloid revolutionary cases shown in Figure 2.12 reflect the flat and paraboloid shapes respectively. The influence of surface energy effects can be found at all results corresponding to the three loading cases. The flat ended loading case provides the maximum displacement whereas the paraboloid revolutionary case yields the minimum displacement. In addition, the influence of the surface energy effects is significant only under the contact area of the loading where $\bar{r}/\bar{a} \leq 1.0$.

2.6.5 Numerical solution for functionally graded layer on a homogeneous elastic layer under uniform vertical surface loading

The elastic properties of the FG layer vary in the z-direction from the elastic properties of Si [100] at the depth $\bar{z}=0.0$ to the elastic properties of Al [111] at the depth $\bar{z}=\bar{h}_{\rm l}$ where $\bar{h}_{\rm l}$ is the normalized thickness of the FG layer as shown in Figure 2.13. The variational pattern of the elastic properties of the FG layer is determined by the grading function in which the exponential function, $L(\bar{z})=L_0e^{\bar{m}L_0\bar{z}}$ where \bar{m} is the grading constant and L_0 is the Lame' constants of Si [100], is selected for all cases. The value of the grading constant \bar{m} is obtained by back calculation from the known elastic properties at the depth $\bar{z}=0.0$ and $\bar{z}=\bar{h}_1$. The FG layer is divided into 10 sublayers where the elastic properties of each layer are assigned in the same manner as the verification model. The underlying homogeneous elastic layer is a layer of Al [111] and its layer thickness is equal to h_2 . The \bar{h}_1/\bar{h}_2 ratio is set to 9.0 where the ratio \bar{H}/\bar{a} and the loading radius \bar{a} are both set to 1.0. This model is subjected to the same loading case as the multi-layered model, Eq. (2.107). The surface elastic properties of the top surface and the interface of this model are equal to the surface properties of Si [100] and Al [111] respectively.

The top surface vertical displacement corresponding to the variation of the thickness ratio between upper and lower layer are illustrated in Figure 2.14 with \bar{H}/\bar{a} being fixed at 1.0. Since Al [111] has lower elastic properties than Si [100], the obtained displacement then becomes maximal when the thickness of Al [111] is 9.0, which is the largest thickness considered in the Figure 2.14. The influence of the total thickness H on the top surface vertical displacement of the FG layer model when the total thickness is increased whereas the first layer thickness remains the same is presented in Figure 2.15. As the thickness increases, the influence of the surface energy effects increases.

The vertical displacement profiles along the radial direction at each profile through the thickness of the multi-layered medium have been plotted to study the surface energy influence when the distance between the selected profiles and the top surface increases. The results illustrated in Figure 2.16 can be implied in the same way as the multi-layered model, i.e. the influence of the surface energy effects on the displacement is lower when the distance between the profile and the top surface increases. The effect of the residual surface stress τ^s on the FG layer problem is studied next. Figure 2.17 shows the displacements profiles at the top surface and the stresses profiles at the interface between the FG layer and the homogeneous layer with the value of τ_R being -0.5, 1.0, 2.0 and 5.0. The similar trend to the Si/Al multi-layered model can be observed in Figure 2.17 where the presence of the residual surface stress renders the medium stiffer.

Finally, the influence of grading function on elastic fields of the FG layer is considered. To investigate the difference between the grading function of the FG layer, three grading functions, namely, linear, exponential and power law distributed grading function, have been employed to observe the variation of the top surface vertical displacement and normal stress at the interface. The linear grading function is given by

$$L(\overline{z}) = L^{(1)}(1 + m\overline{z}) \tag{2.112}$$

where
$$m = (L^{(N)} - L^{(1)}) / (L^{(1)} \overline{h}_1)$$
.

In addition, the power law distributed grading function can be expressed as

$$L(\overline{z}) = L^{(1)} \left(1 + \overline{z}/\overline{h}_1\right)^m \tag{2.113}$$

where
$$m = \log_2(L^{(N)}/L^{(1)})$$
 and $\overline{z} \le \overline{h}_1$.

The special case of the FG layer has been introduced to emphasize the difference between the results among gradation functions. The elastic properties of the top surface and the interface, previously assigned as the properties of Si [100] and Al [111] respectively, are substituted by the 1st material and the 2nd material for this special case, which are $\mu_1 = 100$ GPa, $\lambda_1/\mu_1 = 1.5$ for the 1st material and $\mu_2 = 10$ GPa, $\lambda_2/\mu_2 = 1.5$ for the 2nd material. The ratio \bar{h}_2/\bar{h}_1 for this special case is set to 1.5, the thickness \bar{h}_1 is 0.4, the ratio \bar{H}/\bar{a} is kept at 1.0 and the surface quantities at the top surface and the interface remain unchanged from the FG model. The results show that the grading function that yields the stiffest medium is the linear distribution, followed by the exponential and the power law respectively as shown in Figure 2.18. However, the results also

show that the selection of grading function is significant only for the extreme cases where the variation of elastic properties and the thickness is large enough.

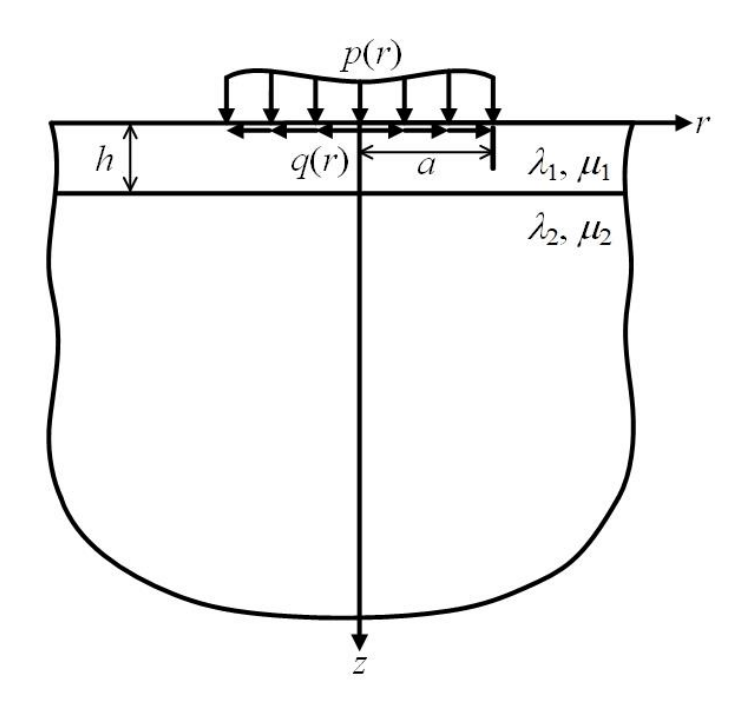


Figure 2.1 Layered elastic half-space subjected to axisymmetric surface loading

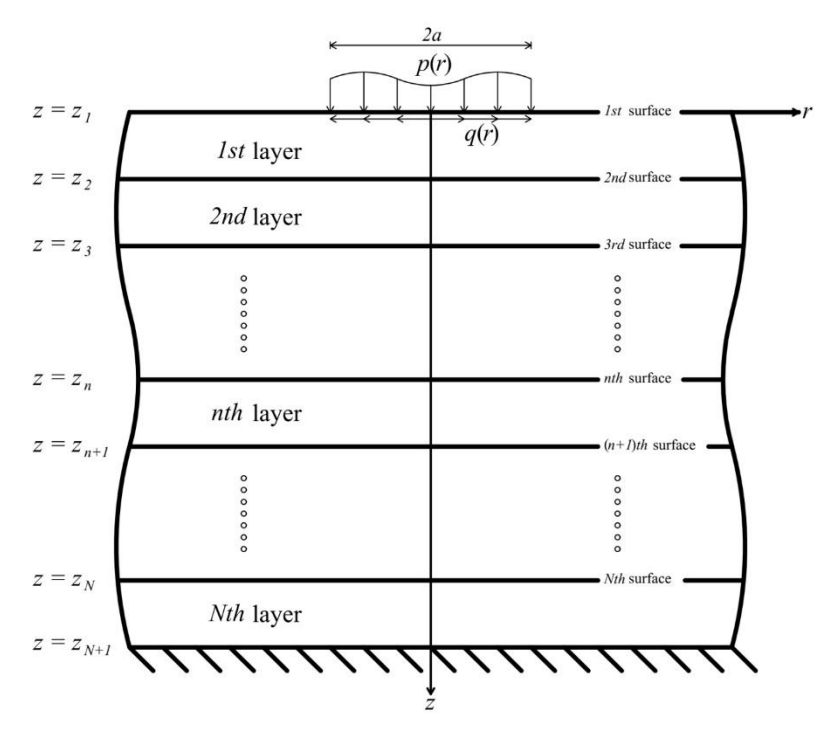
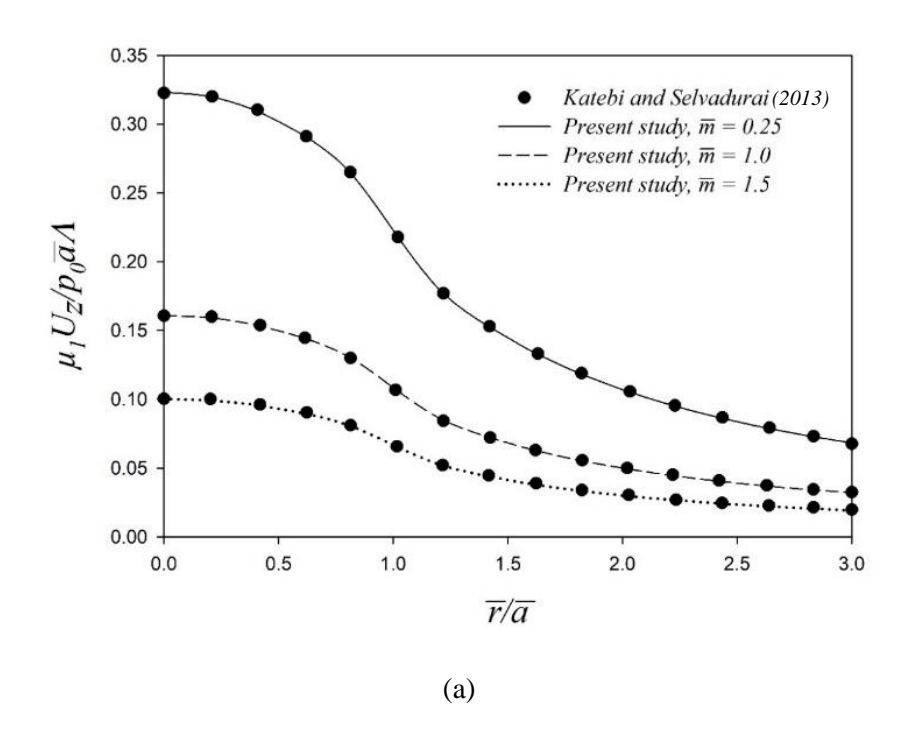


Figure 2.2 Multi-layered elastic medium over rigid base under axisymmetric surface loading



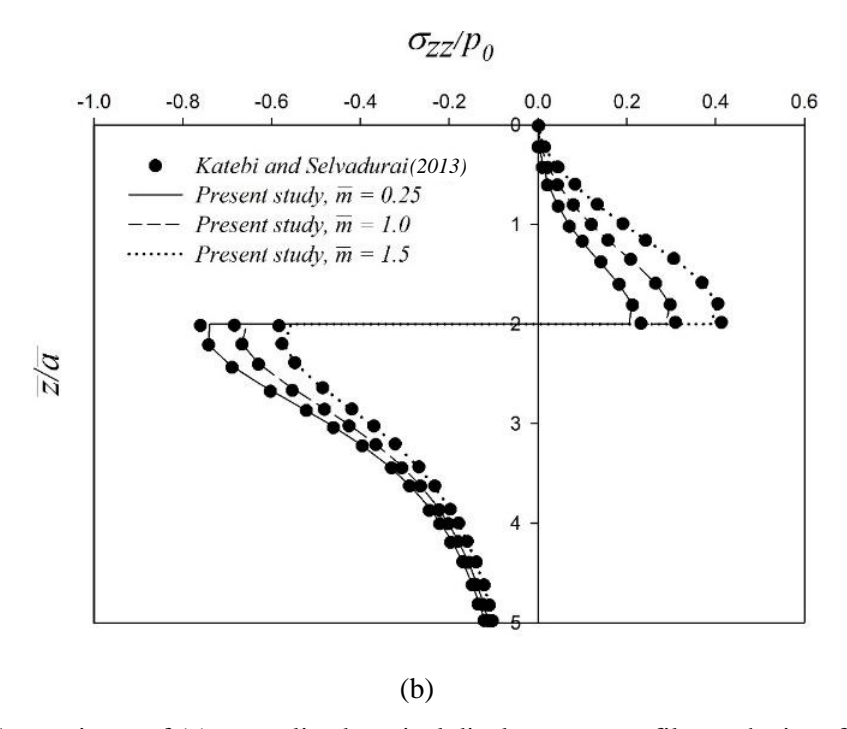


Figure 2.3 Comparisons of (a) normalized vertical displacement profiles at the interface; and (b) normalized normal stress profiles along the *z*-axis of a FG layer over an elastic half-space

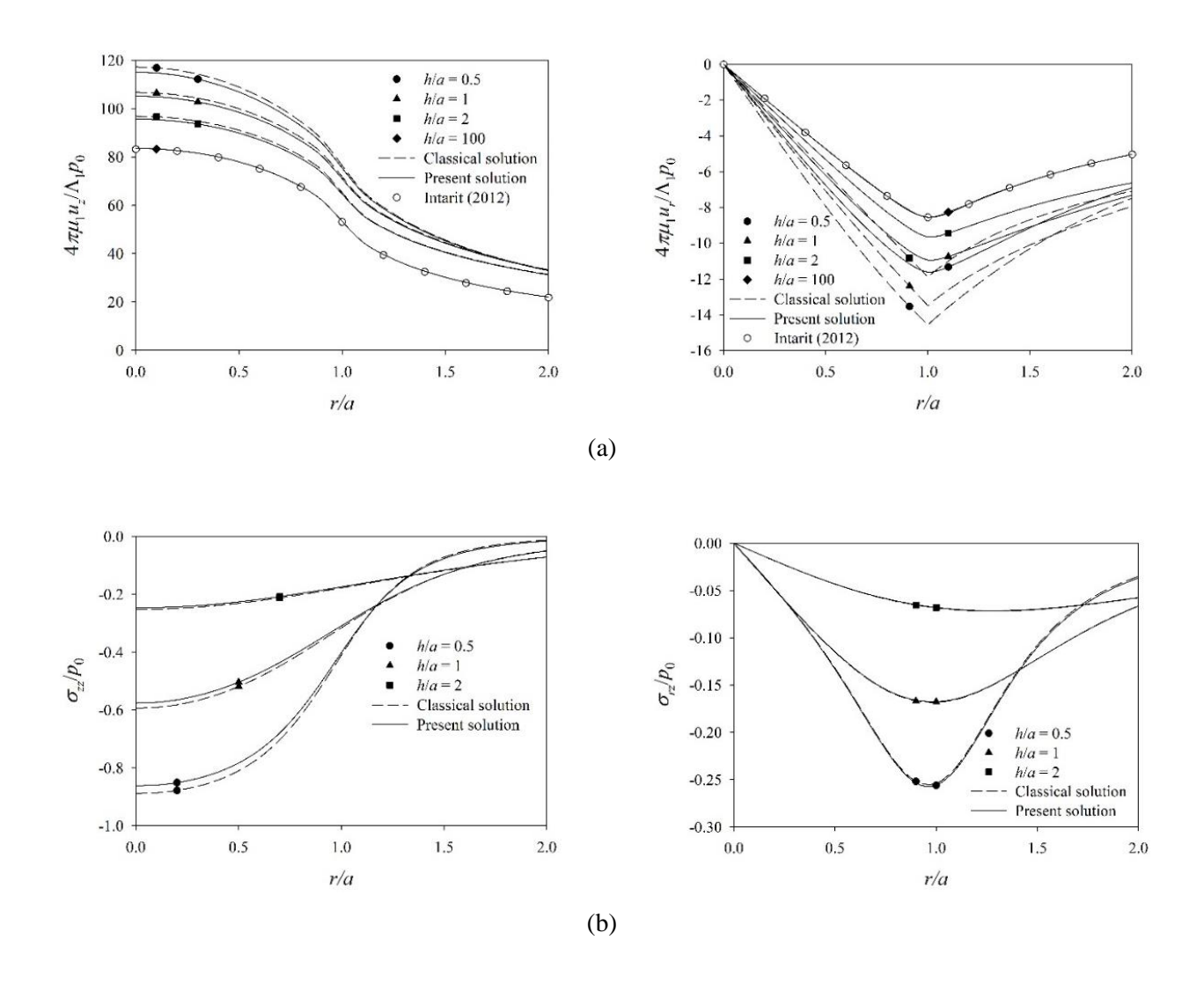


Figure 2.4 Radial variations of elastic fields under the vertical loading for different values of layer thickness (h/a): (a) surface displacements (z = 0) and (b) stresses at the interface (z = h).

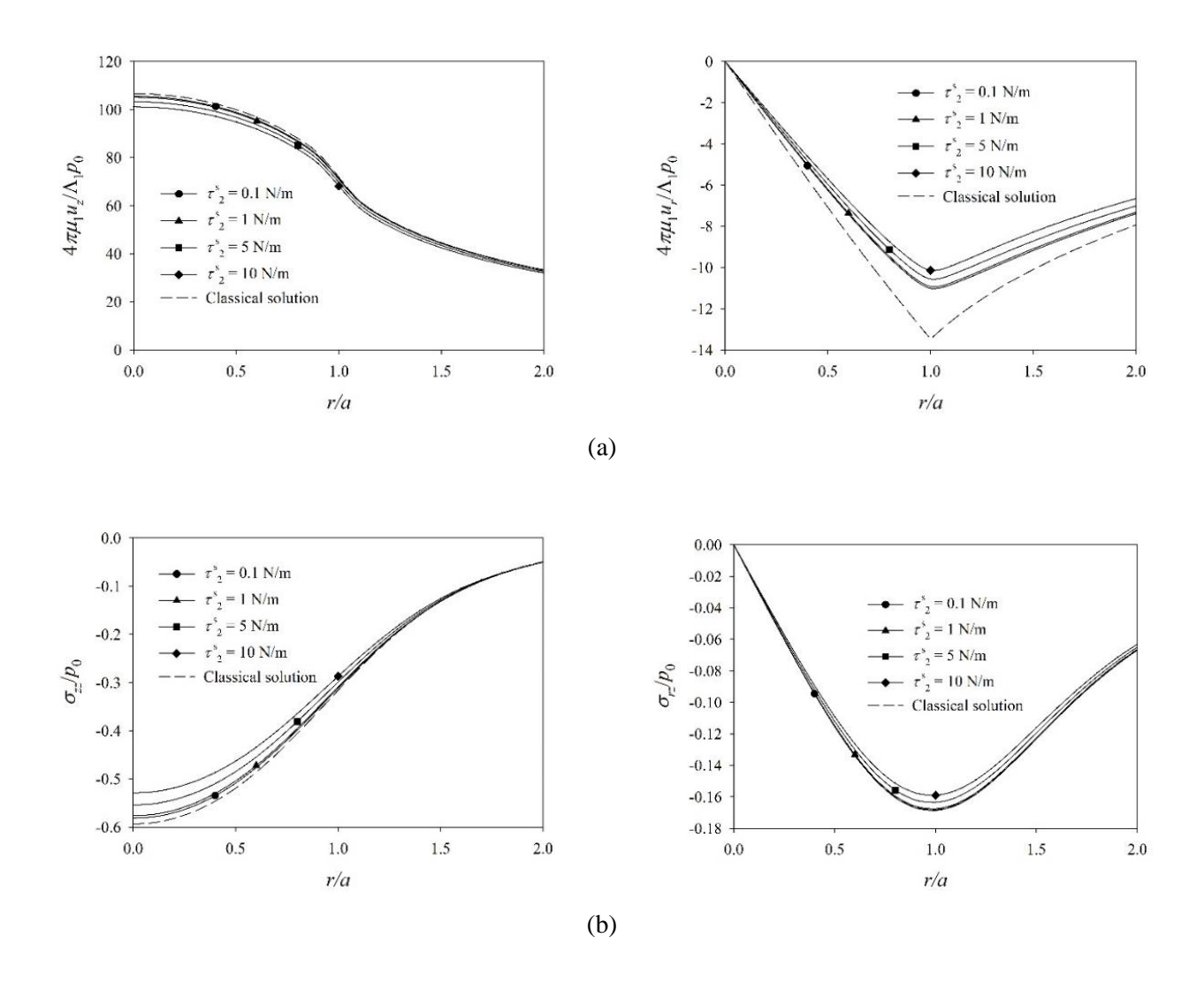


Figure 2.5 Radial variations of elastic fields under the vertical loading for h/a = 1 and different magnitudes of residual surface stress (τ^{s_2}): (a) surface displacements (z = 0) and (b) stresses at the interface (z = h).

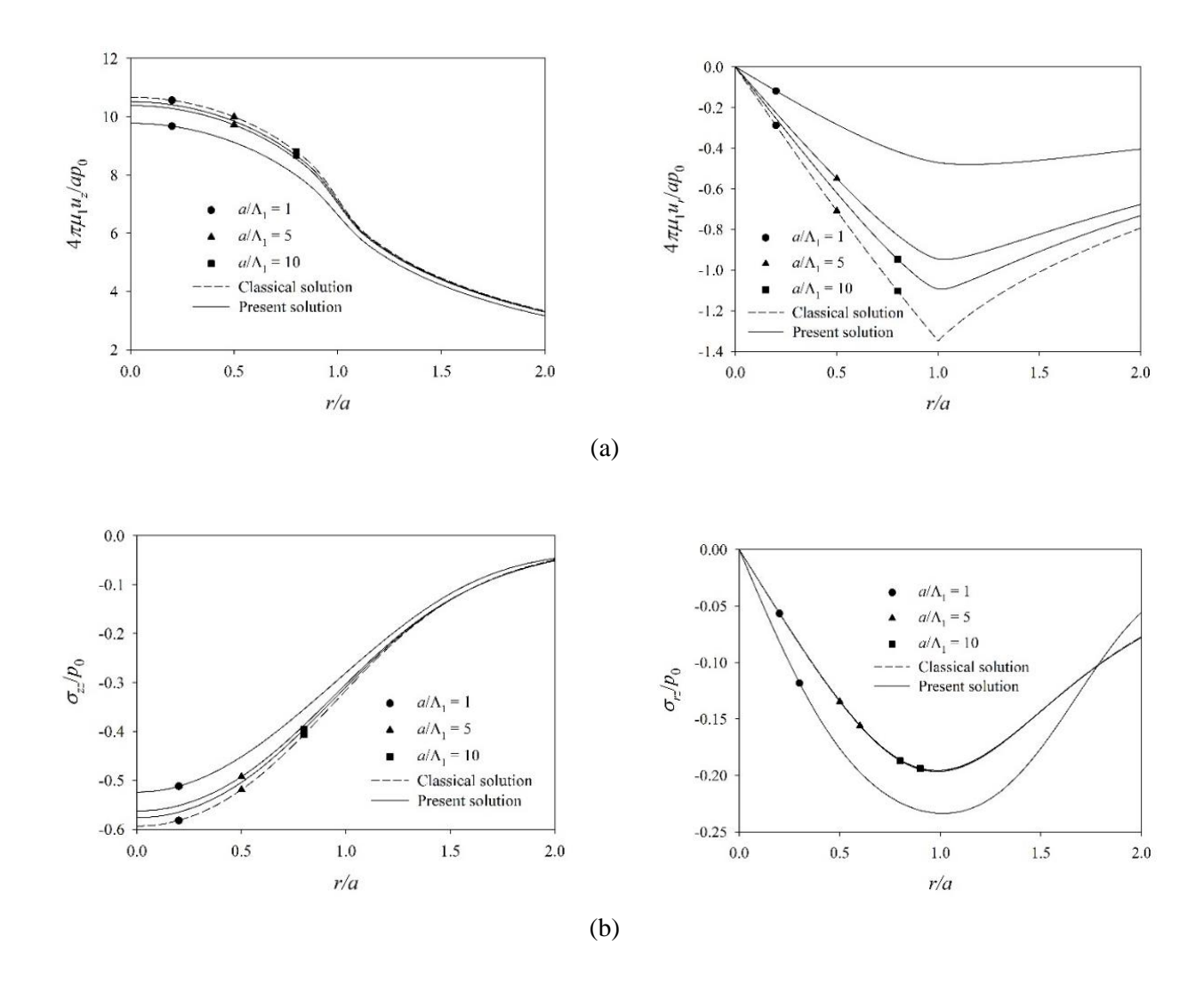


Figure 2.6 Radial variations of elastic fields under the vertical loading for h/a = 1 and different values of loading radius (\overline{a}): (a) surface displacements (z = 0) and (b) stresses at the interface (z = h).

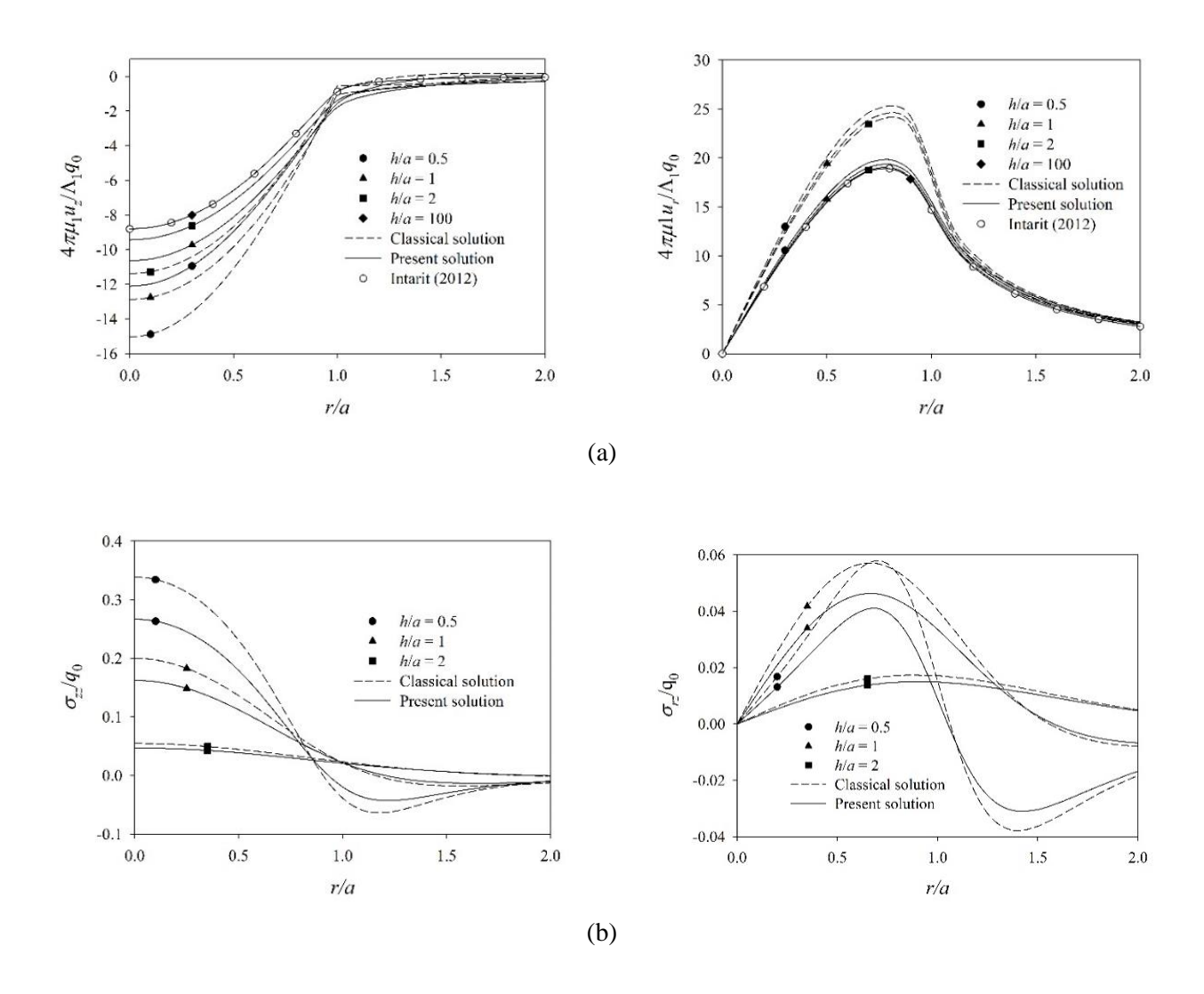


Figure 2.7 Radial variations of elastic fields under the radial loading for different values of layer thickness (h/a): (a) surface displacements (z = 0) and (b) stresses at the interface (z = h).

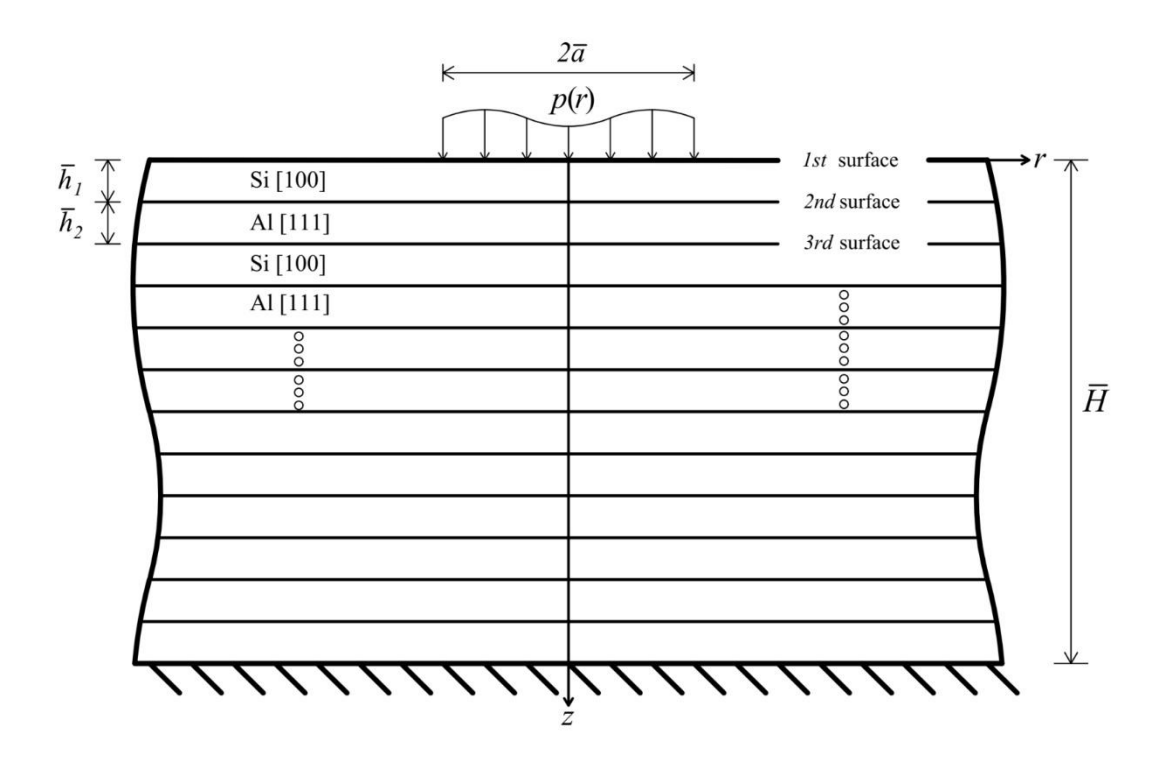


Figure 2.8 Multi-layered medium consisting of Si [100] and Al [111] under vertical surface loading

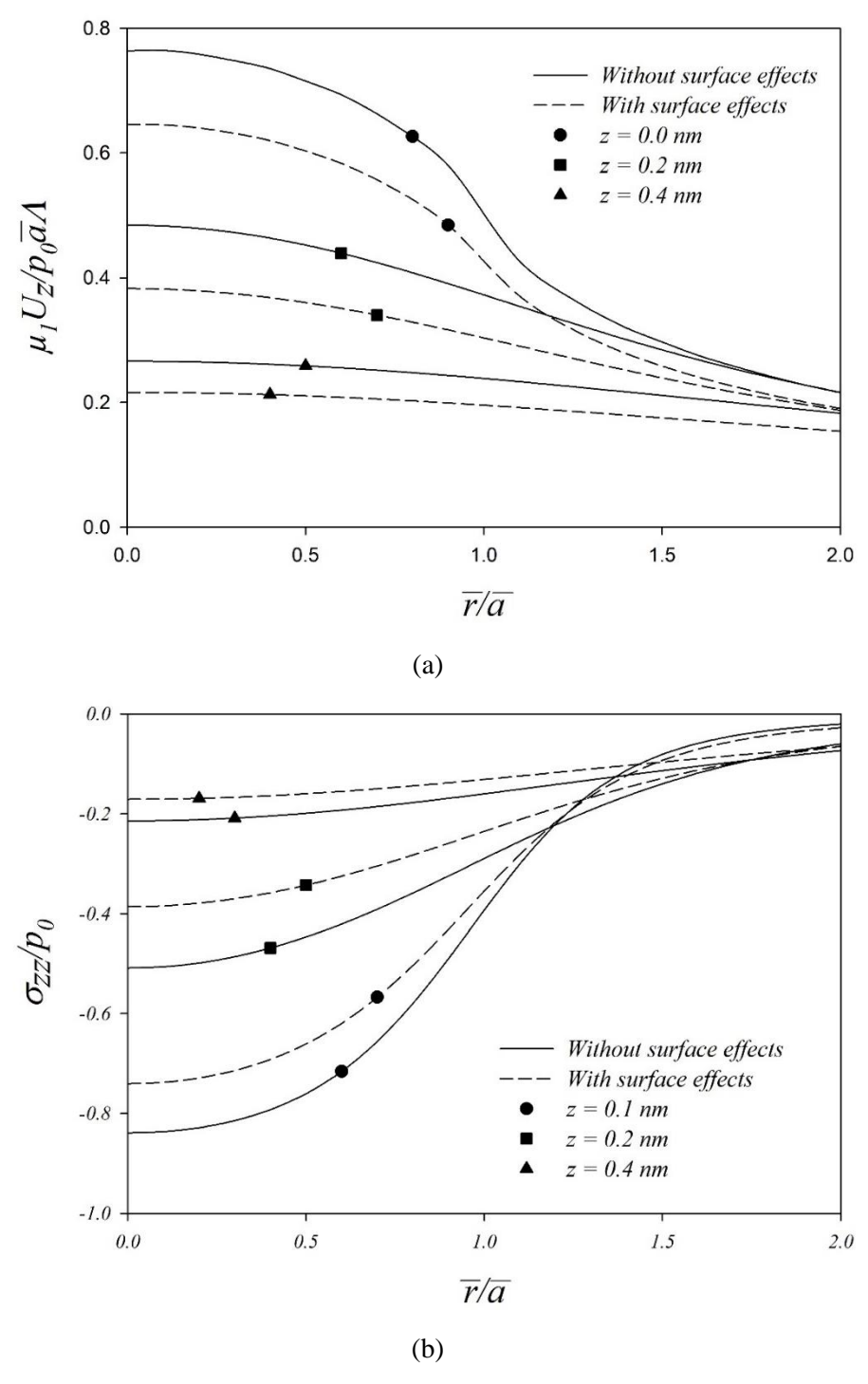


Figure 2.9 Radial profiles of elastic fields of the Si/Al multi-layered medium at defferent depths: (a) normalized vertical displacement; and (b) normalized normal stress

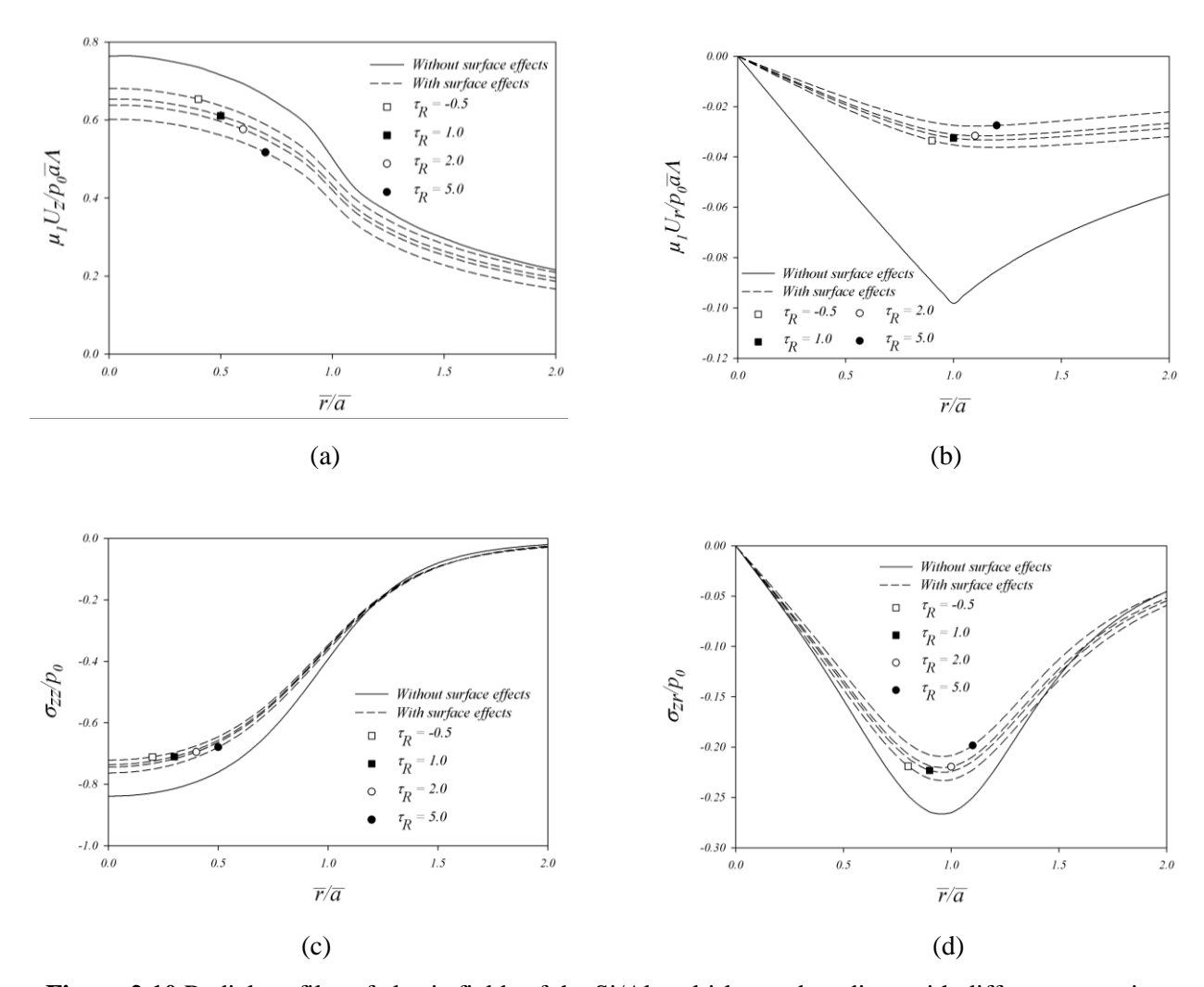


Figure 2.10 Radial profiles of elastic fields of the Si/Al multi-layered medium with different τ_R ratios: (a) normalized vertical surface displacement; (b) normalized radial surface displacement; (c) normalized normal stress at z=0.1 nm; (d) normalized shear stress at z=0.1 nm

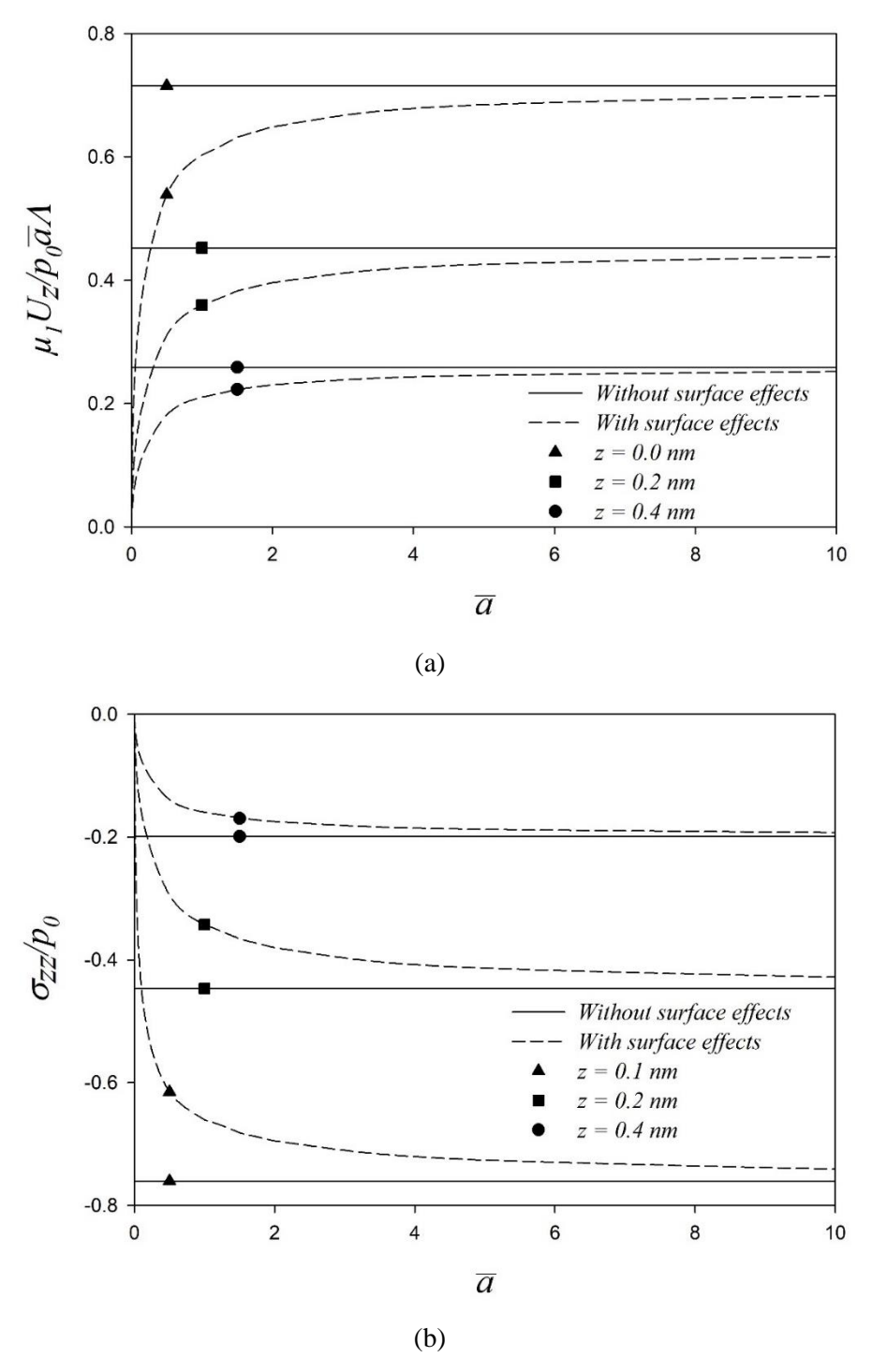


Figure 2.11 Variation of elastic fields of the Si/Al multi-layered medium with normalized loading radius \overline{a} at different depths: (a) normalized vertical displacement; (b) normal stress

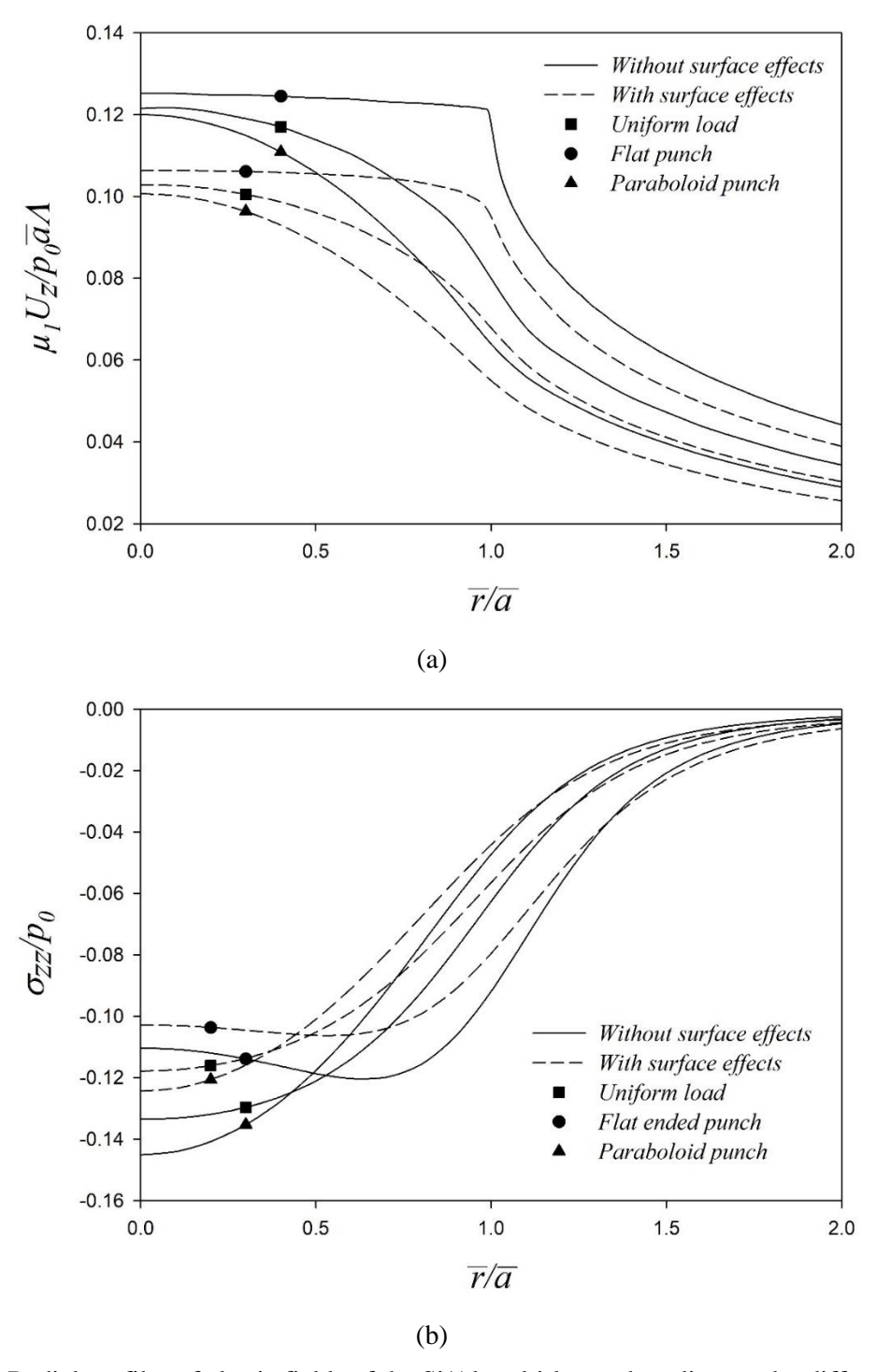


Figure 2.12 Radial profiles of elastic fields of the Si/Al multi-layered medium under different types of surface loading: (a) normalized vertical surface displacement; and (b) normalized normal stress at z = 0.1 nm

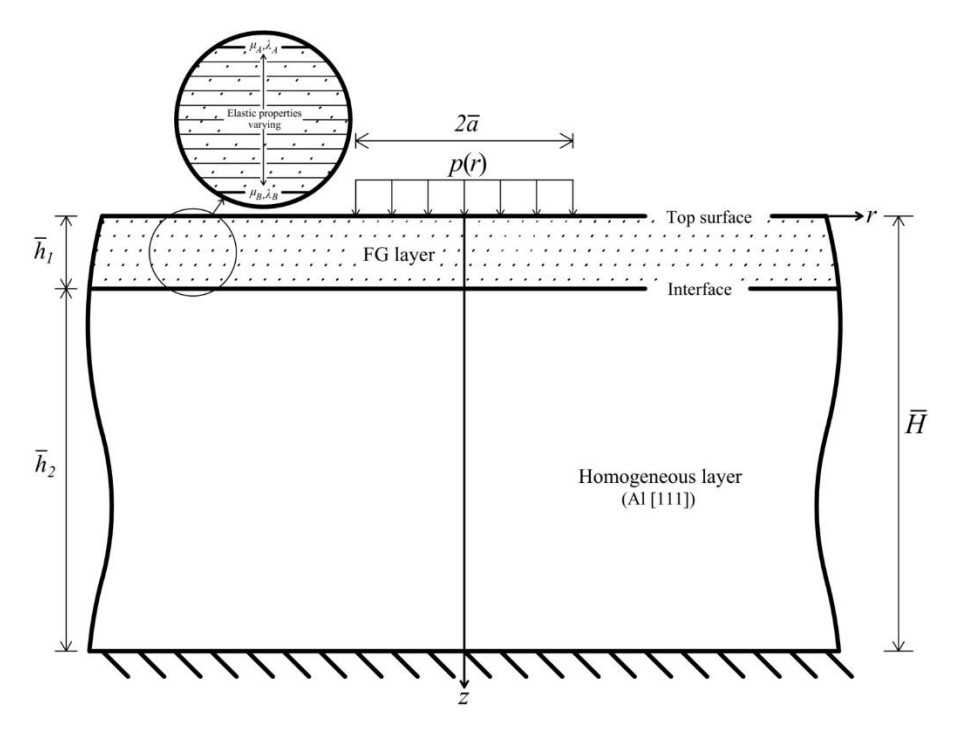


Figure 2.13 FG layer over an elastic medium under uniform vertical surface loading

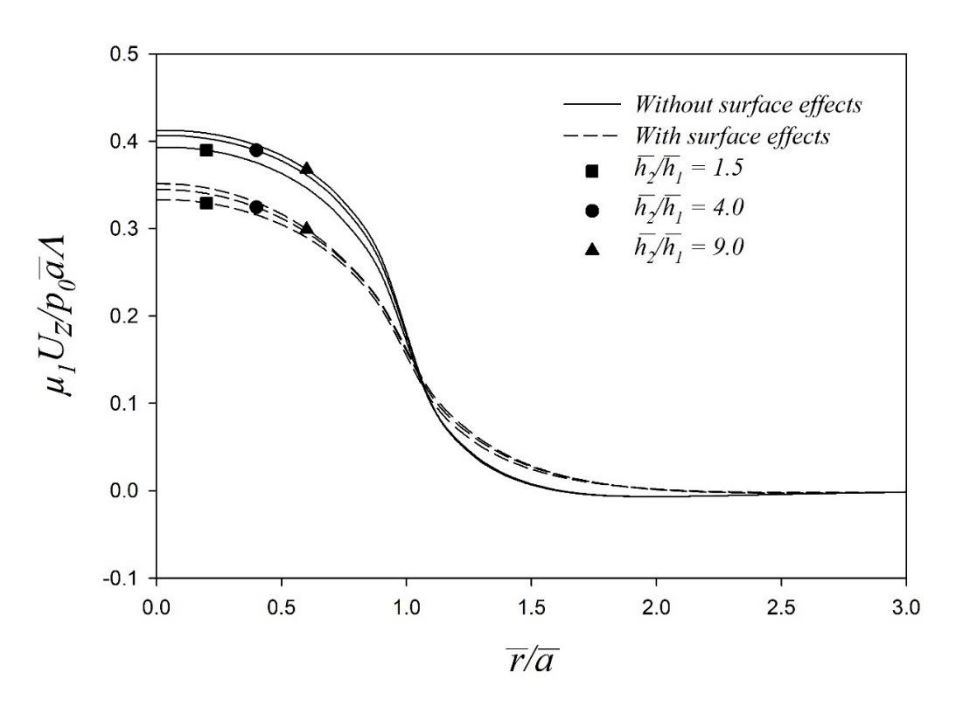


Figure 2.14 Radial profiles of normalized vertical surface displacement of the FG elastic medium with different \bar{h}_2/\bar{h}_1 ratios

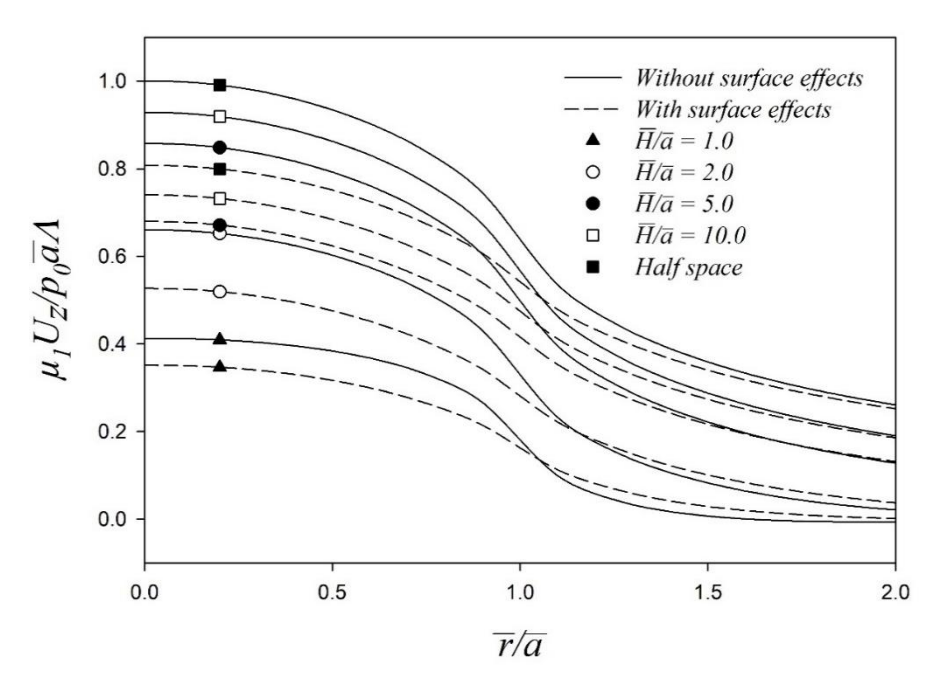


Figure 2.15 Radial profiles of normalized vertical surface displacement of the FG elastic medium with different \bar{H}/\bar{a} ratios

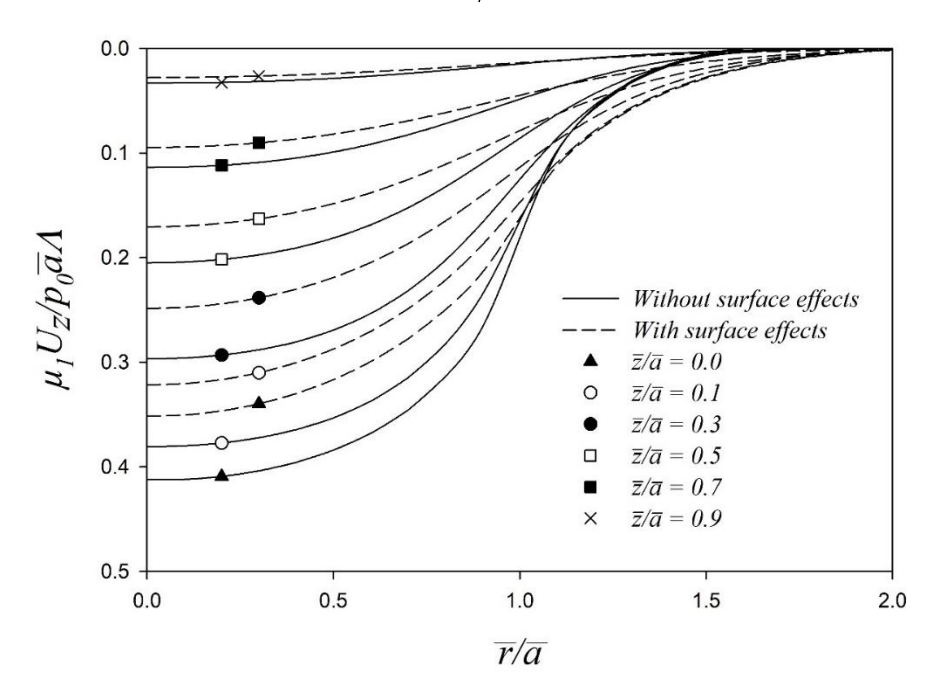


Figure 2.16 Radial profiles of normalized vertical displacement of the FG elastic medium at different depths

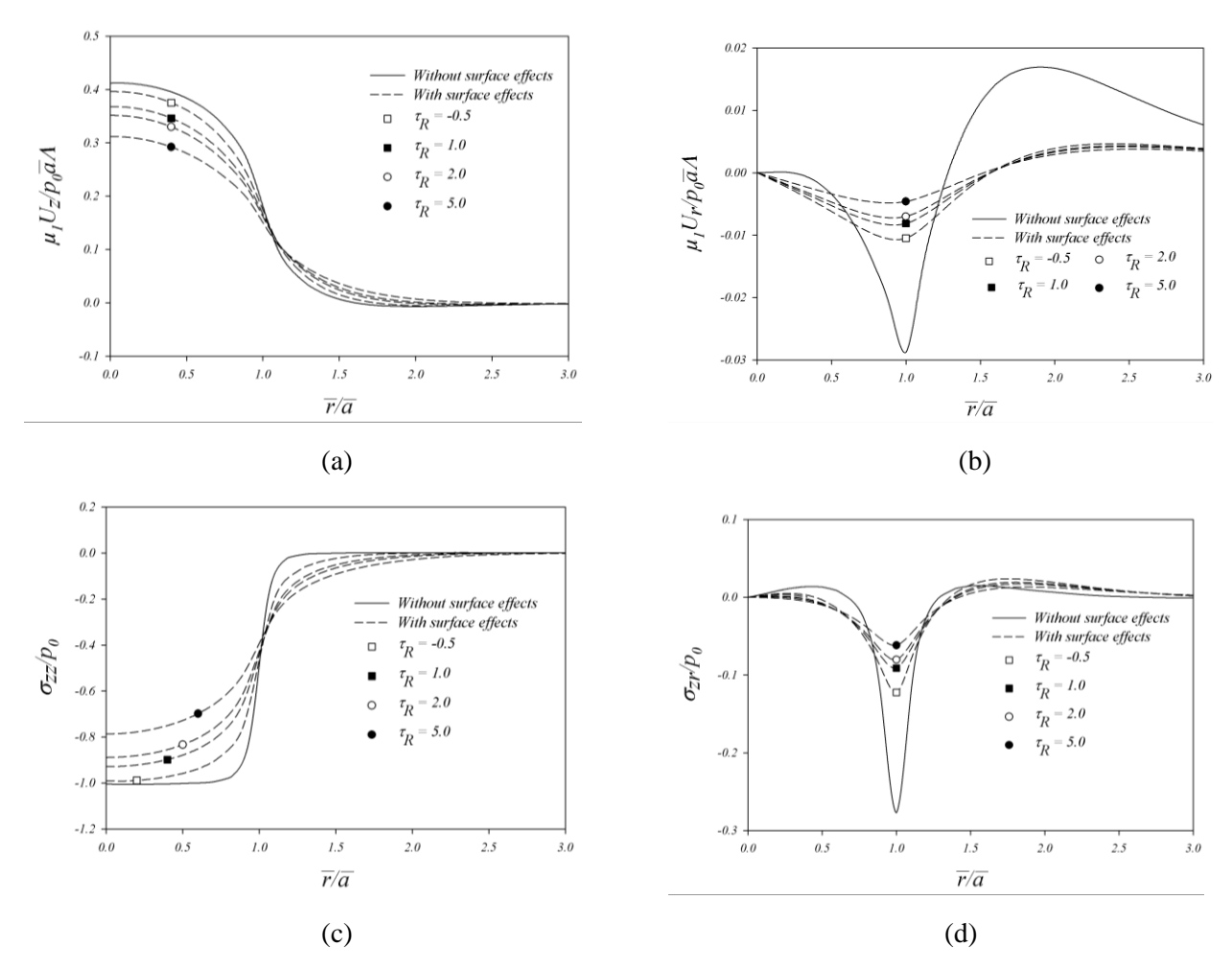


Figure 2.17 Radial profiles of elastic fields of the FG elastic medium with different τ_R ratios: (a) normalized vertical surface displacement, (b) normalized radial surface displacement; (c) normalized normal stress at the interface, (d) shear stress at the interface

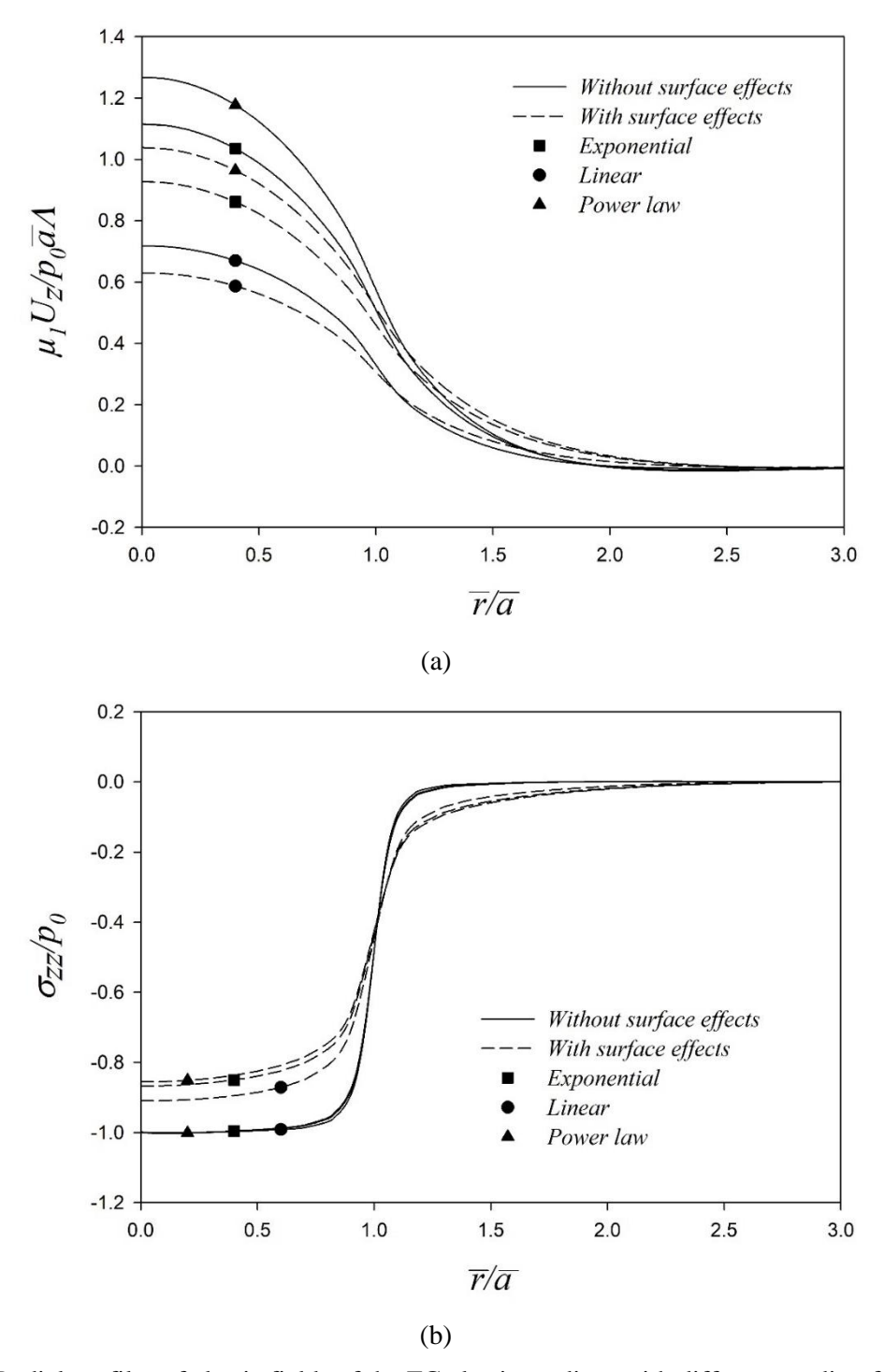


Figure 2.18 Radial profiles of elastic fields of the FG elastic medium with different grading functions: (a) normalized vertical surface displacement; and (b) normalized normal stress at the interface

Table 2.1 Comparison of normalized surface displacements and stresses at the interface of a layered elastic half-space under uniformly distributed normal traction for $\mu_1/\mu_2 = 5$ and h/a = 1.

	$\mu_1 u_z / a p_0$		$\mu_1 u_r / ap_0$		$\sigma_{\!\scriptscriptstyle zz}\!/p_0$		σ_{rz}/p_0	
r/a	Gerrard (1969)	Present solution	Gerrard (1969)	Present solution	Gerrard (1969)	Present solution	Gerrard (1969)	Present solution
0.0	0.9945	0.9944	0.0000	0.0000	0.4260	0.4260	0.0000	0.0000
0.5	0.9442	0.9440	-0.0746	-0.0746	0.3790	0.3790	0.0867	0.0867
1.0	0.7651	0.7649	-0.1363	-0.1363	0.2526	0.2526	0.1303	0.1303
2.0	0.4630	0.4629	-0.1048	-0.1048	0.0657	0.0657	0.0719	0.0719
3.0	0.3179	0.3177	-0.0747	-0.0748	0.0174	0.0174	0.0307	0.0307
5.0	0.1867	0.1866	-0.0420	-0.0421	0.0010	0.0010	0.0069	0.0069
10.0	0.0933	0.0932	-0.0217	-0.0218	0.0001	0.0000	0.0009	0.0009

Table 2.2 Comparison of normalized surface displacements and stresses at the interfaces of a layered elastic half-space under linearly distributed tangential traction for $\mu_1/\mu_2 = 5$ and h/a = 1.

	$\mu_1 u_z / aq_0$		$\mu_1 u_r / aq_0$		$\sigma_{\!\scriptscriptstyle zz}\!/q_0$		$\sigma_{rz}\!/q_0$	
r/a	Gerrard (1969)	Present solution	Gerrard (1969)	Present solution	Gerrard (1969)	Present solution	Gerrard (1969)	Present solution
0.0	0.1188	0.1189	0.0000	0.0000	0.1150	0.1150	0.0000	0.0000
0.5	0.0941	0.0941	-0.0952	-0.0952	0.0803	0.0803	0.0359	0.0359
1.0	0.0253	0.0253	-0.0934	-0.0934	0.0173	0.0173	0.0312	0.0312
2.0	0.0044	0.0044	-0.0198	-0.0198	-0.0068	-0.0068	-0.0005	-0.0005
3.0	-0.0003	-0.0003	-0.0087	-0.0087	-0.0028	-0.0028	-0.0020	-0.0020
4.0	-0.0006	-0.0005	-0.0051	-0.0051	-0.0010	-0.0010	-0.0012	-0.0012
5.0	-0.0003	-0.0003	-0.0036	-0.0036	-0.0004	-0.0004	-0.0007	-0.0007
10.0	0.0001	0.0001	-0.0014	-0.0014	0.0000	0.0000	-0.0001	-0.0001

Table 2.3 Material properties employed in numerical study.

Material parameters	Upper layer Si [100]	Underlying half-space Al [111]
$\lambda (N/m^2)$	78.0849×10^9	58.17×10^9
μ (N/m ²)	40.2256×10^9	26.13×10^9
$\tau^s(N/m)$	0.6056	1
$\lambda^{s}(N/m)$	4.4939	6.8511
$\mu^s(N/m)$	2.7779	-0.376
$\kappa^s(N/m)$	10.0497	6.0991

CHAPTER III

MODELING OF NANO-BEAMS

This chapter presents the modeling and analysis of buckling, post-buckling, and bending responses of nano-scale beams with the consideration of both surface and nonlocal effects. The chapter is organized by first briefly summarizing background and relevant past studies, then presenting the problem formulation, key governing equations and solution methodology, and finally reporting significant findings and important remarks.

3.1 Background and Review

Nano-scale components and devices such as transistors, sensors, actuators and resonators used in the nano-electro-mechanical systems (NEMS) and parts of nano-chips have been largely developed due to their extraordinary physical and mechanical properties. As a result, studies towards the characterization of mechanical properties at such a tiny scale have rapidly gained interest from many investigators. Understanding the mechanical behavior and other related properties (e.g., bending, buckling, post-buckling, and vibration) of slender nano-components, which are commonly found as parts of nano-devices and nano-systems, is obviously essential and generally required in the design procedure to ensure the integrity and safety throughout their usage.

Owing to the positive features which are based principally upon the simplicity of fundamental governing physics and low requirement of computational resources, in comparison with atomistic and molecular dynamics simulations, the classical continuum-based techniques have been increasingly proposed and extensively employed, in the past three decades, to study nano-beam problems. In general, existing classical beam theories (e.g., Timoshenko and Gere 1961; Reddy 2018) have been enhanced by integrating Eringen nonlocal constitutive law (e.g., Eringen 1976, 1983, 2002; Peddieson et al. 2003; Reddy 2007; Reddy and Pang 2008; Reddy et al. 2014) and Gurtin-Murdoch surface elasticity model (e.g., Gurtin and Murdoch 1975, 1978; Gurtin et al. 1998; Preethi et al. 2015) to be capable of handling nano-scale phenomena, such as the surface and nonlocal effects and size-dependent behavior observed from experimental investigations and atomistic calculations.

Results from an extensive literature survey have indicated that work towards the modeling of mechanical properties of nano-scale elements using continuum-based theories has been continuously grown in the last decade; however, most of existing studies were found limited to certain nano-scale influences. For instance, the classical beam theory enhanced by Eringen nonlocal constitutive law was proposed to predict the buckling loads, post-buckling shapes, bending and vibration responses of nano-rods/tubes/ribbons (Wang et al., 2006; Reddy, 2007; Wang and Liew, 2007; Pradhan and Phadikar, 2009), nano-wires (Janghorban, 2012), nano-elements or nano-beams (Wang et al., 2008; Glavardanov et al., 2012; Potapov, 2013; Eltaher et al., 2013; Şimşek and Yurtcu, 2013; Emam, 2013; Koutsoumaris et al., 2017; Vila et al., 2017). Results from those studies indicated that nonlocal parameters play a crucial role on both the value and size-dependent behavior of predicted solutions when the characteristic length of elements is within a nano-scale level. To capture the surface energy effects and size dependency commonly found in nano-scale structures, Gurtin-Murdoch surface elasticity theory was also utilized, by

several investigators, along with various beam theories such as Timoshenko, Euler-Bernoulli, Levinson and Reddy models (Reddy, 2007) to examine buckling, post-buckling, vibration and bending responses of nano-wires (He and Lilley, 2008; Wang and Feng, 2009; Jiang and Yan, 2010; Wang et al., 2010; Wang and Yang, 2011; Liu et al., 2012; Chiu and Chen, 2013; Li et al., 2014; Dong et al., 2014), and nano-beams (Jian-Gang and Ya-Pu, 2007; Liu and Rajapakse, 2010; Bar On et al., 2010; Liu et al., 2011; Sapsathiarn and Rajapakse, 2012; Ansari et al., 2013; Giunta et al., 2013). In those studies, analytical, semi-analytical, and numerical techniques were proposed to construct solutions of associated mathematical models and some predicted results were also found in agreement with existing experimental evidences (He and Lilley, 2008; Jiang and Yan, 2010; Chiu and Chen, 2013). In addition, results from those investigations also confirmed the vital role of the surface energy effect when the size of structures reduces to a nano-scale level and the size-dependency characteristics of predicted responses.

By recognizing the significant role of both nonlocal and surface energy effects in the modeling of nano-scale structures, only few investigators have simultaneously included both Eringen nonlocal constitutive law and Gurtin-Murdoch surface elasticity theory in the simulations of nano-scale elements. For instance, Juntarasaid et al. (2012) considered both effects together with the linearized Euler-Bernoulli beam model to derive analytical solutions of buckling load and small deflection of nano-beams subjected to different boundary conditions. It should be pointed out that while their mathematical model can adequately capture the nano-scale influence but the contribution of the residual stress within the bulk material due to the non-zero residual surface tension present within the material surface was still not considered. Later, Mahmoud et al. (2012) used both the surface and nonlocal elasticity models along with the linearized Euler-Bernoulli beam theory to derive a key differential equation governing the deflected shape of nano-beams under transverse loadings. A standard finite element procedure was adopted to construct approximate solutions and an extensive parametric study was performed to examine the important role of both surface and nonlocal parameters on the size dependency of predicted solutions. Hu et al. (2014) integrated the nonlocal linear elasticity and surface stresses into the classical linearized beam theory to examine the buckling load and vibration of nano-wires. Analytical solutions for both cases were derived using a fundamental approach in the differential-equation theory. It is worth noting that in their formulation, the initial residual stress within the bulk was completely ignored and the effect of the residual surface tension was lumped into the fictitious longitudinal force. Also, Wu et al. (2015) presented a continuum-based mathematical model by integrating small-rotation Euler-Bernoulli beam theory, surface elasticity theory, and nonlocal linear elasticity to examine the bending response of nano-wires under various boundary conditions. Most recently, Preethi et al. (2015) presented a nonlocal nonlinear finite element formulation for the Timoshenko beam theory accounting for the surface stress effects as well as Eringen's nonlocal elasticity. Hosseini-Hashemi et al. (2015) used both the Eringen nonlocal continuum field theory and the Gurtin-Murdoch surface elasticity model to investigate the effect of the nano-beam length, thickness to length ratio, mode number, amplitude of deflection to the radius of gyration ratio and nonlocal parameters on the normalized natural frequencies of nano-beams with both positive and negative surface elasticity.

While applications of both nonlocal and surface elasticity theories to the investigation of mechanical responses of nano-scale elements have been well recognized in the literature, most of existing studies were carried out mainly in the context of linearized beam theories and use of nonlinear kinematics in the modeling is still relatively few (e.g., Preethi et al., 2015; Hosseini-

Hashemi et al., 2015). Mathematical models relying upon small displacement and rotation assumptions generally pose several restrictions in terms of responses to be predicted and, also, the capability to simulate nano-elements which are often slender and undergo large deflections under applied loads. In addition, the integration of both nonlocal and surface energy effects in the simulations was still limited to certain scenarios, and contribution of the initial residual stress within the bulk material, when Gurtin-Murdoch surface elasticity model was utilized, was fully neglected in most of previous investigations. The contribution of the non-zero residual surface tension was integrated mainly via the fictitious longitudinal force. This ignorance can lead to either inaccurate or erroneous predicted solutions as pointed out by Wang et al. (2010).

The present study aims mainly to close this gap in the literature. An efficient numerical solution procedure is established to determine nonlinear responses of nano-beams by integrating both Eringen nonlocal constitutive law and Gurtin-Murdoch surface elasticity along with Euler-Bernoulli beam theory. The influence of the residual stress within the bulk material induced by the residual surface tension of the material layer is also incorporated into the modeling through the moment-curvature relationship of the beam. The problem is formulated within the context of the large displacement and rotation and the final set of exact governing equations is then solved by an efficient nonlinear solver. One of the novel features of the proposed method is the solution procedure that is free of discretization; as the direct consequence, the technique generally yields very accurate results comparable to the analytical solution and then suitable for use as the reliable benchmark solutions. The nano-scale influence and size-dependency of predicted solutions are also fully examined and a selected set of results is reported and discussed.

3.2 Problem Formulation

In this section, a clear problem description is presented along with the integration of three basic field equations (i.e., equilibrium equations, constitutive relations, and kinematics) to form a complete set of nonlinear differential equations governing the deflected shape of a nano element undergoing large displacements and rotations.

3.2.1 Problem Description

Consider a perfectly straight, prismatic, nano-beam of length l with a rectangular cross-section of width b and depth h. The nano-beam can be divided into two regions, the bulk part which is made of a homogeneous, isotropic, linearly elastic material governed by Eringen nonlocal constitutive law and the material surface which is governed by Gurtin-Murdoch surface-elasticity model. All material constants associated with both models are fully prescribed and assumed spatially independent. In the present study, the nano-beam is free of interior loads and subjected to two different sets of boundary conditions, a fixed-free nano-beam under longitudinal and transverse concentrated forces at the free end (see Figure 3.1(a)) and a fixed-rollered nano-beam under a longitudinal concentrated force and a concentrated moment at the rollered end (see Figure 3.1(b)). The direction of all applied loads remains unchanged throughout the loading history.

The problem statement is to establish a solution procedure capable of determining the mechanical response of the given nano-beams including buckling load, post-buckling, and bending response with the consideration of both surface stresses and nonlocal effects. In addition, the size-dependency and material parameters characterizing the nano-scale influence of predicted solutions are also investigated.

3.2.2 Basic Equations

A classical Euler-Bernoulli beam theory (e.g., Lowe, 1971; Reddy, 2004, 2018), Eringen nonlocal linear elasticity theory (e.g., Eringen 1976, 1983, 2002; Peddieson et al. 2003; Reddy 2007; Reddy and Pang 2008; Reddy et al., 2014) and the Gurtin-Murdoch surface elasticity model (e.g., Gurtin and Murdoch 1975, 1978; Gurtin et al. 1998; Preethi et al. 2015) are integrated to form the basic field equations governing responses of the nano-beam undergoing large displacements and rotations.

A centroidal axis of a nano-beam in its undeformed state is shown schematically in Figure 3.2(a). This one-dimensional representation together with the information of the cross section fully describes the three-dimensional aspect of the initial beam geometry. Under the action of external loads, the beam displaces to a new configuration with a deformed centroidal axis defined by a locus of points (x(S), y(S)) where $S \in [0, l]$ denotes the initial arc-length coordinate measured from the left end to any cross section in its undeformed state. The deformed arc-length coordinate measured from the left end to any cross section in its deformed state is denoted by $s \in [0, l']$ where l' is the arc length of the deformed centroidal axis. Note that the information of the deformed centroidal axis along with the assumed kinematics of the cross section gives the complete description of the deformation of the entire beam. The displacements of any cross section located at a point (S,0) in the x- and y- directions are denoted by u = u(S) and v = v(S), respectively, and they are related to the coordinates x(S) and y(S) by

$$u(S) = x(S) - S$$
; $v(S) = y(S)$ (3.1)

Due to the slenderness of typical nano-beams, it is reasonable to neglect the contribution of the axial deformation in the response prediction and the centroidal axis of the beam is assumed inextensible in the present investigation. Based on such assumption along with the consideration of the deformed centroidal axis of the beam, it leads to the following relationship among the displacements u and v, the rotation of the cross section θ , and the initial and deformed arc length S and S:

$$ds/dS = 1; \quad \sin \theta = dv/dS; \quad \cos \theta = dx/dS = 1 + du/dS \tag{3.2}$$

The first relation of (3.2) indicates that there is no difference of using the initial or deformed arc length S and s as the reference coordinate. From equilibrium of the deformed infinitesimal element of length ds in the absence of interior loads (see free body diagram in Figure 3.2(b)), the resultant forces in the x- and y- directions and the resultant bending moment at any cross section, denoted by f_x , f_y and m, respectively, satisfy the following differential equations:

$$df_{x}/dS = 0; \quad df_{x}/dS = 0 \tag{3.3}$$

$$dm/dS = f_x \sin \theta + f_y \cos \theta \tag{3.4}$$

It is obviously seen from (3.3) that an element, that is free of interior loads, possesses the constant resultant forces f_x and f_y along its entire length. The resultant axial force F and the resultant shear force V (i.e., resultant forces normal and parallel to the deformed cross section, respectively) can be related to the force resultants f_x and f_y by

$$F(\theta) = f_x \cos \theta - f_y \sin \theta \tag{3.5}$$

$$V(\theta) = f_{x} \sin \theta + f_{y} \cos \theta \tag{3.6}$$

To establish the relationship between the resultant bending moment m and the deformation of the cross section, the well-known kinematics assumption of the cross section (i.e., plane section remains plane) together with Gurtin-Murdoch surface elasticity and Eringen nonlocal elasticity theories is utilized. The beam element is treated as a composite consisting of the interior part, called the bulk material, and the remaining zero-thickness material layer, called the material surface (see Figure 3.3). The material surface is governed by the following Gurtin-Murdoch constitutive relation (Gurtin and Murdoch 1975, 1978; Gurtin et al. 1998; Preethi et al. 2015):

$$\sigma_{\alpha\beta}^{s} = \tau^{s} \delta_{\alpha\beta} + 2(\mu^{s} - \tau^{s}) \varepsilon_{\alpha\beta}^{s} + (\lambda^{s} + \tau^{s}) \varepsilon_{\gamma\gamma}^{s} \delta_{\alpha\beta} + \tau^{s} u_{\alpha,\beta}^{s} \quad ; \quad \sigma_{3\alpha}^{s} = \tau^{s} u_{3,\alpha}^{s}$$

$$(3.7)$$

where the superscript "s" is employed to designate quantities associated with the surface; Greek indices range from 1 to 2 and repeated index implies the summation over its range; $\sigma_{3\alpha}^s$ and $\sigma_{\alpha\beta}^s$ denote components of the out-of-plane and in-plane surface stresses, respectively; $\varepsilon_{\alpha\beta}^s$ denotes components of the in-plane surface strain; u_3^s and u_{α}^s denote components of the out-of-plane and in-plane surface displacement, respectively; μ^s and λ^s denote surface Lamé constants; τ^s denotes the residual surface tension in the unstrained state; and $\delta_{\alpha\beta}$ is a two-dimensional Kronecker symbol. For the bulk material, the bulk stress σ_{ij}^b are related to the bulk strain ε_{ij}^b via Eringen nonlocal, isotropic constitutive relation (Eringen 1976, 1983, 2002; Peddieson et al. 2003; Reddy 2007; Reddy and Pang 2008; Reddy et al., 2014)

$$[1 - (e_0 a)^2 \Delta] \sigma_{ij}^b = 2\mu^b \varepsilon_{ij}^b + \lambda^b \delta_{ij} \varepsilon_{kk}^b$$
(3.8)

where e_0 is a non-dimensional constant; a denotes the internal intrinsic length of the material; Δ denotes the Laplace operator; μ^b and λ^b denote bulk Lamé constants; and lower case indices range from 1 to 3 and repeated index imply the summation over its range. It is worth noting that due to the presence of the residual surface tension at the initial unstrained state, the bulk stress does not vanish to maintain the equilibrium state and the presence of this bulk residual stress is considered in the present study. By ignoring the boundary and corner effects, the bulk residual stress, denoted by σ^{b0}_{ij} , can be assumed homogeneous and obtained from static equilibrium of the cross section at the unstrained state (see Figure 3.3). For the beam with the rectangular cross section, the bulk residual stress takes the form

$$[\sigma_{ij}^{b0}] = \begin{bmatrix} -2(1/h + 1/b)\tau^{s} & 0 & 0\\ 0 & -2\tau^{s}/h & 0\\ 0 & 0 & -2\tau^{s}/b \end{bmatrix}$$
 (3.9)

where b and h are width and depth of the cross section. The resultant bending moment m at any cross section can be obtained from

$$m = m^b + m^s = -\int_{\rho} \sigma_{11}^b x_3 dA - \int_{\rho\rho} \sigma_{11}^s x_3 d\Gamma$$
 (3.10)

where m^b, m^s are resultant bending moment from the bulk and surface parts, respectively, and \mathcal{C} and $\partial \mathcal{C}$ denote the cross section and its boundary, respectively. By enforcing kinematics of the cross section from Euler-Bernoulli beam theory, the normal strains ε_{11}^b and ε_{11}^s at any coordinate x_3 from the centroid of the cross section are given by

$$\varepsilon_{11}^b = -\frac{d\theta}{dS}x_3, \quad \varepsilon_{11}^s = -\frac{d\theta}{dS}x_3 \tag{3.11}$$

By employing (3.10)-(3.11) along with (3.7)-(3.8) in the absence of the residual surface tension and the bulk residual stress and then carrying out the integration over the cross section and its boundary, it yields the relationship between the resultant bending moment m and the rotation gradient $d\theta/dS$ as

$$m = (e_0 a)^2 \frac{d^2 m}{dS^2} + K \frac{d\theta}{dS}$$
 (3.12)

where K denotes the modified flexural rigidity of the cross section defined by

$$K = \left(1 + \frac{6}{h} + \frac{2}{b}\right)EI\tag{3.13}$$

in which $E = \mu^b (2\mu^b + 3\lambda^b)/(\mu^b + 3\lambda^b)$ denotes Young's modulus of the bulk material, $I = bh^3/12$ denotes the area moment of inertia of the cross section, $\overline{h} = h/\Lambda$, $\overline{b} = b/\Lambda$, $\Lambda = E^s/E$, and $E^s = \mu^s (2\mu^s + 3\lambda^s)/(\mu^s + 3\lambda^s)$. To take the influence of the residual surface tension and the non-zero bulk residual stress into account, a procedure based on the theory of elasticity with the residual stress and the principle of virtual work similar to that employed by Wang et al. (2010) is adopted. It is found that the final relationship between m and $d\theta/dS$ is identical to (3.12) except that the modified flexural rigidity K changes to

$$K = \left[1 + \frac{6}{\overline{h}} + \frac{2}{\overline{b}} + \frac{2\overline{\tau}^{s}}{\Lambda \overline{b}} \left(2v^{2} \frac{\overline{b}^{2}}{\overline{h}^{2}} - \frac{\overline{l}^{2}}{\overline{h}^{2}}\right)\right] EI$$
(3.14)

where $\bar{l} = l/\Lambda$, $\bar{\tau}^s = \tau^s/E$, and v is Poisson's ratio of the bulk material. It is apparent from (3.13) that in the absence of the residual surface tension (i.e., $\bar{\tau}^s = 0$), the modified flexural rigidity K is always larger than that of the classical case EI and such discrepancy becomes more significant when the dimension of the cross section is relatively small in comparison with the intrinsic length parameter Λ . On the contrary, presence of the positive residual surface tension can reverse the effect due to the residual compressive stress generated within the bulk material and such influence is substantially magnified when the slenderness ratio of the member increases. In various earlier investigations (He, and Lilley, 2008; Wang and Feng, 2009; Jiang and Yan, 2010; Juntarasaid et al., 2012), the modified flexural rigidity of the beam was computed from (3.13) which is free of the residual surface tension. The influence of τ^s is treated separately by ignoring the bulk residual stress and the equilibrium of the entire body in the unstrained state is maintained differently by introducing a set of forces at the boundary of the surface. In this point of view, the treatment of

the surface effect and the residual surface tension with the integration of the bulk residual stress offered in the present study is more direct and should provide a more realistic mathematical model for simulating responses of nano-beams.

By substituting the equilibrium equation (3.4) into the constitutive relation (3.12), it yields the moment-curvature relationship

$$\bar{m} = \left\{ \eta + \mu \bar{F}(\theta) \right\} \frac{d\theta}{d\bar{S}} \tag{3.15}$$

where $\eta = K/EI$ $\overline{m} = ml/EI$, $\mu = (e_0 a)^2/l^2$, $\overline{S} = S/l$ and $\overline{F}(\theta) = \overline{f_x} \cos \theta - \overline{f_y} \sin \theta$ with $\overline{f_x} = f_x l^2/EI$, $\overline{f_y} = f_y l^2/EI$. By substituting (3.15) into (3.4), an alternative form of the moment equilibrium equation is obtained as

$$\frac{d}{d\bar{S}} \left[\left\{ \eta + \mu \bar{F}(\theta) \right\} \frac{d\theta}{d\bar{S}} \right] = \bar{V}(\theta) \tag{3.16}$$

where $\bar{V}(\theta) = \bar{f}_x \sin \theta + \bar{f}_y \cos \theta$. To suit the direct integration of the equilibrium equation (3.16) with respect to the rotation θ , its left hand side is first re-expressed by using the chain rule as

$$\frac{d}{d\overline{S}} \left[\left\{ \eta + \mu \overline{F}(\theta) \right\} \frac{d\theta}{d\overline{S}} \right] = \frac{d\theta}{d\overline{S}} \cdot \frac{d}{d\theta} \left[\left\{ \eta + \mu \overline{F}(\theta) \right\} \frac{d\theta}{d\overline{S}} \right]$$
(3.17)

By substituting the relation (3.17) into the equilibrium equation (3.16) and then multiplying both sides by a function $\eta + \mu \bar{F}(\theta)$, the resulting differential equation can be subsequently integrated to obtain

$$\left[\left\{\eta + \mu \overline{F}(\theta)\right\} \frac{d\theta}{d\overline{S}}\right]^2 = C - 2\eta \overline{F}(\theta) - \mu \overline{F}^2(\theta)$$
(3.18)

where C is a constant of integration and can be determined from the boundary conditions. It is apparent from (3.15) that the sign of both normalized bending moment \bar{m} and the term $\{\eta + \mu \bar{F}(\theta)\}d\theta/d\bar{S}$ must be identical; as a result, only one of the two solutions of $d\theta/d\bar{S}$ obtained from (3.18) is physically admissible. The unique solution can be, therefore, expressed in the form

$$\frac{d\overline{S}}{d\theta} = \frac{sgn(\overline{m})\{\eta + \mu \overline{F}(\theta)\}}{\sqrt{C - 2\eta \overline{F}(\theta) - \mu \overline{F}^2(\theta)}}$$
(3.19)

where $sgn(\bar{m})$ is a moment-dependence function defined by

$$sgn(\overline{m}) = \begin{cases} -1 & \text{if } \overline{m} < 0\\ 0 & \text{if } \overline{m} = 0\\ 1 & \text{if } \overline{m} > 0 \end{cases}$$

$$(3.20)$$

Combining (3.19) and the geometric relations (3.2) yields the following two differential equations governing the displacements u and v

$$\frac{d\overline{u}}{d\theta} = \frac{sgn(\overline{m})(\cos\theta - 1)\left\{\eta + \mu\overline{F}(\theta)\right\}}{\sqrt{C - 2\eta\overline{F}(\theta) - \mu\overline{F}^2(\theta)}}$$
(3.21)

$$\frac{d\overline{v}}{d\theta} = \frac{sgn(\overline{m})\sin\theta\left\{\eta + \mu\overline{F}(\theta)\right\}}{\sqrt{C - 2\eta\overline{F}(\theta) - \mu\overline{F}^2(\theta)}}$$
(3.22)

where $\bar{u} = u/l$ and $\bar{v} = v/l$. A set of three differential equations (3.19), (3.21) and (3.22) is sufficient for obtaining the key governing equations of nano-beams under various end conditions. It is worth noting that both η and μ appearing in above equations are essential parameters related to the surface stresses and nonlocal linear elasticity, respectively, and are used to simulate the nano-scale influence on the mechanical response of nano-beams. By setting $\eta = 1$ and $\mu = 0$, above equations reduce directly to those obtained by Rungamornrat and Tangnovarad (2011) for a classical beam in the absence of surface stresses and nonlocal elasticity. By performing the direct integration of (3.19), (3.21) and (3.22) with respect to the independent variable θ from $\bar{S} = 0$ to $\bar{S} = \xi \in [0,1]$, it leads to

$$\xi = \int_{\theta_{1}}^{\theta(\xi)} \frac{sgn(\overline{m})\left\{\eta + \mu \overline{F}(\theta)\right\}}{\sqrt{C - 2\eta \overline{F}(\theta) - \mu \overline{F}^{2}(\theta)}} d\theta \tag{3.23}$$

$$\overline{u}(\xi) - \overline{u}_1 = \int_{\theta_1}^{\theta(\xi)} \frac{sgn(\overline{m})(\cos\theta - 1)\left\{\eta + \mu \overline{F}(\theta)\right\}}{\sqrt{C - 2\eta \overline{F}(\theta) - \mu \overline{F}^2(\theta)}} d\theta \tag{3.24}$$

$$\overline{v}(\xi) - \overline{v}_1 = \int_{\theta_1}^{\theta(\xi)} \frac{sgn(\overline{m})\sin\theta\left\{\eta + \mu\overline{F}(\theta)\right\}}{\sqrt{C - 2\eta\overline{F}(\theta) - \mu\overline{F}^2(\theta)}} d\theta \tag{3.25}$$

where $\overline{u}_1 = \overline{u}(\overline{S} = 0)$, $\overline{v}_1 = \overline{v}(\overline{S} = 0)$ and $\theta_1 = \theta(\overline{S} = 0)$. By setting $\xi = 1$, the relations (3.23)-(3.25) become

$$1 = \int_{\theta_1}^{\theta_2} \frac{sgn(\bar{m}) \left\{ \eta + \mu \bar{F}(\theta) \right\}}{\sqrt{C - 2\eta \bar{F}(\theta) - \mu \bar{F}^2(\theta)}} d\theta \tag{3.26}$$

$$\overline{u}_2 - \overline{u}_1 = \int_{\theta_1}^{\theta_2} \frac{sgn(\overline{m})(\cos\theta - 1)\left\{\eta + \mu \overline{F}(\theta)\right\}}{\sqrt{C - 2\eta \overline{F}(\theta) - \mu \overline{F}^2(\theta)}} d\theta \tag{3.27}$$

$$\overline{v}_{2} - \overline{v}_{1} = \int_{\theta_{1}}^{\theta_{2}} \frac{sgn(\overline{m})\sin\theta\left\{\eta + \mu\overline{F}(\theta)\right\}}{\sqrt{C - 2\eta\overline{F}(\theta) - \mu\overline{F}^{2}(\theta)}} d\theta \tag{3.28}$$

where $\bar{u}_2 = \bar{u}(\bar{S}=1)$, $\bar{v}_2 = \bar{v}(\bar{S}=1)$ and $\theta_2 = \theta(\bar{S}=1)$. A system of nonlinear algebraic equations (3.26)-(3.28) together with the well-posed essential and natural boundary conditions of the nanobeam is sufficient for determining the unknown constant C and the kinematical unknowns from a set $\{\bar{u}_1, \bar{u}_2, \bar{v}_1, \bar{v}_2, \theta_1, \theta_2\}$. Once all primary unknowns at both ends of the member are solved, the displacement and rotation of any cross section can be readily obtained from the relations (3.23)-

(3.25). The reactive forces can be also determined from equilibrium of the whole beam in the deformed state whereas the internal forces at any cross section such as the axial force F, the shear force V and the bending moment m are obtained from the method of sections.

3.2.3 Linearized Equations for Buckling Load Analysis

For a perfectly straight nano-beam under proper end restraints and subjected only to a pure axial compression force P, it is apparent that the straight configuration (i.e., $u=v=\theta=0$) together with the pure axial state (i.e., $f_x=-P$, $f_y=m=0$) is always an equilibrium configuration (i.e., equations (3.2)-(3.4) and (3.12) are automatically satisfied). Besides this trivial solution, it is more informative to determine the critical compression force P at the onset of the buckling, i.e., a state that the beam begins to admit a non-straight equilibrium configuration. At the onset of the buckling, the rotation of the cross section θ is infinitesimally small and, as a result, the first order approximations such as $\sin\theta\approx\theta$, $\cos\theta\approx1$ are admissible. At this particular state, the kinematical relations (3.2), the equilibrium equations (3.3)-(3.4), and the moment-curvature relationship (3.15) can be reduced to

$$d\overline{u}/d\overline{S} = 0; \quad d\overline{v}/d\overline{S} = \theta$$
 (3.29)

$$d\overline{f}_{x}/d\overline{S} = 0$$
; $d\overline{f}_{y}/d\overline{S} = 0$ (3.30)

$$d\overline{m}/d\overline{S} = \overline{f}_x \theta + \overline{f}_y \tag{3.31}$$

$$\bar{m} = (\eta + \mu \bar{f}_x) d\theta / d\bar{S} \tag{3.32}$$

The first relation of (3.29) indicates that \overline{u} must be constant throughout the beam and identically vanishes if the longitudinal displacement is prevented at a particular point within the beam. Similarly, the first equation of (3.30) along with the prescribed compression force P at the end of the beam implies that $\overline{f}_x = -Pl^2/EI \equiv -p$. By substituting $\overline{f}_x = -p$ and the second equation of (3.29) into (3.31) and (3.32), it yields the normalized resultant force \overline{f}_y and normalized bending moment \overline{m} in terms of the normalized displacement \overline{v}

$$\overline{f}_{y} = (\eta - \mu p) \frac{d^{3}\overline{v}}{d\overline{S}^{3}} + p \frac{d\overline{v}}{d\overline{S}}$$
(3.33)

$$\bar{m} = (\eta - \mu p) \frac{d^2 \bar{\nu}}{d\bar{S}^2} \tag{3.34}$$

Finally, the linearized governing equation for the normalized displacement \bar{v} is obtained, by substituting (3.33) into the second equation of (3.30), as

$$\frac{d^4\overline{v}}{d\overline{S}^4} + \lambda^2 \frac{d^2\overline{v}}{d\overline{S}^2} = 0 \tag{3.35}$$

where $\lambda = \sqrt{p/(\eta - \mu p)}$. A linear, homogeneous, fourth-order, ordinary differential equation (3.35) along with the prescribed end conditions is sufficient for formulating an Eigen problem for finding the buckling load and buckled shape of the nano-beam.

3.3 Key Governing Equations

Basic equations established in the previous section are employed to formulate the key governing equations essential for determining post-buckling and bending responses of nano-beams under different end conditions illustrated in Figure 3.1. The enforcement of essential and natural boundary conditions to obtain both the unknown constant *C* and a final set of governing equations is clearly demonstrated.

3.3.1 Fixed-free Nano-Beams

Consider a nano-beam clamped at the left end and subjected to a longitudinal force P and a transverse force Q at the right end as shown in Figure 3.1(a). Essential and natural boundary conditions at the ends of the beam are given by $\overline{u}_1 = 0$, $\overline{v}_1 = 0$, $\overline{f}_x(1) = -Pl^2/EI \equiv -p$, $\overline{f}_y(1) = -Ql^2/EI \equiv -q$ and $\overline{m}(1) = 0$. From the two force natural boundary conditions and equilibrium equations (3.3), the internal resultant forces \overline{f}_x and \overline{f}_y at any cross section of the beam are obtained as

$$\overline{f}_{x}(\overline{S}) = -p, \quad \overline{f}_{y}(\overline{S}) = -q \quad \forall \overline{S} \in [0,1]$$
 (3.36)

The normalized axial and shear forces at any cross section, for this particular case, are given by

$$\bar{F}(\theta) = -p\cos\theta + q\sin\theta \tag{3.37}$$

$$\bar{V}(\theta) = -p\sin\theta - q\cos\theta \tag{3.38}$$

The relation (3.15) together with the moment natural boundary condition $\overline{m}(1) = 0$ implies that

$$\frac{d\theta}{d\overline{S}}(\overline{S}=1)=0 \tag{3.39}$$

By applying the relation (3.18) at $\overline{S} = 1$ and then using the condition (3.39), the unknown constant C can be obtained as

$$C = 2\eta \bar{F}(\theta_2) + \mu \bar{F}^2(\theta_2) \tag{3.40}$$

By substituting the constant C from (3.40) and all essential boundary conditions into (3.26)-(3.28), it yields a system of nonlinear algebraic equations governing the unknown displacements and rotation at the right end of the beam (i.e., \bar{u}_2 , \bar{v}_2 and θ_2)

$$1 = \int_{0}^{\theta_{2}} \frac{\eta + \mu \overline{F}(\theta)}{\sqrt{2\eta \left\{ \overline{F}(\theta_{2}) - \overline{F}(\theta) \right\} + \mu \left\{ \overline{F}^{2}(\theta_{2}) - \overline{F}^{2}(\theta) \right\}}} d\theta \tag{3.41}$$

$$\overline{u}_{2} = \int_{0}^{\theta_{2}} \frac{\left\{ \eta + \mu \overline{F}(\theta) \right\} (\cos \theta - 1)}{\sqrt{2\eta \left\{ \overline{F}(\theta_{2}) - \overline{F}(\theta) \right\} + \mu \left\{ \overline{F}^{2}(\theta_{2}) - \overline{F}^{2}(\theta) \right\}}} d\theta \tag{3.42}$$

$$\overline{v}_{2} = \int_{0}^{\theta_{2}} \frac{\left\{ \eta + \mu \overline{F}(\theta) \right\} \sin \theta}{\sqrt{2\eta \left\{ \overline{F}(\theta_{2}) - \overline{F}(\theta) \right\} + \mu \left\{ \overline{F}^{2}(\theta_{2}) - \overline{F}^{2}(\theta) \right\}}} d\theta \tag{3.43}$$

Note that the moment-dependent function $sgn(\overline{m})$ is taken equal to 1 without loss of generality since the deflected shape possesses a single-curvature and the normalized bending moment \overline{m} at any cross section possesses the same sign. A system of nonlinear algebraic equations can be further specialized to the bending and post-buckling cases by taking p=0 and q=0, respectively. Once the displacements and rotation at the free end are solved, the displacement and rotation at any interior point $\overline{S} = \xi \in (0,1)$ can be obtained from

$$\xi = \int_{0}^{\theta(\xi)} \frac{\eta + \mu \overline{F}(\theta)}{\sqrt{2\eta \left\{ \overline{F}(\theta_2) - \overline{F}(\theta) \right\} + \mu \left\{ \overline{F}^2(\theta_2) - \overline{F}^2(\theta) \right\}}} d\theta \tag{3.44}$$

$$\overline{u}(\xi) = \int_{0}^{\theta(\xi)} \frac{\left\{ \eta + \mu \overline{F}(\theta) \right\} (\cos \theta - 1)}{\sqrt{2\eta \left\{ \overline{F}(\theta_2) - \overline{F}(\theta) \right\} + \mu \left\{ \overline{F}^2(\theta_2) - \overline{F}^2(\theta) \right\}}} d\theta \tag{3.45}$$

$$\overline{v}(\xi) = \int_{0}^{\theta(\xi)} \frac{\left\{ \eta + \mu \overline{F}(\theta) \right\} \sin \theta}{\sqrt{2\eta \left\{ \overline{F}(\theta_2) - \overline{F}(\theta) \right\} + \mu \left\{ \overline{F}^2(\theta_2) - \overline{F}^2(\theta) \right\}}} d\theta \tag{3.46}$$

where $\theta(\xi)$ denotes the rotation at any interior point $\overline{S} = \xi \in (0,1)$. Normalized support reactions at the clamped end, denoted by $\overline{R}_x = R_x l^2 / EI$, $\overline{R}_y = R_y l^2 / EI$ and $\overline{R}_m = R_m l / EI$, can be obtained, from equilibrium of the whole beam in its deformed state, as

$$\bar{R}_{x} = p \; ; \quad \bar{R}_{y} = -q \; ; \quad \bar{R}_{m} = -p\bar{v}_{2} - q(1 + \bar{u}_{2})$$
 (3.47)

The normalized axial force \overline{F} and the normalized shear force \overline{V} at any point $\overline{S} = \xi \in (0,1)$ can be determined from (3.37) and (3.38), respectively, whereas the normalized bending moment \overline{m} can be computed from

$$\overline{m} = q(1 + \overline{u}_2 - \xi - \overline{u}(\xi)) + p(\overline{v}_2 - \overline{v}(\xi)) \tag{3.48}$$

3.3.2 Fixed-roller supported Nano-Beams

Consider a nano-beam beam clamped at the left end, roller-supported at the right end, and subjected to a longitudinal force P and the moment M at the right end as shown in Figure 3.1(b). The corresponding essential and natural boundary conditions at the ends of the beam are given by $\bar{u}_1 = 0$, $\bar{v}_1 = 0$, $\bar{v}_2 = 0$, $\bar{f}_x(1) = -Pl^2/EI \equiv -p$ and $\bar{m}(1) = Ml/EI \equiv \bar{m}_0$. From the force natural boundary condition along with the fact that the internal resultant forces \bar{f}_x is constant throughout the member, it can be concluded that

$$\overline{f}_{x}(\overline{S}) = -p, \ \forall \overline{S} \in [0,1]$$

The normalized axial and shear forces at any cross section, for this particular case, are given by

$$\bar{F}(\theta) = -p\cos\theta - \bar{f}_{v}\sin\theta \tag{3.50}$$

$$\bar{V}(\theta) = -p\sin\theta + \bar{f}_{v}\cos\theta \tag{3.51}$$

For this particular case, the member contains an interior inflection point and the vanishing of the bending moment at that particular point implies

$$\frac{d\theta}{d\overline{S}}(\theta = \theta_z) = 0 \tag{3.52}$$

where θ_z is the rotation at the inflection point. By enforcing (3.52) together with (3.18), the constant C is obtained, for this particular case, by

$$C = 2\eta \bar{F}(\theta_z) + \mu \bar{F}^2(\theta_z) \tag{3.53}$$

By substituting (3.53) and all essential boundary conditions into (3.26)-(3.28), it leads to a system of nonlinear algebraic equations

$$1 = \int_{0}^{\theta_{2}} \frac{sgn(\overline{m}) \left\{ \eta + \mu \overline{F}(\theta) \right\}}{\sqrt{2\eta \left\{ \overline{F}(\theta_{z}) - \overline{F}(\theta) \right\} + \mu \left\{ \overline{F}^{2}(\theta_{z}) - \overline{F}^{2}(\theta) \right\}}} d\theta$$
(3.54)

$$\overline{u}_{2} = \int_{0}^{\theta_{2}} \frac{sgn(\overline{m}) \left\{ \eta + \mu \overline{F}(\theta) \right\} (\cos \theta - 1)}{\sqrt{2\eta \left\{ \overline{F}(\theta_{z}) - \overline{F}(\theta) \right\} + \mu \left\{ \overline{F}^{2}(\theta_{z}) - \overline{F}^{2}(\theta) \right\}}} d\theta$$
(3.55)

$$0 = \int_{0}^{\theta_{2}} \frac{sgn(\overline{m}) \left\{ \eta + \mu \overline{F}(\theta) \right\} \sin \theta}{\sqrt{2\eta \left\{ \overline{F}(\theta_{z}) - \overline{F}(\theta) \right\} + \mu \left\{ \overline{F}^{2}(\theta_{z}) - \overline{F}^{2}(\theta) \right\}}} d\theta$$
(3.56)

By using the relations (3.15), (3.18), (3.53) along with the natural boundary condition $\overline{m}(1) = \overline{m}_0$, it yields

$$\overline{m}_0^2 = 2\eta \left\{ \overline{F}(\theta_z) - \overline{F}(\theta_2) \right\} + \mu \left\{ \overline{F}^2(\theta_z) - \overline{F}^2(\theta_2) \right\}$$
(3.57)

After properly incorporating the moment-dependent function $sgn(\bar{m})$ to each part of the beam, the nonlinear equations (3.54)-(3.56) now become

$$1 = \int_{0}^{\theta_{2}} \frac{\eta + \mu \overline{F}(\theta)}{\sqrt{\overline{m}_{0}^{2} + 2\eta \{\overline{F}(\theta_{2}) - \overline{F}(\theta)\}} + \mu \{\overline{F}^{2}(\theta_{2}) - \overline{F}^{2}(\theta)\}} d\theta - 2 \int_{0}^{\theta_{2}} \frac{\eta + \mu \overline{F}(\theta)}{\sqrt{2\eta \{\overline{F}(\theta_{z}) - \overline{F}(\theta)\}} + \mu \{\overline{F}^{2}(\theta_{z}) - \overline{F}^{2}(\theta)\}} d\theta$$
(3.58)

$$\overline{u}_{2} = \int_{0}^{\theta_{2}} \frac{\left\{ \eta + \mu \overline{F}(\theta) \right\} (\cos \theta - 1)}{\sqrt{\overline{m}_{0}^{2} + 2\eta \left\{ \overline{F}(\theta_{2}) - \overline{F}(\theta) \right\} + \mu \left\{ \overline{F}^{2}(\theta_{2}) - \overline{F}^{2}(\theta) \right\}}} d\theta - 2 \int_{0}^{\theta_{2}} \frac{\left\{ \eta + \mu \overline{F}(\theta) \right\} (\cos \theta - 1)}{\sqrt{2\eta \left\{ \overline{F}(\theta_{2}) - \overline{F}(\theta) \right\} + \mu \left\{ \overline{F}^{2}(\theta_{2}) - \overline{F}^{2}(\theta) \right\}}} d\theta$$

$$(3.59)$$

$$0 = \int_{0}^{\theta_{2}} \frac{\left\{\eta + \mu \overline{F}(\theta)\right\} \sin \theta}{\sqrt{\overline{m}_{0}^{2} + 2\eta \left\{\overline{F}(\theta_{2}) - \overline{F}(\theta)\right\} + \mu \left\{\overline{F}^{2}(\theta_{2}) - \overline{F}^{2}(\theta)\right\}}} d\theta - 2 \int_{0}^{\theta_{2}} \frac{\left\{\eta + \mu \overline{F}(\theta)\right\} \sin \theta}{\sqrt{2\eta \left\{\overline{F}(\theta_{2}) - \overline{F}(\theta)\right\} + \mu \left\{\overline{F}^{2}(\theta_{2}) - \overline{F}^{2}(\theta)\right\}}} d\theta$$

$$(3.60)$$

A final system of four nonlinear algebraic equations (3.57)-(3.60) is sufficient for determining four unknown quantities θ_2 , θ_z , \bar{u}_2 , \bar{f}_y and it can be specialized to the bending and post-buckling cases by taking p=0 and $\bar{m}_0=0$, respectively. Once the unknowns θ_2 , θ_z , \bar{u}_2 , \bar{f}_y are determined, the displacement and rotation at any interior point $\bar{S}=\xi\in(0,1)$ can be obtained from (3.23)-(3.25) together with the value of moment-dependent function $sgn(\bar{m})$ throughout the member. To facilitate such calculations, the nano-beam is separated into three segments with $sgn(\bar{m})$ possessing the same value within each segment as follows: the first segment is taken from the clamped end to the interior inflection point with the rotation at any normalized coordinate ξ ranging from 0 to θ_z ; the second segment is taken from the interior inflection point to the point of zero rotation with the rotation at any normalized coordinate ξ ranging from θ_z to 0; and the last segment is taken from the point of zero rotation to the right end with the rotation at any normalized coordinate ξ ranging from 0 to θ_z . Again, by enforcing equilibrium of the beam in its deformed state, the normalized support reactions at the clamped end, denoted by $\bar{R}_x = R_x l^2 / EI$, $\bar{R}_y = R_y l^2 / EI$ and $\bar{R}_m = R_m l / EI$, can be obtained as

$$\bar{R}_x = p; \quad \bar{R}_y = -\bar{f}_y; \quad \bar{R}_m = -\bar{m}_0 - \bar{f}_y(1 + \bar{u}_2)$$
 (3.61)

and the reaction at the right end is simply \overline{f}_y . The normalized axial force and shear force \overline{F} , \overline{V} at any point $\overline{S} = \xi \in (0,1)$ can be readily computed from (3.50)-(3.51) in terms of \overline{f}_y and $\theta(\xi)$ whereas the normalized bending moment \overline{m} can be computed from

$$\overline{m} = \overline{m}_0 + \overline{f}_{y}[1 + \overline{u}_2 - \xi - \overline{u}(\xi)] - p\overline{v}(\xi)$$
(3.62)

3.4 Solution Methodology

In this section, a solution procedure for determining the buckling load, post-buckling and bending responses of the nano-beam is established. A selected, efficient numerical technique for solving a system of nonlinear algebraic equations and the quadrature rule adopted in the numerical evaluation of all involved integrals are briefly summarized.

3.4.1 Determination of Buckling Load

The buckling load of a nano-beam with prescribed end conditions can be determined using a standard procedure analogous to that employed by Timoshenko and Gere (1961) in the determination of the buckling load of elastic columns. The buckled shape of the nano-beam is obtained, by solving the ordinary differential equation (3.35), as

$$\overline{v}(\overline{S}) = C_1 \cos \lambda \overline{S} + C_2 \sin \lambda \overline{S} + C_3 \overline{S} + C_4 \tag{3.63}$$

where C_1 , C_2 , C_3 and C_4 are unknown constants depending on the prescribed end conditions. By enforcing four boundary conditions, two at each end, it leads to a system of characteristic equations governing the buckling load

$$\mathbf{A}(\lambda)\mathbf{C} = \mathbf{0} \tag{3.64}$$

where $\mathbf{A}(\lambda)$ is a 4x4-matrix whose entries depend only on λ and prescribed end conditions; $\mathbf{C} = \{C_1 \ C_2 \ C_3 \ C_4\}^T$; and $\mathbf{0}$ is a zero vector. Since the governing ordinary differential equation (3.35), written in terms of λ , is of the same form as that of the classical case (without the surface and nonlocal effects), the buckled shape (3.63) and the form of characteristic equations (3.64) are identical to those of the classical case. In particular, all eigen pairs $(\lambda_i, \mathbf{C}_i)$, $i=1,2,\ldots$, associated with (3.64) are identical for both the present case and the classical case. Due to this fact, there is no need to resolve the Eigen problem (3.64) again, and the eigen pairs $(\lambda_i, \mathbf{C}_i)$, $i=1,2,\ldots$ reported in the literature for the buckling of columns equally apply (e.g., Timoshenko and Gere 1961). If the lowest buckling load is of interest, the minimum eigenvalue λ_{\min} from the set $\{\lambda_1, \lambda_2, \lambda_3, \ldots\}$ is required, and it takes the value π , $\pi/2$, 2π , π , and 1.4303π for pinned-roller supported, fixed-free, fixed-fixed, fixed-guided, and fixed-rollered beams, respectively. From the definition $\lambda = \sqrt{p/(\eta - \mu p)}$ and the available λ_{\min} , the normalized buckling load p takes the form

$$p = \frac{\lambda_{\min}^2 \eta}{1 + \lambda_{\min}^2 \mu} \tag{3.65}$$

The buckled shape corresponding to λ_{\min} can be obtained from (3.63) and the eigenvector \mathbf{C}_{\min} . For the classical case (without the surface and nonlocal effects, i.e., $\eta = 1, \mu = 0$), the normalized buckling load, denoted by p^c , simply takes the form $p^c = \lambda_{\min}^2$. For the comparison purpose, we also introduce the ratio p/p^c (or P_{cr}/P_{cr}^c where P_{cr} , P_{cr}^c denote the buckling loads of the present case and the classical case, respectively)

$$\frac{p}{p^{c}} = \frac{P_{cr}}{P_{cr}^{c}} = \frac{\eta}{1 + \lambda_{\min}^{2} \mu}$$
 (3.66)

3.4.2 Nonlinear Solver

To obtain the response of fixed-free and fixed-roller supported nano-beams, the two systems of nonlinear algebraic equations (3.41)-(3.43) and (3.57)-(3.60) must be solved. Due to the strong nonlinearity of those governing equations and their fully coupled feature, their solution can be obtained numerically using the well-known Newton-Raphson iterative scheme (e.g., Reddy, 2015). For a given loading history, an arc-length scheme is employed along with taking the solution at the previous load step as the initial guess of the current step to accelerate the convergence of numerical solutions.

3.4.3 Quadrature for Involved Weakly Singular Integrals

It is evident that integrands of all integrals contained in the governing nonlinear algebraic equations (3.41)-(3.43) and (3.58)-(3.63) exhibit weakly singular behavior at points where the bending moment vanishes, e.g., the free end of a nano-beam shown in Figure 3.1(a) and the interior inflection point of a nano-beam shown in Figure 3.1(b). While such embedded singularity does

not affect the convergence of those integrals in the sense of Riemann, it renders the numerical integration by standard Gaussian quadrature computationally inefficient. To overcome such difficulty, a standard technique based upon the integrand regularization through a variable transformation is employed. For brevity, the proposed procedure is demonstrated only for the governing equation (3.41) where the singularity exists at the right end of the beam; its application to other governing equations and the singularity present at other locations is also valid. By first introducing the following variable transformation

$$\phi = (\theta_2 - \theta)^{\gamma} \tag{3.67}$$

where γ is a selected constant. The Jacobian of transformation (3.67) is given by

$$J = \frac{d\theta}{d\phi} = -\frac{1}{\gamma} (\theta_2 - \theta)^{1-\gamma} \tag{3.68}$$

By substituting (3.67) and (3.68) into (3.41), it leads to

$$1 = \frac{1}{\gamma} \int_{0}^{(\theta_2)^{\gamma}} \frac{\left\{ \eta + \mu \bar{F}(\theta) \right\} (\theta_2 - \theta)^{1 - \gamma}}{\sqrt{2\eta \left\{ \bar{F}(\theta_2) - \bar{F}(\theta) \right\} + \mu \left\{ \bar{F}^2(\theta_2) - \bar{F}^2(\theta) \right\}}} d\phi$$
 (3.69)

It is evident from (3.37) that the function $h(\theta) = 2\eta \left\{ \overline{F}(\theta_2) - \overline{F}(\theta) \right\} + \mu \left\{ \overline{F}^2(\theta_2) - \overline{F}^2(\theta) \right\}$ appearing in the square root sign of (3.69) is regular and zero at $\theta = \theta_2$ and, by carrying out Taylor series expansion about $\theta = \theta_2$, $h(\theta)$ can be represented by

$$h(\theta) = h'(\theta)(\theta_2 - \theta) + \mathcal{C}((\theta_2 - \theta)^2) \tag{3.70}$$

Using (3.70) together with the regularity of the function $\eta + \mu \overline{F}(\theta)$, the integrand of the integral in (3.69) is of $\mathcal{O}((\theta_2 - \theta)^{1/2 - \gamma})$. The weak singularity of such integral can be, therefore, removed by choosing $\gamma = 1/2$. Once the integrand is completely regularized, the final integral can be integrated accurately and efficiently by standard Gaussian quadrature.

3.5 Results and Discussion

In this section, a selected set of numerical results obtained from the proposed technique is reported and also compared with existing solutions of the classical case to verify both the formulation and implementations. The influence of both surface stresses and nonlocal elasticity on the buckling load, post-buckling and bending responses for both fixed-free and fixed-rollered nano-beams is also discussed. In the numerical study, material parameters reported by Juntarasaid et al. (2012) are employed; for instance, the modulus of elasticity and Poisson's ratio of the bulk material are taken as E = 76 GPa and v = 0.3 whereas the surface modulus of elasticity and the residual surface tension are taken as $E^s = 1.22$ N/m and $\tau^s = 0.89$ N/m, respectively. In addition, the nonlocal parameters suggested by Yang and Lim (2011) (i.e., $\mu \le 0.04$, $e_0 < 14$) and $e_0 a = 10$ nm are employed. To investigate the size dependency of solutions, the length l, the width b, and the depth h of the nano-beam are scaled from the dimensions l_0 , b_0 , b_0 of a reference nano-beam by a proportional ratio β (i.e., $l = \beta l_0$, $b = \beta b_0$ and $b = \beta h_0$). In addition, four different models including Model-1 without the surface and nonlocal effects (i.e., $\eta = 1, \mu = 0$), Model-2 considering

only the surface effect (i.e., $\mu = 0$), Model-3 considering only the nonlocal effect (i.e., $\eta = 1$), and Model-4 considering both the surface and nonlocal effects are utilized in the simulations to clearly demonstrate the role of both surface stresses and nonlocal elasticity on the response of nano-beams.

3.5.1 Modified Flexural Rigidity and Nonlocal Parameter

It is apparent from the above formulation that the role of the surface and nonlocal effects in the governing equations is completely described by two parameters, one associated with the normalized, modified flexural rigidity η and the other corresponding to the nonlocal parameter μ . As indicated by (3.14), the normalized, modified flexural rigidity η depends not only on the dimensions of the cross section h, b but also on the surface modulus of elasticity E^s , the residual surface tension τ^s , and the length of the beam l. The relationship between η and E^s is shown in Figure 3.4 for $\tau^s = \{0,0.89\} N/m$, $h_0/b_0 = \{0.5,1,2\}$, and $l_0/h_0 = \{5,10,15\}$. It can be concluded that increase of the surface modulus of elasticity tends to enhance the modified flexural rigidity for the fixed value of residual surface tension. Clearly, the modified flexural rigidity is always greater than the classical flexural rigidity (i.e., $\eta \ge 1$) for $\tau^s = 0$ whereas its value can be significantly lower than that of the classical case when the positive τ^s is present. In addition, η depends on both the aspect ratio of the cross section and the slenderness ratio of the beam for non-zero τ^s but is independent of the slenderness ratio when $\tau^s = 0$. In summary, increase of the surface modulus of elasticity tends to stiffen the nano-beam and this influence is more significant when the slenderness ratio of the beam becomes smaller and the aspect ratio of the cross section becomes larger. The relationship between η and the residual surface tension τ^s for $E^s = 1.22 N/m$ is also shown in Figure 3.5(a). Unlike the surface modulus of elasticity, increase of the residual surface tension tends to soften the nano-beam and, apparently, such influence becomes more prominent for the beam with small slenderness ratio and large aspect ratio of the cross section. The relationship between the nonlocal parameter μ and the length of the nano-beam is also reported in Figure 3.5(b) for different values of $(e_0 a)^2 = \alpha (e_0 a)_{ref}^2$ where $(e_0 a)_{ref}^2 = 10 nm$ and $\alpha = \{0.1, 1, 10\}$. As evident from these results, the nonlocal parameter μ decreases as the beam length increases and, therefore, the nonlocal effect can be neglected for a sufficiently long element.

3.5.2 Buckling Load of Nano-beams

While the explicit buckling formula established in the present study applies for nano-beams with any prescribed end conditions, results for the buckling load of two representative cases, the fixed-free and fixed-rollered nano-beams, are presented, for brevity, to demonstrate the role of the surface stresses and nonlocal elasticity. In addition, the size dependent behavior of predicted buckling solutions is also explored.

To investigate the size dependency of solutions for this particular case, the reference aspect ratio $h_0/b_0=1$ with $h_0=10\,nm$ is employed. The normalized buckling loads for both fixed-free and fixed-rollered nano-beams are reported in Figure 3.6, for three different reference slenderness ratios $l_0/h_0=\{5,10,15\}$ and all four models. It can be seen from these results that the predicted normalized buckling loads from the Model-2 and the Model-4 exhibit strong size dependence and, in particular, the discrepancy of solutions relative to the classical case is quite significant when the size of the beam is in the range of nanometers. In addition, the Model-2 and the Model-4 predict

lower buckling loads for both fixed-free and fixed-rollered nano-beams in comparison with that of the classical case. Such finding is clearly different from the conclusion of the earlier work of Juntarasaid et al. (2012). This is due mainly to the fact that the presence of the positive residual surface tension generates the compressive residual stress in the bulk material and this, as a result, reduces the modified flexural rigidity of the beam. Apparently, ignorance of such bulk residual stress cannot capture the reduction of the beam stiffness.

The influence of the surface modulus of elasticity, the residual surface tension, and the nonlocal parameter is also investigated. In such numerical experiments, the reference length of the beam l_0 , the proportional ratio β , the reference slenderness ratio l_0/h_0 , the reference aspect ratio of the cross section h_0/b_0 are taken as $l_0=100$ nm, $\beta=5$, $l_0/h_0=\{5,10,15\}$, $h_0/b_0=1$, respectively. The normalized buckling load P_{cr}/P_{cr}^c of the fixed-free and fixed-rollered nano-beams is reported as a function of the surface modulus of elasticity in Figure 3.7 for $\tau^s=0.89$ N/m. It can be deduced from these results that the increase in the surface modulus of elasticity tends to stiffen the nanobeams. Also, the relationship between the normalized buckling load P_{cr}/P_{cr}^c and the residual surface tension is presented in Figure 3.8 for the fixed-free and fixed-rollered nano-beams with $E^s=1.22$ N/m. Unlike the influence of the surface modulus, the increase in the residual surface tension tends to soften the nano-beams or, equivalently, reduce the buckling load. Finally, the normalized buckling load P_{cr}/P_{cr}^c as a function of the nonlocal parameter μ is reported in Figure 3.9 for $E^s=1.22$ N/m and $\tau^s=0.89$ N/m. It can be concluded that as μ increases, the normalized buckling load clearly reduces.

3.5.3 Post-buckling of Nano-beams

Now, let us consider the post-buckling response of the fixed-free and fixed-rollered nano-beams subjected only to the pure axial compression. Specifically, the transverse force Q for the fixed-free beam and the moment M for the fixed-rollered beam are taken to be zero.

Results for the tip rotation (θ_2) of the fixed-free and fixed-rollered nano-beams under various values of the normalized tip load p obtained from the Model-1 are reported in Figure 3.10. These results are compared with the analytical solution presented by Timoshenko and Gere (1961) for the fixed-free case and with those obtained by the semi-analytical technique proposed by Rungamornrat and Tangnovarad (2011) for the fixed-rollered nano-beam. It is apparent that the proposed technique yields highly accurate numerical solutions for the classical case.

Next, results predicted by all four different models are investigated to study the influence of both the surface stresses and nonlocal elasticity on the post-buckling response of nano-beams. In the numerical study, various values of the proportional ratio β are considered while maintaining the reference slenderness ratio $l_0/h_0=10$ and the reference aspect ratio of the cross section $h_0/b_0=1$ in order to demonstrate the size-dependent behavior of the solution. The normalized maximum longitudinal displacement of the nano-beam under two different values of the normalized compression tip load, i.e., $p=\{2.5,5\}$ for the fixed-free case and $p=\{20.5,21.5\}$ for the fixed-rollered case, is reported in Figure 3.11 as a function of the proportional ratio β and for all four models. The post-buckling shapes are shown in Figures 3.12 and 3.13 for the fixed-free case with $p=\{2.5,5\}$ and $\beta=\{0.5,5\}$ and the fixed-rollered case with $p=\{20.5,21.5\}$ and $\beta=\{5,15\}$,

respectively. Results predicted by the models including the surface stresses (i.e., Model-2 and Model-4) significantly deviate from those of the classical case and presence of the surface effect considerably lowers the apparent bending stiffness of the beam if its length l is comparable to the intrinsic length of the material surface $\Lambda = E^s/E$. Likewise, the role of the nonlocal elasticity depends primarily on the length scale of the problem relative to the parameter μ ; in particular, if the length of the beam decreases to the nano-scale level, the effect in reducing the member stiffness is prominent. It is also evident from this set of results that the discrepancy between responses predicted by the model incorporating only the surface stresses (i.e., Model-2) and the classical solution is much larger than that predicted by the model considering only the nonlocal effect (i.e., Model-3). In addition, the Model-4 yields results nearly identical to those obtained from the Model-2. Similar to the fixed-free case, all models incorporating the nano-scale influence (i.e., Model-2, Model-3 and Model-4) exhibit strong size-dependent behavior. In particular, as the size of the member decreases to that comparable to the intrinsic length scale of the material surface, the influence of both surface stresses and nonlocal elasticity are substantial and they must be properly taken into account in the modeling to reasonably capture the nano-scale phenomena.

To further demonstrate the crucial role of the surface parameters on the post-buckling behavior of fixed-free and fixed-rollered nano-beams, the normalized maximum longitudinal displacement of the beam ($\bar{u}_{\rm max} = u_{\rm max}/l$) for various values of the surface modulus of elasticity and the residual surface tension while maintaining value of the nonlocal parameter. Simulations are carried out for $h_0/b_0=1$, $l_0/h_0=\{5,10,15\}$, and $\beta=5$, p=5 for the fixed-free nano-beam and $\beta=15$, p=20.5 for the fixed-rollered nano-beam. The normalized maximum longitudinal displacement is reported in Figure 3.14 as a function of the surface modulus of elasticity for a fixed $\tau^s=0.89\,N/m$ and in Figure 3.15 as a function of the residual surface tension for a fixed $E^s=1.22\,N/m$. It can be deduced from obtained results that the increase in the surface modulus of elasticity tends to stiffen the nano-beams whereas increase in the residual surface tension tends to reverse such effect.

To also explore the role of the dimensionless nonlocal parameter (μ) on the post-buckling of nano-beams, the analysis is performed for various values of μ with fixed values of $E^s = 1.22 N/m$ and $\tau^s = 0.89 N/m$ whereas other parameters are taken to be the same as the previous simulations. Results for the normalized maximum longitudinal displacement are reported as a function of μ in Figure 3.16. It is seen that the post-buckling displacement is strongly dependent on the nonlocal parameter and such influence becomes more prominent when the slenderness ratio of the member increases.

3.5.4 Bending of Nano-beams

Now, the bending response of the fixed-free and fixed-rollered nano-beams is investigated; in particular, the longitudinal load P at the end of the beam is taken to be zero for both cases. To verify the proposed technique, solutions for the classical case (without the surface stresses and nonlocal effects, i.e., $\eta=1$ and $\mu=0$) are obtained first and then compared with available benchmark solutions. Results generated by the Model-1 for the deflected shape of the fixed-free nano-beam under a normalized transverse load q=2 and the fixed-rollered nano-beam under a normalized end moment $\overline{m}_0=1/3$ are reported in Figure 3.17 along with the reference solution

presented by Liu et al. (2012) and those generated by a reliable finite element software. The good agreement between computed results and the benchmark solutions should confirm the formulation and proposed solution technique.

To investigate the influence of the surface stresses and nonlocal elasticity on the bending behavior of both fixed-free and fixed-rollered nano-beams, the analysis is carried out using all four models (i.e., Model-1, Model-2, Model-3 and Model-4) and obtained results are compared. To consider the size-dependent behavior of predicted solutions, various values of the proportional ratio β with the fixed slenderness ratio $l_0/h_0 = 10$ and the fixed aspect ratio of the cross section $h_0/b_0 = 1$ are considered. The normalized maximum transverse displacement ($\bar{v}_{max} = v_{max}/l$) for the fixed-free nano-beam under the normalized transverse load $q = \{2,4\}$ and the fixed rollered nanobeam under the normalized end moment $\overline{m}_0 = \{2, 2.5\}$ is reported in Figure 3.18. The deflected shapes of the fixed-free nano-beam with $q = \{2,4\}$ and the fixed-rollered nano-beam with $\overline{m}_0 = \{2, 2.5\}$ are also shown in Figures 3.19 and 3.20, respectively. The proportional ratio $\beta = \{0.5, 5\}$ with the reference length of the beam $l_0 = 100 nm$ is used in this simulation. It is seen that the presence of the surface stresses tends to soften the nano-beam (i.e., reduce the apparent bending stiffness) whereas the nonlocal elasticity shows significantly less influence on the deflected shape in comparison with the classical case. This, as a consequence, renders the solutions predicted by the Model-2 and the Model-3 significantly different but those predicted by the Model-2 and the Model-4 only slightly different. It is obviously seen from Figure 3.18 that when the length of the nano-beam becomes smaller, results obtained from the Model-2, Model-3 and Model-4 increasingly deviate from the classical solution and, when the beam length is relatively large in comparison with the intrinsic length Λ , solutions predicted by all models are nearly identical. It is worth emphasizing that the observed discrepancy, for a particular beam length l, is more pronounced when the models incorporating the surface stresses (i.e., Model-2 and Model-4) are utilized. Based on the characteristic of the displacements and deflected shapes observed in the numerical study, the reduction of the apparent bending stiffness can become substantial when the size of the beam decreases to a nano-scale (i.e., comparable to the intrinsic length Λ of the material surface), and this implies the necessity to incorporate the surface stresses and the nonlocal effects in the mathematical model to physically capture the nano-scale influence.

To further investigate the influence of the surface modulus of elasticity and the residual surface tension on the bending behavior, responses of the beam for various values of E^s and τ^s are obtained and compared. In the simulations, $l_0 = 100 \, nm$, $\beta = 5$, $h_0/b_0 = 1$, $l_0/h_0 = \{5,10,15\}$, q = 2 for the fixed-free nano-beam, and $\overline{m}_0 = 2.5$ for the fixed-roller-supported nano-beam are employed. The relationship between the maximum transverse displacement \overline{v}_{max} of the fixed-free and fixed-rollered nano-beams versus the surface modulus of elasticity E^s for $\tau^s = 0.89 \, N/m$ is shown in Figure 3.21. It can be deduced from this set of results that the increase in the surface modulus of elasticity tends to stiffen the nano-beams or, equivalently, reduce the deflection of the beam relative to the classical case. In addition, the maximum transverse displacement versus the residual surface tension τ^s for $E^s = 1.22 \, N/m$ is reported in Figure 3.22 for both the fixed-free and fixed-rollered nano-beams. Unlike the influence of the surface modulus of elasticity, the increase in the residual surface tension tends to soften the nano-beam. It is also evident from these results that

when the slenderness ratio of the member becomes larger, the influence of the surface effect is more prominent.

To also examine the role of the nonlocal parameter μ on the bending response of nanobeams, results are obtained for various values of μ while E^s and τ^s remain fixed (i.e., $E^s=1.22N/m$ and $\tau^s=0.89N/m$). Similar to the previous case, $l_0=100nm$, $\beta=5$, $h_0/b_0=1$, $l_0/h_0=\{5,10,15\}$, q=2 for the fixed-free nano-beam, and $\overline{m}_0=2.5$ for the fixed-rollered nanobeam are employed in the simulations. Results for the normalized maximum transverse displacements are reported as a function of the nonlocal parameter μ in Figure 3.23. As evident from these results, the bending response of the nano-beams exhibits strong dependence on the nonlocal parameter, and this influence is more significant when the slenderness ratio of the beam increases.

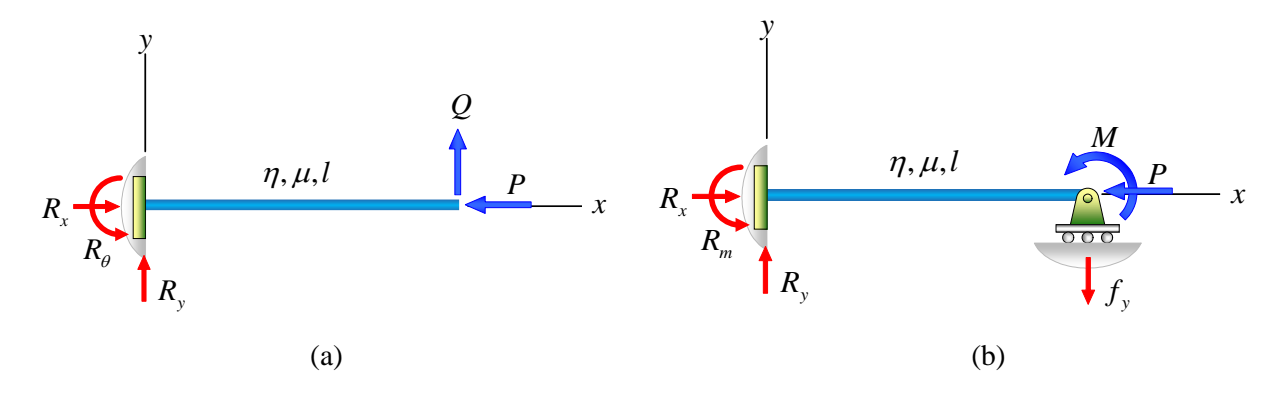


Figure 3.1 Schematic of (a) perfectly straight nano-beam clamped at the left end and subjected to longitudinal force P and transverse force Q at the right end and (b) perfectly straight nano-beam clamped at the left end, roller-supported at the right end and subjected to longitudinal force P and moment M at the right end.

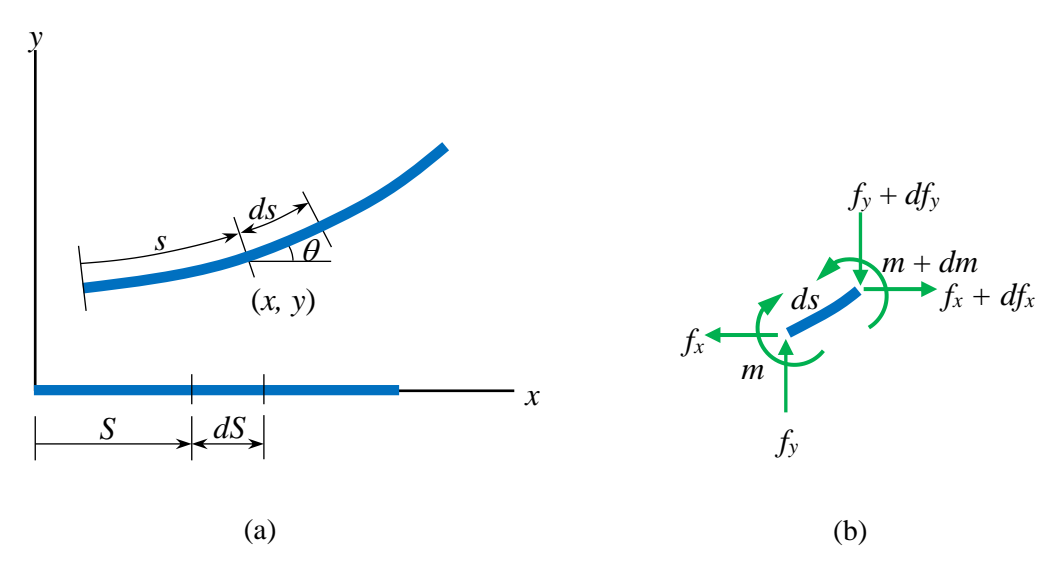


Figure 3.2 (a) Schematic of deformed and undeformed configurations of centroidal axis of nano-beam and (b) free body diagram of infinitesimal deformed element.

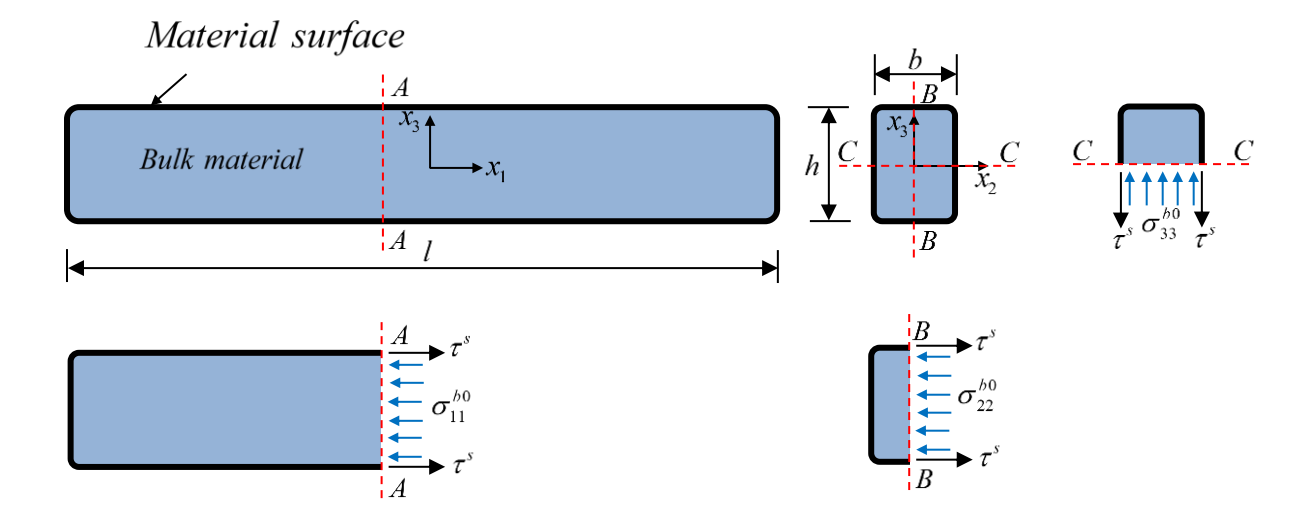


Figure 3.3 Schematic of beam element treated as composite consisting of bulk material and material surface in unstrained state.

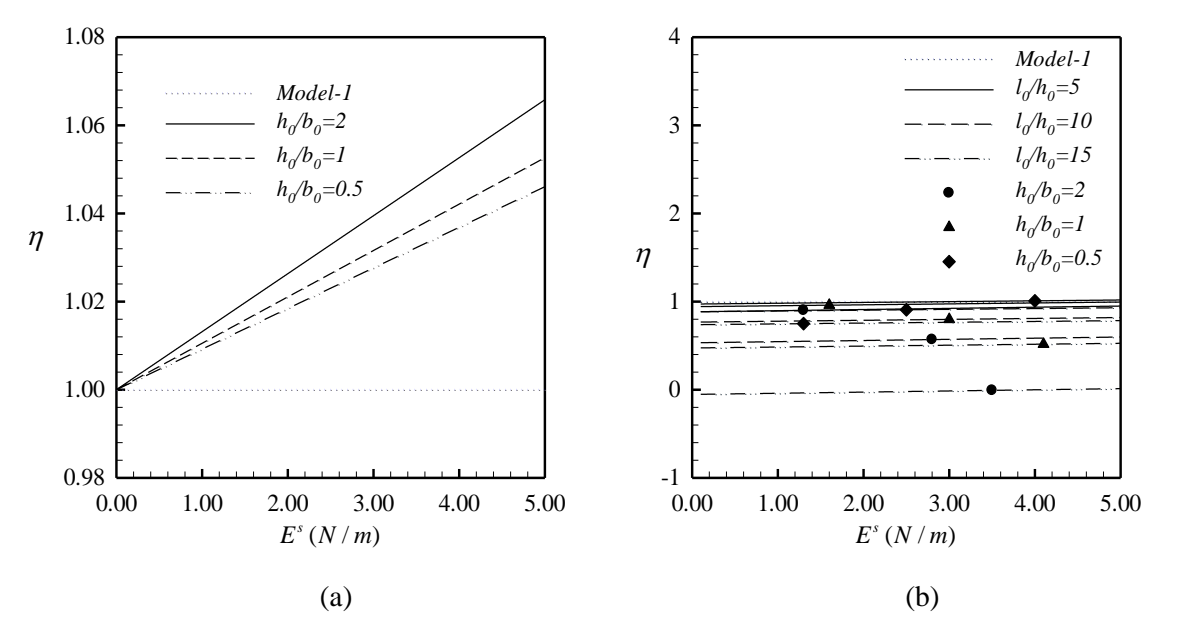


Figure 3.4 Relationship between normalized flexural rigidity η and surface modulus of elasticity E^s for E=76 GPa, v=0.3, $h_0=10$ nm: (a) $\tau^s=0$ and (b) $\tau^s=0.89$ N/m.

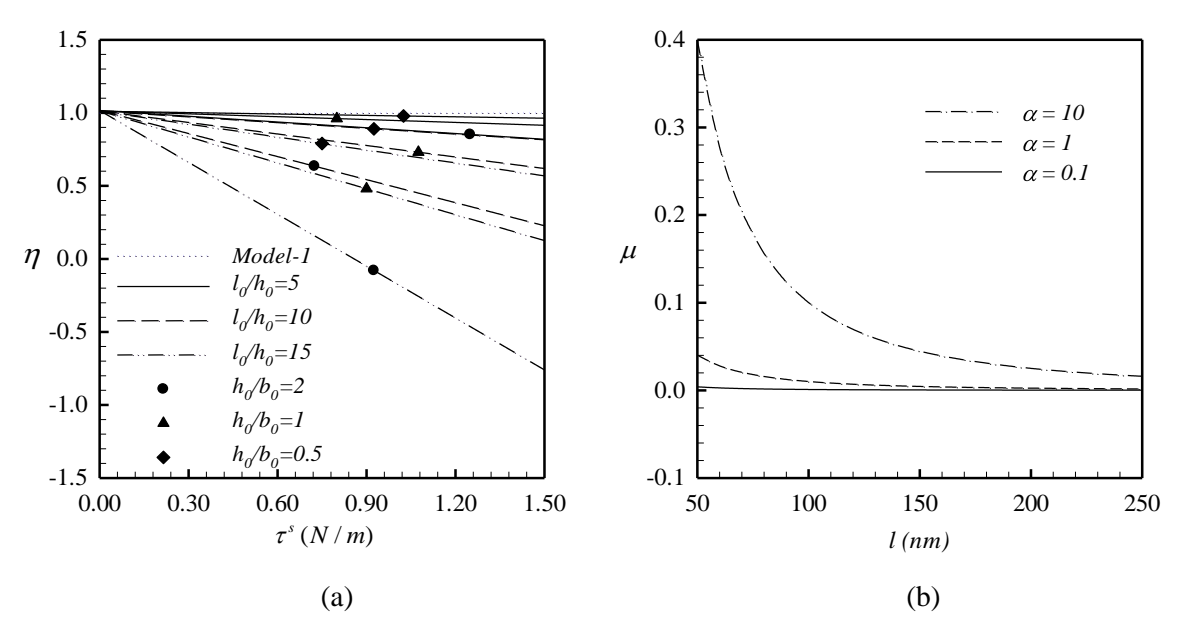


Figure 3.5 (a) Relationship between normalized flexural rigidity η and the residual surface tension τ^s of nano-beam with different slenderness ratio l_0 / $h_0 \in \{5,10,15\}$ and different aspect ratio of cross section h_0 / $h_0 \in \{2,1,0.5\}$ for E=76 GPa, v=0.3, $h_0=10$ nm and (b) relationship between nonlocal parameter μ and length of nano-beam l for $(e_0a)_{ref}=10$ nm with different α

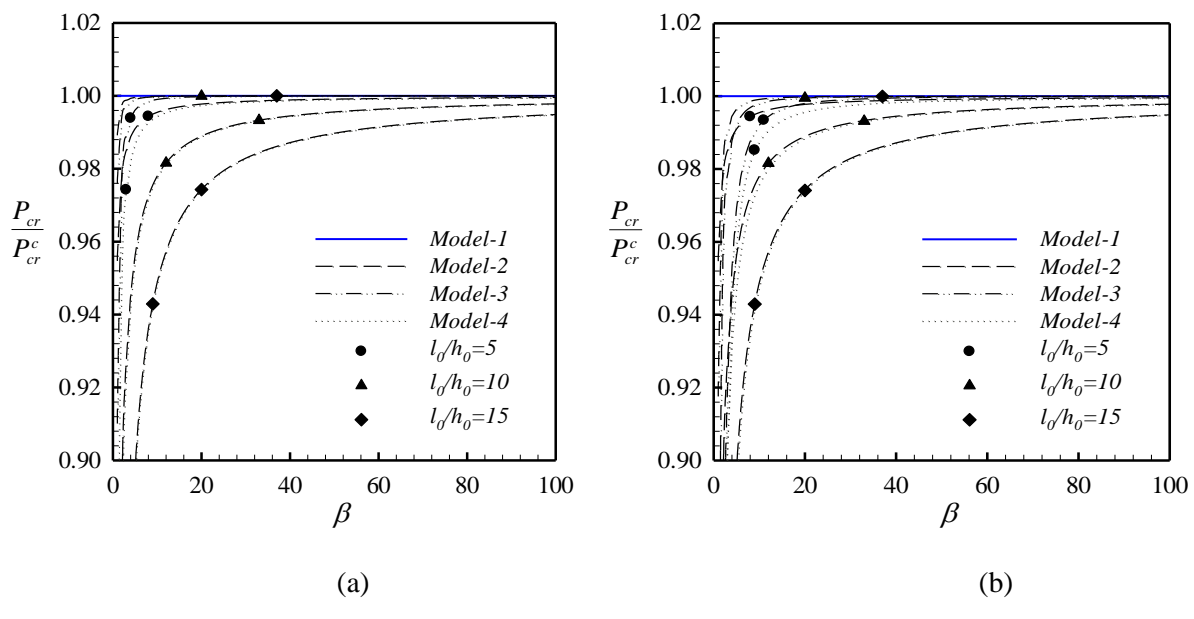


Figure 3.6 Relationship between normalized buckling load P_{cr} / P_{cr}^c and proportional ratio β of the nanobeam with different slenderness ratio l_0 / $h_0 \in \{5,10,15\}$ for E = 76 GPa, $\nu = 0.3$, $E^s = 1.22$ N / m, $\tau^s = 0.89$ N / m, $e_0a = 10$ nm, h_0 / $h_0 = 1$, $h_0 = 10$ nm: (a) fixed-free nano-beam and (b) fixed-roller supported nano-beam.

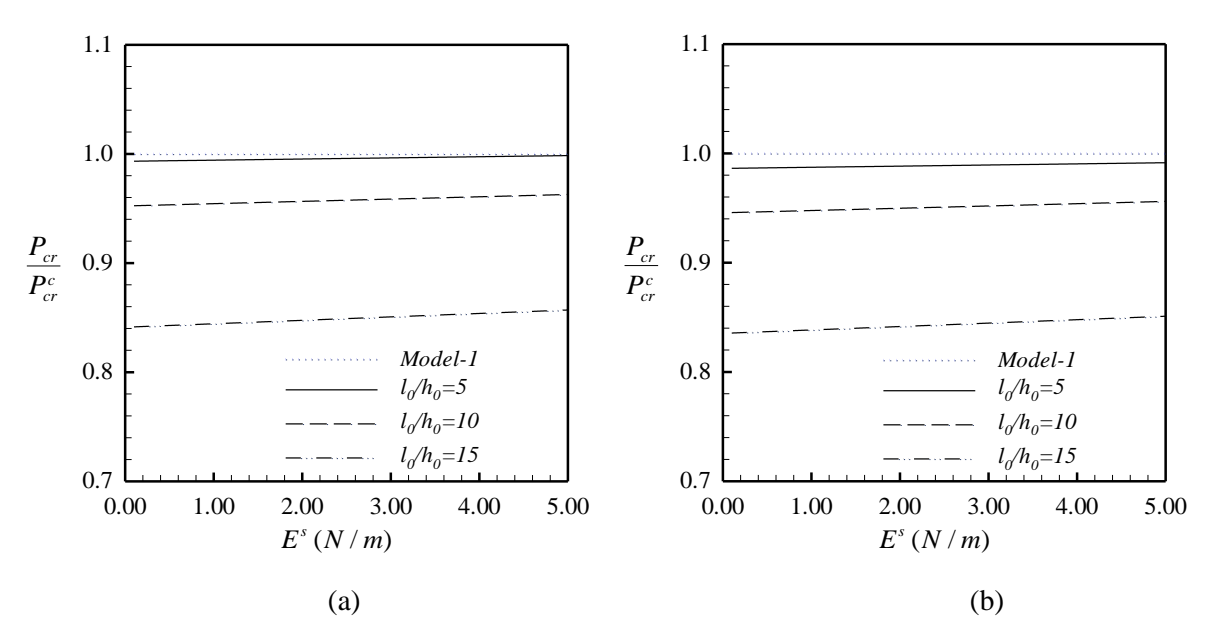


Figure 3.7 Relationship between normalized buckling load P_{cr} / P_{cr}^c and surface modulus of elasticity E^s with different slenderness ratio l_0 / $h_0 \in \{5,10,15\}$ for E=76 GPa, v=0.3, $\tau^s=0.89$ N / m, $e_0a=10$ nm, h_0 / $h_0=1$, $l_0=100$ nm, $\beta=5$: (a) fixed-free nano-beam and (b) fixed-roller supported nano-beam.

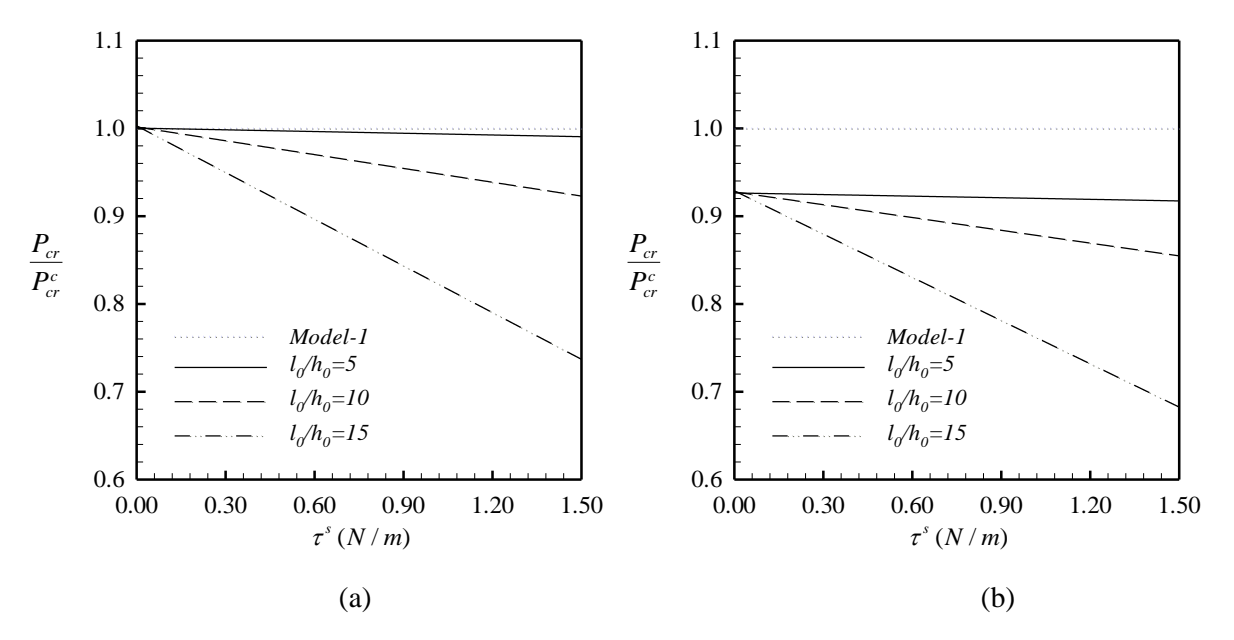


Figure 3.8 Relationship between normalized buckling load P_{cr} / P_{cr}^c and residual surface tension τ^s with different slenderness ratio l_0 / h_0 = {5,10,15} for E = 76 GPa, ν = 0.3, E^s = 1.22 N / m, e_0a = 10 nm, h_0 / h_0 = 1, h_0 = 100 nm, h_0 = 5: (a) fixed-free nano-beam and (b) for fixed-roller supported nano-beam.

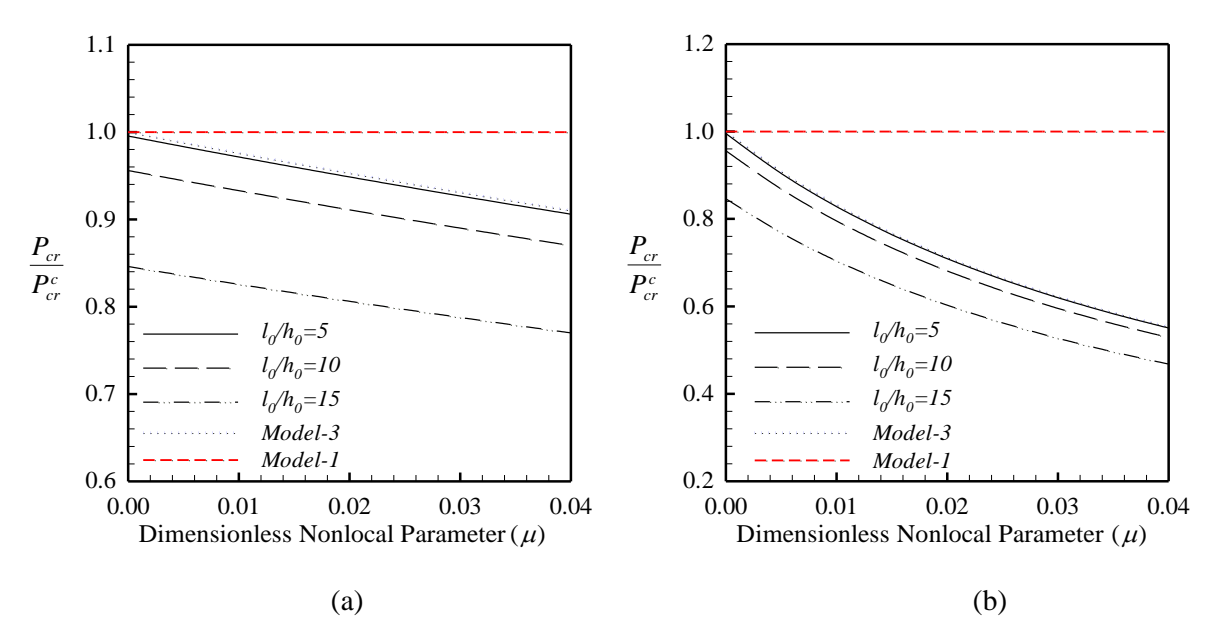


Figure 3.9 Relationship between normalized buckling load P_{cr} / P_{cr}^c and nonlocal parameter μ with different slenderness ratio l_0 / h_0 = {5,10,15} for E = 76GPa, ν = 0.3, E^s = 1.22N / m, τ^s = 0.89 N / m, h_0 / h_0 = 1, h_0 = 100nm, h_0 = 5: (a) fixed-free nano-beam and (b) fixed-roller supported nano-beam.

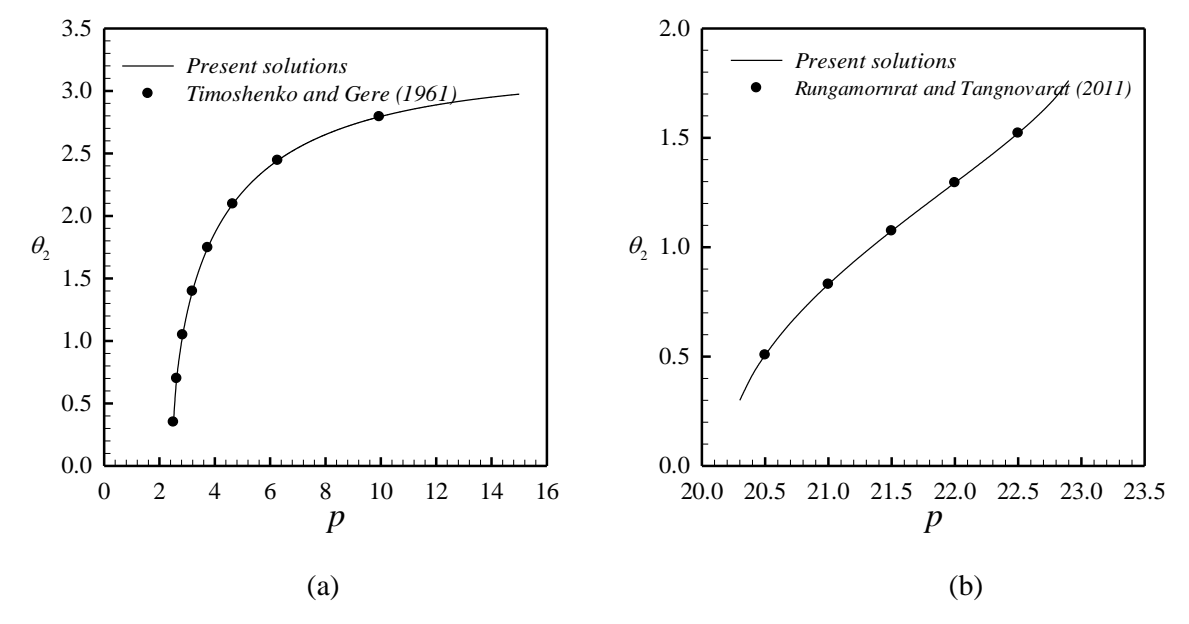


Figure 3.10 Relationship between normalized tip load p and tip rotation θ_2 for (a) fixed-free beam and (b) fixed-roller supported beam. Obtained results are compared with the available benchmark solution.

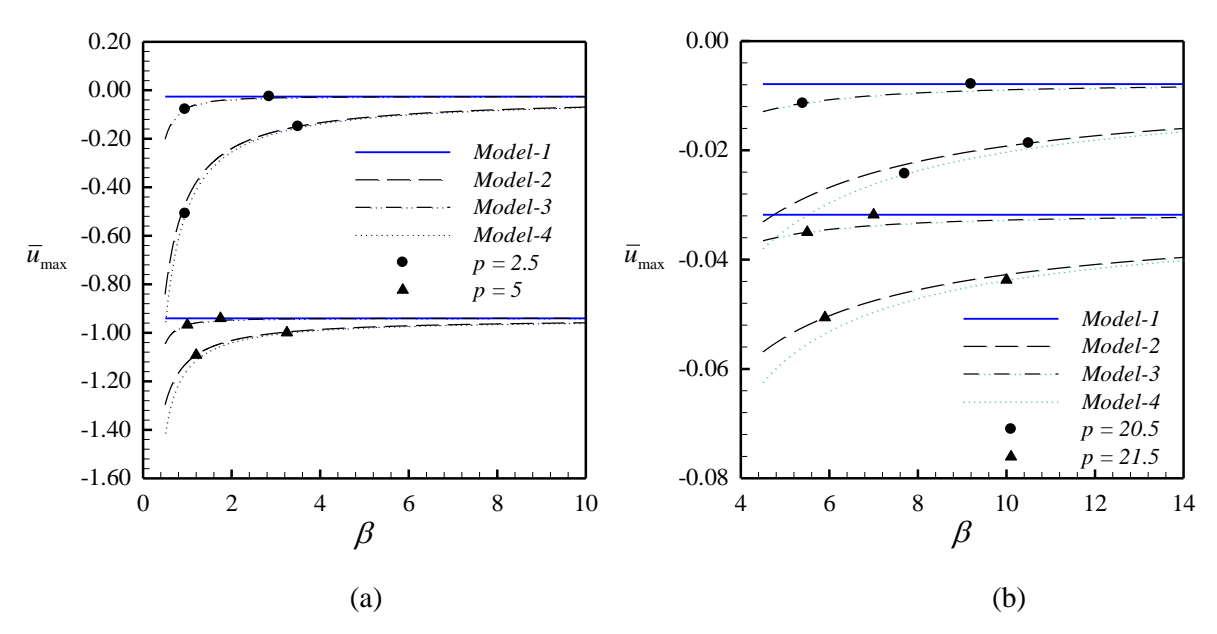


Figure 3.11 Relationship between proportional ratio β and normalized maximum longitudinal displacement \overline{u}_{\max} for E=76 GPa, $\nu=0.3$, $E^s=1.22$ N/m, $\tau^s=0.89$ N/m, $e_0a=10$ nm, $h_0/b_0=1$, $l_0/h_0=10$, $l_0=100$ nm: (a) fixed-free nano-beam under normalized compression force $p=\{2.5,5\}$ and (b) fixed-roller supported nano-beam under normalized compression force $p=\{20.5,21.5\}$.

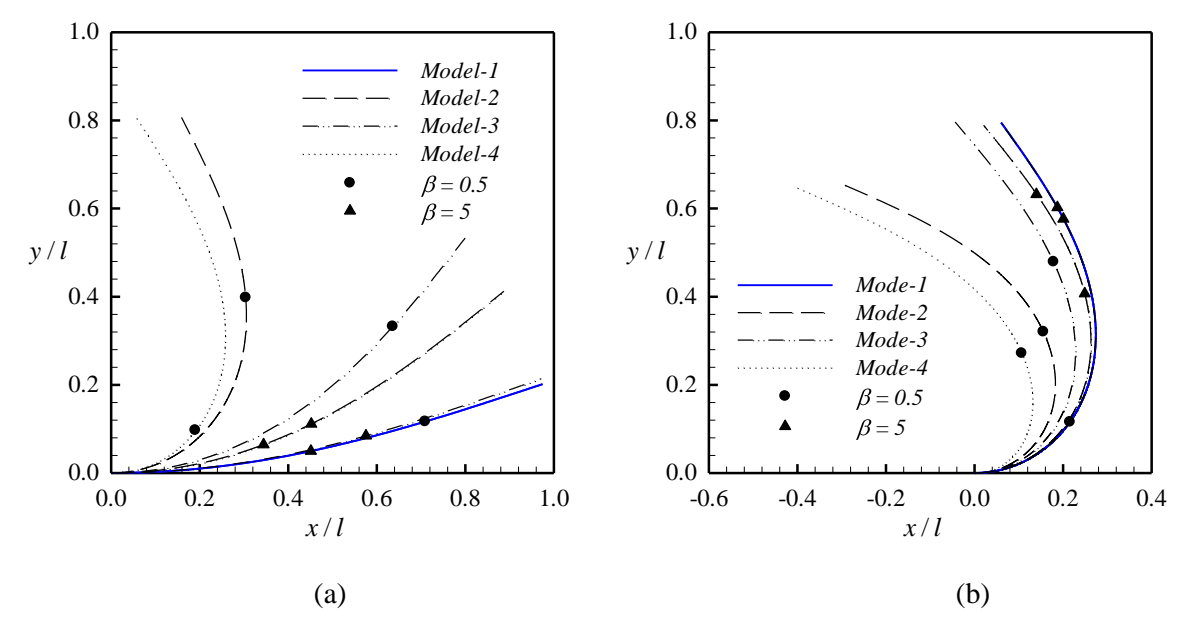


Figure 3.12 Post-buckling shape of fixed-free nano-beam for E = 76 GPa, v = 0.3, $E^s = 1.22$ N/m, $\tau^s = 0.89$ N/m, $e_0a = 10$ nm, $h_0/b_0 = 1$, $l_0/h_0 = 10$, $l_0 = 100$ nm with two values of proportional ratio $\beta = \{0.5, 5\}$ and two values of normalized compression force: (a) p = 2.5 and (b) p = 5.

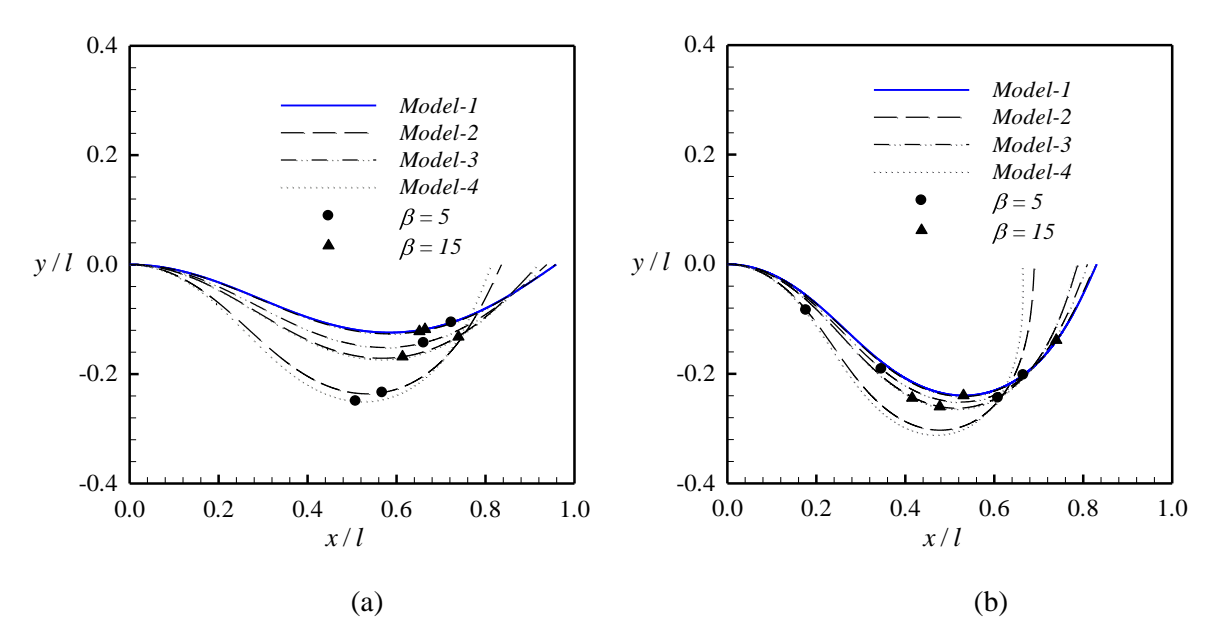


Figure 3.13 Post-buckling shape of fixed-roller supported nano-beam for E=76 GPa, v=0.3, $E^s=1.22$ N/m, $\tau^s=0.89$ N/m, $e_0a=10$ nm, $h_0/b_0=1$, $l_0/h_0=10$, $l_0=100$ nm with two values of proportional ratio $\beta=\{5,15\}$ and two values of normalized compression force: (a) p=20.5 and (b) p=21.5.

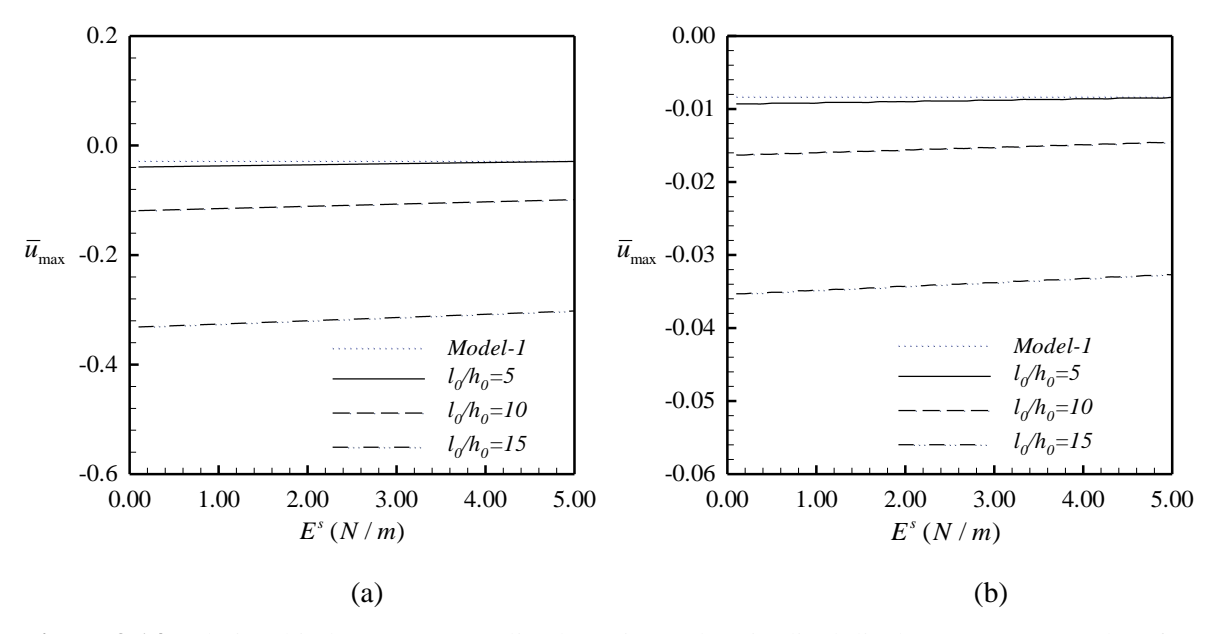


Figure 3.14 Relationship between normalized maximum longitudinal displacement $\overline{u}_{\text{max}}$ and surface modulus of elasticity E^s with different slenderness ratio l_0 / h_0 = {5,10,15} for E = 76GPa, ν = 0.3, τ^s = 0.89 N / m, e_0a = 10 nm, h_0 / b_0 = 1, l_0 = 100 nm: (a) fixed-free nano-beam with β = 5, p = 2.5 and (b) fixed-roller supported nano-beam with β = 15, p = 20.5.

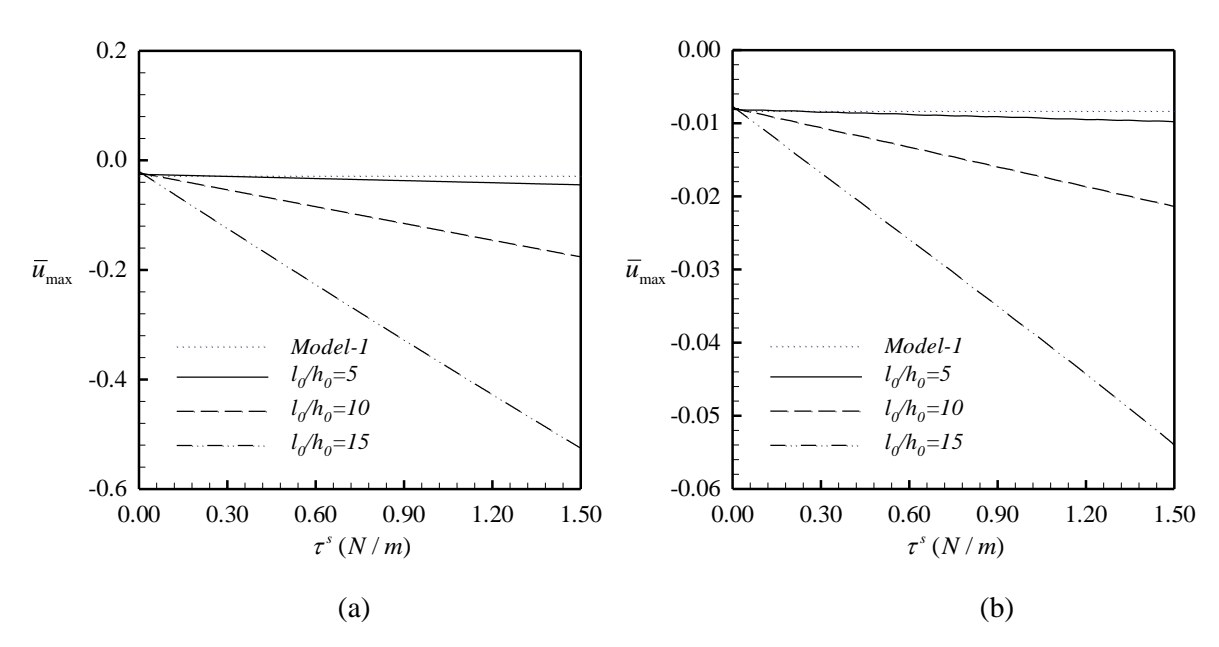


Figure 3.15 Relationship between normalized maximum longitudinal displacement $\overline{u}_{\text{max}}$ and residual surface tension τ^s with different slenderness ratio l_0 / h_0 = {5,10,15} for E = 76GPa, v = 0.3, E^s = 1.22 N / m, e_0a = 10 nm, h_0 / h_0 = 1, h_0 = 100 h_0 (a) fixed-free nano-beam with h_0 = 5, h_0 = 2.5 and (b) fixed-roller supported nano-beam with h_0 = 15, h_0 = 20.5.

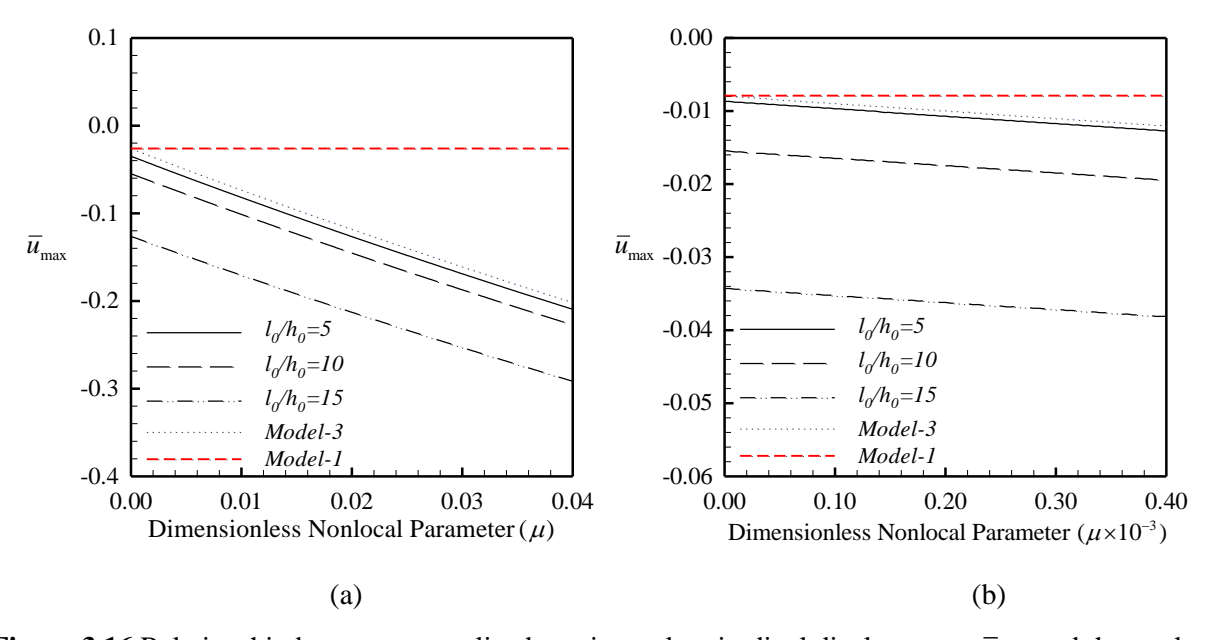


Figure 3.16 Relationship between normalized maximum longitudinal displacement \overline{u}_{\max} and the nonlocal parameter μ with different slenderness ratio l_0 / h_0 = {5,10,15} for E = 76GPa, ν = 0.3, E^s = 1.22N / m, τ^s = 0.89N / m, h_0 / h_0 = 1, l_0 = 100nm: (a) fixed-free nano-beam with β = 5, p = 2.5 and (b) fixed-roller supported nano-beam with β = 15, p = 20.5.

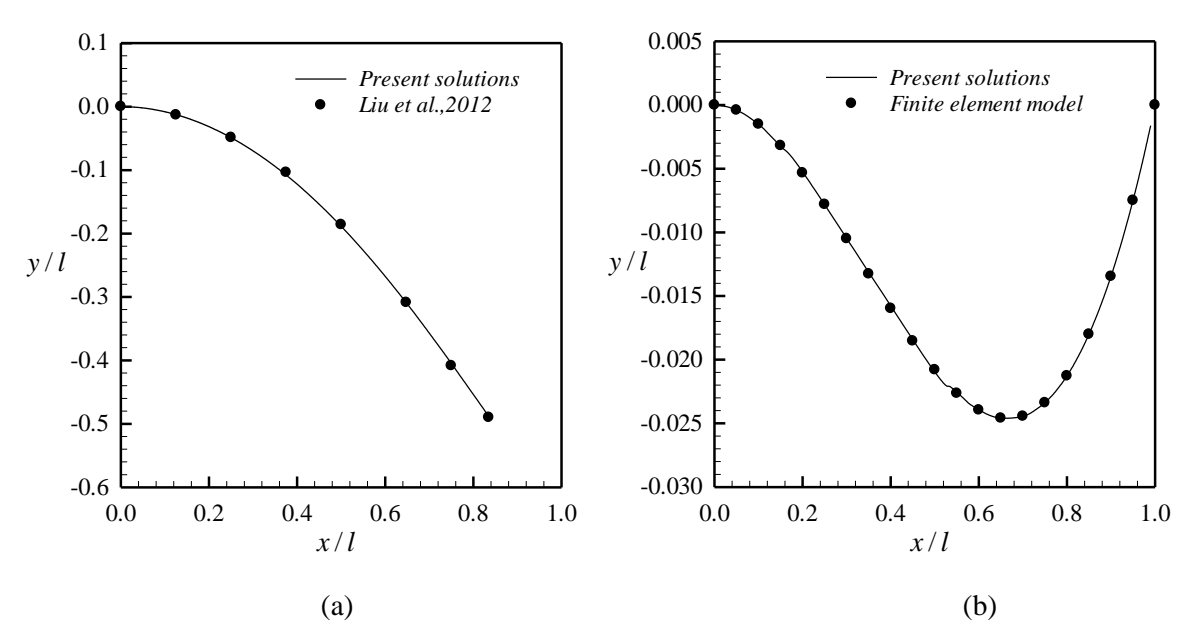


Figure 3.17 Deformed shape of nano-beams obtained from Model-1 for (a) fixed-free nano-beam subjected to normalized transverse force q=2 and (b) fixed-roller supported nano-beam subjected to normalized end moment $\overline{m}_0 = 1/3$.

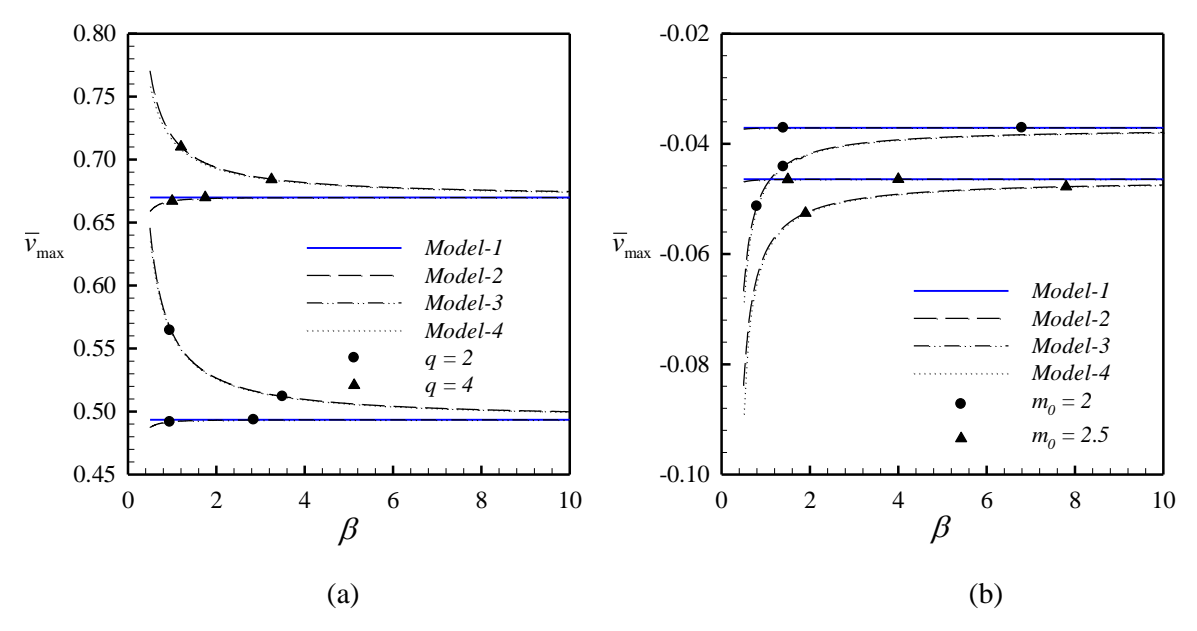


Figure 3.18 Relationship between proportional ratio β and normalized maximum transverse displacement \overline{v}_{\max} for E=76 GPa, v=0.3, $E^s=1.22$ N/m, $\tau^s=0.89$ N/m, $e_0a=10$ nm, h_0 / $b_0=1$, l_0 / $h_0=10$, $l_0=100$ nm: (a) fixed-free nano-beam under normalized end transverse load $q=\{2,4\}$ and (b) fixed-rolle supported nano-beam under normalized end moment $\overline{m}_0=\{2,2.5\}$.

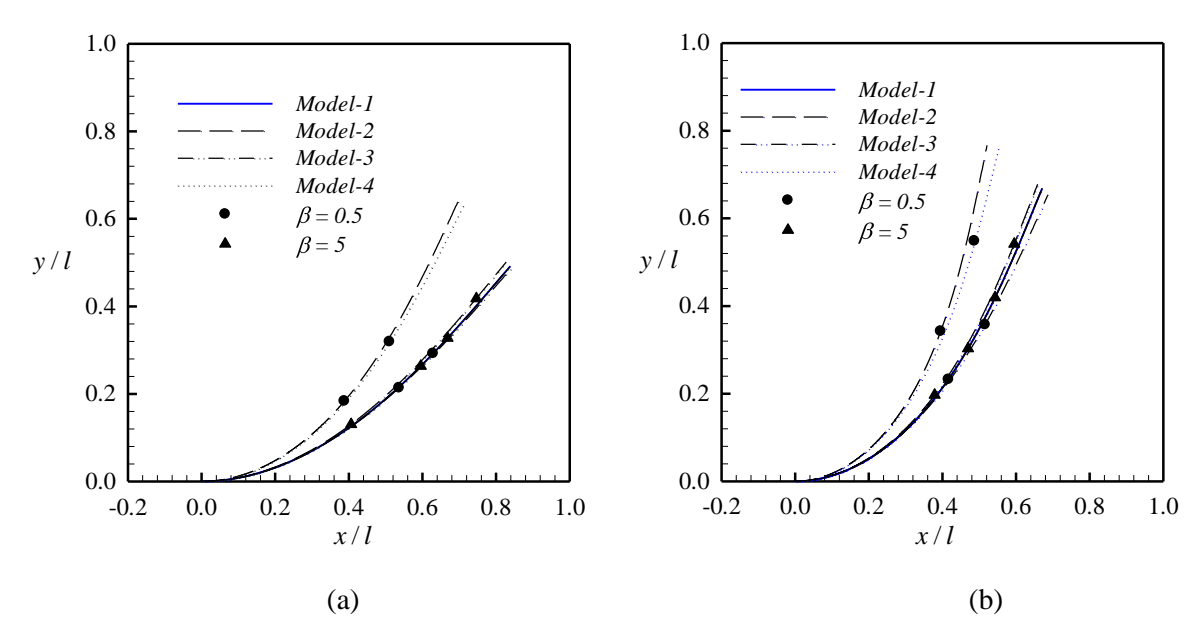


Figure 3.19 Deformed shape of fixed-free nano-beam for E = 76 GPa, v = 0.3, $E^s = 1.22$ N/m, $\tau^s = 0.89$ N/m, $e_0a = 10$ nm, $h_0/b_0 = 1$, $l_0/h_0 = 10$, $l_0 = 100$ nm with two values of proportional ratio $\beta = \{0.5, 5\}$ and two values of normalized end transverse force (a) q = 2 and (b) q = 4.

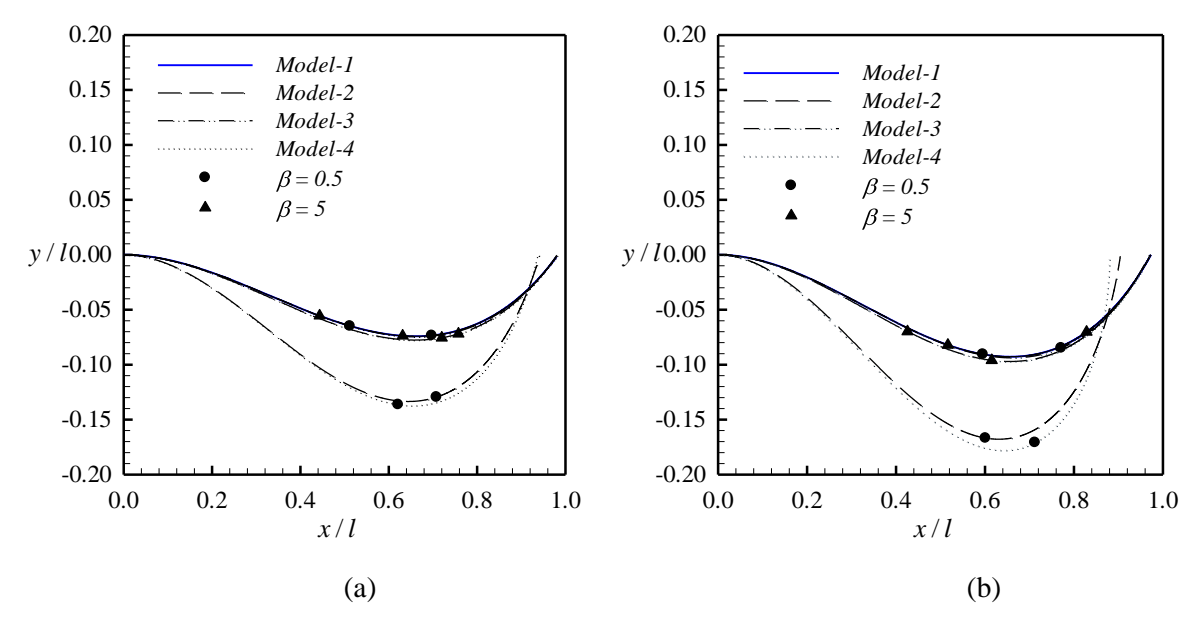


Figure 3.20 Deformed shape of fixed-roller supported nano-beam for E=76 GPa, v=0.3, $E^s=1.22$ N/m, $\tau^s=0.89$ N/m, $e_0a=10$ nm, $h_0/b_0=1$, $l_0/h_0=10$, $l_0=100$ nm with two values of proportional ratio $\beta=\{0.5,5\}$ and two values of normalized end moment (a) $\overline{m}_0=2$ and (b) $\overline{m}_0=2.5$.

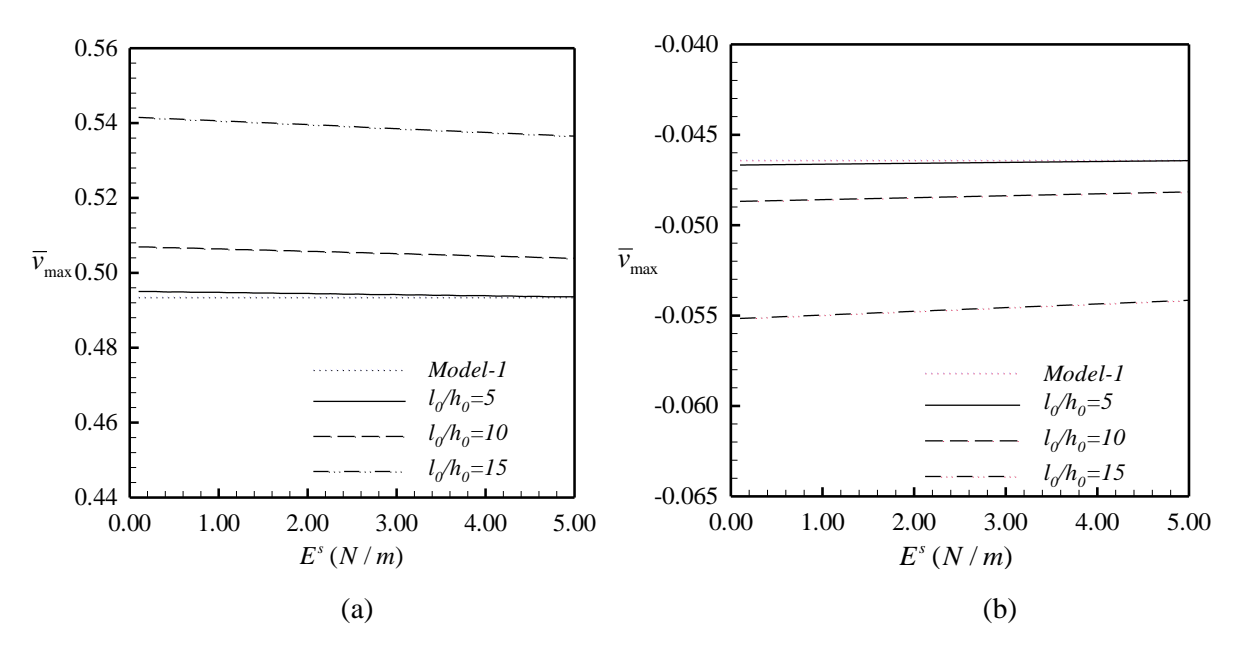


Figure 3.21 Relationship between normalized maximum transverse displacement $\overline{v}_{\text{max}}$ and surface modulus of elasticity E^s with different slenderness ratio $l_0/h_0=\{5,10,15\}$ for E=76 GPa, v=0.3, $\tau^s=0.89$ N/m, $e_0a=10$ nm, $h_0/b_0=1$, $l_0=100$ nm, $\beta=5$: (a) fixed-free nano-beam with q=2 and (b) fixed-roller supported nano-beam with $\overline{m}_0=2.5$.

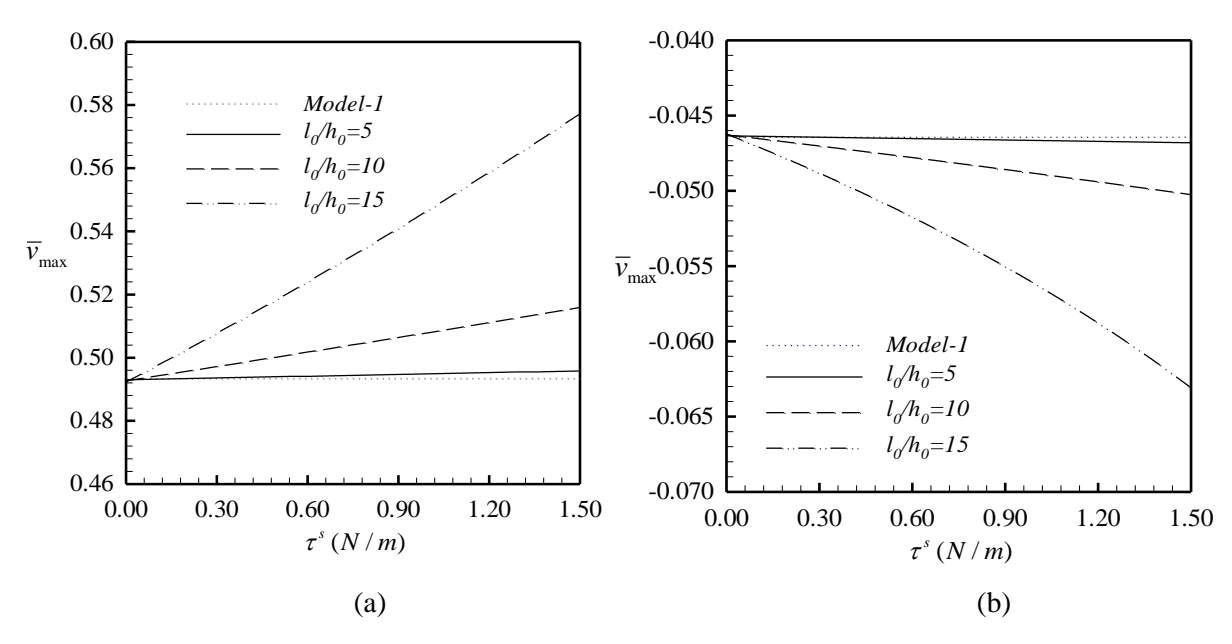


Figure 3.22 Relationship between normalized maximum transverse displacement $\overline{v}_{\text{max}}$ and residual surface tension τ^s with different slenderness ratio l_0 / h_0 = {5,10,15} for E = 76 GPa, ν = 0.3, E^s = 1.22 N / m, e_0a = 10 nm, h_0 / b_0 = 1, l_0 = 100 nm, β = 5: (a) fixed-free nano-beam with q = 2 and (b) fixed-roller supported nano-beam with \overline{m}_0 = 2.5.

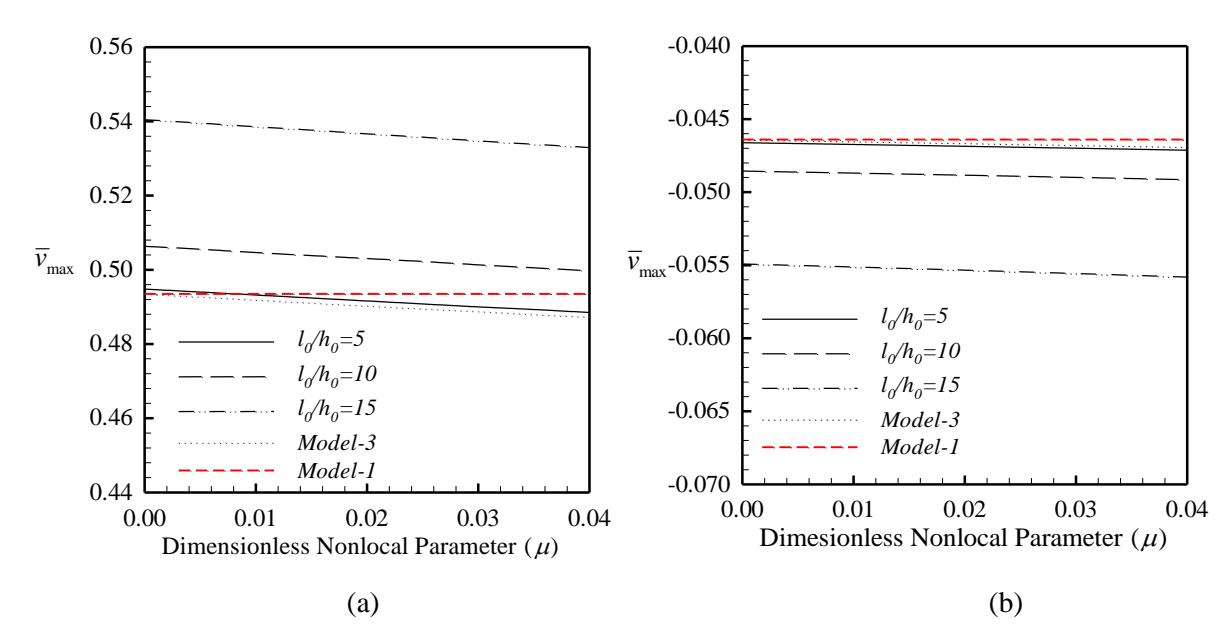


Figure 3.23 Relationship between normalized maximum transverse displacement \overline{v}_{\max} and nonlocal parameter μ with different slenderness ratio l_0 / $h_0 \in \{5,10,15\}$ for E=76GPa, $\nu=0.3$, $E^s=1.22$ N/m, $\tau^s=0.89$ N/m, h_0 / $b_0=1$, $l_0=100$ nm, $\beta=5$: (a) fixed-free nano-beam with q=2 and (b) fixed-roller supported nano-beam with $\overline{m}_0=2.5$.

CHAPTER IV

MODELING OF NANO-CRACKS

This chapter presents the modeling and analysis of nano-size cracks in an elastic whole space with the consideration of surface effects via Gurtin-Murdoch surface elasticity theory. The chapter is organized into two parts, the first part associated with the treatment of a penny-shaped crack under axisymmetric loading on its surface and the second part corresponding to the development of an efficient numerical technique capable of handling non-planar cracks of arbitrary shapes and subjected to general loading conditions. For each part, the background and review indicating the current advances in the area is briefly summarized, then the problem formulation and solution procedure are clearly presented, and finally results and crucial findings are addressed.

4.1 Penny-shaped Crack

In this section, a penny-shaped crack in an infinite elastic medium subjected to vertical pressure loading at the crack surface under the influence of surface stress is considered. The Gurtin-Murdoch continuum theory of elastic material surfaces is adopted and the Hankel integral transform is employed to solve this axisymmetric boundary-value problem. A set of simultaneous dual integral equations is solved by employing an appropriate numerical solution scheme. Selected numerical results are presented to portray the influence of the surface stress on the elastic field.

4.1.1 Background and Review

In recent years, studies on mechanics of nanomaterials and nanostructures have become increasingly important in various advanced engineering applications. In nano-scale structures, the influence of excess energy associated with the surface/interface atoms, called surface/interfacial free energy, is significant due to their high surface-to-volume ratio (e.g., see Yakobson, 2003; Huang and Wang, 2006). As a result, their mechanical behavior becomes size-dependent (Wong et al., 1997). Atomistic simulations are powerful techniques to accurately analyze problems related to nano-scale systems however they require a very large computational effort. Thus studying problems at the nano-scale based on the modified continuum mechanics concepts accounting for surface energy effects is an attractive option to obtain first-approximations for this class of problems.

A rigorous theory based on the continuum mechanics concepts was developed to incorporate the surface and interfacial energy effects by Gurtin and Murdoch (1975; 1978). The surface is modeled as a zero thickness layer perfectly bonded to the underlying bulk material. Miller and Shenoy (2000) examined the size effects of nano-scale plates and bars by employing the Gurtin-Murdoch continuum model and found that the results were in excellent agreement with those obtained from atomistic simulations. Several researchers analyzed nano-scale mechanics problems based on the Gurtin-Murdoch theory and neglected the out-of-plane components of surface stress (e.g. Tian and Rajapakse 2007; Zhao 2009; Zhao and Rajapakse 2009; Intarit et al. 2010; Zhao and Rajapakse 2013; Rahman and Mahmoud 2016). Later, Wang et al. (2010) showed that the out-of-plane components of surface stress could be significant even in the case of small deformations particularly for curved and rotated surfaces. Intarit et al. (2011) considered the complete set of surface stresses in the analysis of a two-dimensional elastic layer under buried loading and found

that the elastic field depends significantly on the surface elastic constants and residual surface stress. The complete version of the Gurtin-Murdoch model was also employed to study problems of an elastic layer under axisymmetric surface loading (Rungamornrat et al., 2016) and rigid frictionless indentation on an elastic half-space (Pinyochotiwong et al., 2013). In addition, influence of surface stress is also important in problems involving soft elastic solids (He and Lim, 2006).

Fracture mechanics, which is concerned with the mechanical behavior of materials in the presence of cracks, has important practical applications. The study of cracks in devices and structures encountered in engineering applications is essential for both reliability and safety. Several crack problems were studied in the context of classical continuum theory in the presence of crack surface tension. Wu (1999), and Wu and Wang (2000, 2001) investigated the influence of surface tension on cracks and proposed that surface tension induced a pair of point loads at the crack tip. With the assumption of a blunt crack-tip, Wang et al. (2008) and Fu et al. (2008) found that surface stress has a significant influence on stresses and displacements in the vicinity of crack tip, especially when the curvature of the crack tip is in the nano-scale. The solutions of Mode-I, II and III cracks were derived with the consideration of surface stresses by assuming that the crack tip stresses are finite by Kim et al. (2010a, 2011b). The above studies dealt exclusively with plane crack (2-D) problems whereas it is useful to examine more practical crack geometries such as penny-shaped cracks. The classical penny-shaped crack problem has been extensively studied (e.g. Sneddon 1946; Florence and Goodier 1963; He and Hutchinson 1981; Fabrikant 1986) but studies related to its counterpart with surface elasticity based on the Gurtin-Murdoch theory are very limited. Recently, a numerical procedure based on the coupling of the standard finite element technique and the boundary integral equation method was proposed by Nguyen et al. (2015) to investigate nano-sized penny-shaped cracks in an infinite elastic medium under mode-I loading. However, their formulation accounts only for the residual surface tension and ignores the influence of the surface Lamé constants. A review of literature indicates that an analytical solution for the penny-shaped crack problem with the complete version of the Gurtin-Murdoch theory has not yet been reported.

4.1.2 Governing Equations and General Solutions

Consider a penny-shaped crack with radius a in an infinite elastic medium and subjected to axisymmetric vertical loading p(r) as shown in Figure 4.1. In the present study, a sharp-crack-tip model is applied and, as a result, the crack geometry can be fully described by two geometrically identical, flat, circular surfaces on the plane z = 0. The elastic medium is governed by the Gurtin-Murdoch continuum theory (Gurtin and Murdoch 1975, 1978). In the absence of body forces, the equilibrium equations, constitutive laws and strain-displacement relations of an isotropic bulk material are given by

$$\sigma_{ij,j} = 0 \tag{4.1}$$

$$\sigma_{ij} = 2\mu\varepsilon_{ij} + \lambda\delta_{ij}\varepsilon_{kk} \tag{4.2}$$

$$\varepsilon_{ij} = \frac{1}{2} \left(u_{i,j} + u_{j,i} \right) \tag{4.3}$$

where u_i , σ_{ij} and ε_{ij} denote respectively the components of displacement, stress and strain tensors; and μ and λ are Lamé constants of the bulk material.

On the crack surface, the equilibrium equation, constitutive laws and strain-displacement relations can be expressed as (Gurtin and Murdoch 1975, 1978):

$$\sigma_{i\alpha,\alpha}^s + \sigma_{ij}n_j = 0 \tag{4.4}$$

$$\sigma_{\beta\alpha}^{s} = \tau^{s} \delta_{\beta\alpha} + 2(\mu^{s} - \tau^{s}) \varepsilon_{\beta\alpha} + (\lambda^{s} + \tau^{s}) \varepsilon_{\gamma\gamma} \delta_{\beta\alpha} + \tau^{s} u_{\beta,\alpha}^{s}$$

$$\tag{4.5}$$

$$\varepsilon_{\alpha\beta}^{s} = \frac{1}{2} \left(u_{\alpha,\beta}^{s} + u_{\beta,\alpha}^{s} \right) \tag{4.6}$$

where the superscript 's' is used to denote the quantities corresponding to the surface; μ^s and λ^s are surface Lamé constants; τ^s is the residual surface stress (or surface tension) under unstrained conditions; n_i denotes the components of unit normal vector of the surface; and Greek subscripts take the value of 1 or 2, while the Latin subscripts vary from 1 to 3.

Due to the symmetry of the system shown in Figure 4.1 about the *z*-axis, a cylindrical coordinate system (r, θ, z) is used in the formulation, and the elastic field is independent of q, i.e. $u_{\theta} = 0$ and $\sigma_{r\theta} = \sigma_{z\theta} = 0$. The general solutions for the bulk stresses and displacements can be expressed by using Hankel integral transforms as (Sneddon, 1951),

$$\sigma_{rr} = \int_{0}^{\infty} \xi \left[\lambda \frac{d^{3}\Phi}{dz^{3}} + (\lambda + 2\mu) \xi^{2} \frac{d\Phi}{dz} \right] J_{0}(\xi r) d\xi - \frac{2(\lambda + \mu)}{r} \int_{0}^{\infty} \xi^{2} \frac{d\Phi}{dz} J_{1}(\xi r) d\xi$$

$$(4.7)$$

$$\sigma_{\theta\theta} = \lambda \int_{0}^{\infty} \xi \left[\frac{d^{3}\Phi}{dz^{3}} - \xi^{2} \frac{d\Phi}{dz} \right] J_{0}(\xi r) d\xi + \frac{2(\lambda + \mu)}{r} \int_{0}^{\infty} \xi^{2} \frac{d\Phi}{dz} J_{1}(\xi r) d\xi$$

$$(4.8)$$

$$\sigma_{zz} = \int_{0}^{\infty} \xi \left[\left(\lambda + 2\mu \right) \frac{d^{3}\Phi}{dz^{3}} - \left(3\lambda + 4\mu \right) \xi^{2} \frac{d\Phi}{dz} \right] J_{0}(\xi r) d\xi \tag{4.9}$$

$$\sigma_{rz} = \int_{0}^{\infty} \xi^{2} \left[\lambda \frac{d^{2} \Phi}{dz^{2}} + (\lambda + 2\mu) \xi^{2} \Phi \right] J_{1}(\xi r) d\xi \tag{4.10}$$

$$u_r = \frac{\lambda + \mu}{\mu} \int_0^\infty \xi^2 \frac{d\Phi}{dz} J_1(\xi r) d\xi \tag{4.11}$$

$$u_{z} = \int_{0}^{\infty} \xi \left[\frac{d^{2}\Phi}{dz^{2}} - \frac{\lambda + 2\mu}{\mu} \xi^{2}\Phi \right] J_{0}(\xi r) d\xi$$

$$(4.12)$$

where,

$$\Phi(\xi, z) = (A + Bz)e^{-|\xi|z} \tag{4.13}$$

Note that $J_n(\xi)$ denotes the Bessel functions of the first kind of order n. In addition, A and B are arbitrary functions to be determined from the boundary conditions.

4.1.3 Solution of Boundary Value Problem

Due to the symmetry about z-axis and the assumption that surface tension is constant, the boundary conditions on the crack surface (z = 0) can be expressed as,

$$\sigma_{zz} + \tau^s \left(\frac{d^2 u_z}{dr^2} + \frac{1}{r} \frac{du_z}{dr} \right) = -p(r) \quad \text{when } 0 < r < a$$

$$\tag{4.14}$$

$$u_z = 0$$
 when $a < r < \infty$ (4.15)

$$\sigma_{rz} + \kappa^{s} \left(\frac{d^{2}u_{r}}{dr^{2}} + \frac{1}{r} \frac{du_{r}}{dr} - \frac{u_{r}}{r^{2}} \right) = 0 \text{ when } 0 < r < a$$
 (4.16)

$$\sigma_{rz} = 0$$
 when $a < r < \infty$ (4.17)

where $\kappa^s = 2\mu^s + \lambda^s$ is a surface material constant. It is worth noting that the boundary conditions (4.14) and (4.16) are only applicable to flat crack surfaces located on the plane z = 0 (resulting directly from the sharp-crack-tip assumption). The treatment of crack-face conditions associated with non-flat crack surfaces resulting from other crack models (e.g., a blunt crack model) is not considered in the present study.

By substituting stresses and displacements from Eqs. (4.7) - (4.12) into Eqs. (4.14) - (4.17), the boundary conditions can be expressed to a set of simultaneous dual integral equations as

$$\int_{0}^{\infty} \sum_{i=1}^{2} c_{ij} \left(\overline{\xi}\right) f_{j} \left(\overline{\xi}\right) J_{\nu_{i}} \left(\overline{\xi}\overline{r}\right) d\overline{\xi} = h_{i} \left(\overline{r}\right) \quad \text{when } 0 < \overline{r} < 1$$

$$(4.18)$$

$$\int_{0}^{\infty} \sum_{i=1}^{2} d_{ij} \left(\overline{\xi}\right) f_{j} \left(\overline{\xi}\right) J_{\nu_{i}} \left(\overline{\xi}\overline{r}\right) d\overline{\xi} = g_{i} \left(\overline{r}\right) \quad \text{when } 1 < \overline{r} < \infty$$

$$(4.19)$$

where
$$i = 1, 2; \ \bar{i} = \xi a; \ \bar{r} = r/a; \ c = \begin{bmatrix} 2(\lambda + \mu)\frac{\overline{\xi}^4}{a^4} + \frac{\lambda + \mu}{\mu}\tau^s \frac{\overline{\xi}^5}{a^5} & 2\mu\frac{\overline{\xi}^3}{a^3} + 2\tau^s\frac{\overline{\xi}^4}{a^4} \\ 2(\lambda + \mu)\frac{\overline{\xi}^4}{a^4} + \frac{\lambda + \mu}{\mu}\frac{\overline{\xi}^5}{a^5}\kappa^s & -2\lambda\frac{\overline{\xi}^3}{a^3} + \frac{\lambda + \mu}{\mu}\kappa^s\frac{\overline{\xi}^4}{a^4} \end{bmatrix};$$

$$d = \begin{bmatrix} \frac{\lambda + \mu \overline{\xi}^{3}}{\mu a^{3}} & 2\frac{\overline{\xi}^{2}}{a^{2}} \\ 2(\lambda + \mu)\frac{\overline{\xi}^{4}}{a^{4}} & -2\lambda\frac{\overline{\xi}^{3}}{a^{3}} \end{bmatrix}; f = \begin{bmatrix} A(\overline{\xi}) \\ B(\overline{\xi}) \end{bmatrix}; v = \begin{bmatrix} 0 \\ 1 \end{bmatrix}; h = \begin{bmatrix} -\overline{p}(\overline{r}) \\ 0 \end{bmatrix}; g = \begin{bmatrix} 0 \\ 0 \end{bmatrix} \text{ and } \overline{p}(\overline{r}) = ap(\overline{r}).$$

Eqs. (4.18) and (4.19) can then be reduced to,

$$\int_{0}^{\infty} \sum_{j=1}^{2} e_{ij} \left(\overline{\xi}\right) \psi_{j} \left(\overline{\xi}\right) J_{\nu_{i}} \left(\overline{\xi}\overline{r}\right) d\overline{\xi} = h_{i} \left(\overline{r}\right) \quad \text{when } 0 < \overline{r} < 1$$

$$(4.20)$$

$$\int_{0}^{\infty} \psi_{i}(\overline{\xi}) J_{\nu_{i}}(\overline{\xi} r) d\overline{\xi} = 0 \qquad \text{when } 1 < \overline{r} < \infty$$

$$\tag{4.21}$$

where
$$\psi_i(\overline{\xi}) = \sum_{j=1}^2 d_{ij}(\overline{\xi}) f_j(\overline{\xi})$$
 and $e = cd^{-1} = \begin{bmatrix} \frac{2\mu(\lambda+\mu)}{\lambda+2\mu} \frac{\overline{\xi}}{a} + \tau^s \frac{\overline{\xi}^2}{a^2} & \frac{\mu}{\lambda+2\mu} \\ -\frac{\mu}{\lambda+2\mu} \kappa^s \frac{\overline{\xi}^2}{a^2} & 1 + \frac{\lambda+3\mu}{2\mu(\lambda+2\mu)} \kappa^s \frac{\overline{\xi}}{a} \end{bmatrix}$. To solve

Eqs. (4.20) and (4.21), ψ_i is defined as (Erdogan and Bahar, 1964),

$$\psi_{j}\left(\overline{\xi}\right) = \overline{\xi}^{1-\beta_{j}} \sum_{m=0}^{\infty} \varphi_{jm} J_{\nu_{j}+2m+\beta_{j}}\left(\overline{\xi}\right)$$

$$(4.22)$$

Eq. (4.21) will be automatically satisfied due to the following properties of Sonine-Schafheitlin integrals (Magnus and Oberhettinger, 1954).

$$\int_{0}^{\infty} \overline{\xi}^{1-\beta_{j}} J_{\nu_{i}}(\overline{\xi}\overline{r}) J_{\nu_{i}+2m+\beta_{j}}(\overline{\xi}) d\overline{\xi} = 0 \quad \text{when } \overline{r} > 1, \ 2(\nu_{j}+m+1) > 0 \text{ and } \beta_{j} > 0$$

$$(4.23)$$

Eq. (4.20) can then be written as

$$\sum_{m=0}^{\infty} \sum_{j=1}^{2} \varphi_{jm} \int_{0}^{\infty} x^{1-\beta_{j}} e_{ij}\left(\overline{\xi}\right) J_{\nu_{i}}\left(\overline{\xi}\overline{r}\right) J_{\nu_{j}+2m+\beta_{j}}\left(\overline{\xi}\right) d\overline{\xi} = h_{i}\left(\overline{r}\right) \quad \text{when } 0 < \overline{r} < 1$$

$$(4.24)$$

where φ_{jm} are the unknown coefficients to be determined. Multiplying both sides of Eq. (4.24) by $\bar{r}^{1+\nu_i} \left(1-\bar{r}^2\right)^{\beta_i-1} \mathfrak{F}_k \left(\nu_i+\beta_i,1+\nu_i,\bar{r}^2\right)$, $k=0,1,2,\ldots,m$ and then integrating with respect to \bar{r} from 0 to 1 yields (Tranter, 1951),

$$\sum_{m=0}^{\infty} \sum_{j=1}^{2} \varphi_{jm} \int_{0}^{\infty} x^{1-\beta_{j}-\beta_{i}} e_{ij} \left(\overline{\xi}\right) J_{\nu_{i}+2k+\beta_{i}} \left(\overline{\xi}\right) J_{\nu_{j}+2m+\beta_{j}} \left(\overline{\xi}\right) d\overline{\xi} = Q_{i} \left(\nu_{i}, \beta_{i}, k\right)$$

$$(4.25)$$

where
$$Q_i(v_i, \beta_i, k) = \frac{\Gamma(v_i + k + 1)}{2^{\beta_i - 1}\Gamma(v_i + 1)\Gamma(k + \beta_i)} \int_0^1 h_i(\overline{r}) \overline{r}^{1+v_i} (1 - \overline{r}^2)^{\beta_i - 1} \mathfrak{I}_k(v_i + \beta_i, 1 + v_i, \overline{r}^2) d\overline{r}$$
 and \mathfrak{I}_n is

the following Jacobi polynomial, which is defined in terms of hypergeometric series (Magnus and Oberhettinger, 1954) as,

$$\mathfrak{I}_{n}(\alpha,\gamma,x) = {}_{2}F_{1}(-n,\alpha+n;\gamma;x) \tag{4.26}$$

and ${}_{2}F_{1}(a,b;c;x)$ is the hypergeometric function.

The coefficients φ_{jm} can be obtained by solving Eq. (4.25). Note that the unspecified constant, β_j , in Eq. (4.25) must be positive to make the integral appearing in Eq. (4.25) to converge. Finally, the arbitrary functions A and B can be expressed as:

$$A(\overline{\xi}) = \frac{\lambda \mu}{(\lambda + \mu)(\lambda + 2\mu)} \frac{a^3}{\overline{\xi}^3} \left[\psi_1(\overline{\xi}) + \frac{a}{\lambda \overline{\xi}} \psi_2(\overline{\xi}) \right]$$
(4.27)

$$B(\overline{\xi}) = \frac{\mu}{(\lambda + 2\mu)} \frac{a^2}{\overline{\xi}^2} \left[\psi_1(\overline{\xi}) - \frac{a}{2\mu \overline{\xi}} \psi_2(\overline{\xi}) \right]$$
(4.28)

4.1.4 Numerical Results and Discussion

In this section, selected numerical results are presented to portray the influence of surface energy effects on the elastic field. The solutions for stresses and displacements can be obtained from Eqs. (4.7)-(4.12) with the arbitrary functions, A and B, given by Eqs. (4.27) and (4.28). In this study, the semi-infinite integrals in Eqs. (4.7)-(4.12) are evaluated by using a globally adaptive numerical quadrature scheme based on 21-point Gauss-Kronrod rule (Piessens et al., 1983). The surface elastic constants can be obtained from atomistic simulations (Miller and Shenoy 2000; Shenoy 2005; Dingreville and Qu 2007). In particular, Si [100] is chosen, in the numerical study, as a representative material with the bulk and surface properties $\lambda/\mu = 1.94$, $\mu = 40.2262$ GPa, $\lambda^s = 4.4939$ N/m, $\mu^S = 2.7779$ N/m and $\tau^s = 0.6506$ N/m (Miller and Shenoy, 2000). In addition, following non-dimensional quantities, $r_0 = r/\Lambda_0$, $z_0 = z/\Lambda_0$ and $a_0 = a/\Lambda_0$ where $\Lambda_0 = \kappa^s/\mu$ is a reference length-scale parameter defined in terms of κ^s and μ of Si [100]. The numerical results in the present study correspond to the case of a penny-shaped crack in an infinite elastic medium subjected to a uniformly distributed vertical load, p_0 , applied on the crack surface (i.e. $p(r) = p_0$ in Figure 4.1).

The arbitrary functions A and B, given by Eqs. (4.27) and (4.28), are expressed as the combination of ψ_1 and ψ_2 , which are given in terms of infinite series as shown in Eq. (4.22). The convergence and accuracy of the present solution are first verified by plotting vertical stress in the vicinity of the crack tip to determine the appropriate number of terms, m, used in the series expansion defined in Eq. (4.22). Figure 4.2 shows a comparison of non-dimensional vertical stress in the vicinity of crack obtained from the present scheme with no surface stress effects (i.e. $\kappa^s = \tau^s = 0$) for different m values with the classical solution given by Fabrikant (Fabrikant, 1989). It is seen that accurate results are obtained from the present solution scheme for $m \ge 60$. In Figure 4.3, the present solutions for vertical stress and crack opening displacement are compared with the classical solutions provided by Fabrikant (Fabrikant, 1989) and the numerical solutions given by Nguyen et al. (2015), which ignore the surface Lamé constants (i.e. $\kappa^s = 0$), to confirm the high accuracy of the present solution scheme.

Figures 4.4 and 4.5 show the influence of surface energy effects on elastic field in the vicinity of crack. A non-dimensional crack radius of $a_0 = 1.0$ is considered in the numerical study. Variations of non-dimensional vertical stresses and non-dimensional crack opening displacement along the *r*-direction are shown in Figures 4.4 and 4.5 for different values of surface residual stress (τ^s) and surface material constant (κ^s) respectively. Note that the broken lines in Figure 4.4 denote the classical elasticity solution (Fabrikant, 1989) and, during the variation of either τ^s or κ^s , all other material parameters associated with Si [100] remain unchanged.

The solutions for non-dimensional vertical stress close to the crack tip given in Figures 4.4(a) and 4.5(a) show the effects of surface residual stress and surface elastic constants respectively. Surface residual stress has a major influence on the crack tip vertical stress field whereas the influence of surface elastic constants is negligible. Note that the difference observed in Figure 4.5(a) between the classical elasticity solution and the present solution is primarily due to the effect of surface residual stress. It is observed that the presence of surface stress results in a substantial reduction of the crack tip vertical stress. Similar behavior was also observed in the 2-D crack solution by Kim et al. (2011), in which the assumption of finite stress at crack tip is considered. The present solutions in Figures 4.4 and 4.5 also indicate that the order of singularity of stress is lower than the square root singularity corresponding to the classical solutions. This finding is

consistent with that pointed out by several investigators (e.g., Sendova and Walton 2010; Walton 2012; Kim and Ru 2013; Walton 2014; Ferguson et al. 2015), in particular, the stress singularity along the crack front reduces from the square-root to logarithmic singularity when the surface stresses are accounted for in the mathematical model. The crack opening displacement solutions presented in Figures 4.4(b) and 4.5(b) indicates that the magnitude of crack opening displacement is substantially reduced due to the presence of surface stress. This is physically realistic as a stretched (tensioned) crack face would be stiffer similar to a cable under tension. Here again, the surface elastic constants show almost negligible influence on the crack opening displacement.

In Figure 4.6, a set of numerical results are shown to demonstrate the size-dependent behavior of the present solution when the influence of surface energy effects (surface stress and surface elastic constants) is included. Solutions are presented for the radial variation of crack tip vertical stress and crack opening displacement across the crack surface for Si [100]. The corresponding non-dimensional solution for the classical elasticity case is also shown, and it is size-independent. It is found that as the crack size increases the current solution accounting for surface energy effects moves toward the classical solution. This is physically realistic as a stretched larger crack would show increasing crack opening displacements. The results show that a smaller crack has a lower crack tip stress and crack opening displacement.

The influence of surface residual stress and crack radius respectively on non-dimensional vertical stress at the vicinity of crack tip, i.e. at r/a = 1.01, and non-dimensional crack opening displacements at the center of crack are presented in Figures 4.7 and 4.8. The corresponding solutions for the classical elasticity case are also shown in both figures. It is evident from Figure 4.7 that the residual surface stress (τ) displays strong influence on the crack tip stress and the central crack opening displacement. The stress and displacement both rapidly decrease, from their classical elasticity counterparts, with increasing the surface residual stress before approaching their limiting values. The size-dependent behavior due to the presence of surface stress effects can be clearly observed in Figure 4.8. Both crack tip stress and central crack opening displacement obtained from the current model accounting for surface stress effects depend significantly on the crack size (a_0) for relatively small values of a_0 . Such size-dependency gradually vanishes as a_0 increases, and both stress and displacement converge to the corresponding classical solutions, which are shown as the broken lines in Figure 4.8.

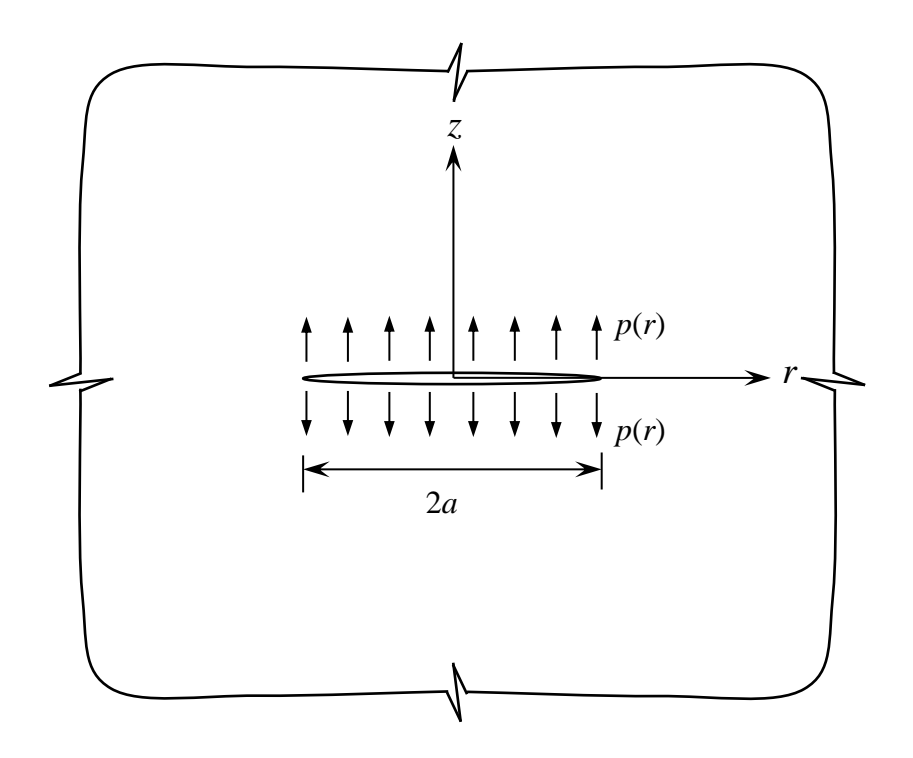


Figure 4.1 Penny-shaped crack in infinite elastic medium under vertical loading

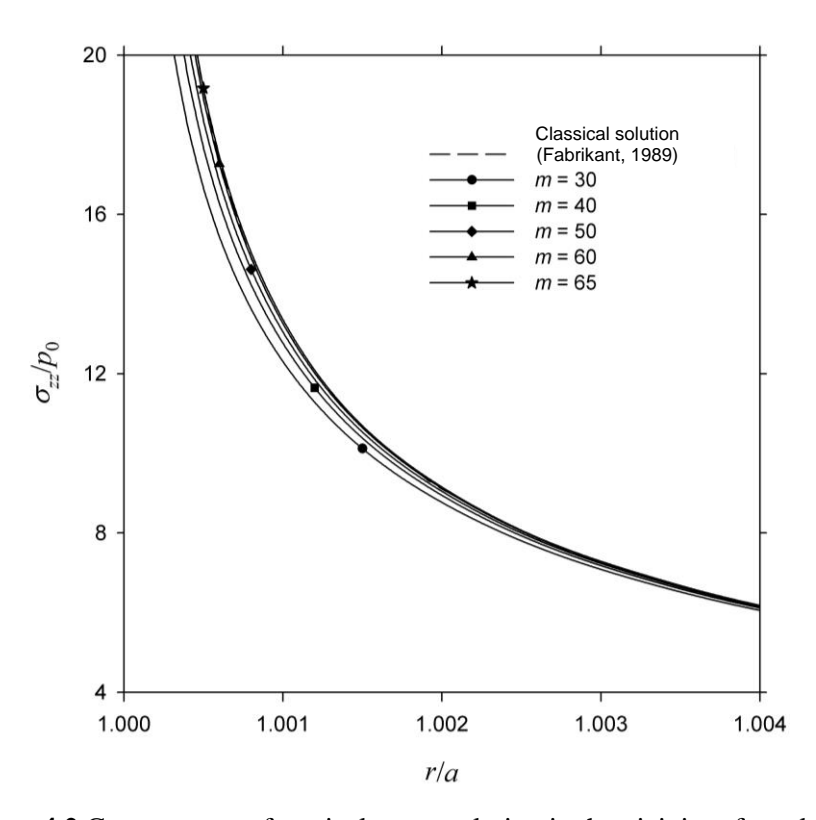


Figure 4.2 Convergence of vertical stress solution in the vicinity of crack tip

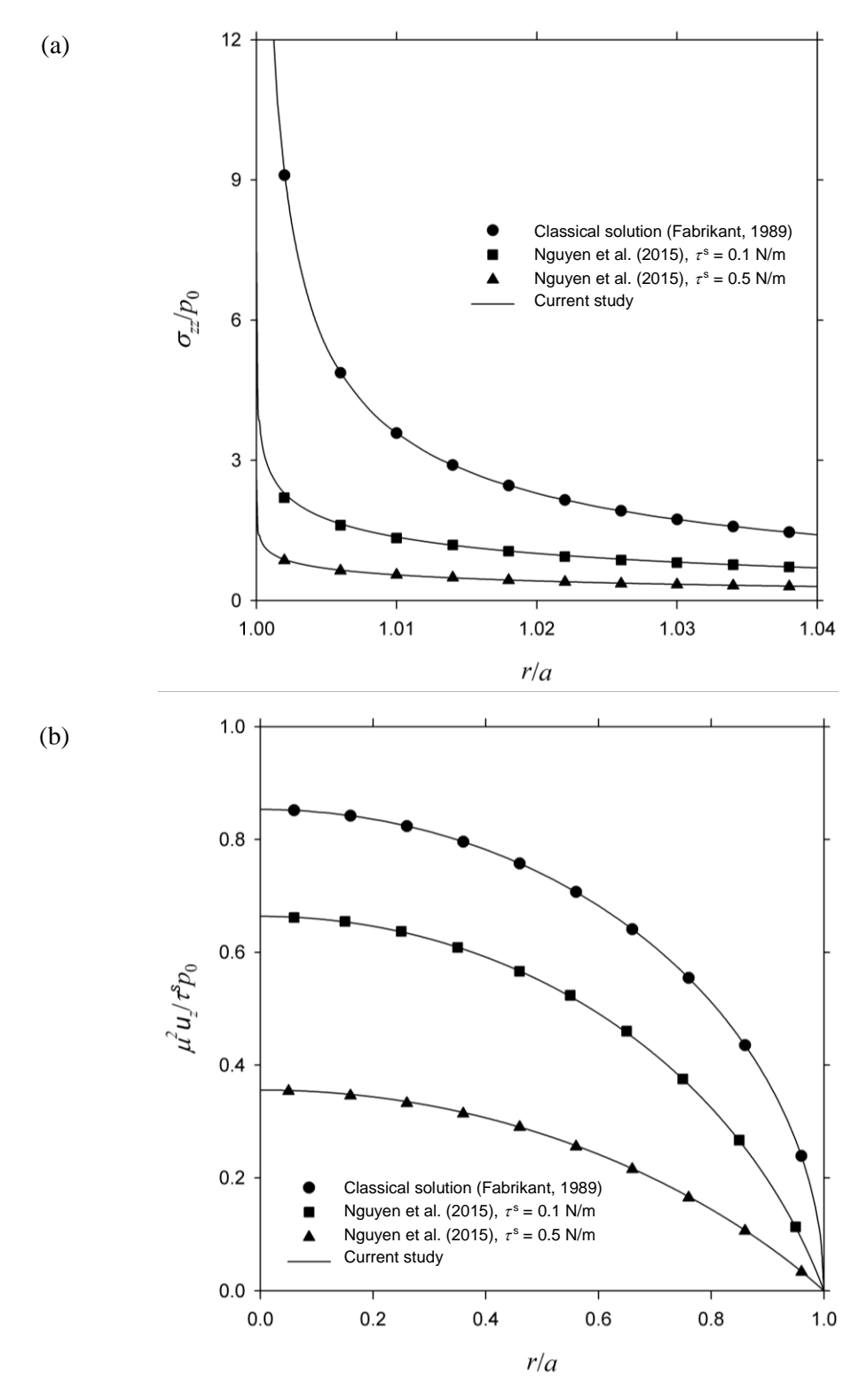


Figure 4.3 Comparison with existing solutions: (a) Vertical stress; (b) Crack opening displacement.

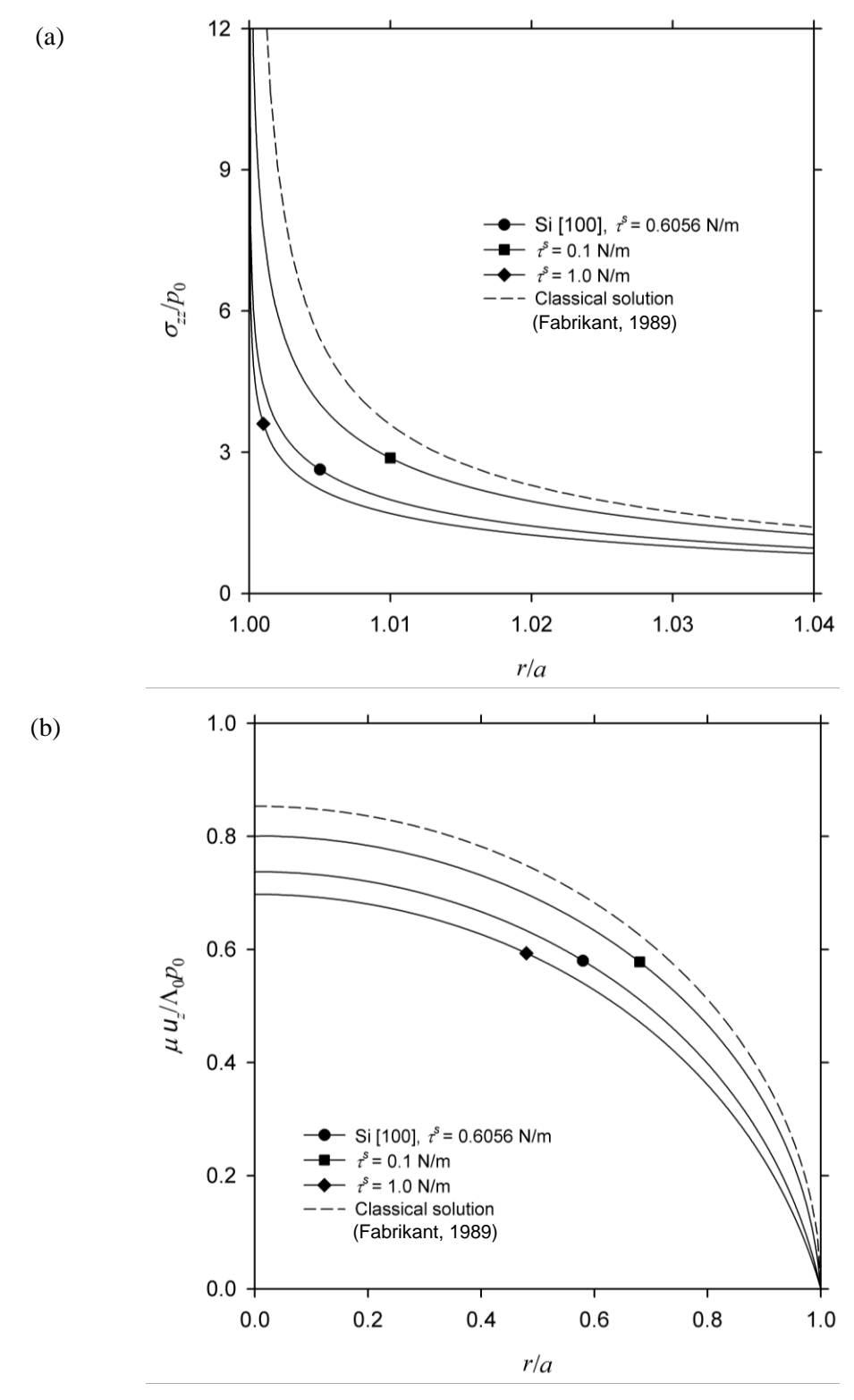


Figure 4.4 Variation of elastic field for different magnitudes of surface residual stress (τ^s): (a) Vertical stress; (b) Crack opening displacement.

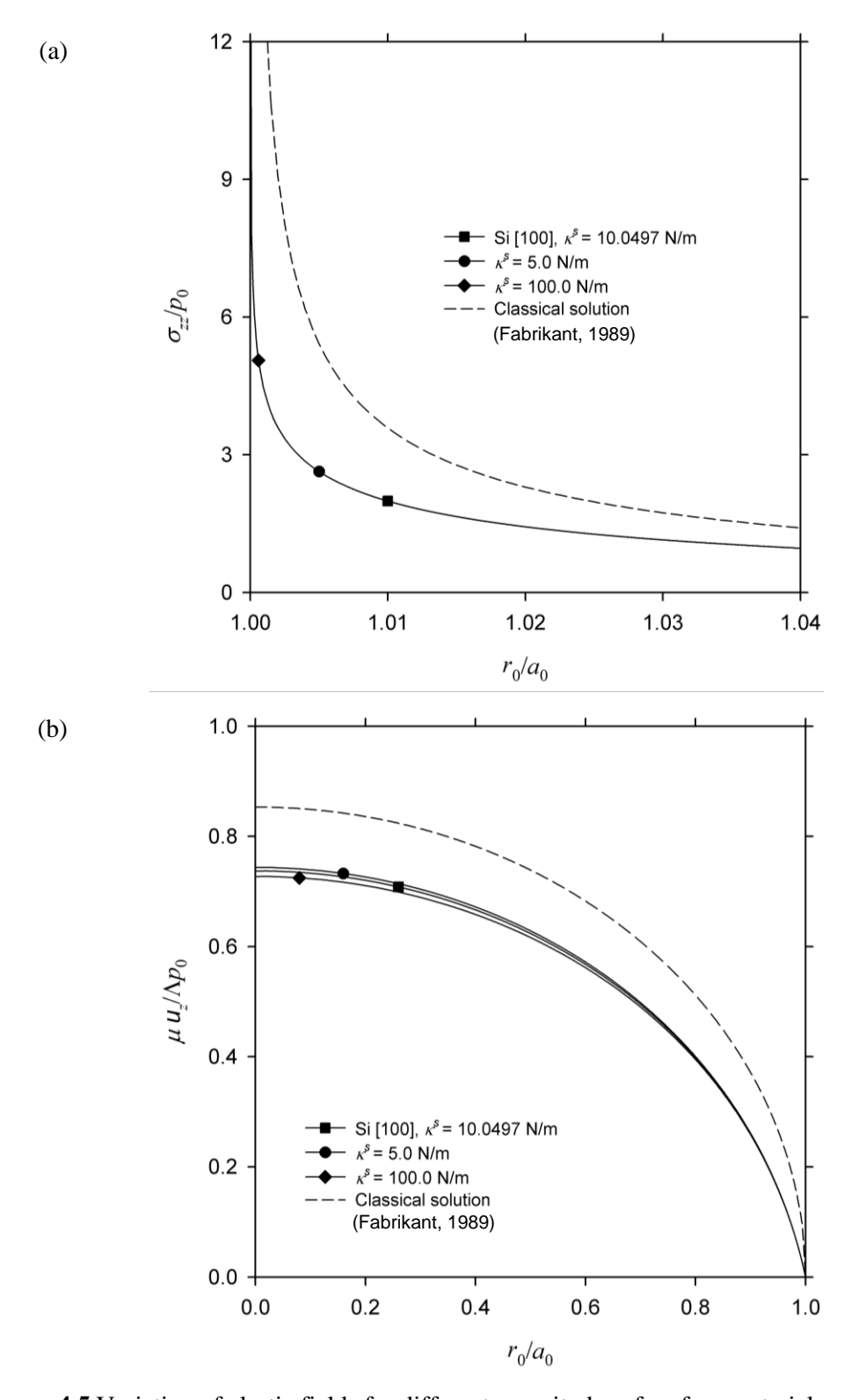
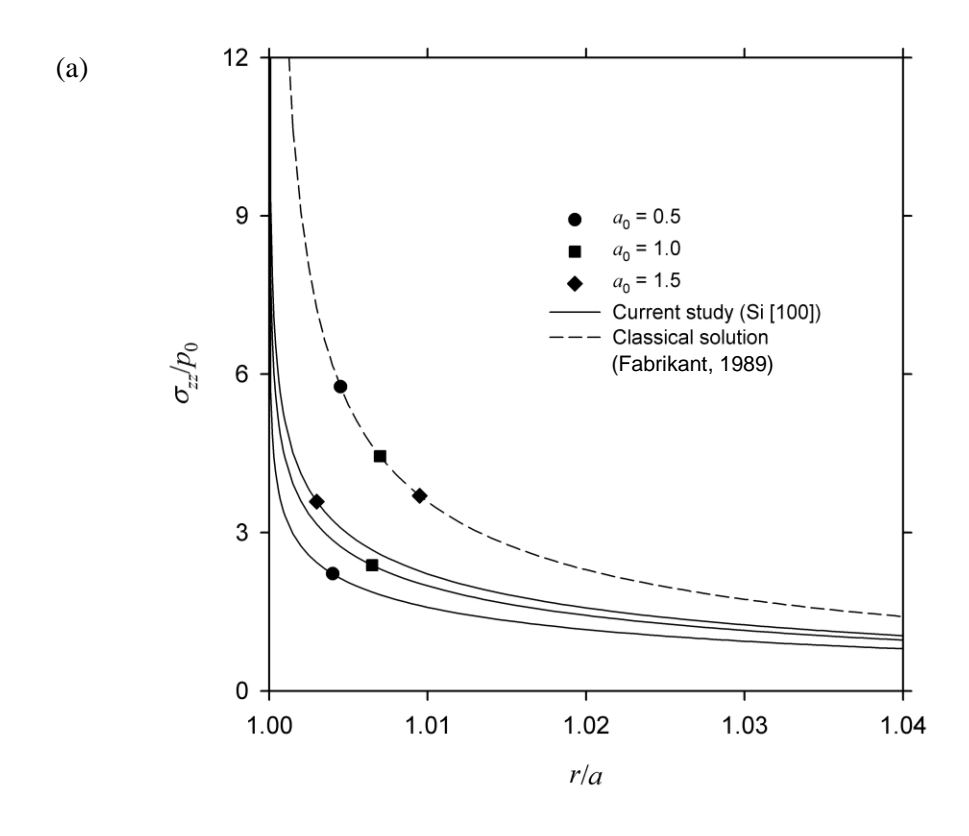


Figure 4.5 Variation of elastic fields for different magnitudes of surface material constant (κ^s) : (a) Vertical stress; (b) Crack opening displacement.



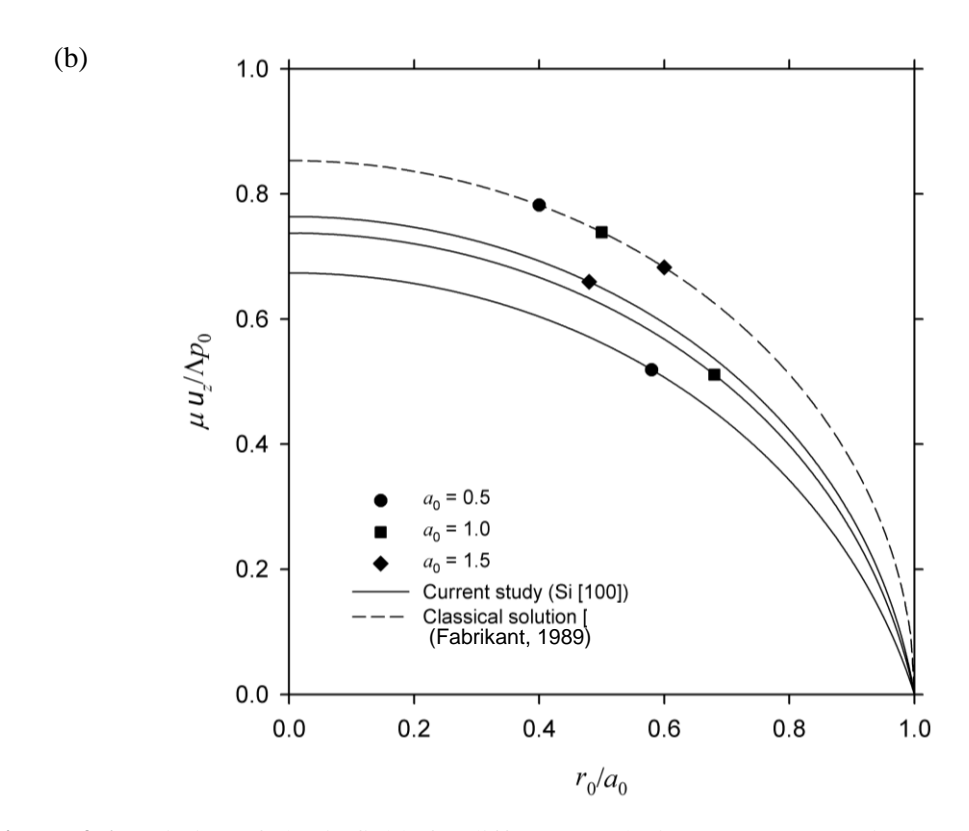
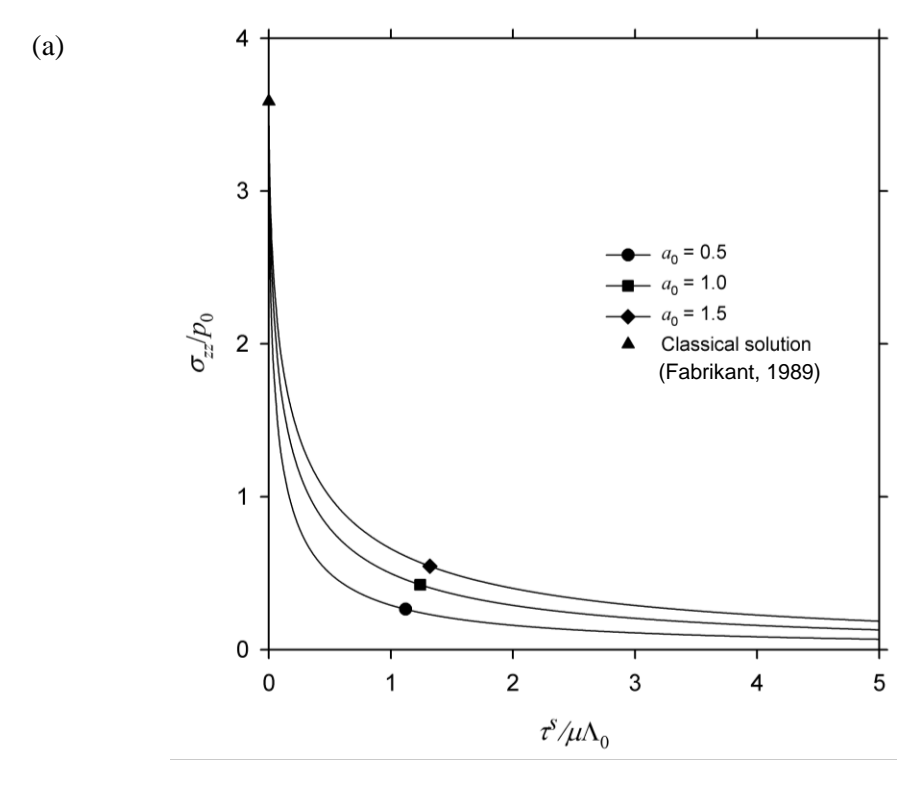


Figure 4.6 Variation of elastic fields for different crack sizes (a_0) : (a) Vertical stress; (b) Crack opening displacement.



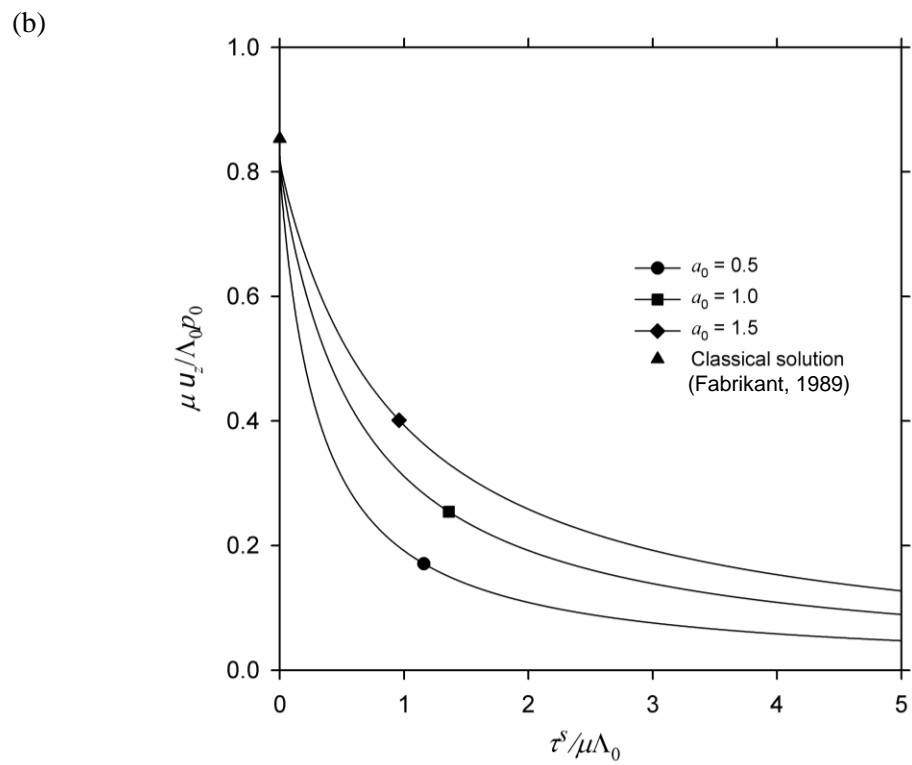
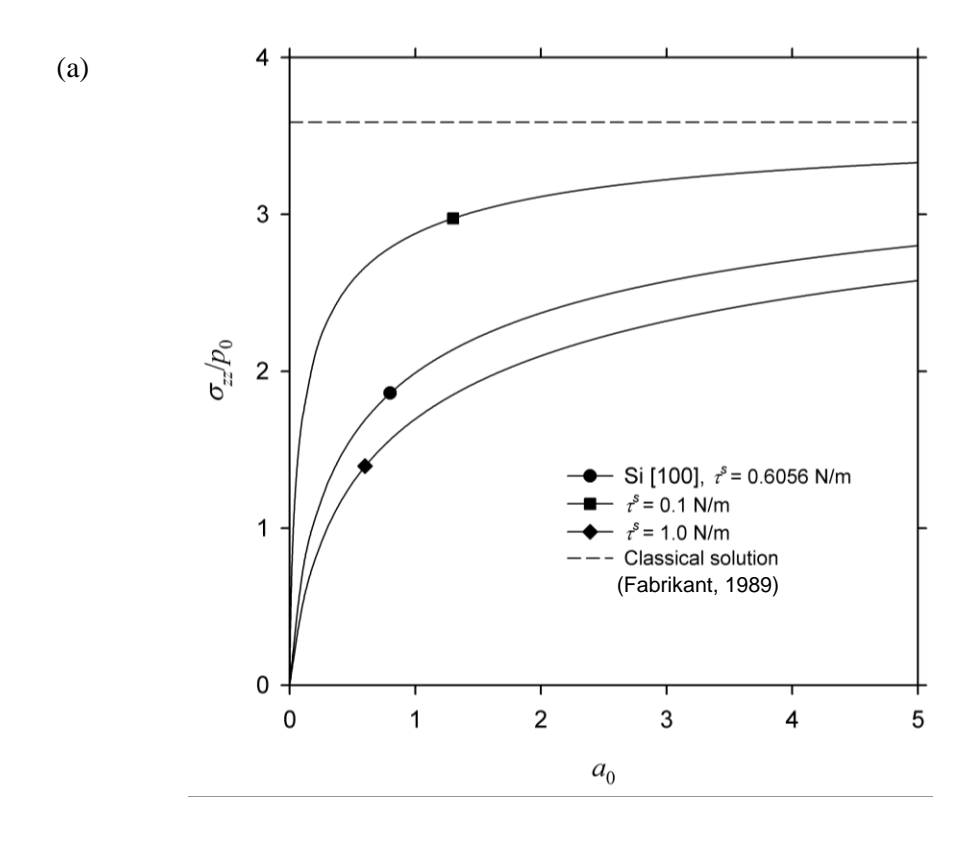


Figure 4.7 Non-dimensional elastic fields under vertical loading against residual surface stresses (τ) for difference crack sizes (a_0): (a) Vertical stresses in the vicinity of crack tip; (b) Crack opening displacements at the center of crack.



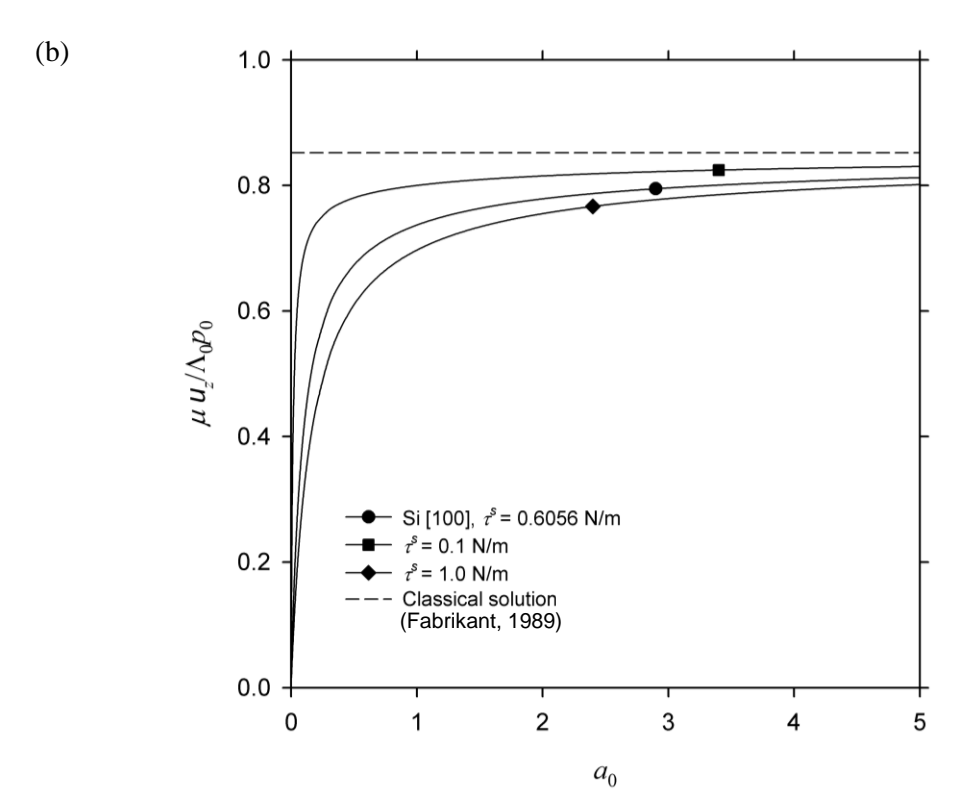


Figure 4.8 Size-dependency of non-dimensional (a) crack tip stress at r/a = 1.01; and (b) central crack opening displacement for different magnitudes of surface residual stress (τ^s).

4.2 Non-planar Cracks

This section presents an efficient and accurate numerical technique for the analysis of non-planar, nano-sized cracks in three-dimensional, linearly elastic, infinite media. The continuum theory of linear elasticity together with Gurtin–Murdoch surface elasticity theory is employed to form a mathematical model capable of simulating non-planar cracks with the influence of surface stresses. The governing equation for the bulk medium is established in terms of weakly singular boundary integral equations containing only unknowns on the crack surface whereas that governing the curved material surfaces attached to the crack is formulated in a weak-form using the weighted residual technique and tangential derivative operators. A fully coupled system of governing equations is then solved numerically via a coupling between the weakly singular, boundary integral equation method and the standard finite element procedure. A numerical study is performed for certain scenarios and preliminary results are compared with existing benchmark cases to not only verify the implemented scheme but also demonstrate its computational efficiency and robustness. In addition, the role and influence of surface parameters such as the surface elastic constants and residual surface tensions on the behavior of predicted solutions are fully investigated and significant findings are reported.

4.2.1 Background and Review

The Gurtin-Murdoch surface elasticity model has also been employed in the modeling of nanosized cracks; however, based-on an extensive literature survey, most of existing studies were still restricted to problems of relatively simple settings, simplified formulations and limited-capability solution techniques. For instance, investigations of nanosized cracks under various loading conditions using either the two-dimensional, blunt-crack models (e.g., Wang et al., 2007; Fu et al., 2008, 2010; Fang et al., 2009; Wang and Li, 2013) and two-dimensional, classical sharp-crack models (e.g., Kim et al., 2010b, 2011a, 2011b; Nan and Wang, 2012, 2013, 2014; Walton, 2012, 2014; Ferguson et al., 2015) can be found. In those investigations, analytical, semi-analytical or numerical techniques were proposed to solve the associated boundary value problem. It should be noted that while the use of two-dimensional models in the simulation significantly reduces both theoretical and computational efforts, it, at the same time, poses several major drawbacks including the loss of information in the out-of-plane direction and the limited capability to treat cracks with general geometry and loading conditions. Recently, Intarit et al. (2012) and Intarit (2013) successfully established an analytical technique based on Love's strain potential and the Hankel integral transform to examine the influence of surface stresses, via the Gurtin-Murdoch model, on the near-front field of nanosized cracks in three-dimensional elastic media. Nevertheless, due to the key limitation of their solution technique, only a penny-shaped crack under axisymmetric loads can be considered. In practical situations, problems of nanosized cracks can be very complex in terms of geometries, loading conditions, and influences to be treated (e.g., the surface free energy and residual surface tension). As a result, the development of a fully three-dimensional model together with efficient and powerful numerical procedures to enhance the capability of existing techniques is essential and still requires rigorous investigations. Recently, Nguyen et al. (2015) proposed a computational procedure based on the coupling of the standard finite element technique and the boundary integral equation method to model nanosized planar cracks in an infinite elastic medium. While their technique is applicable to planar cracks of arbitrary shapes, the formulation is still restricted to a limited version of Gurtin-Murdoch model accounting only the residual surface tension and the implementation was carried out within the context of pure mode-I loading conditions. The contribution of the in-plane surface elasticity and the mixed-mode condition to the elastic near-front field was fully disregarded. Later, Nguyen et al. (2016) extended the work of Nguyen et al. (2015) to model three-dimensional nano-sized, planar cracks in an infinite elastic medium. While their technique is applicable to treat the full version of Gurtin–Murdoch model for arbitrary shapes and mechanical loading conditions, the formulation was still derived specifically for planar crack surfaces. The treatment of arbitrary, non-planar cracks is still required further investigations.

4.2.2 Problem Description

Consider a three-dimensional infinite elastic medium Ω containing an isolated, arbitrary-shape, non-planar crack as illustrated in Figure 4.9(a). Both the crack surfaces are represented by two geometrically identical non-planar smooth surfaces S_c^+ and S_c^- with the corresponding outward unit normal n^+ and n^- , respectively. The medium Ω is considered free of the body force and remote loading but subjected to prescribed arbitrary tractions on the crack surfaces S_c^+ and S_c^- , which are denoted by t_0^+ and t_0^- , respectively (see Figure 4.9(b)). An infinitesimally thin material layer on each crack surface possesses a constant residual surface tension τ_s and surface elastic constants μ_s and λ_s , whereas the bulk cracked medium is made of a homogeneous, isotropic, linear elastic material with the shear modulus μ and Poisson's ratio ν . The problem statement is to determine the complete elastic field within the bulk cracked medium by taking the influence of surface stresses on both material layers into account. Fracture-related information such as the relative crack-face displacement and local stress field in the vicinity of the crack front is also of primary interest.

4.2.3 Problem Formulation and Solution Technique

In the formulation of the boundary value problem, the whole medium is decomposed into three parts: the bulk cracked medium (see Figure 4.9(c)), the zero-thickness material layer S_c^+ and the zero-thickness material layer S_c^- (see Figure 4.9(d)). The bulk cracked medium is simply the whole medium without the two infinitesimally thin material layers lying on the crack surfaces. Since both material layers possess zero thickness, the geometry of the bulk cracked medium is clearly identical to that of the whole cracked medium. The key difference between the bulk cracked medium and the original cracked medium is that the formed is homogeneous and the non-planar crack surfaces S_c^+ and S_c^- in the bulk cracked medium are subjected to unknown tractions (exerted directly by the two material layers) t_b^+ and t_b^- , respectively. The material layer S_C^+ is treated as a two-sided surface with one side subjected to the prescribed general traction t_0^+ and the other side subjected to the unknown traction t_s^+ exerted by the bulk cracked medium (see Figure 4.9(d)). Similarly, the material layer S_c^- is treated as a two-sided surface with one side subjected to the prescribed general traction t_0^- and the other side subjected to the unknown traction t_s^- exerted by the bulk cracked medium (see Figure 4.9(d)). Mechanical responses of the bulk medium are governed by a classical theory of linear elasticity and the final governing equations are formulated in terms of a pair of weakly singular, weak-form boundary integral equations for the displacement and traction (e.g., Li and Mear 1998; Rungamornrat and Mear 2008). For the two non-planar material layers, their behavior is modeled by the full version of Gurtin-Murdoch surface elasticity theory (Gurtin and Murdoch 1975; Gurtin and Murdoch 1978; Murdoch 2005) and the standard weighted residual technique is adopted to derive the governing weak-form equations (see details in the work of Nguyen et al. 2015 and Nguyen et al. 2016). The two systems of governing equations are then coupled by enforcing the continuity of the displacement and traction across the interface of the bulk cracked medium and the two non-planar material layers. The final system governing equations for the infinite medium containing the non-planar crack with the consideration of surface stress effects is given by

$$\mathcal{Q}(\tilde{\mathbf{u}}^{s\Sigma}, \mathbf{u}^{\Sigma}) + \mathcal{B}(\tilde{\mathbf{u}}^{s\Sigma}, \mathbf{t}^{\Sigma}) = \mathcal{R}_{\mathbf{l}}(\tilde{\mathbf{u}}^{s\Sigma})$$

$$\mathcal{B}(\tilde{\mathbf{t}}^{\Sigma}, \mathbf{u}^{\Sigma}) + \mathcal{C}(\tilde{\mathbf{t}}^{\Sigma}, \mathbf{t}^{\Sigma}) + \mathcal{D}(\tilde{\mathbf{t}}^{\Sigma}, \mathbf{u}^{\Delta}) = 0$$

$$\mathcal{D}(\mathbf{t}^{\Sigma}, \tilde{\mathbf{u}}^{\Delta}) + \mathcal{E}(\tilde{\mathbf{u}}^{\Delta}, \mathbf{u}^{\Delta}) = \mathcal{R}_{\mathbf{l}}(\tilde{\mathbf{u}}^{\Delta})$$

$$(4.29)$$

where the bilinear integral operators $\mathcal{A}, \mathcal{B}, \mathcal{C}, \mathcal{D}, \mathcal{E}$ are defined by

$$\mathcal{B}(\mathbf{X}, \mathbf{Y}) = \frac{1}{2} \int_{S_{+}^{+}} X_{p}(\mathbf{y}) Y_{p}(\mathbf{y}) dS(\mathbf{y})$$
(4.30)

$$\mathcal{C}(\mathbf{X}, \mathbf{Y}) = -\int_{S_{c}^{+}} X_{p}(\mathbf{y}) \int_{S_{c}^{+}} U_{j}^{p}(\boldsymbol{\xi} - \mathbf{y}) Y_{j}(\boldsymbol{\xi}) dS(\boldsymbol{\xi}) dS(\mathbf{y})$$

$$\tag{4.31}$$

$$\mathcal{D}(\mathbf{X},\mathbf{Y}) = -\int_{S_c^+} X_p(\mathbf{y}) \int_{S_c^+} G_{mj}^p(\boldsymbol{\xi} - \mathbf{y}) D_m Y_j(\boldsymbol{\xi}) dS(\boldsymbol{\xi}) dS(\mathbf{y}) + \int_{S_c^+} X_p(\mathbf{y}) \int_{S_c^+} H_{ij}^p(\boldsymbol{\xi} - \mathbf{y}) n_i(\boldsymbol{\xi}) Y_j(\boldsymbol{\xi}) dS(\boldsymbol{\xi}) dS(\mathbf{y})$$

(4.32)

$$\mathcal{E}(\mathbf{X}, \mathbf{Y}) = -\int_{S_c^+} D_t X_k(\mathbf{y}) \int_{S_c^+} C_{mj}^{tk}(\boldsymbol{\xi} - \mathbf{y}) D_m Y_j(\boldsymbol{\xi}) dS(\boldsymbol{\xi}) dS(\mathbf{y}) + \mathcal{F}(\mathbf{X}, \mathbf{Y})$$
(4.33)

$$\mathcal{A}(\mathbf{X}, \mathbf{Y}) = \frac{\lambda_s}{2} \int_{S_c^+} tr(D_s \mathbf{X}) tr(D_s \mathbf{Y}) dS + \frac{\mu_s}{4} \int_{S_c^+} [D_s \mathbf{X} + (D_s \mathbf{X})^T] : [D_s \mathbf{Y} + (D_s \mathbf{Y})^T] dS$$

$$+\frac{\tau_{s}}{2} \int_{S_{c}^{+}} (\boldsymbol{n} \otimes \boldsymbol{n}) (\nabla_{s} \mathbf{X}) : (\nabla_{s} \mathbf{Y}) dS - \frac{\lambda_{s}}{2} \int_{\partial S_{c}^{+}} \mathbf{X} \cdot \left\{ \left[tr(D_{s} \mathbf{Y}) \right] \mathbf{I} \right\} \boldsymbol{v} d\Gamma$$

$$-\frac{\mu_{s}}{2} \int_{\partial S_{c}^{+}} \mathbf{X} \cdot \left\{ \mathbf{I} \left[D_{s} \mathbf{Y} + (D_{s} \mathbf{Y})^{T} \right] \right\} \boldsymbol{v} d\Gamma - \frac{\tau_{s}}{2} \int_{\partial S_{c}^{+}} \mathbf{X} \cdot \left[(\boldsymbol{n} \otimes \boldsymbol{n}) \nabla_{s} \mathbf{Y} \right] \boldsymbol{v} d\Gamma$$

$$(4.34)$$

$$-\tau_{S}\int_{S^{\pm}}\overline{\kappa}(\mathbf{X}\cdot\boldsymbol{n})(\operatorname{div}_{S}\mathbf{Y})dS$$

$$\mathcal{F}(\mathbf{X}, \mathbf{Y}) = \frac{\lambda_{s}}{2} \int_{S_{c}^{+}} tr(D_{s}\mathbf{X})tr(D_{s}\mathbf{Y})dS + \frac{\mu_{s}}{4} \int_{S_{c}^{+}} [D_{s}\mathbf{X} + (D_{s}\mathbf{X})^{T}] : [D_{s}\mathbf{Y} + (D_{s}\mathbf{Y})^{T}]dS$$

$$+ \frac{\tau_{s}}{2} \int_{S_{c}^{+}} (\mathbf{n} \otimes \mathbf{n})(\nabla_{s}\mathbf{X}) : (\nabla_{s}\mathbf{Y})dS - \tau_{s} \int_{S_{c}^{+}} \overline{\kappa} (\mathbf{X} \cdot \mathbf{n}) \operatorname{div}_{s} \mathbf{Y} dS$$

$$(4.35)$$

and the linear integral operators $\{\mathcal{R}_1, \mathcal{R}_2\}$ are defined, in terms of the prescribed data t_0^{Σ} and t_0^{Δ} , by

$$\mathcal{R}_{1}(\mathbf{X}) = \frac{1}{2} \int_{S_{c}^{+}} X_{l}(\mathbf{y}) t_{0l}^{\Sigma}(\mathbf{y}) dS(\mathbf{y}) + 2\tau^{s} \int_{S_{c}^{+}} \bar{\kappa} X_{l}(\mathbf{y}) n_{l}(\mathbf{y}) dS(\mathbf{y})$$

$$(4.36)$$

$$\mathcal{R}_{2}(\mathbf{X}) = \frac{1}{2} \int_{S_{c}^{+}} X_{l}(\mathbf{y}) t_{0l}^{\Delta}(\mathbf{y}) dS(\mathbf{y})$$

$$(4.37)$$

where ∇_s denotes the surface gradient; D_s is the tangential derivative; $\bar{\kappa}$ is the initial mean curvature of the non-planar crack surface; \mathbf{I} is the inclusion map which is defined by $\mathbf{I} = \mathbf{P}^T$ with $\mathbf{P} = \mathbf{1} - \mathbf{n} \otimes \mathbf{n}$, $\mathbf{1}$ denoting the identity matrix, and \otimes denoting the exterior product; \mathbf{v} is a vector contained in the crack surface and normal to the crack front; and all other remaining notations are the same as those defined in the work of Nguyen et al. (2016). To determine numerical solutions of the resulting fully coupled system (4.29), the BIEM-FEM coupling technique is utilized as follows. The weakly singular BIEM is employed to discretize the boundary integral equations for the bulk cracked medium (see details in Rungamornrat and Mear, 2008). The standard Galerkin FEM is utilized to discretize the weak-form equations for the two non-planar material layers; the treatment is similar to that employed in the analysis of a curved membrane (see details in Hansbo and Larson, 2014; Hansbo et al., 2015).

4.2.4 Preliminary Results and Discussion

To verify the present formulation and numerical implementations of the proposed solution scheme, a representative problem associated with an isolated, planar crack is considered and computed results are then compared with the benchmark solutions generated by a technique proposed by Nguyen et al. (2016). Consider a penny-shaped crack of radius a embedded in an isotropic, linear elastic unbounded media as shown schematically in Figure 4.10(a). The cracked medium is subjected to a uniformly distributed, self-equilibrated, normal traction $t_3^+ = -t_3^- = \sigma_0$ at the crack surface (see Figure 4.10(b)). In the numerical study, properties of the bulk cracked medium and the material layers are chosen identical to those utilized by Nguyen et al. (2016) (i.e., $E = 107 \ GPa$, v = 0.33; $\lambda_s = 4.4939 \ N/m$, $\mu_s = 2.7779 \ N/m$, and $\tau_s = 0.6056 \ N/m$). Three meshes of the crack surface used in the analysis are presented in Figure 4.10(d) where meshes 1, 2 and 3 contain 20 elements and 77 nodes, 88 elements and 297 nodes, 216 elements and 665 nodes, respectively. This problem has been previously solved by Nguyen et al. (2016) using the FEM-SGBEM coupling technique and their results are used as the reference solutions to validate the current proposed technique in the particular case involving planar cracks.

The normalized crack opening displacements (CODs) and the normalized vertical stresses near the crack front, when the influence of surface stresses is considered, are reported in Figure 4.11 along with the benchmark numerical solution generated by FEM-SGBEM coupling technique proposed by Nguyen et al. (2016) and the exact solution for the classical case given by Tada et al. (2000) and Kachanov et al. (2003). It is seen that numerical results obtained from the proposed BIEM-FEM coupling technique are slightly mesh dependent, highly accurate, and almost indistinguishable from the reference solutions for both the crack opening displacement and the near-front vertical stresses σ_{33} . It can also be demonstrated from the results shown in Figure 4.11 that the model incorporating the surface stresses yield results significantly different from those predicted by the classical theory. The medium tends to be much stiffer than the classical case, when the influence of surface stresses is taken into account. Let us consider, next, the same circular crack subjected to the self-equilibrated, uniformly distributed, shear traction $t_1^+ = -t_1^- = \tau_0^-$ as illustrated in Figure 4.10(c). The same material properties and meshes as those considered in the previous case are used in the analysis. Results for the crack sliding displacements (CSDs) and the stresses in the vicinity of the crack front along the x_1 -direction (the direction of the applied shear traction) are reported in Figure 4.12. It is seen that numerical solutions exhibit very good convergence and excellent agreement with both the reference solution generated by Nguyen et al. (2016) and the exact solution given by Kachanov et al. (2003) for the classical case. It can be seen from results in Figure 4.12(a) that the surface stresses significantly influence the CSDs. It can also be argued from Figure 4.12(b) that the shear stress σ_{13} in the vicinity of the crack front is strongly influenced by the surface stresses. The magnitude of the predicted stresses near the crack front reduces considerably from the classical solution when the surface stresses are present.

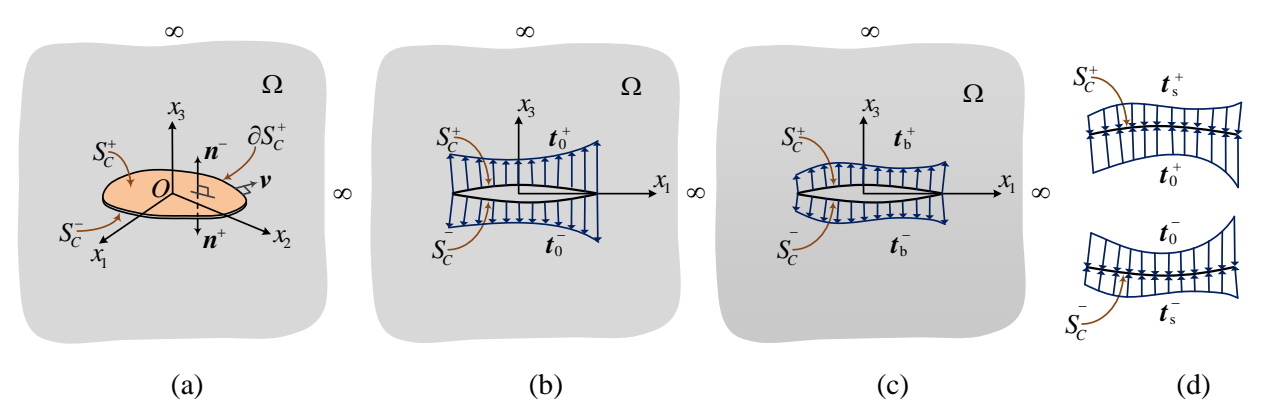


Figure 4.9 Schematics of (a) non-planar crack embedded in three-dimensional, linear elastic, infinite medium, (b) prescribed general tractions on crack surfaces, (c) bulk cracked medium, (d) zero-thickness layers S_C^+ and S_C^- .

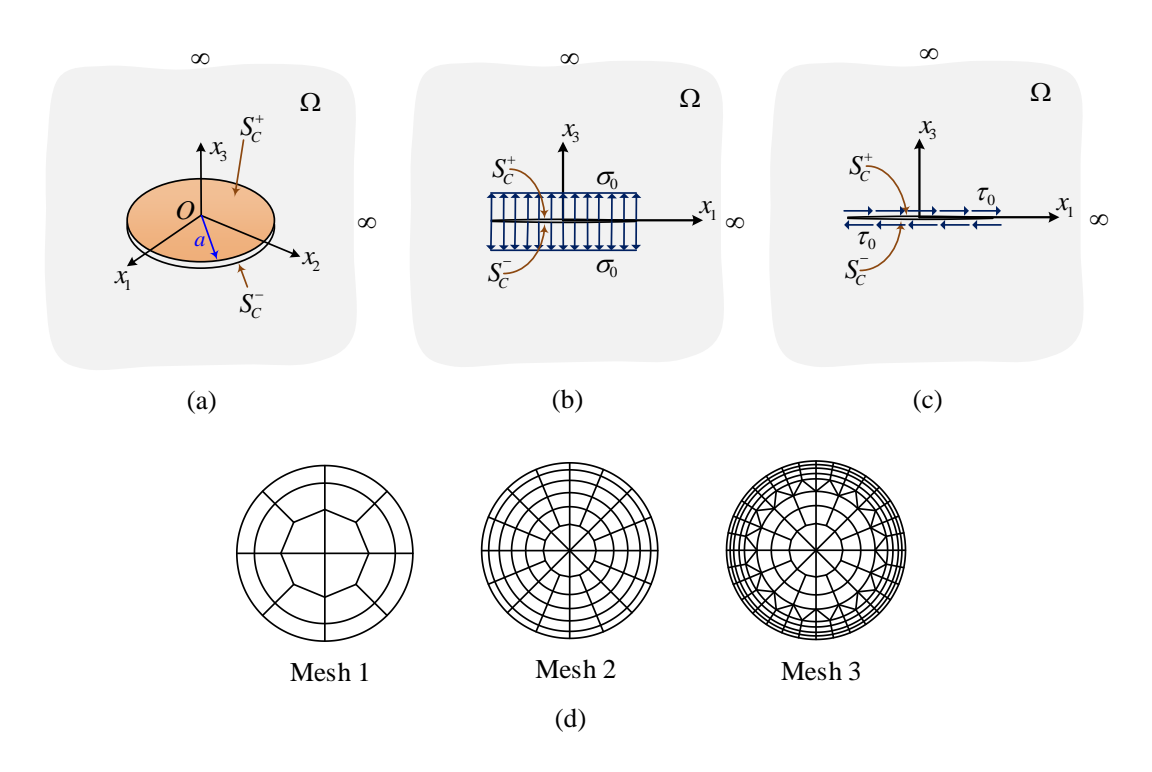
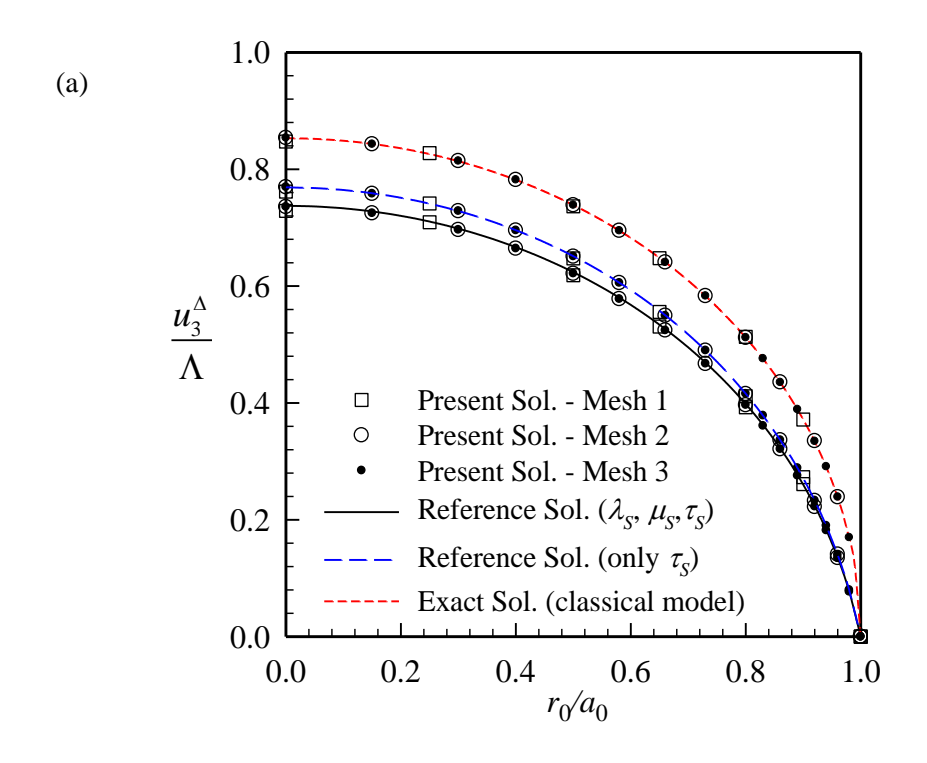


Figure 4.10 (a) Schematic of circular crack of radius a embedded in linear elastic unbounded media; (b) crack surface subjected to uniform normal traction $t_3^+ = -t_3^- = \sigma_0$; (c) crack surface subjected to uniform shear traction $t_1^+ = -t_1^- = \tau_0^-$; and (d) meshes adopted in analysis.



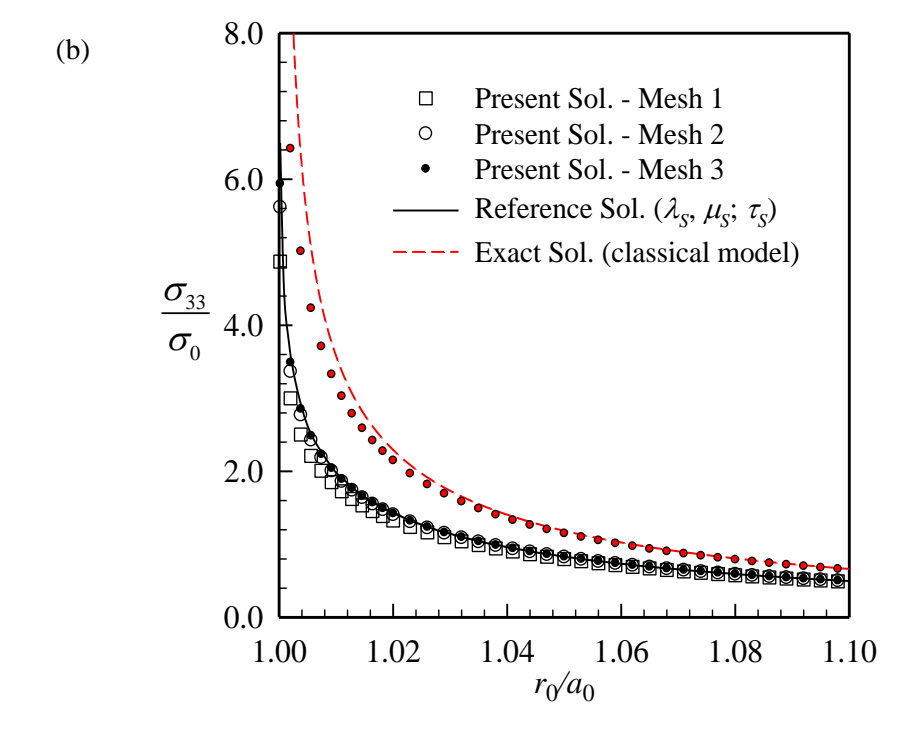
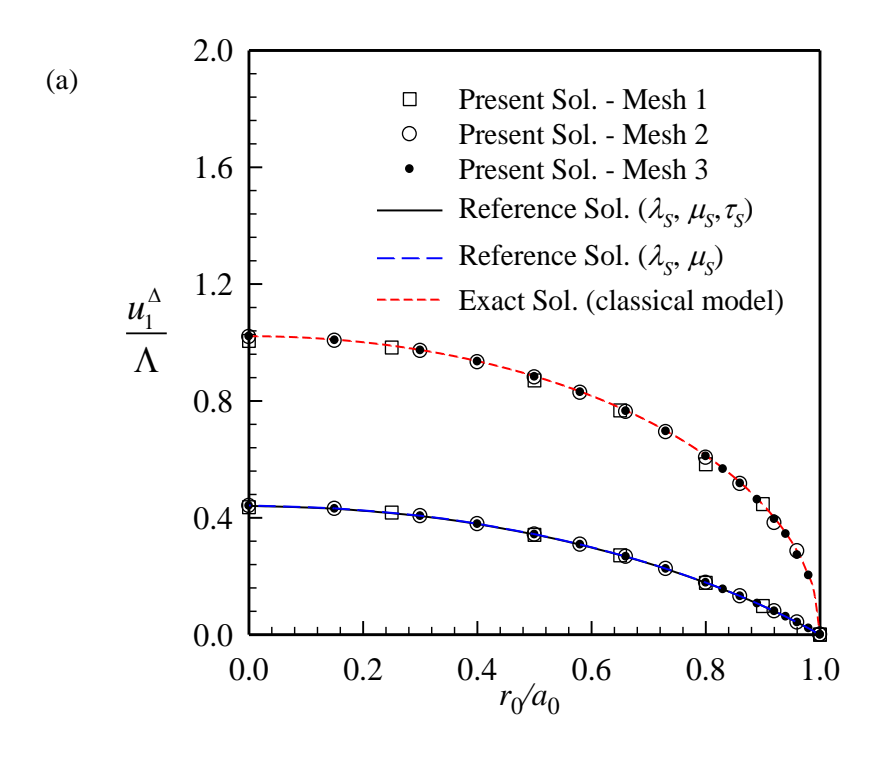


Figure 4.11 Results for (a) normalized crack opening displacements and (b) normalized vertical stresses in the vicinity of the crack-front.



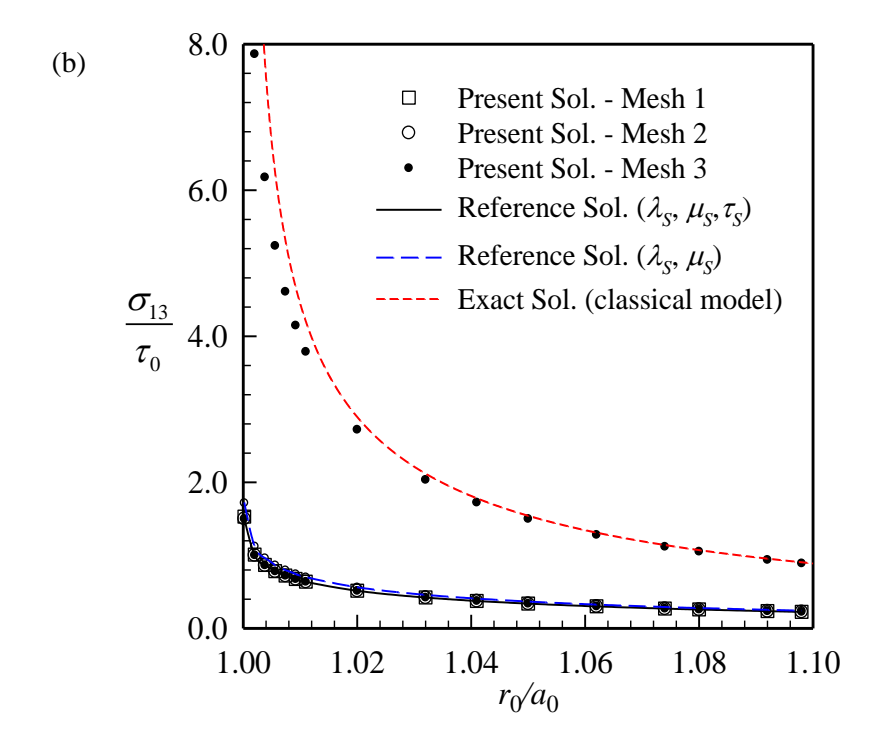


Figure 4.12 Results for (a) normalized crack sliding displacements and (b) normalized near-tip shear stress along the x_1 -direction.

CHAPTER V

NANO-INDENTATION

This chapter presents the analysis of axisymmetric indentation with consideration of surface energy effects under frictionless and adhesive contacts by adopting a complete Gurtin-Murdoch continuum model theory of surface elasticity. The indentation problem with arbitrary axisymmetric profiles is formulated by employing the displacement Green's functions, derived with the aid of Hankel integral transform technique. The unknow contact pressure distribution under an indenter of axisymmetric profiles is determined by using Green's functions, which are defined by the solutions of surface displacements of an elastic medium. The accuracy of the proposed solution scheme is verified by comparing with existing solutions. Selected numerical results are presented to portray the influence of surface stresses on elastic fields of an elastic layer and a layered elastic half-space under nano-indentation.

5.1 Background and Review

Indentation techniques have been widely used in practice to obtain the mechanical properties such as hardness and elastic modulus. For example, Doerner and Nix (1986); and Oliver and Pharr (1992) determined plastic and elastic properties of thin films by using depth-sensing indentation, in which Young's modulus can be calculated from the slope of the linear portion of the unloading curve while hardness can be obtained from the load-displacement data. In the past, several researchers presented elastic solutions of indentation problems by employing continuum mechanics models. The classical solution of axisymmetric contact problem of an elastic half-space is obtained by Boussinesq (1885). Harding and Sneddon (1945); and (Sneddon, 1965) established a solution of the axisymmetric Boussinesq problem, which enabled them to deduce simple formulas giving the penetration of a punch of arbitrary profile by using Hankel integral transform techniques. The indentation problem related to flat-ended rigid cylindrical punch for an elastic layer perfectly bonded to a rigid base was considered by Lebedev and Ufliand (1958). Dhaliwal and Rau (1970; 1972) presented axisymmetric rigid indentation on elastic layer lying over an elastic foundation under a rigid punch of arbitrary profiles. Chen and Engel (1972) analyzed rigid indentation on one and two elastic layers bonded to a homogeneous half-space. In addition, Yang (2003) investigated the effect of thickness for an elastic thin film on a rigid base under a rigid flatended cylindrical indenter. In his paper, the frictionless condition on both contact interfaces, i.e. between the indenter and the film, and between the film and the rigid base, is assumed.

The above solutions to indentation problem were obtained based on the assumption of frictionless contact surface. If the coefficient of friction between a rigid indenter and an elastic medium is large enough, the indenter is prevented from any sliding on the contact area. This condition is known as an adhesive contact problem, and it is mathematically more complicated than the case of frictionless contact. For the indentation with adhesive contact, the top surface of elastic medium is decomposed into a surface outside the contact region on which both normal and shear stresses are identically zero, and a surface inside the contact region on which the normal displacement is prescribed in terms of the indentation depth and the radial displacement is zero at every point of the contact region. The analysis of indentation with adhesive contact was first performed incrementally for a growth in the contact radius (Goodman, 1962; Mossakovskii, 1954,

1963). Spence (1968a, b) introduced a self-similarity approach for a flat-ended cylinder and a parabolic punch, corrected some misprints in the Mossakovskii examples (Mossakovskii, 1963), and also presented the solution for a conical punch. By adopting Mossakovskii approach, Borodich and Keer (2004) obtained the exact solution to the axisymmetric adhesive elastic contact problem for punches whose shapes are described by monomial functions. A detailed and comprehensive analysis of the literature related to the adhesive contact problems is given by Galin and Gladwell (2008); and Borodich (2014). Recently, Selvadurai and Katebi (2015) examined the axisymmetric adhesive contact problem between a rigid circular plate and an incompressible elastic half-space where the shear modulus of the elastic material varies exponentially with depth.

Nowadays, nanoindentation is employed to investigate the mechanical properties of various devices such as nanoelectromechanical systems (NEMS). For nano-scale systems, the influence of excess energy associated with the surface/interface atoms, called surface/interfacial free energy, is significant due to their high surface-to-volume ratio, and the mechanical behavior then becomes size-dependent (Wong et al., 1997). Based on continuum mechanics models, the surface energy effects, which are generally ignored in studying the mechanical behavior, must be taken into account in modified continuum-based simulations for nanoscale problems. Several continuum-based models have been proposed to account the surface stress and the size-dependent material behaviors such as the couple stress theory (Mindlin and Tiersten, 1962; Toupin, 1964), the strain gradient elasticity theory (Mindlin, 1964; Gao and Zhou, 2013) and the surface elasticity theory (Gurtin and Murdoch 1975, 1978). Over the last twenty years, the Gurtin-Murdoch model has been widely employed for studying various continuum mechanics problems. For example, problems related to an elastic medium under surface loading (Zhao and Rajapakse, 2009; Zhao and Rajapakse, 2013; Rungamornrat et al., 2016; Tirapat et al., 2017; Mi, 2017); contact problem (Gao et al., 2013; Zhou and Gao, 2013; Gao et al., 2014); nanobeam (Ansari et al., 2014; Azizi et al., 2015); nanoplate (Sapsathiarn and Rajapakse, 2013; Ansari and Gholami, 2016); and nanosized cracks (Intarit et al., 2017).

In the context of nanoindentation problems, Zhao (2009) derived an analytical solution of a frictionless nanoindentation problem, in which elastic fields within the half-space caused by flatended cylindrical, conical and spherical rigid indenters are presented. Although Gurtin-Murdoch continuum model used in the formulation is not complete (e.g. no out-of-plane term), numerical result showed a size-dependent behavior due to the surface energy effect, i.e. when the contact area becomes smaller, the material becomes stiffer. Pinyochotiwong et al. (2013) later generalized the work of Zhao (2009) to investigate mechanical response of an elastic half-space under rigid axisymmetric indentation by adopting a complete version of Gurtin-Murdoch model and the Hankel integral transform. The finite element method was also employed by Attia and Mahmoud (2015) to consider a frictionless nanoindentation problem on a functionally graded layered elastic medium with the influence of surface stresses.

This study presents the analysis of axisymmetric rigid indentation with consideration of surface energy effects under frictionless and adhesive contacts by adopting a complete Gurtin-Murdoch continuum model for theory of surface elasticity. The foundamental solutions of an elastic layer and a layered elastic half-space with consideration of surface stresses derived by Intarit (2012) and Tirapat et al. (2017), respectively are employed in the formulation of axisymmetric indentation problem as a mixed-boundary value problem. The displacement boundary condition at the top surface is expressed in terms of displacement Green's function,

obtained by employing the Hankel integral transform method. The unknow contact pressure distribution under an indenter of axisymmetric profiles is determined by using Green's functions, which are defined by the solutions of surface displacements of an elastic layer and a layered elastic half-space. The accuracy of the proposed solution scheme is verified by comparing with existing solutions. Selected numerical results are presented to portray the influence of surface stresses on an elastic layer and a layered elastic half-space under nano-indentation.

5.2 Formulation of Nano-Indentation Problems

Consider an elastic medium subjected to axisymmetric rigid punch under the action of a vertical force *P*. According to Gurtin-Murdoch surface elasticity theory (Gurtin and Murdoch, 1975; Gurtin and Murdoch, 1978), the elastic medium consists of two different parts, i.e. the bulk material and the surface, which is a zero-thickness layer perfectly bonded to the bulk material without slipping. The field equations of the bulk material are identical to those given by the classical elasticity for axisymmetric deformations. On the surface, the generalized Young-Laplace equation (Povstenko, 1993), the surface constitutive relations and the strain-displacement relationship (Gurtin and Murdoch, 1975; Gurtin and Murdoch, 1978; Gurtin et al., 1998) are given by Eqs. (2.5) to (2.8).

5.2.1 Nano-Indentation on Elastic Layer

Consider an elastic layer of finite thickness t perfectly bonded to a rigid base subjected to axisymmetric frictionless indentation under the action of a vertical force P with an arbitrary indenter profile fully described by $v^P(r)$ as shown in Figure 5.1. For convenience, the profile of the indenter is defined such that $v^P(r) = 0$ along the axis of the indenter (r = 0) whereas the final radius of the contact region and the indentation depth resulting from the force P at the center of the indenter are represented by a and d, respectively. In the present study, the indenter profile is assumed to be smooth at any interior point of the contact region (i.e., the unit normal vector to the surface of the indenter, or equivalently, $d\delta/dr$ is well-defined for r < a) whereas along the boundary r = a, the profile could be non-smooth. An indenter with a well-defined $dv^P(r)/dr$ for $r \le a$ [see Figure 5.1(a)] is termed here a smooth-contact indenter, whereas an indenter with a well-defined $dv^P(r)/dr$ only for r < a, such as a flat-ended cylindrical indenter shown in Figure 5.1(b), is called a non-smooth-contact indenter.

For the indentation problem shown in Figure 5.1, the top surface of the layer is decomposed into a surface outside the contact region (r > a) on which the traction (both normal and shear) is identically zero, and a surface inside the contact area $(r \le a)$ on which the vertical displacement is defined in terms of the indentation depth d and the indenter profile $v^P(r)$. In addition, the shear traction at any point of the contact region is also vanished due to the assumption of frictionless contact surface. According to the Gurtin-Murdoch model, the continuity of displacement and traction is enforced along the interface of the surface and the bulk material of the elastic layer. The mixed boundary value problem for the indentation shown in Figure 5.1 can then be expressed for the bulk material as.

$$u_z|_{z=0} = d - v^p(r), \ \ 0 \le r \le a$$
 (5.1)

$$\sigma_{z} \Big|_{z=0} + \tau^{s} \left(\frac{d^{2}u_{z}}{dr^{2}} + \frac{1}{r} \frac{du_{z}}{dr} \right)_{z=0} = 0, \ a < r < \infty$$
 (5.2)

$$\sigma_{r_c}|_{z=0} + \kappa^s \left(\frac{d^2 u_r}{dr^2} + \frac{1}{r} \frac{d u_r}{dr} - \frac{u_r}{r^2} \right)_{r=0} = 0, \quad 0 \le r < \infty$$
 (5.3)

$$u_r\big|_{r=t} = 0, \quad 0 \le r \le \infty \tag{5.4}$$

$$u_z\big|_{z=t} = 0, \quad 0 \le r \le \infty \tag{5.5}$$

where κ^s denotes a surface material constant, in which $\kappa^s = 2\mu^s + \lambda^s$. Note that the residual surface stress is assumed to be constant in the present study.

By using the method of superposition, the vertical displacements on the contact surface can be expressed in the form of an integral equation, and Eq. (5.1) can then be written as,

$$\int_{0}^{a} G_{zz}(r, r^{*}) p(r^{*}) dr^{*} = d - \delta(r)$$
(5.6)

where $p(r^*)$ is the normal traction distribution in the contact region and $G_{zz}(r,r^*)$ denotes the Green's function corresponding to the vertical displacement at any distance r on the contact surface due to a unit vertical ring load applied on the elastic layer at the radius r^* . The Green's function, $G_{zz}(r,r^*)$, can be obtained from the boundary value problem given by Eqs. (5.3) to (5.5) together with the following boundary condition,

$$\sigma_{zz}|_{z=0} + \tau^{s} \left(\frac{d^{2}u_{z}}{dr^{2}} + \frac{1}{r} \frac{du_{z}}{dr} \right)_{z=0} = \delta(r - r^{*})$$
(5.7)

To solve this boundary value problem for the required Green's function, the Hankel integral transform technique was employed, and it can be shown that (Intarit, 2012)

$$G_{zz}(r,r^{*}) = \frac{\lambda + \mu}{\mu} \int_{0}^{\infty} \left\{ \frac{(\lambda + 2\mu)(\lambda + 3\mu)}{2(\lambda + \mu)^{2}} \sinh(2t\xi) - \frac{t\xi(\lambda + 2\mu)}{\lambda + \mu} + \frac{\Lambda\xi}{\lambda + 2\mu} \left[\frac{(\lambda + 3\mu)^{2}}{2(\lambda + \mu)} (\cosh(2t\xi) - 1) - t^{2}\xi^{2}(\lambda + \mu) \right] \right\} \frac{r^{*}J_{0}(\xi r^{*})J_{0}(\xi r)}{I} d\xi$$
 (5.8)

where

$$I = (\lambda + 3\mu) \left[\cosh(2t\xi) + \Lambda \xi \sinh(2t\xi) \right] + 2t\xi^{2} (\lambda + \mu) (\Lambda + t) + \frac{\lambda^{2} + 4\lambda\mu + 5\mu^{2}}{\lambda + \mu}$$

$$+ \tau^{s} \left\{ (\lambda + 3\mu) \left[\frac{(\lambda + 3\mu)}{2\mu(\lambda + 2\mu)} \Lambda \xi^{2} \cosh(2t\xi) + \frac{(\lambda + 2\mu)}{2\mu(\lambda + \mu)} \xi \sinh(2t\xi) - \frac{(\lambda + 3\mu)}{2\mu(\lambda + 2\mu)} \Lambda \xi^{2} \right] \right\}$$

$$- \frac{(\lambda + 2\mu)}{\mu} t\xi^{2} - \frac{(\lambda + \mu)^{2}}{\mu(\lambda + 2\mu)} \Lambda t^{2} \xi^{4}$$

$$(5.9)$$

In order to obtain the normal contact traction, the pressure distribution in the contact region, denoted by $p(r^*)$, is represented by the following equation.

$$p(r^*) = \sum_{j=1}^{m} \alpha_j f_j(r^*)$$
(5.10)

where α_j (j = 1,...,m) denotes a set of undetermined coefficients and f_j is a given function of r^* . Substituting the contact pressure distribution, given by Eq. (5.10), into Eq. (5.6) leads to

$$\sum_{i=1}^{m} \alpha_{j} \int_{0}^{a} G_{zz}(r, r^{*}) f_{j}(r^{*}) dr^{*} = d - v^{p}(r), \qquad 0 \le r \le a$$
(5.11)

By applying a collocation technique, the above integral equation can be expressed as,

$$\sum_{i=1}^{m} \alpha_{j} \int_{0}^{a} G_{zz} \left(r_{i}, r^{*} \right) f_{j} \left(r^{*} \right) dr^{*} = d - v^{p}(r_{i}), \qquad \text{for all } r_{i}, \ i = 1, 2, ..., m$$
(5.12)

The coefficient α_j can be obtained by solving Eq. (5.12), and the normal contact traction can then be determined. In the present study, the unknown pressure distribution is approximated in terms of axisymmetric polynomial functions such that

$$p(r^*) = \sum_{j=1}^{m} \alpha_j (r^*)^{j-1}$$
 (5.13)

Once the normal traction distribution in the contact area, $p(r^*)$, is obtained, all elastic fields at any point in the layer under axisymmetric indentation can be determined from the following equation.

$$R(r,z) = \int_0^\infty R_z(r,z,r^*) p(r^*) dr^*$$
(5.14)

where R(r,z) denotes displacements and stresses at a point (r,z) of an elastic layer under axisymmetric indentation on the top surface; and $R_z(r,z,r^*)$ denotes the Green functions corresponding to displacements and stresses at a point (r,z) of an elastic layer due to a unit normal ring load applied at the top surface of the layer at the radius r^* . In addition, the Green function $R_z(r,z,r^*)$, expressed in the forms of Hankel integral transforms, is given elsewhere (Rungamornrat et al., 2016; Intarit, 2012).

5.2.2 Nano-Indentation on Layered Elastic Medium

Consider a layered elastic half-space consisting of two elastic materials with different properties perfectly bonded together, in which the upper material is an elastic layer of finite thickness h and subjected to axisymmetric indentation of a radius a under the action of a vertical force P as shown in Figure 5.2. If the coefficient of friction between a rigid flat-ended cylindrical punch and a layered elastic half-space is high enough, the indenter is prevented from any sliding on the contact area. This condition is known as an adhesive contact. For axisymmetric adhesive indentation, the surface of the upper layer can be decomposed into a surface outside the contact region (r > a) on which both normal and shear stresses are identically zero, and a surface inside the contact region $(r \le a)$ on which the normal displacement is prescribed in terms of the indentation depth d and the radial displacement is zero at every point of the contact region. To solve this indentation problem, the subscript "1" is used to represent the quantities corresponding to the bulk of the upper layer

and the surface. In addition, the subscript "2" is employed to represent the quantities associated with the bulk of the half-space and the interface between the layer and the half-space. The mixed boundary conditions at the top surface for the adhesive contact problem can then be expressed as,

$$u_{z1}\Big|_{z=0} = d; \qquad 0 \le r \le a$$
 (5.15)

$$u_{r1}\big|_{r=0} = 0; \qquad 0 \le r \le a$$
 (5.16)

$$\sigma_{zz1}\big|_{z=0} + \tau_1^s \left(\frac{d^2 u_{z1}}{dr^2} + \frac{1}{r} \frac{du_{z1}}{dr}\right)_{z=0} = 0; \quad a < r < \infty$$
(5.17)

$$\sigma_{rz1}\big|_{z=0} + \kappa_1^s \left(\frac{d^2 u_{r1}}{dr^2} + \frac{1}{r} \frac{d u_{r1}}{dr} - \frac{u_{r1}}{r^2} \right)_{z=0} = 0; \quad a < r < \infty$$
(5.18)

The continuity of displacements and stresses at the interface between the layer and the half-space can then be expressed as,

$$u_{z1}\Big|_{z=h} - u_{z2}\Big|_{z=h} = 0; \quad r > 0$$
 (5.19)

$$u_{r1}\Big|_{z=h} - u_{r2}\Big|_{z=h} = 0; \quad r > 0$$
 (5.20)

$$\sigma_{zz1}\big|_{z=h} - \sigma_{zz2}\big|_{z=h} + \tau_2^s \left(\frac{d^2 u_{z2}}{dr^2} + \frac{1}{r} \frac{d u_{z2}}{dr}\right)_{z=h} = 0; \quad r > 0$$
(5.21)

$$\sigma_{rz1}\big|_{z=h} - \sigma_{rz2}\big|_{z=h} + \kappa_2^s \left(\frac{d^2 u_{r2}}{dr^2} + \frac{1}{r} \frac{d u_{r2}}{dr} - \frac{u_{r2}}{r^2}\right)_{z=h} = 0; \quad r > 0$$
(5.22)

where $\{\sigma_{zz}, \sigma_{rz}\}$ denote the stress components of the bulk; and $\{u_r, u_z\}$ denote the displacement components of the bulk. In addition, $\kappa_i^s = 2\mu_i^s + \lambda_i^s$ (i = 1,2).

By using the method of superposition, the normal and radial surface displacements are given by Eqs. (5.15) and (5.16), can be expressed in the form of integral equations as,

$$\int_{0}^{a} U_{z}^{N}(r,r') \cdot p(r') dr' + \int_{0}^{a} U_{z}^{R}(r,r') \cdot q(r') dr' = d; \ 0 \le r \le a$$
(5.23)

$$\int_{0}^{a} U_{r}^{N}(r,r') \cdot p(r') dr' + \int_{0}^{a} U_{r}^{R}(r,r') \cdot q(r') dr' = 0; \quad 0 \le r \le a$$
(5.24)

where $U_i^j(r,r')$ denotes the Green's function corresponding to the normal (i=z) or radial (i=r) surface displacement at any distance r on the contact surface due to a unit normal (j=N) or a unit radial (j=R) ring load acting on the surface of the upper layer at the radius r'. The Green's functions corresponding to the normal and radial surface displacements of a layered elastic half-space with consideration of surface energy effects can be expressed in the form of Hankel integral transform respectively as,

$$U_{z}^{k}(r,r') = -\left(\overline{\lambda}_{1}+1\right)\Lambda_{1}\int_{0}^{\infty}\xi^{2}\left\{A\xi + B\left(\frac{2}{\overline{\lambda}_{1}+1}\right) + C\xi - D\left(\frac{2}{\overline{\lambda}_{1}+1}\right)\right\}J_{0}(\xi\overline{r})d\xi$$

$$(5.25)$$

$$U_r^k(r,r') = (\overline{\lambda_1} + 1)\Lambda_1 \int_0^\infty \xi^2 \left\{ -A\xi + B + C\xi + D \right\} J_1(\xi\overline{r}) d\xi \tag{5.26}$$

where $\bar{\lambda}_1 = \lambda_1/\mu_1$; $\bar{r} = r/\Lambda_1$; and $\Lambda_1 = \kappa_1^s (\lambda_1 + 2\mu_1)/2\mu_1(\lambda_1 + \mu_1)$. In addition, A, B, C and D are the arbitrary functions of the applied surface loads at any the radius r', which are given explicitly in Eqs. (2.38) to (2.41), and the superscript "k" is used to denote a unit normal ring load (k = N) or a unit radial ring load (k = R) acting on the surface of the upper layer.

For the analysis of the adhesive contact problem, the normal traction p(r) and the shear traction q(r) can be represented as discrete regions of uniform traction acting over annular elements. The contact surface under the indenter is discretized into a number of Ne annular elements. It is assumed that p(r) and q(r) are constant within each ring element. The vertical and radial surface displacements at the contact surface, Eqs. (5.25) and (5.26), can then be expressed as.

$$\begin{bmatrix} \mathbf{U}_{\mathbf{z}}^{\mathbf{N}} & \mathbf{U}_{\mathbf{z}}^{\mathbf{R}} \\ \mathbf{U}_{\mathbf{r}}^{\mathbf{N}} & \mathbf{U}_{\mathbf{r}}^{\mathbf{R}} \end{bmatrix} \begin{pmatrix} \mathbf{p} \\ \mathbf{q} \end{pmatrix} = \begin{pmatrix} \mathbf{d} \\ \mathbf{0} \end{pmatrix}$$
 (5.27)

where the elements $U_z^k(r_i,r_j)$ and $U_r^k(r_i,r_j)$ (i,j=1,2,...,Ne) of the matrices \mathbf{U}_z^k and \mathbf{U}_r^k , respectively denote the Green's functions corresponding to the normal and radial surface displacements of a layered elastic half-space at the center of the i^{th} ring element subjected to a uniform annular normal load (k=N) or a uniform annular radial load (k=R) over the j^{th} ring element. In addition,

$$\mathbf{p} = \langle p(r_1) \quad p(r_2) \dots p(r_{Ne}) \rangle^T$$
(5.28)

$$\mathbf{q} = \left\langle q(r_1) \quad q(r_2) \dots q(r_{N_e}) \right\rangle^T \tag{5.29}$$

$$\mathbf{d} = \langle d \qquad d \dots d \rangle^{\mathsf{T}} \tag{5.30}$$

If a frictionless contact between a rigid flat-ended cylindrical punch and a layered elastic half-space is considered, the shear traction vanishes and the surface displacement at the top surface in Eq. (5.27) is then reduced to

$$\sum_{j=1}^{Ne} U_z^N \left(r_i, r_j \right) \cdot p \left(r_j \right) = d \tag{5.31}$$

Once the normal traction p(r) and the shear traction q(r) in the contact area are obtained, all elastic fields within the bulk material of the layered half-space under axisymmetric indentation as shown in Figure 5.2 can be determined from the following equation:

$$R(r,z) = \int_{0}^{\infty} R^{N}(r,z;r') \cdot p(r') dr' + \int_{0}^{\infty} R^{R}(r,z;r') \cdot q(r') dr'$$
(5.32)

where R(r,z) denotes elastic fields, which are displacements and stresses, at any point (r,z) of the layered half-space; $R^N(r,z;r')$ and $R^R(r,z;r')$ are the Green's functions corresponding to elastic

fields at any point (r, z) within the bulk due to a unit normal load and a unit radial load (ring or annular) respectively acting on the surface of the upper layer at the radius r'. Note that the elastic fields within the bulk of the layered half-space, expressed in the form of Hankel integral transforms, are given elsewhere (Tirapat et al., 2017).

5.3 Numerical results

A computer program based on the solution procedure described in the previous section has been developed to study axisymmetric rigid indentation on an elastic layer and a layered elastic half-space with consideration of surface energy effects under frictionless and adhesive contacts.

5.3.1 Verification

First, the accuracy of Green's functions employed in the formulation of the indentation problem is validated by considering the case of an elastic layer with finite thickness t with a rigid base subjected to uniformly distributed normal traction p_0 over a circular area of radius a with consideration of surface energy effects. It is noted that the Green's function $G_{zz}(r,r^*)$, given by

Eq. (5.8), is expressed as a semi-infinite integral with respect to ξ where a closed form solution cannot be obtained. The evaluation of Green's functions is then performed by employing a globally adaptive numerical quadrature scheme (Piessens et al., 1983) that subdivides the interval of integration and employs a 21-point Gauss-Kronrod rule to estimate the integral over each subinterval. The subdivision continues until the error from the approximation is less than a specified tolerance. In the numerical study, it is convenient to introduce the following nondimensional quantities: $r_0 = r/\Lambda$; $z_0 = z/\Lambda$; $t_0 = t/\Lambda$; $a_0 = a/\Lambda$; $d_0 = d/\Lambda$; and $\alpha_0 = \alpha\Lambda$, where $\Lambda =$ $\kappa^{s}(\lambda+2\mu)/2\mu(\lambda+\mu)$, and it has the dimension of length. Aluminum was used for the layer material with $\lambda/\mu = 2.226$ (Meyers and Chawla, 1999), and Al [1 1 1] was employed for the surface with $\Lambda = 0.153$ nm and $\tau^s = 1$ N/m (Miller and Shenoy, 2000). The surface elastic constants can be obtained from atomistic simulations (Miller and Shenoy, 2000; Dingreville et al., 2005). Figure 5.3(a) presents comparison of normalized vertical displacements at the surface along the radial direction between the present solution and the solution given by Zhao (2009) for the case when the out-of-plane contribution of the residual surface stress is ignored. Comparison between the current solution and the existing solution (Rungamornrat et al., 2016) for the layer with the complete Gurtin-Murdoch surface elasticity model is also shown in Figure 5.3(b). It is evident from both figures that the present solutions are in excellent agreement with the two benchmark solutions.

The accuracy of the present solution is then verified with existing solution for nano-indentation problem. Figure 5.4 presents a comparison for axisymmetric indentation on an elastic half-space between the present solutions (with t/a = 200) and the solutions by Pinyochotiwong et al. (2013). The half-space material properties are identical to those of the elastic layer considered in Figure 5.3. Profiles of normalized contact traction and surface vertical displacement along the radial direction are presented under flat-ended cylindrical (non-smooth-contact) indenter in Figure 5.4(a) and paraboloidal (smooth-contact) indenter with $\alpha_0 = 0.5$ in Figure 5.4(b), respectively. Since the contact pressure distribution in the present study is assumed as a series of axisymmetric polynomial functions, profiles of normalized contact pressure in Figures 5.4(a) and 5.4(b) are then plotted for different numbers of terms employed in the series, m, to show the convergence and accuracy of the present solution. It is noted that under a flat-ended cylindrical indenter a vertical

ring load has to be applied at r = a in the current study to account for a ring load induced at the edge of a non-smooth-contact indenter in the presence of the residual surface stress. The applied vertical force P would then be supported by the ring load together with the contact pressure generated under this type of indentation. Comparison presented in Figure 5.4 reveals that the present solutions show a good agreement with the benchmark solutions given by Pinyochotiwong et al. (2013) when $m \ge 15$ for a flat-ended cylindrical indenter and $m \ge 10$ for a paraboloidal indenter, respectively. The appropriate number of terms, m, required in the approximation of the contact pressure is higher for non-smooth-contact indenter due to the singular pressure that exists along the edge of the cylindrical indenter (Pinyochotiwong et al., 2013). Comparison of normalized vertical displacement profiles at the top surface is also shown in Figure 5.4 for both flat-ended cylindrical and paraboloid indenters. The displacement profiles are approximated by using m = 15 and 10, respectively, for the flat-ended cylindrical and paraboloidal indenters. It is clearly seen from Figure 5.4 that a good agreement is also obtained for the comparison of normalized displacement profiles between the present solution and the benchmark solution (Pinyochotiwong et al., 2013) for both types of indenters. All numerical solutions presented hereafter are thus calculated by using m = 15 and m = 10 for the flat-ended cylindrical and the paraboloidal indenters, respectively.

In addition, numerical solution scheme based on the discretization approach outlined in the previous section is implemented into a computer program to study flat-ended cylindrical punch on a layered elastic half-space under adhesive contact as shown in Figure 5.2 The unknown contact traction (both normal and shear) between the rigid indenter and the layered medium can be represented as discrete regions of uniform tractions acting over annular regions as expressed in Eq. (5.27). The required Green's functions, $U_i^j(r,r')$ are determined from a layered elastic half-space subjected to a uniform annular load of unit intensity, which are expressed as semi-infinite integrals with respect to ξ [see Eqs. (5.25) and (5.26)] and the numerical evaluation of Green's function is previously discussed.

The accuracy of the obtained numerical results are validated with existing solutions. The present solution is specialized for the case of the adhesive contact between flat-ended cylindrical punch of radius a and an elastic half-space without surface energy effects. Figure 5.5 shows comparisons between the numerical solutions from the present study and the existing solutions given by Spence (1968). The following material parameters are employed: $\lambda_1 = \lambda_2 = 58.17$ GPa and $\mu_1 = \mu_2 = 26.13$ GPa. In addition, the surface parameters are set to be negligibly small in the present solution (i.e. $\tau_1^s = \tau_2^s \approx 0$ and $\kappa_1^s = \kappa_2^s \approx 0$). Comparisons of normalized contact pressure and surface displacement profiles at the top surface are shown in Figures 5.5(a) and 5.5(b) respectively. Numerical results presented in Figure 5.5(a) indicate that a very good agreement between the present and benchmark solutions is obtained when Ne = 40 for the normalized contact pressures. In addition, both normal and radial surface displacements obtained from the current study agree very closely with the benchmark solutions with Ne = 40 as shown in Figure 5.5(b).

5.3.2 Numerical solution for nano-indentation on elastic layer

Numerical solutions for an elastic layer with constant thickness *t* perfectly bonded to a rigid base subjected to axisymmetric rigid frictionless indentation under an applied vertical load *P* on its surface are presented in this section for particular punch profiles. Selected numerical results are then presented to portray the influence of surface stresses on elastic fields of a finite layer with

rigid base under axisymmetric indentation from flat-ended cylinder (non-smooth-contact) indenter and paraboloidal (smooth-contact) indenter. For the case of flat-ended cylindrical indenter [see Figure 5.1(b)], the contact radius "a" is prescribed and the punch profile is set to be zero, i.e., $v^p(r) = 0$. In addition, for paraboloidal punch, $v^p(r) = \alpha r^2$ where α is a positive constant and the radius of contact region "a" is unknown a priori [see Figure 5.1(a)]. The influence of surface energy effects on axisymmetric indentation on an elastic layer with rigid base is presented for the flat-ended cylindrical indenter with the contact radius of $a_0 = 0.5$, and for the paraboloidal indenter with $\alpha_0 = 0.5$. An elastic layer, with a finite thickness of t/a = 5 and material properties of $\lambda/\mu = 2.226$; $\Lambda = 1$ nm; and $\tau^s = 5$ N/m, is considered in the numerical study.

Figures 5.6 to 5.8 present elastic fields of the elastic layer subjected to the flat-ended cylindrical indenter. Note that the broken lines in all Figures presented hereafter denote the classical solutions corresponding to the indentation on an elastic layer with no surface stress effects (i.e. $\kappa^s = \tau^s \cong 0$). For the classical solution, a square root singularity exists in the contact pressure along the edge of the flat-ended cylindrical indenter (Sneddon, 1965). Equation (5.13) has to be modified by adding another function with square root singularity at r = a in the modeling of the contact pressure for the classical solution. Normalized contact pressure and vertical displacement profiles at the surface along the radial direction are presented in Figure 5.6(a) for different layer thicknesses, i.e., t/a = 2, 5 and 10, with $a_0 = 0.5$. Figure 5.6(b) presents radial profiles of normalized contact pressure and vertical displacement of an elastic layer with t/a = 5 for different values of contact radii, i.e., $a_0 = 0.5$, 1.0 and 1.5, to demonstrate the size-dependent behavior of the present solution. Numerical results shown in Figure 5.6(a) indicate that the contact pressure increases when the layer thickness decreases, and the singularity is observed in the profiles near the edge of the indenter for both classical and present solutions. In addition, the contact pressure in the current study is lower due to the presence of surface stresses. The normalized displacement profiles shown in Figure 5.6(a) reveal that the vertical displacements outside the contact region obtained from the current study are higher than those from the classical elasticity due to the fact that larger indentation force is required in the present solutions to produce the same indentation depth. It is obvious from Figure 5.6(b) that with the consideration of surface stress effects the size-dependency is clearly observed on normalized contact pressure and vertical displacement whereas the classical elasticity solutions are size-independent. In addition, the influence of surface stresses decreases when the radius of the indenter a increases, and the present solution will eventually converge to the corresponding classical solution.

The influence of surface stress is further investigated for different residual surface stress (τ^s) and surface material parameter (Λ) in Figure 5.7(a) and 5.7(b) respectively. In Figure 5.7(a), normalized contact pressure profiles are presented for a material with residual surface stress being varied from 1.0 to 10 N/m and $\Lambda=1$ nm. The influence of surface material parameter is illustrated in Figure 5.7(b) by employing a material with the surface material parameter being varied from 0.1 to 100 and $\tau^s=5$ N/m. It can be seen from both figures that the normalized contact pressure obtained from the current study is lower than the classical solution for all values of residual surface stress and surface material parameter. In addition, the contact pressure shows more dependence on the residual surface stress when compared to the surface material parameter. The contact pressure significantly decreases by increasing the residual surface stress since a larger ring load is generated for higher residual surface stress resulting in smaller contact pressure being developed under the indenter. On the contrary, normalized contact pressure increases with increasing the surface

material parameter. This is physically realistic as a material with increased surface material parameter would possess a stronger surface. As a result, a lower ring load is induced along the indenter edge and higher contact pressure is then generated under the indenter.

Figures 5.8(a) and 5.8(b) show radial profiles of normalized displacements and stresses respectively along the radial direction of an elastic layer under axisymmetric indentation at different depths. It is clearly seen from both Figures. that the surface stress has a notable influence on elastic fields especially in the vicinity of the top surface. In Figure 5.8(a), both vertical and radial displacements from the current study are higher than their classical counterparts. Numerical results shown in Figure 5.8(b) indicate that the presence of surface stresses causes the reduction in stresses under the contact region, whereas outside the contact region the increase of stresses is observed. In addition, the influence of the surface stress becomes negligible when r/a > 3.

A set of numerical solutions presented in Figures 5.9 to 5.11 correspond to the case of an elastic layer compressed by a rigid paraboloidal indenter with $v^p(r) = 0.5 r^2$. It is noted that under a smooth-contact indenter the contact radius "a" is unknown a priori, and it can be determined by enforcing the continuity condition of the vertical stress under the indenter at r = a and z = 0. In addition, no ring load is induced under *smooth-contact* indentation. Figures 5.9(a) and 5.9(b) demonstrates the influence of surface stresses on radial profiles of normalized contact pressure and vertical displacements of an elastic layer with different thicknesses and different contact radii respectively. Numerical results for normalized contact pressure profiles presented in Figure 5.9(a) indicate that no singularity is observed in the contact pressure under a *smooth-contact* indenter. The maximum contact stresses, from both current study and classical elasticity, are found under the center of the indenter, and the pressure gradually decreases with the radial distance. Note that the contact pressure from the classical solution vanishes at r = a, whereas the current solution shows a finite value at that location due to the presence of surface stresses. Similar behavior was also observed for *smooth-contact* indentation on an elastic half-space (Pinyochotiwong et al., 2013). Similar to the case of non-smooth-contact indenter shown in Figure 5.6(a), both classical and present solutions shows a strong dependence on the layer thickness. The contact pressure decreases with the increase of the layer thickness whereas the normalized vertical displacement decreases when the layer thickness decreases. In addition, larger contact pressure and displacement are observed in the current study when compared to the classical solutions since the surface stresses render the layer stiffer and larger indentation force is then required to yield the same indentation depth. To observe the size dependent behavior, the variations of contact pressure and vertical displacement along the radial direction are presented in Figure 5.9(b) for different values of contact radii, i.e., $a_0 = 0.5$, 1.0 and 1.5. As expected, the contact pressure and vertical displacement in the current study depend significantly on the size of the contact radius "a" whereas the classical counterparts are once again size-independent. It is clearly observed from Figure 5.9(b) that the influence of surface stress effects becomes smaller as the contact radius becomes larger and both contact pressure and displacement converge to their classical counterparts.

In Figures 5.10(a) and 5.10(b), the influence of residual surface stress (τ^s) and surface material parameter (Λ) are investigated by varying $\tau^s = 1.0$ - 10 N/m and $\Lambda = 0.1 - 100$ nm respectively. Note that other material parameters remain unchanged during the variation of either τ^s or Λ . Unlike the *non-smooth-contact* indentation shown in Figure 5.7, the present contact pressure is larger than the classical solution for all values of τ^s or Λ . Once again, the contact pressure under *smooth-contact* indentation also shows more dependence on the residual surface

stress. The normalized contact pressure from the current study increases with increasing the residual surface stress and the surface material parameter. Figure 5.11 presents the radial variations of normalized displacements and stresses at various depths under *smooth-contact* indentation. Numerical results shown in this Figure indicate that the surface stresses display similar influence on radial profiles of elastic fields to those shown in Figure 5.8 for *non-smooth-contact* indentation. Once again, both vertical and radial displacements from the current study are larger than the corresponding classical solutions and the presence of surface energy effects results in discrepancy in normal and shear stresses between the present and classical solutions.

The final set of numerical solutions demonstrates the influence of the thickness of an elastic layer and the contact radius on the indentation force. Figure 5.12 presents variation of normalized indentation force with the contact radius a_0 for different layer thicknesses. Note that P_c corresponds to the indentation force on an elastic half-space for the classical case, which is obtained from the current study by ignoring the surface energy effects (i.e., $\kappa^s = \tau^s \cong 0$) with t/a = 200. The flatended cylindrical and paraboloidal indenters are presented in Figures 5.12(a) and 5.12(b), respectively. Note that for the paraboloidal indenter, a punch profile with $\alpha_0 = 0.01$ is used so that the obtained indentation depths are valid for all layer thicknesses under consideration. Numerical results presented in Figure 5.12 indicate that the indentation forces from both current study and classical elasticity depend significantly on the thickness of the layer and the contact radius. It is evident that higher indentation force is required to produce the same indentation depth for a thinner layer. The size-dependency is clearly observed from the present solution for all layer thicknesses under both non-smooth-contact and smooth-contact indentations. In addition, the present solution for the flat-ended cylindrical punch approaches the half-space solution given by Pinyochotiwong et al. (2013) when the layer becomes thicker. A notable feature observed from Figure 5.12 is the fact that the classical solutions for both non-smooth-contact and smooth-contact indentations also display size-dependent behavior for a thin layer ($t_0 \le 10$). This behavior was also observed by Yang (2003) who considered the case of flat-ended cylindrical indenter with frictionless condition on both contact interfaces and no surface stress influence.

5.3.3 Numerical solution for nano-indentation on layered elastic half-space

The influence of surface energy effects on rigid indentation with adhesive contact on a layered elastic half-space is investigated for a flat-ended cylindrical indenter as shown in Figure 5.2. For convenience, the following non-dimensional quantities: $\bar{z} = z/\Lambda_1$; $\bar{h} = h/\Lambda_1$; $\bar{a} = a/\Lambda_1$ and $\bar{d} = a/\Lambda_1$ d/Λ_1 , together with Ne = 40 are used for the numerical results of the adhesive contact problem presented hereafter. In addition, the material properties employed in the top surface and the bulk in the top layer are identical to those considered by Pinyochotiwong et al. (2013) whereas λ_2 = 78.08 GPa, $\mu_2 = 40.23$ GPa for the bulk of the underlying half-space; and $\tau_2^s = 0.3944$ N/m, $\kappa_2^s = -$ 3.9506 N/m at the interface. Note that the broken lines in all figures presented in this section denote the classical solutions corresponding to the indentation on the layered elastic half-space with no surface energy effects (i.e. $\tau^s = \kappa^s \approx 0$). Figures 5.13(a) and 5.13(b), respectively display radial profiles of contact pressure and vertical surface displacement under the indenter for both adhesive and frictionless contacts with $\bar{a} = 1$ and h/a = 1. It is evident from Figure 5.13 that the numerical results from the present study and the classical solution exhibit similar trends for both pressure and displacement profiles, and the surface energy influence renders the layered medium stiffer. Numerical results presented in Figure 5.13(a) indicates that both classical and present solutions show singular contact traction close to the indenter edge. In addition, the traction developed under the adhesive contact is comparatively higher than that under the frictionless contact due to the presence of adhesion resulting in higher indentation force being required for the same indentation depth.

Figures 5.14(a) and 5.14(b) respectively present radial variations of normalized displacements and stresses of a layered elastic half-space under indentation with adhesive contact at different depths for the contact radius of $\bar{a} = 1.0$ and the layer thickness of h/a = 1. Once again, the solutions for elastic fields from the present study and the classical elasticity shown in Figure 5.14 display similar trends. Figure 5.14(a) indicates that both vertical and radial displacements from the present study are higher than the classical elastic solutions. Numerical results for the normalized vertical and shear stresses at various depths shown in Figure 5.14(b) reveal that the presence of surface stresses causes the reduction in stresses under the contact region, whereas outside the contact region the increase of stresses is observed. In addition, the influence of the surface stress becomes negligible when r/a > 2.5.

To demonstrate the effect of the contact area for indentation with adhesive contact and the influence of surface energy effects, Figures 5.15(a) and 5.15(b) show radial variations of normalized contact pressure and surface displacements of the layered half-space with h/a = 1 for different values of the normalized contact radius, i.e. $\bar{a} = a/\Lambda_1 = 0.5$, 1.0 and 1.5. Note that the solution with $\bar{a} = 1.0$ corresponds to the case where the thickness of the layer is equal to the characteristic length (Λ_1). It can be obviously seen from Figure 5.15(a) that the singularity of contact traction (both normal and shear) is observed close to the edge of indenter for both classical and present solutions. It should be noted that under the adhesive contact the normal and radial ring loads have to be applied at r = a in the present solution to account for the two ring loadings induced at the indenter edge due to the presence of the residual surface stress. The applied vertical force P would then be supported by both ring loads together with the contact pressure generated under the indenter. The size-dependency of the present solution is clearly observed in contact pressure and displacement profiles shown in Figure 5.15 whereas the classical elasticity solution is size-independent. It is also found that the influence of surface stress is reduced when the radius of the indenter becomes larger and the present solution eventually converges to the classical solution.

The influence of the residual surface stress (τ^s) on the normalized contact pressure and surface displacement under indentation with adhesive contact are investigated respectively in Figures 5.16(a) and 5.16(b) with $\bar{a}=1$ and h/a=1. The ratio of the residual surface stresses at the top surface and interface is varied, i.e. $\tau_1^s/\tau_2^s=0.5$, 1, 2, 4 whereas other material parameters associated with the upper layer and the underlying half-space remain unchanged. It is obvious that the normal traction and the vertical surface displacement are larger than the shear traction and radial surface displacement respectively. Profiles of normal contact pressure presented in Figure 5.16(a) indicate that the current solutions are lower than the contact pressure from the classical elasticity. The normal pressure significantly decreases by increasing the ratio of residual surface stresses. In addition, the numerical results shown in Figure 5.16(b) reveal that the normalized vertical surface displacements outside the contact area obtained from the present study are higher than the classical solution due to the presence of the residual surface stress, and the layered half-space becomes stiffer with increasing the ratio τ_1^s/τ_2^s .

To study the influence of shear moduli in the layered medium, radial variations of normalized vertical contact pressure and vertical surface displacement with $\bar{a} = 1$ and h/a = 1 for

different values of μ_1/μ_2 are shown in Figure 5.17. It is evident from numerical results on contact pressure and vertical displacement shown in Figure 5.17 that the present and classical solutions display similar behaviors for all values of μ_1/μ_2 , and the surface energy influence renders the layered medium stiffer. Numerical results presented in Figure 5.17(a) reveal that the normal contact traction under the surface energy effects is lower than the classical one. Figure 5.17(b) also shows that the vertical surface displacement outside the contact area obtained from the present study is higher than the classical solution since higher indentation force is required to produce the same indentation depth due to the existence of surface effects.

To demonstrate the size-dependent behavior, the final set of numerical solutions is concerned with the indentation force on a layered elastic half-space with surface energy effects. Figure 5.18 presents variations of normalized indentation force, P/P_c , with the normalized contact radius \bar{a} for different values of the layer thickness h/a. The dotted lines in the figure indicate the normalized indentation forces corresponding to the frictionless contact where the surface energy effects are considered while the dash line corresponds to the classical adhesive contact where the surface energy effects are ignored (i.e. $\tau^s = \kappa^s \approx 0$). In addition, P_c indicates the indentation force on an elastic half-space $(h/a \rightarrow \infty)$ for the classical frictionless case. It is obviously seen from Figure 5.18 that the normalized indentation forces show a significant dependence on the thickness of the upper layer and the contact radius for both adhesive and frictionless contacts due to the influence of surface energy effects. The indentation force increases when the layer thickness decreases. This is physically realistic since the upper layer is softer than the underlying half-space the reduction in the upper layer thickness then renders the layered half-space stiffer. In addition, the indentation force decreases with increasing the contact radius converging to the classical one. Thus, size-dependent behavior is once again observed from the results shown in Figure 5.18, and it is evident that for the same contact area the indentation force under adhesive contact is higher than that under frictionless contact.

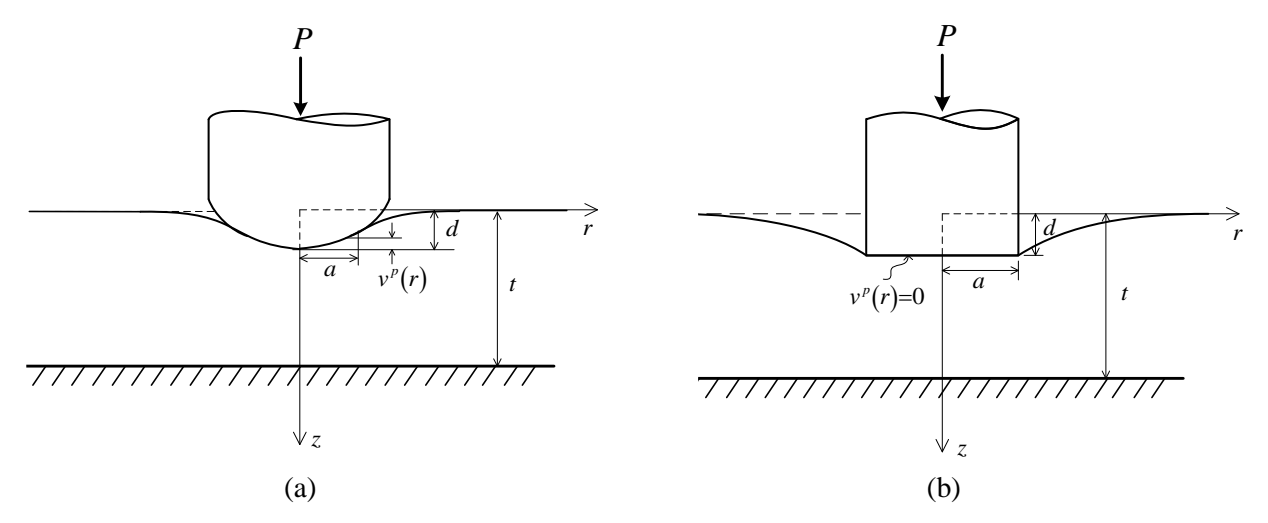


Figure 5.1 Elastic layer with finite thickness under frictionless axisymmetric: (a) *smooth-contact* profile; (b) *non-smooth-contact* profile

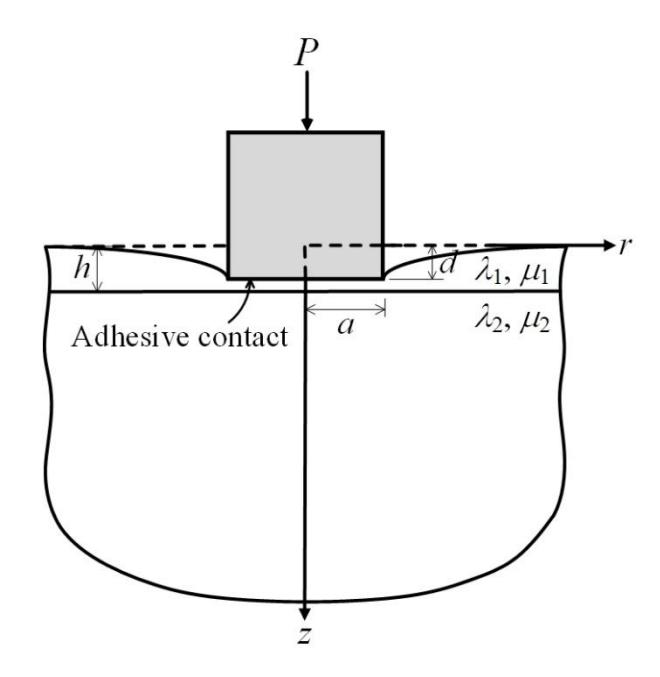


Figure 5.2 Indentation on a layered elastic half-space under rigid flat-ended cylindrical punch of radius *a* with adhesive contact.

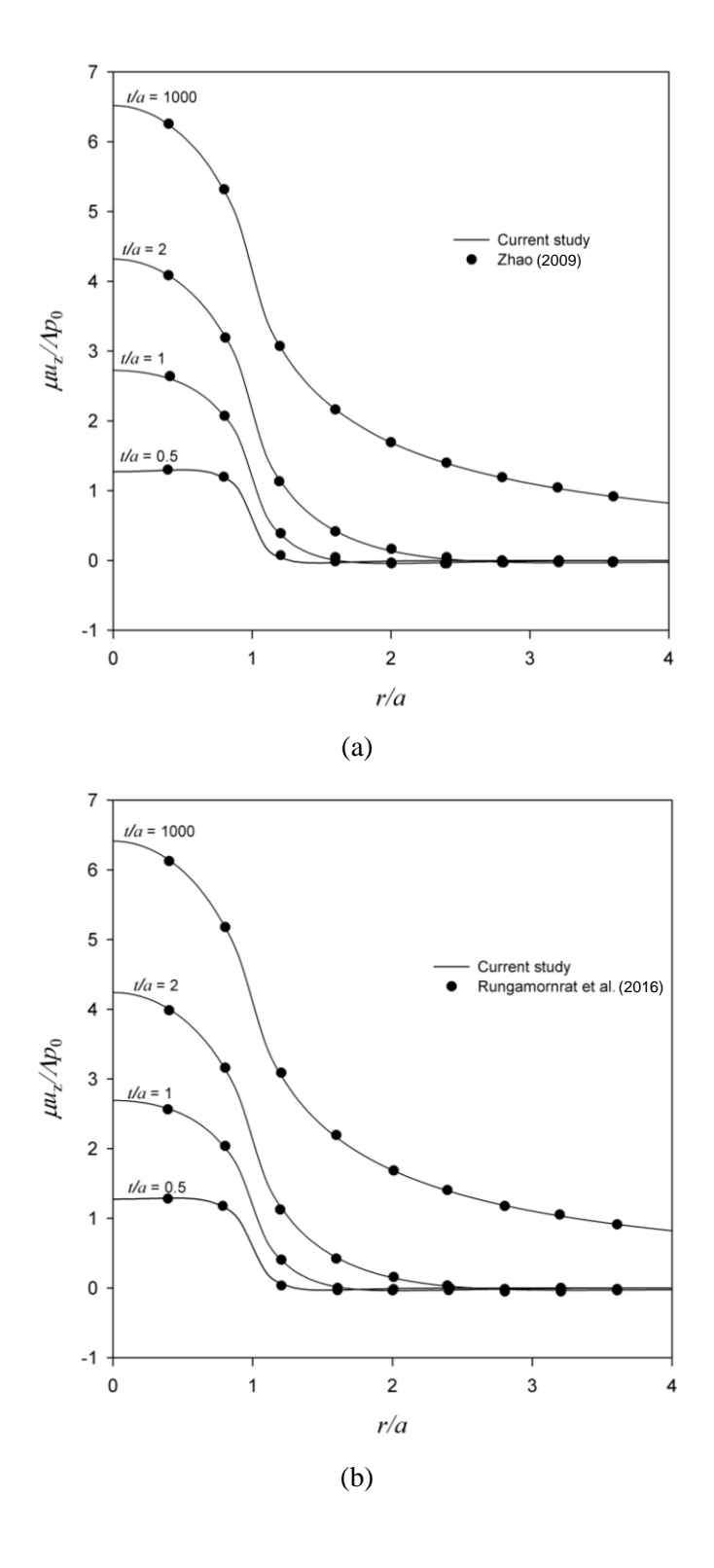


Figure 5.3 Validation of Green's functions for an elastic layer under surface energy effects: (a) without out-of-plane contribution of τ^s ; (b) with complete Gurtin-Murdoch model

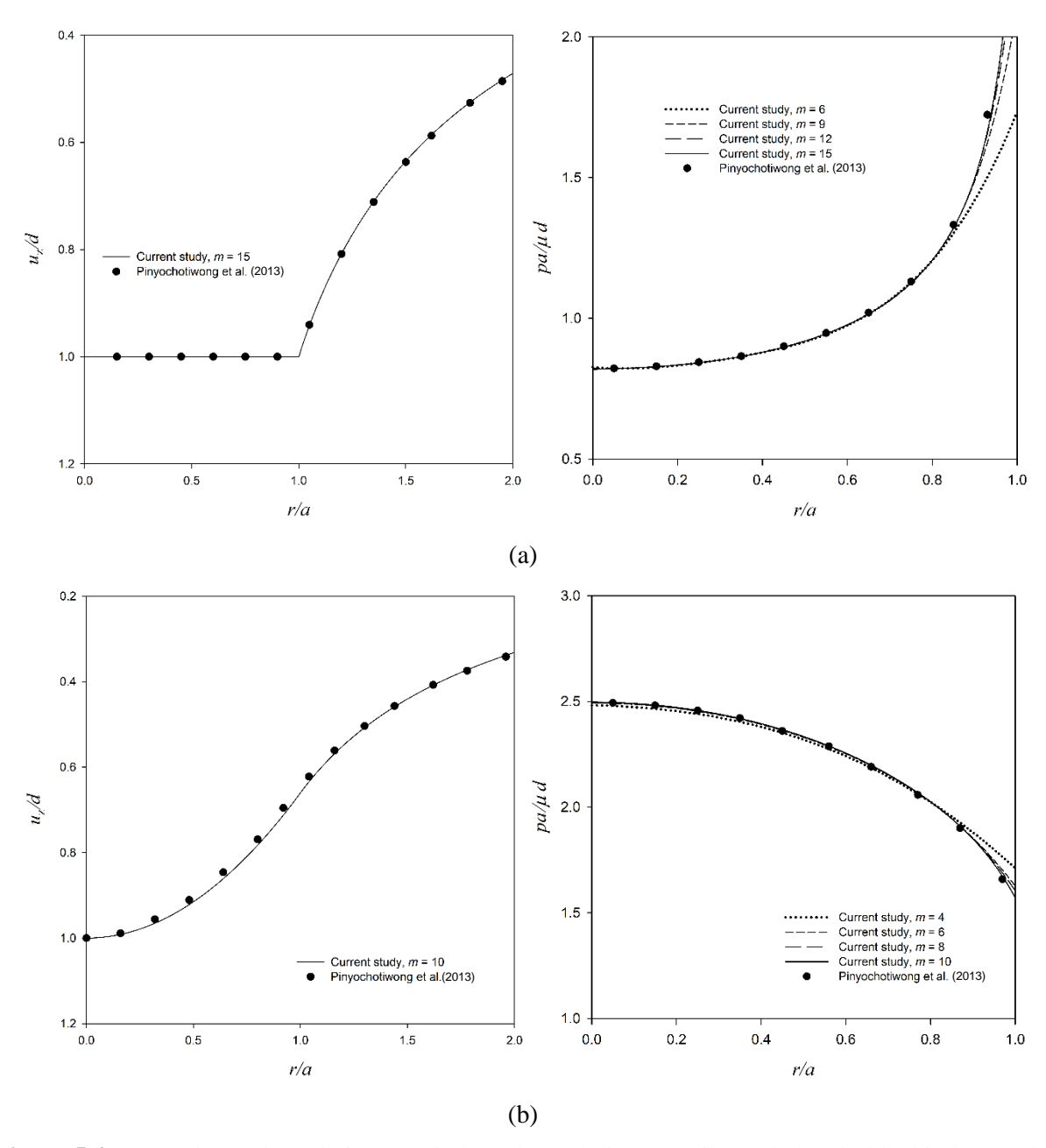


Figure 5.4 Comparison with existing nanoindentation solutions: (a) flat-ended cylindrical indenter; (b) paraboloidal indenter.

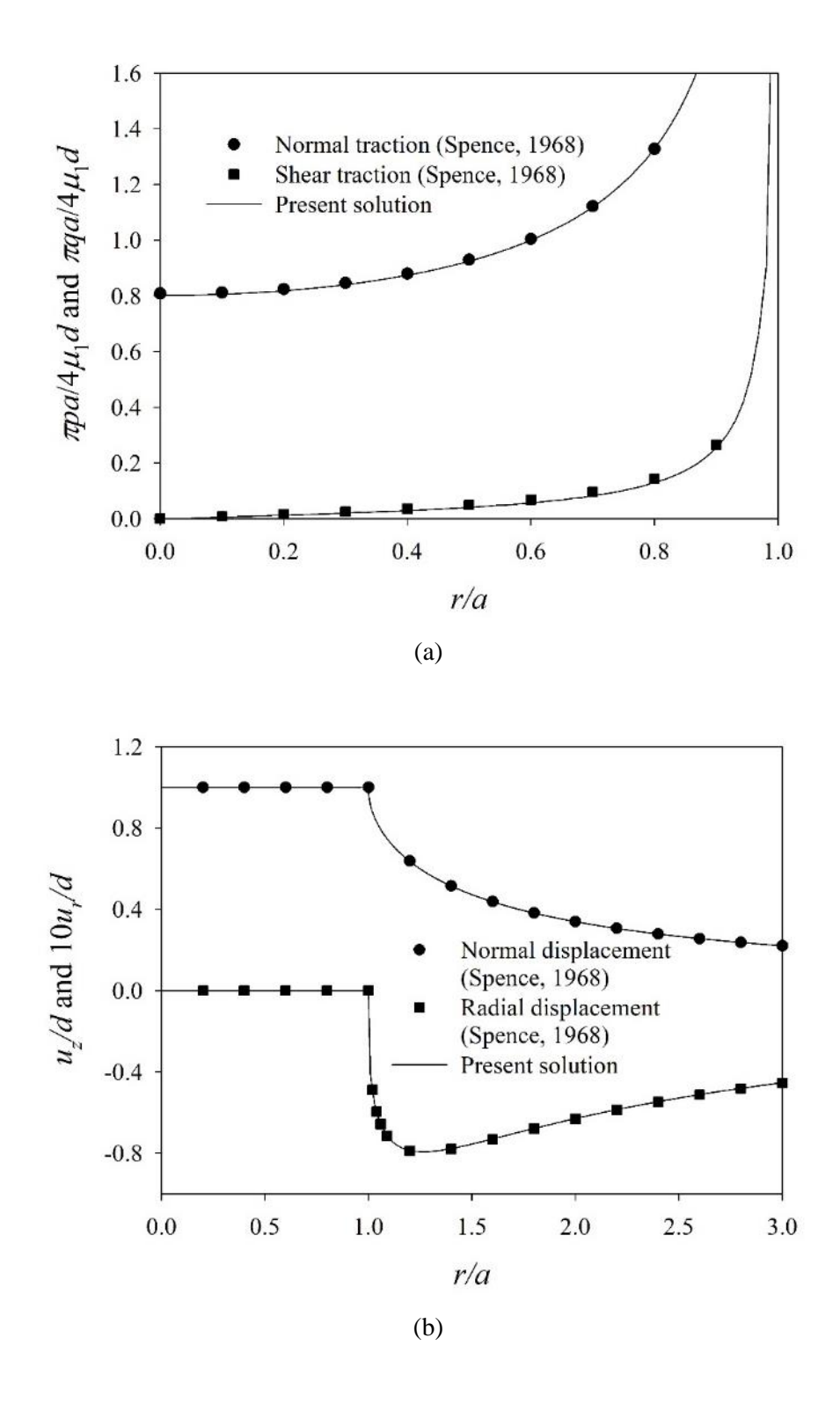


Figure 5.5 Comparison of elastic fields in an elastic half-space under indentation with adhesive contact (no surface energy effect): (a) normalized contact pressure and (b) normalized surface displacements.

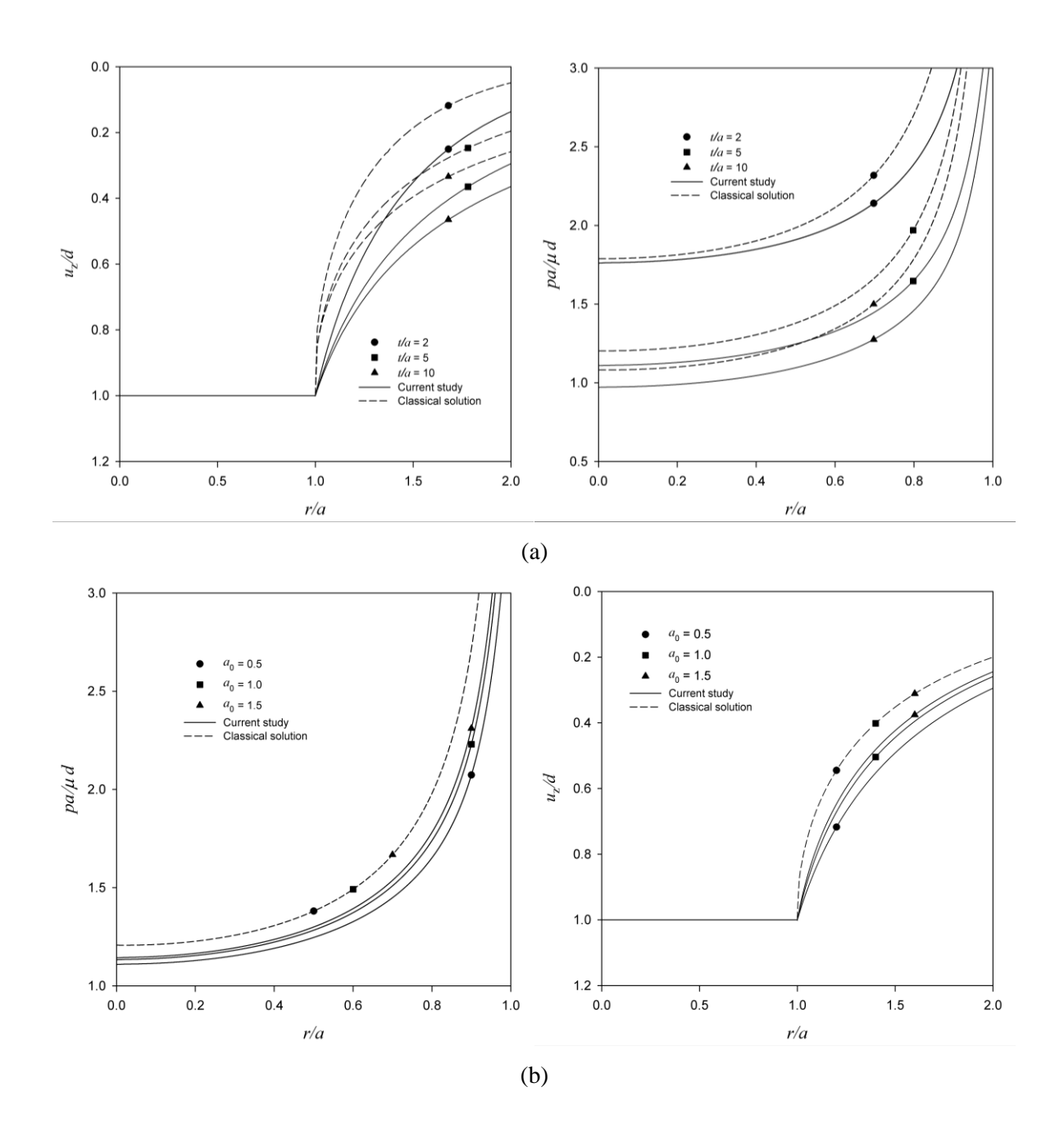


Figure 5.6 Radial profiles of contact pressure and surface vertical displacement under flat-ended cylindrical indenter for: (a) a_0 = 0.5 and different layer thicknesses; (b) t/a = 5 and different contact radii.

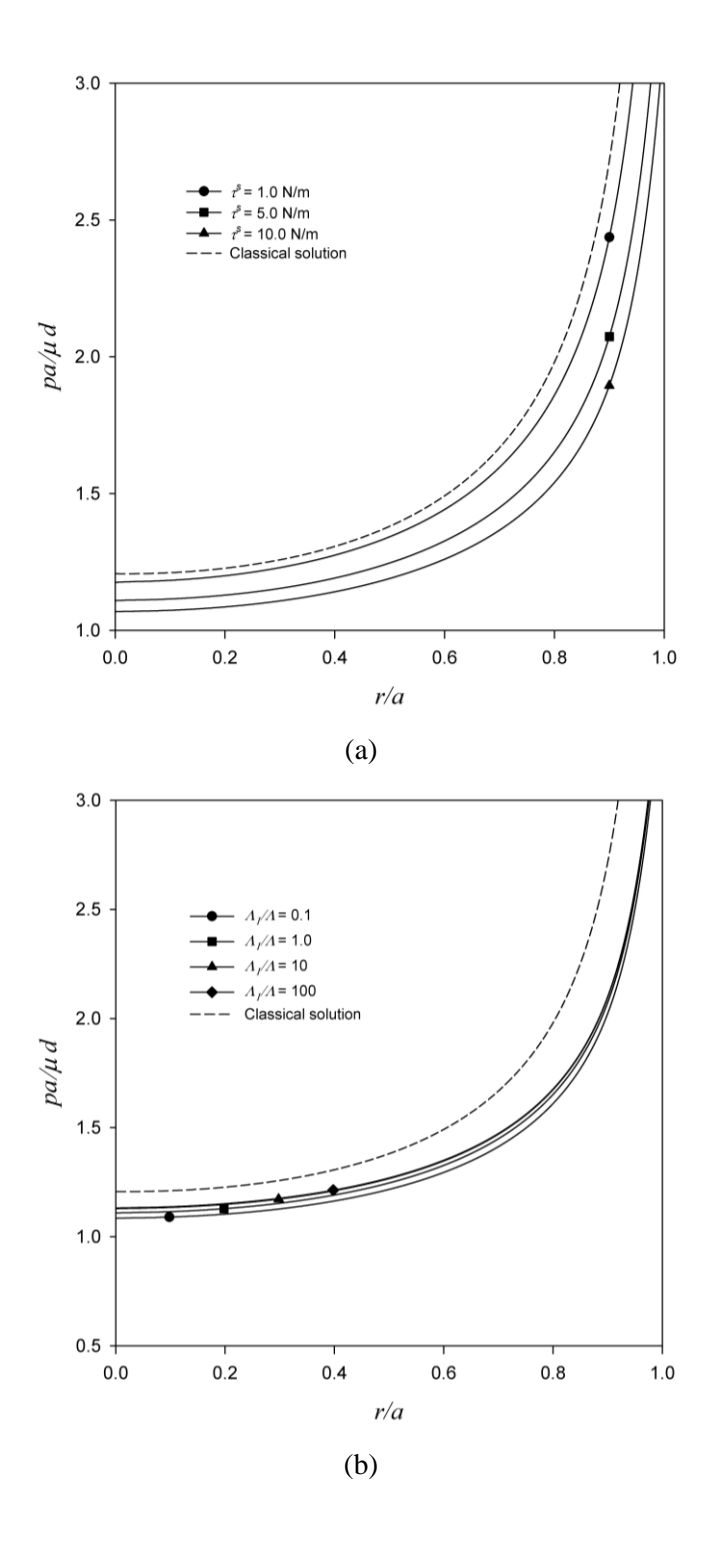


Figure 5.7 Radial profiles of contact pressure under flat-ended cylindrical indenter with a_0 = 0.5 for: (a) different residual surface stresses; (b) different surface material parameters.

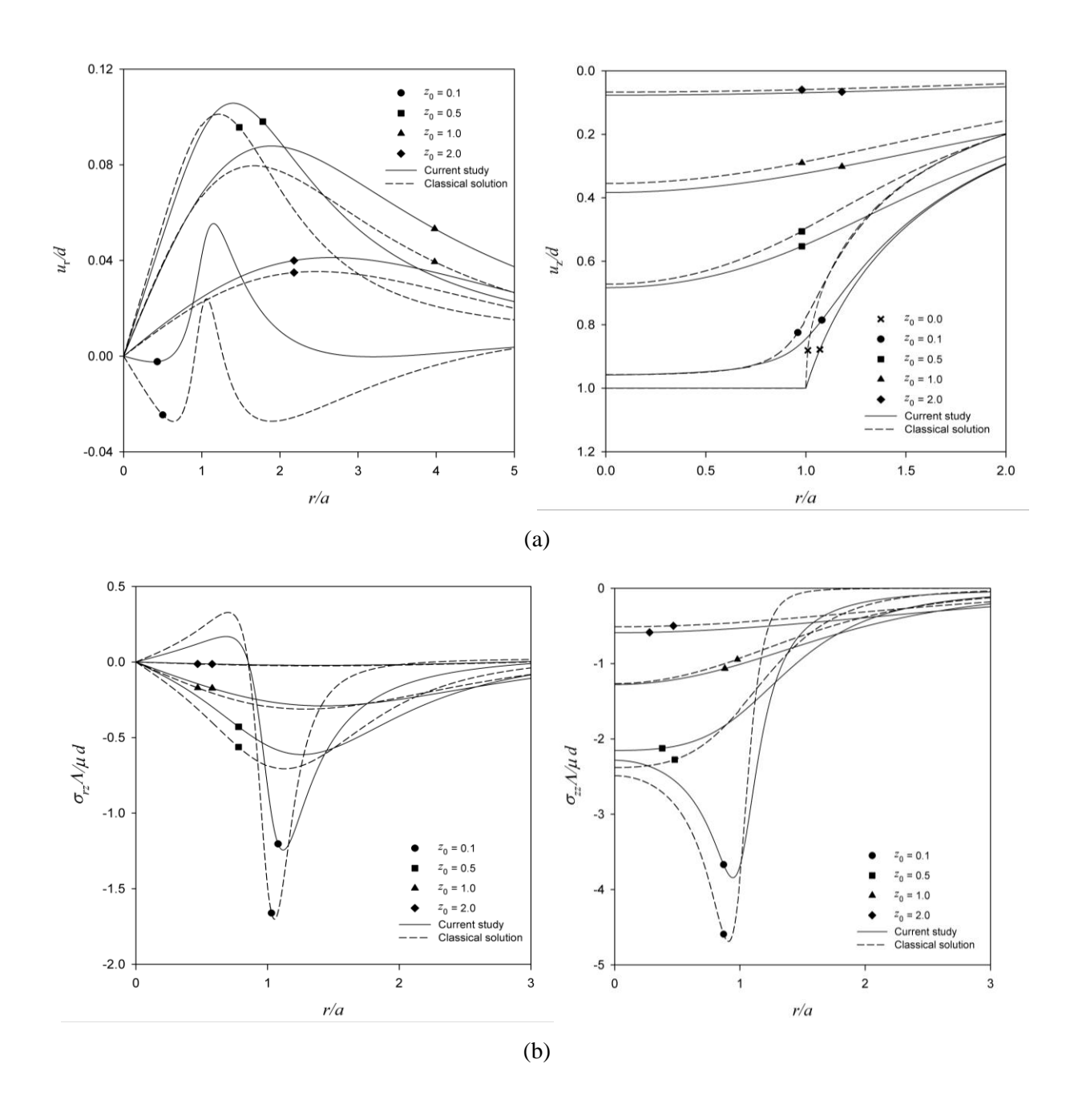


Figure 5.8 Radial profiles of elastic fields at different depths under flat-ended cylindrical indenter with t/a = 5 and $a_0 = 0.5$: (a) normalized displacements (b) normalized stresses.

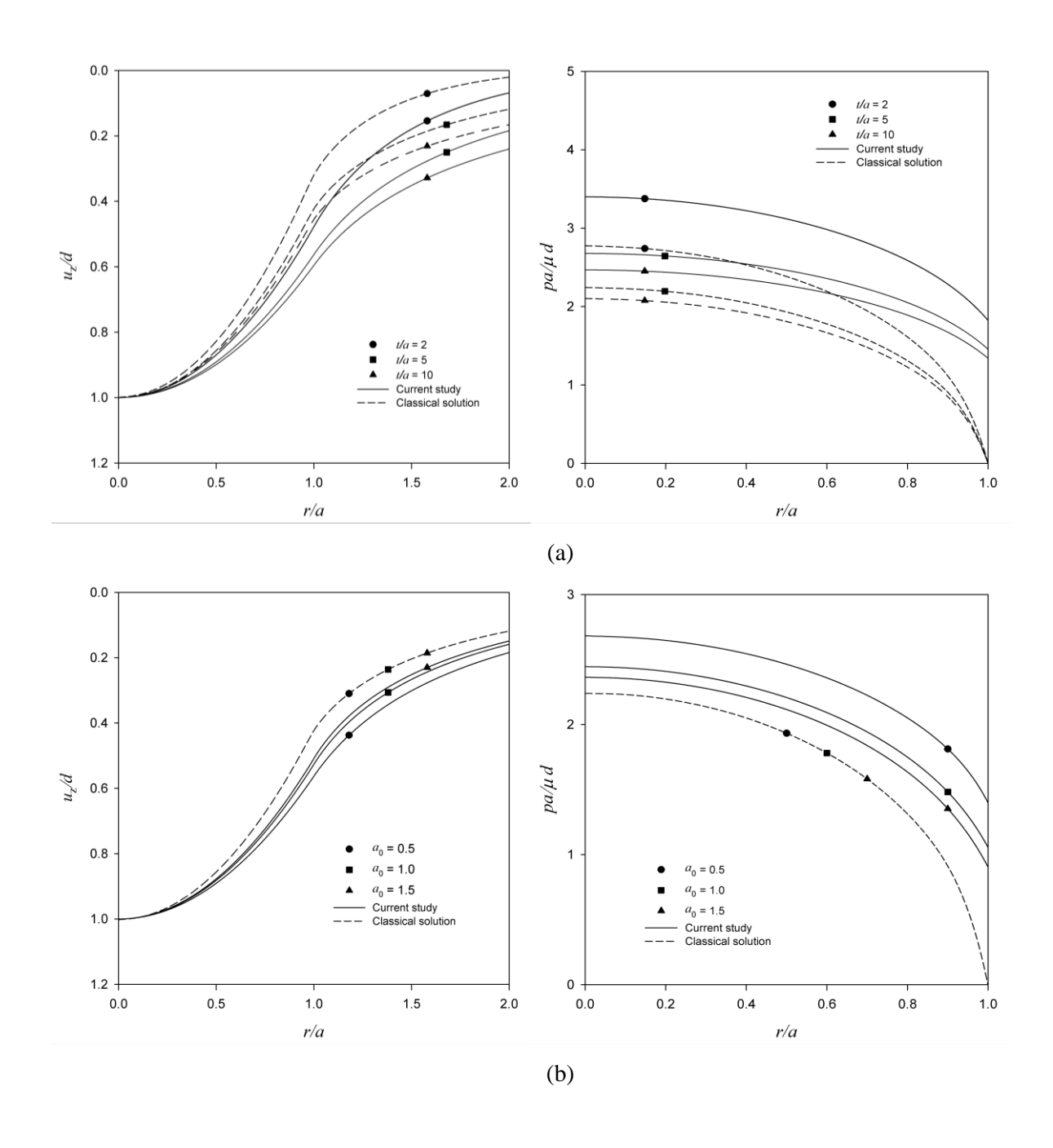


Figure 5.9 Radial profiles of contact pressure and surface vertical displacement under paraboloidal indenter for: (a) a_0 = 0.5 with different layer thicknesses; (b) t/a = 5 with different contact radii.

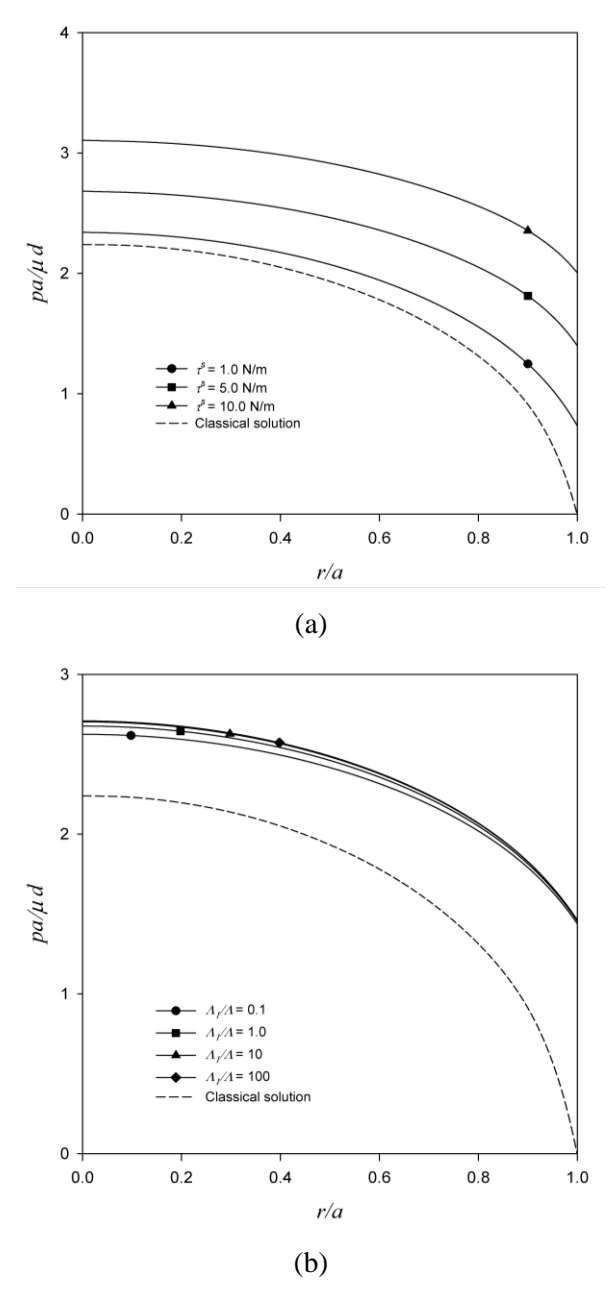


Figure 5.10 Radial profiles of contact pressure under paraboloidal indenter with a_0 = 0.5 for: (a) different residual surface stresses; (b) different surface material parameters.

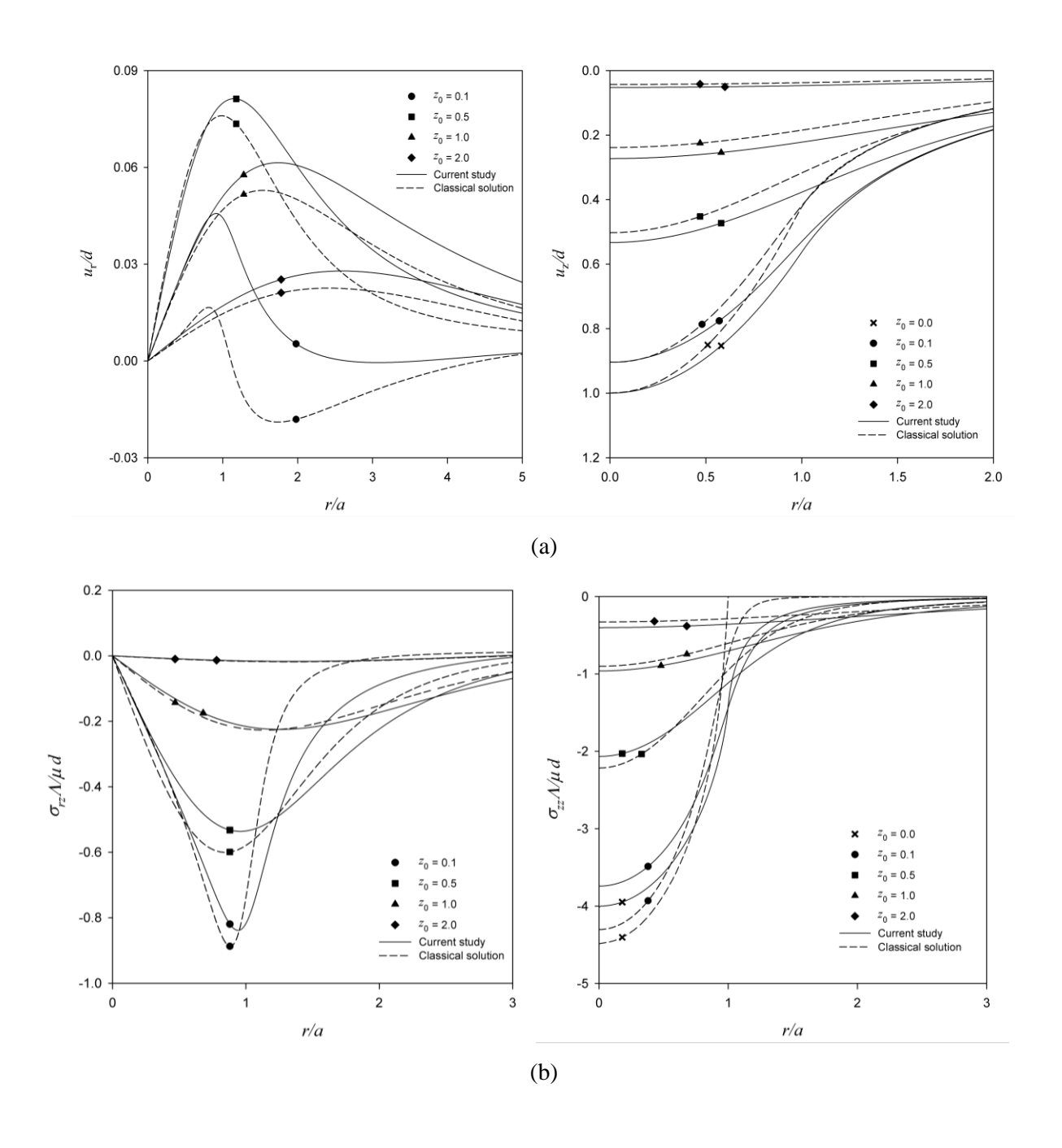


Figure 5.11 Radial profiles of elastic fields at different depths under paraboloidal indenter with t/a = 5 and $a_0 = 0.5$: (a) normalized displacements (b) normalized stresses.

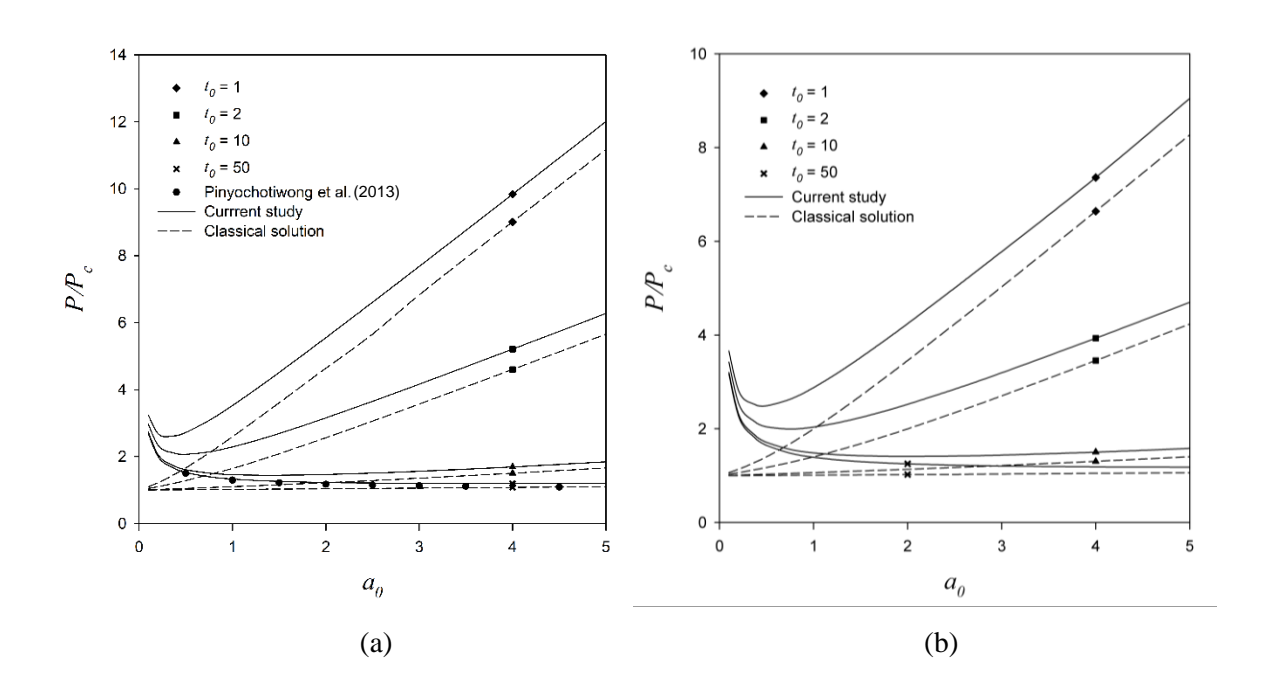


Figure 5.12 Variations of normalized indentation force with a_0 for different layer thicknesses: (a) flatended cylindrical indenter (b) paraboloidal indenter.

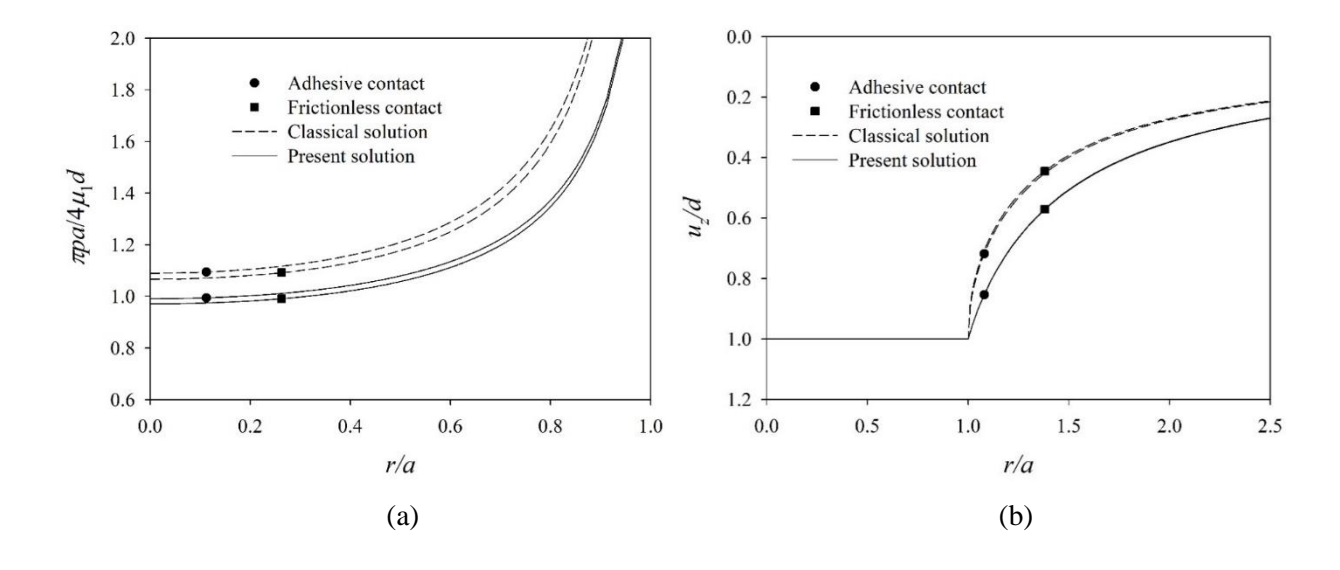


Figure 5.13 Radial variations of elastic fields for different contact conditions with h/a = 1 and $\overline{a} = 1$: (a) normalized contact pressure and (b) normalized vertical surface displacement.

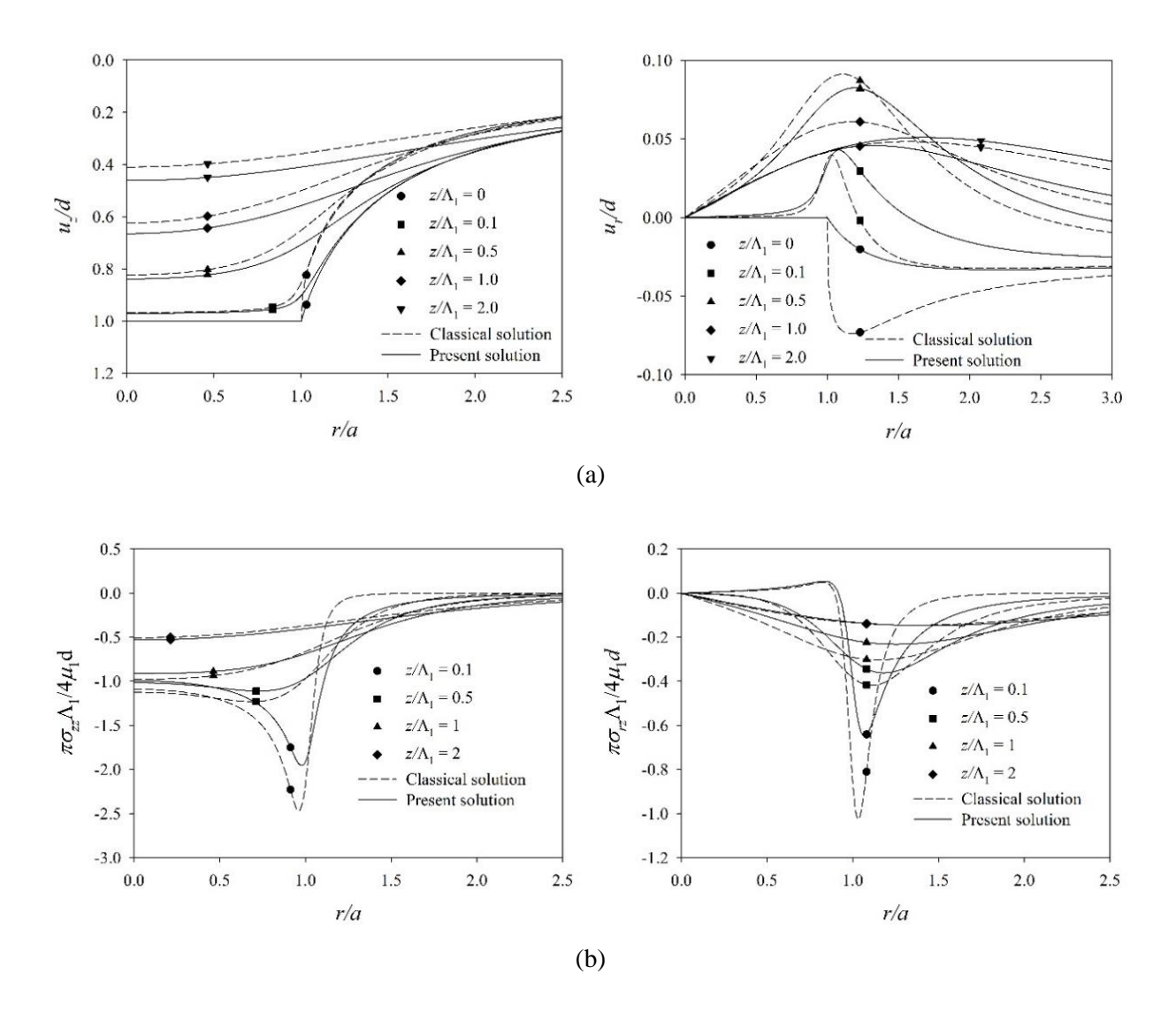


Figure 5.14 Radial variations of elastic fields at different depths with h/a = 1 and $\overline{a} = 1$: (a) normalized displacements and (b) normalized stresses.

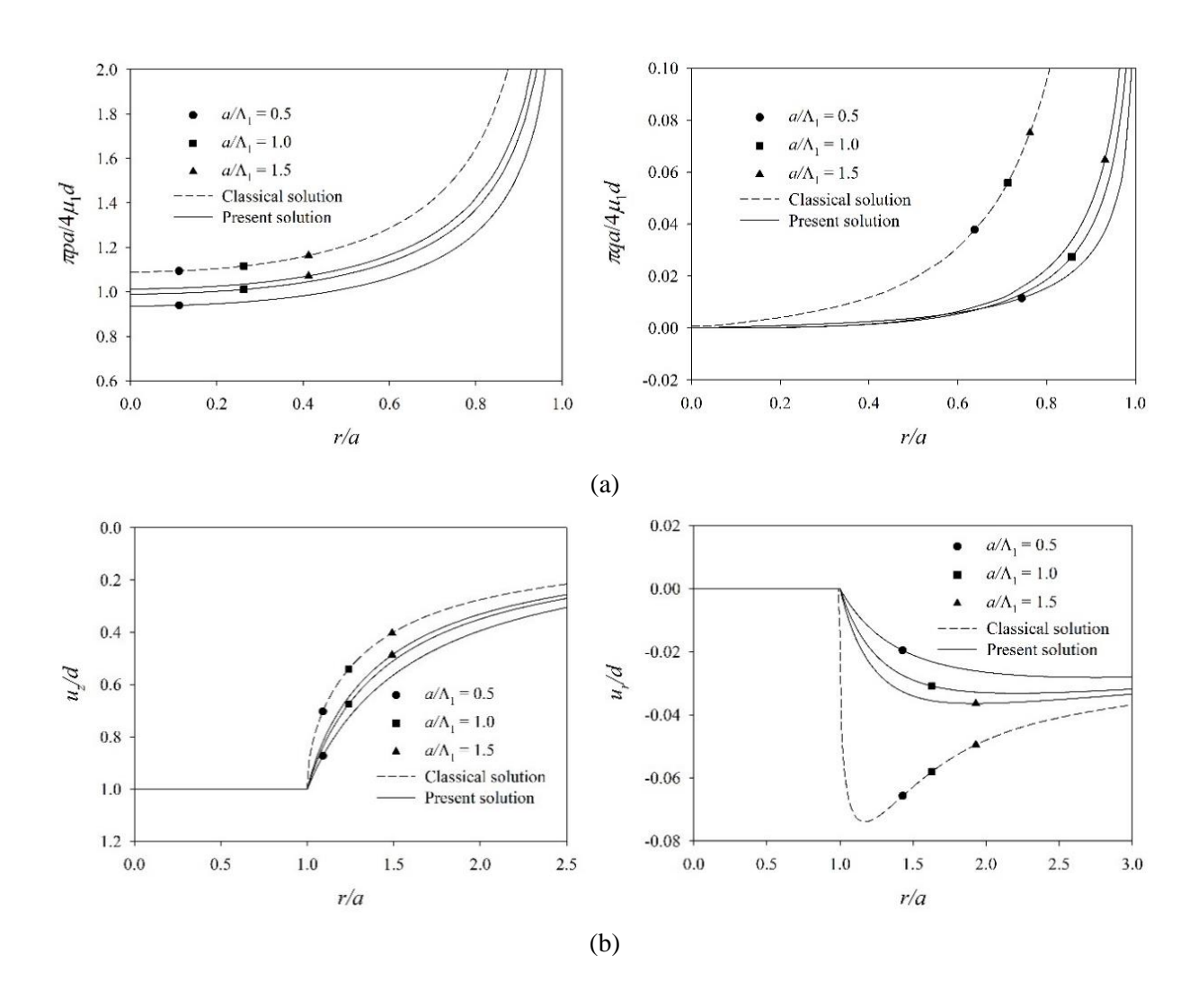


Figure 5.15 Radial variations of elastic fields for different contact radii \overline{a} with h/a = 1: (a) normalized contact pressure and (b) normalized surface displacement.

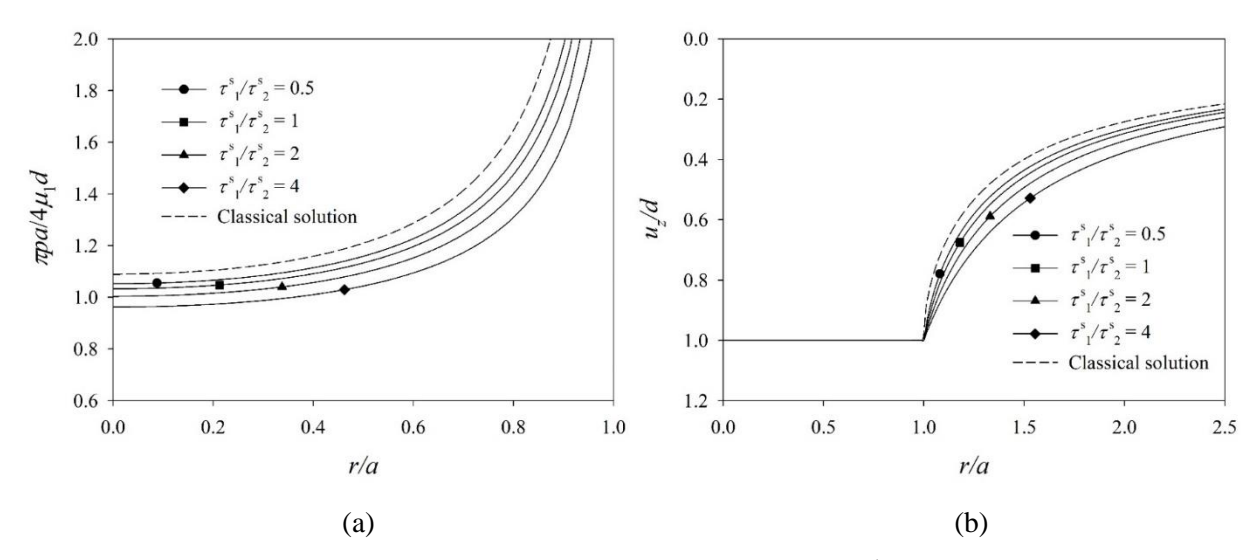


Figure 5.16 Radial variations of elastic fields for different values of τ_1^s / τ_2^s with h/a = 1 and $\overline{a} = 1$: (a) normalized contact pressure and (b) normalized surface displacement.

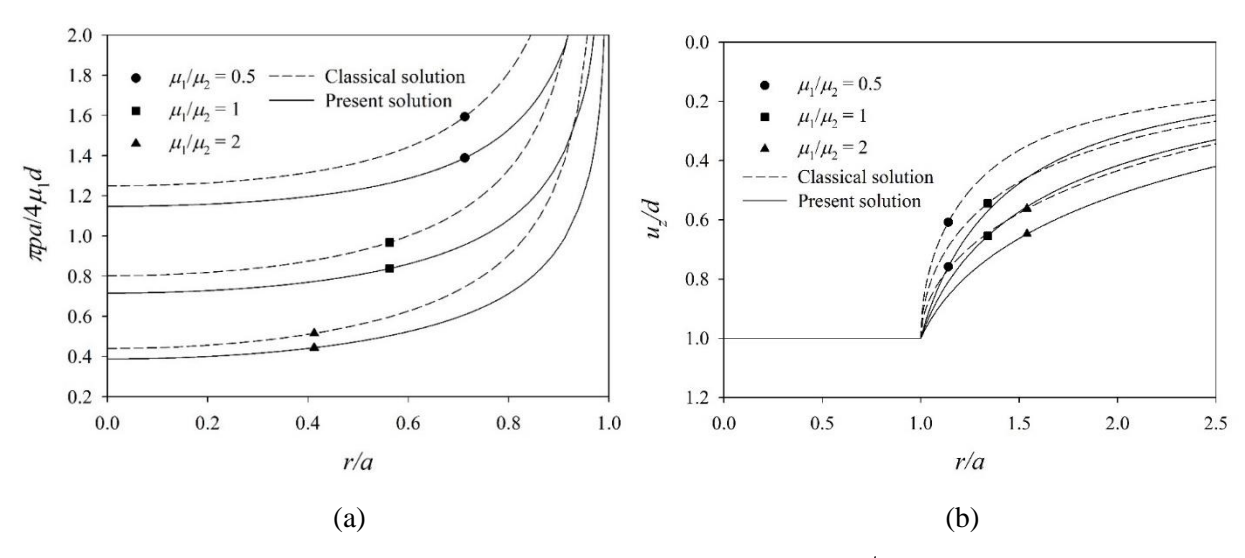


Figure 5.17 Radial variations of elastic fields for different values of μ_1/μ_2 with h/a=1 and $\overline{a}=1$: (a) normalized contact pressure and (b) normalized surface displacement.

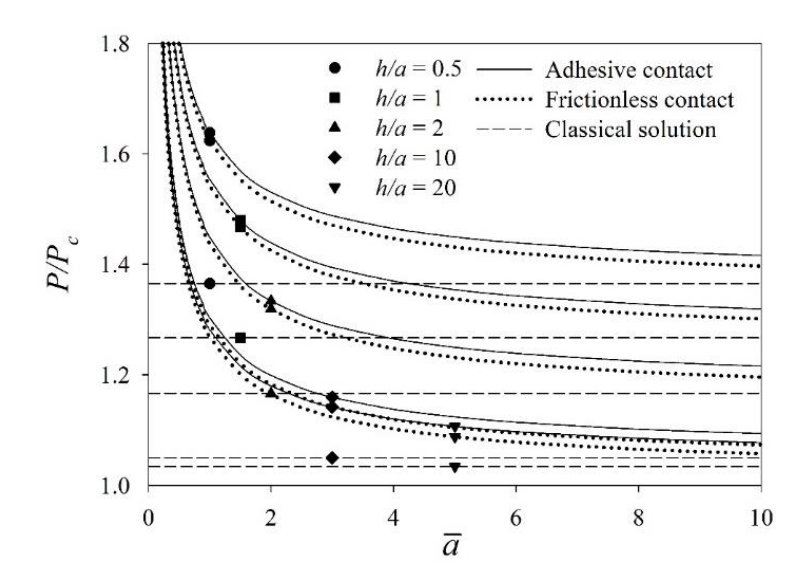


Figure 5.18 Variations of normalized indentation force with \overline{a} for different layer thicknesses and contact conditions.

CHAPTER VI

CONCLUSIONS AND REMARKS

This chapter summarizes both analytical and numerical techniques established in the present investigation for solving various nano-scale problems, i.e., layered media under surface loading, bending and post-buckling of nano-beams, nano-sized cracks and nano-indentations with consideration of surface energy effects. Major findings regarding to both the computational performance of the developed techniques and the extensive parametric study on the influence of the surface stresses and size-dependency of the predicted solutions are presented. Limitations of the current development and the possible extensions for each particular problem are also indicated.

6.1 Layered Media under Surface Loading

The analysis of layered elastic media under the action of axisymmetric surface loading and the influence of the surface energy effects is presented. The boundary value problem corresponding to a layered elastic half-space and a multi-layered elastic medium subjected to axisymmetric normal and tangential traction is formulated based on the complete Gurtin-Murdoch theory of surface elasticity. The analytical solutions using Love's representation and the Hankel integral transform are obtained for both displacement and stress fields. The complete solutions of displacements and stresses corresponding to a layered elastic half-space with the arbitrary functions are obtained by solving the boundary value problem. In addition, an exact stiffness matrix scheme is used to solve the boundary value problem of a multi-layered elastic medium. The solutions are expressed in terms of semi-infinite integrals for problems involving different loading cases, in which, closed-form solutions cannot be obtained due to the complexity of the integrands. The integral with respect to ξ is evaluated by using the numerical quadrature scheme based on 21point Gauss-Kronrod rule. The validity and accuracy of the present solution schemes are comfirmed by comparing with available benchmark solutions. Selected numerical results for radial profiles of displacements and stresses are presented to portray the influence of various parameters on elastic fields for both layered elastic half-space and multi-layered elastic media.

The numerical results indicate that the surface energy effects play an important role in both stress and displacement fields of layered elastic media. The presence of surface stresses renders the layered medium stiffer. Unlike the classical elasticity solution, the present study shows substantial size-dependency of elastic fields. The application of the obtained fundamental solution for nano-indentation is also presented in Chapter V. In addition, the present solution can also be used as a benchmark solution for assessing the accuracy of numerical models such as the finite element and boundary element methods, which can be used to investigate more complicated problems in the presence of surface energy effects.

6.2 Bending and Post-buckling of Nano-beams

A mathematical model and the efficient and accurate solution technique for the nonlinear analysis of nano-beams considering the influence of both surface stresses and nonlocal elasticity have been established. The formulation has been carried out within the regime of large displacements and rotations by combining Euler-Bernoulli beam theory, Gurtin-Mudoch surface elasticity and Eringen nonlocal elasticity. The beam has been treated as a composite consisting of both bulk

material and surface layer in the development of the moment-curvature relationship. The key governing nonlinear differential equations have been developed using the elliptic integral technique and then their linearized version has been summarized and used as a basis for the buckling load analysis. The nonlinear differential equations have been further integrated along with the prescribed boundary conditions to obtain a system of exact nonlinear algebraic equations sufficient for the bending and post-buckling analysis. A solution procedure based on Newton iterative scheme and a selected quadrature has been implemented to solve the fully coupled system of nonlinear equations whereas the explicit analytical expression has been derived for the buckling load. It has been confirmed from numerical experiments that the proposed technique is computationally robust and offers highly accurate numerical solutions without the requirement of discretization.

Results from an extensive numerical study have revealed that the model incorporating both the surface stresses and nonlocal linear elasticity tends to lower the bending stiffness of the beam. The influence of the surface stresses, found in the present study, is quite different from that reported in earlier work. This is due mainly to that the residual stress induced within the bulk material to maintain equilibrium at the initial state has been taken into account in the modeling via the modified flexural rigidity of the beam. The decrease of the beam stiffness as a result of the residual stress within the bulk has been found more prominent than the enhancement of the stiffness by the in-plane modulus of the material surface. Clearly, the enlargement of the surface modulus tends to stiffen the nano-beams while the increase in the residual surface tension leads to the reverse effect. Obtained results also indicate that the nonlocal parameter plays a crucial role on the response prediction and its influence becomes more prominent when the slenderness ratio of the beam increases. The buckling loads, post-buckling and bending response predicted by the proposed model (incorporating both the surface and nonlocal effects) have been found highly sizedependent. It can be also remarked that as the size of the nano-beam is comparable to the intrinsic length scale of the material surface, solutions predicted by the proposed model are significantly different from those associated with the classical case. This finding clearly emphasizes the necessity to properly incorporate both the surface stresses and nonlocal effect in the modeling of nano-scale problems. While the modeling strategy and the solution procedure have been successfully established in the present study, problems treated are still limited to single nanoelements without interior loads. The enhancement of the modeling capability to handle more complex nano-systems consisting of multiple elements and subjected to general applied loads should be the potential extension and requires further investigation.

6.3 Nano-size Cracks

A theoretical model is first presented for a penny-shaped crack in an infinite elastic medium in the presence of surface energy effects. The formulation is based on the the Gurtin-Murdoch continuum theory and the application of Hankel integral transforms. It is shown that the solution to the crack problem can be reduced to a set of simultaneous dual integral equations similar to the classical elasticity case. The integral equation system is solved numerically and shows good convergence. The numerical results indicate that the surface energy effects have a significant influence on both stress and displacement fields of a medium with crack. The surface residual stress has a far significant influence on the elastic field compared to the surface elastic constants. Surface residual stress reduces the crack opening displacement and the near-front vertical stress. As a result, the strength of stress singularity along the crack front is clearly lowered when compared to the

classical case. In contrast to the classical crack solution, the present study shows substantial size-dependency of elastic field. Both crack tip stress field and crack opening displacement show substantial dependency on the crack size and the magnitude of non-dimensional vertical stress, and crack opening displacement increase with increasing crack length. For larger cracks, the influence of surface energy is smaller. The present solution can be used as a benchmark for assessing the accuracy of numerical models based on the finite element and boundary element methods that can be used to analyze more complicated crack problems in the presence of surface energy effects.

Also, an accurate and computationally efficient numerical procedure capable of modeling isolated non-planar cracks in three-dimensional, linearly elastic, infinite media has been established by integrating the influence of surface stresses into the underlying mathematical model. The key governing equations have been formulated by combing the classical theory of linear elasticity for the cracked bulk medium and the full version of Gurtin–Murdoch surface elasticity model for the infinitesimally thin, material layers on the top of the non-planar crack surfaces. A fully coupled system of governing equations, obtained by enforcing the continuity along the material interface, has been solved numerically by the BIEM-FEM coupling procedure. Results for a penny-shaped crack problem have been obtained and compared with the benchmark solutions to confirm the validity of the formulation and numerical implementations. Based on those preliminary results for the fracture related data (e.g., relative crack-face displacement and the near-front stress field), the proposed technique yields highly accurate numerical solutions and the good convergence behavior. The computational performance of the proposed technique when applied to the case of non-planar cracks is still under investigation.

6.4 Nano-indentation on Layered Media

The influence of surface energy effects on layered media under rigid indentation with consideration of frictionless and adhesive contacts is investigated based on Gurtin-Murdoch theory of surface elasticity. The mixed-boundary value problem is formulated with the displacement Green's functions constructed from the fundamental solutions of an elastic layer and a layered elastic half-space with consideration of surface stresses derived by Intarit (2012) and Tirapat et al. (2017). The unknown contact pressure distribution under an indenter of axisymmetric profiles is determined by using either collocation or discretization method. The accuracy of the proposed solution scheme is confirmed by comparing with existing solutions. Presented numerical results indicate a significant influence of surface energy effects on elastic fields in the layered media, especially in the vicinity of the contact area. The presence of surface stresses renders the layered media stiffer, and size-dependent behavior is observed. In addition, the indentation force depends significantly on the layer thickness, the shear moduli in the layered medium, and the contact radius under the influence of surface stresses. The present solution can be used as a benchmark solution in the development of numerical techniques such as the finite element and boundary element methods for analysis of more complicated problems related to nano-indentation on a layered media under the influence of surface energy effects.

REFERENCE

Abdel Rahman, A.A., Mahmoud, F.F. (2016). Analysis of nanocontact problems of layered viscoelastic solids with surface energy effects under different loading patterns. Acta Mechanica 227, 527-548.

Ansari, R., Gholami, R. (2016). Size-dependent modeling of the free vibration characteristics of postbuckled third-order shear deformable rectangular nanoplates based on the surface stress elasticity theory. Composites Part B: Engineering 95, 301-316.

Ansari, R., Mohammadi, V., Faghih Shojaei, M., Gholami, R., Rouhi, H. (2014). Nonlinear vibration analysis of Timoshenko nanobeams based on surface stress elasticity theory. European Journal of Mechanics - A/Solids 45, 143-152.

Ansari, R., Mohammadi, V., Shojaei, M.F., Gholami, R., Sahmani, S. (2013). Postbuckling characteristics of nanobeams based on the surface elasticity theory. Composites Part B: Engineering 55, 240-246.

Attia, M.A., Mahmoud, F.F. (2015). Analysis of nanoindentation of functionally graded layered bodies with surface elasticity. International Journal of Mechanical Sciences 94, 36-48.

Azizi, S., Safaei, B., Fattahi, A., Tekere, M. (2015). Nonlinear vibrational analysis of nanobeams embedded in an elastic medium including surface stress effects. Advances in Materials Science and Engineering 2015.

Borodich, F.M. (2014). Chapter Three - The Hertz-Type and Adhesive Contact Problems for Depth-Sensing Indentation, in: Bordas, S.P.A. (Ed.), Advances in Applied Mechanics. Elsevier, pp. 225-366.

Borodich, F.M., Keer, L.M. (2004). Contact problems and depth-sensing nanoindentation for frictionless and frictional boundary conditions. International Journal of Solids and Structures 41, 2479-2499.

Boussinesq, J. (1885). Application des potentiels à l'étude de l'équilibre et du mouvement des solides élastiques: principalement au calcul des déformations et des pressions que produisent, dans ces solides, des efforts quelconques exercés sur une petite partie de leur surface ou de leur intérieur: mémoire suivi de notes étendues sur divers points de physique, mathematique et d'analyse. Gauthier-Villars.

Burmister, D.M. (1945). The General Theory of Stresses and Displacements in Layered Systems. I. Journal of Applied Physics 16, 89-94.

Chen, W., Engel, P. (1972). Impact and contact stress analysis in multilayer media. International Journal of Solids and Structures 8, 1257-1281.

Chiu, M.-S., Chen, T. (2013). Bending and resonance behavior of nanowires based on Timoshenko beam theory with high-order surface stress effects. Physica E: Low-dimensional Systems and Nanostructures 54, 149-156.

Dhaliwal, R.S., Rau, I.S. (1970). The axisymmetric Boussinesq problem for a thick elastic layer under a punch of arbitrary profile. International Journal of Engineering Science 8, 843-856.

Dingreville, R., Qu, J. (2007). A semi-analytical method to compute surface elastic properties. Acta Materialia 55, 141-147.

Dingreville, R., Qu, J., Cherkaoui, M. (2005). Surface free energy and its effect on the elastic behavior of nano-sized particles, wires and films. Journal of the Mechanics and Physics of Solids 53, 1827-1854.

Doerner, M.F., Nix, W.D. (1986). A method for interpreting the data from depth-sensing indentation instruments. Journal of Materials research 1, 601-609.

Dong, S., Zhou, J., Hui, D., Pang, X., Wang, Q., Zhang, S., Wang, L. (2014). Interaction between edge dislocations and amorphous interphase in carbon nanotubes reinforced metal matrix nanocomposites incorporating interface effect. International Journal of Solids and Structures 51, 1149-1163.

Eltaher, M., Emam, S.A., Mahmoud, F. (2013). Static and stability analysis of nonlocal functionally graded nanobeams. Composite Structures 96, 82-88.

Emam, S.A. (2013). A general nonlocal nonlinear model for buckling of nanobeams. Applied Mathematical Modelling 37, 6929-6939.

Erdogan, F., Bahar, L. (1964). On the solution of simultaneous dual integral equations. Journal of the Society for Industrial and Applied Mathematics 12, 666-675.

Eringen, A. (1976). Continuum physics. Academic Press, New York, NY.

Eringen, A.C. (1983). On differential equations of nonlocal elasticity and solutions of screw dislocation and surface waves. Journal of Applied Physics 54, 4703-4710.

Eringen, A.C. (2002). Nonlocal continuum field theories. Springer-Verlag, New York, NY.

Fabrikant, V.I. (1986). Inverse crack problem in elasticity. Acta mechanica 61, 29-36.

Fabrikant, V.I. (1989). Applications of Potential Theory in Mechanics: A Selections of New Results. Kluwer Academic: The Netherlands.

Fang, Q.H., Liu, Y., Liu, Y.W., Huang, B.Y. (2009). Dislocation emission from an elliptically blunted crack tip with surface effects. Physica B: Condensed Matter 404, 3421-3424.

Feng, X.-Q., Wang, T.-J., Gao, W. (2008). Surface effects on the near-tip stresses for mode-I and mode-III cracks. Journal of Applied Mechanics 75, 011001-011001.

Ferguson, L.A., Muddamallappa, M., Walton, J.R. (2015). Numerical simulation of mode-III fracture incorporating interfacial mechanics. International Journal of Fracture 192, 47-56.

Florence, A., Goodier, J. (1963). The linear thermoelastic problem of uniform heat flow disturbed by a penny-shaped insulated crack. International Journal of Engineering Science 1, 533-540.

Fu, X.L., Wang, G.F., Feng, X.Q. (2008). Surface effects on the near-tip stress fields of a mode-II crack. International Journal of Fracture 151, 95-106.

Fu, X.L., Wang, G.F., Feng, X.Q. (2010). Surface effects on mode-I crack tip fields: A numerical study. Engineering Fracture Mechanics 77, 1048-1057.

Galin, L.A., Gladwell, G.M.L. (2008). Contact Problems: The legacy of L.A. Galin. Springer Netherlands.

Gao, X.-L., Liu, M. (2012). Strain gradient solution for the Eshelby-type polyhedral inclusion problem. Journal of the Mechanics and Physics of Solids 60, 261-276.

Gao, X.-L., Zhou, S.-S. (2013). Strain gradient solutions of half-space and half-plane contact problems. Zeitschrift für Angewandte Mathematik und Physik (ZAMP), 1-24.

Gao, X., Hao, F., Fang, D., Huang, Z. (2013). Boussinesq problem with the surface effect and its application to contact mechanics at the nanoscale. International Journal of Solids and Structures 50, 2620-2630.

Gao, X., Hao, F., Huang, Z., Fang, D. (2014). Mechanics of adhesive contact at the nanoscale: The effect of surface stress. International Journal of Solids and Structures 51, 566-574.

Georgiadis, H., Anagnostou, D. (2008). Problems of the Flamant–Boussinesq and Kelvin type in dipolar gradient elasticity. Journal of Elasticity 90, 71-98.

Gerrard, G.M. (1969). Tables of stresses, strains and displacement in two-layer elastic systems under various traffic loads. Australian Road Research Board, Vic.

Giunta, G., Koutsawa, Y., Belouettar, S., Hu, H. (2013). Static, free vibration and stability analysis of three-dimensional nano-beams by atomistic refined models accounting for surface free energy effect. International Journal of Solids and Structures 50, 1460-1472.

Glavardanov, V., Spasic, D., Atanackovic, T. (2012). Stability and optimal shape of Pflüger micro/nano beam. International Journal of Solids and Structures 49, 2559-2567.

Goodman, L.E. (1962). Contact Stress Analysis of Normally Loaded Rough Spheres. Journal of Applied Mechanics 29, 515-522.

Gupta, P.K., Walowit, J. (1974). Contact stresses between an elastic cylinder and a layered elastic solid. Journal of lubrication technology 96, 250-257.

Gurtin, M.E., Murdoch, A.I. (1975). A continuum theory of elastic material surfaces. Archive for rational mechanics and analysis 57, 291-323.

Gurtin, M.E., Murdoch, A.I. (1978). Surface stress in solids. International Journal of Solids and Structures 14, 431-440.

Gurtin, M.E., Weissmüller, J., Larché, F. (1998). A general theory of curved deformable interfaces in solids at equilibrium. Philosophical Magazine A 78, 1093-1109.

Hansbo, P., Larson, M.G. (2014). Finite element modeling of a linear membrane shell problem using tangential differential calculus. Computer Methods in Applied Mechanics and Engineering 270, 1-14.

Hansbo, P., Larson, M.G., Larsson, F. (2015). Tangential differential calculus and the finite element modeling of a large deformation elastic membrane problem. Computational Mechanics 56, 87-95.

Harding, J., Sneddon, I. (1945). The elastic stresses produced by the indentation of the plane surface of a semi-infinite elastic solid by a rigid punch, Mathematical Proceedings of the Cambridge Philosophical Society. Cambridge University Press, pp. 16-26.

He, J., Lilley, C.M. (2008). Surface effect on the elastic behavior of static bending nanowires. Nano letters 8, 1798-1802.

He, L.H., Lim, C.W. (2006). Surface Green function for a soft elastic half-space: Influence of surface stress. International Journal of Solids and Structures 43, 132-143.

He, M., Hutchinson, J. (1981). The penny-shaped crack and the plane strain crack in an infinite body of power-law material. Journal of Applied Mechanics 48, 830-840.

Hosseini-Hashemi, S., Nazemnezhad, R., Rokni, H. (2015). Nonlocal nonlinear free vibration of nanobeams with surface effects. European Journal of Mechanics-A/Solids 52, 44-53.

Hu, K.-M., Zhang, W.-M., Zhong, Z.-Y., Peng, Z.-K., Meng, G. (2014). Effect of surface layer thickness on buckling and vibration of nonlocal nanowires. Physics Letters A 378, 650-654.

Huang, G.-Y., Yu, S.-W. (2007). Effect of Surface Elasticity on the Interaction Between Steps. Journal of Applied Mechanics 74, 821-823.

Huang, Z., Wang, J.-x. (2006). A theory of hyperelasticity of multi-phase media with surface/interface energy effect. Acta Mechanica 182, 195-210.

Intarit, P. (2012). Solutions of Elastic Medium with Surface Stress Effects. Chulalongkorn University.

Intarit, P., Senjuntichai, T., Rajapakse, R. (2010). Dislocations and internal loading in a semi-infinite elastic medium with surface stresses. Engineering Fracture Mechanics 77, 3592-3603.

Intarit, P., Senjuntichai, T., Rungamornrat, J., Rajapakse, R. (2012). Stress analysis of penny-shaped crack considering the effects of surface elasticity. Proceedings of 20th Annual International Conference on Composites or Nano Engineering (ICCE-20), Ramada Beijing North Hotel, Beijing, P.R.China.

Intarit, P., Senjuntichai, T., Rungamornrat, J., Rajapakse, R. (2017). Penny-shaped crack in elastic medium with surface energy effects. Acta Mechanica 228, 617-630.

Intarit, P., Senjuntichai, T., Rungamornrat, J., Rajapakse, R.K.N.D. (2011). Surface elasticity and residual stress effect on the elastic field of a nanoscale elastic layer. Interaction and multiscale mechanics 4, 85-105.

Janghorban, M. (2012). Static analysis of tapered nanowires based on nonlocal Euler-Bernoulli beam theory via differential quadrature method. Latin American Journal of Solids and Structures 9, 299-307.

Jiang, L., Yan, Z. (2010). Timoshenko beam model for static bending of nanowires with surface effects. Physica E: Low-dimensional systems and Nanostructures 42, 2274-2279.

Jiangang, G., Yapu, Z. (2007). The size-dependent bending elastic properties of nanobeams with surface effects. Nanotechnology 18(29), 295701.

Juntarasaid, C., Pulngern, T., Chucheepsakul, S. (2012). Bending and buckling of nanowires including the effects of surface stress and nonlocal elasticity. Physica E: Low-dimensional Systems and Nanostructures 46, 68-76.

Kachanov, M.L., Shafiro, B., Tsukrov, I. (2003). Handbook of Elasticity Solutions. Kluwer Academic Publishers

Katebi, A., Selvadurai, A.P.S. (2013). Undrained behaviour of a non-homogeneous elastic medium: the influence of variations in the elastic shear modulus with depth. Géotechnique 63, 1159-1169.

Kim, C.I., Ru, C., Schiavone, P. (2013). A clarification of the role of crack-tip conditions in linear elasticity with surface effects. Mathematics and Mechanics of Solids 18, 59-66.

Kim, C.I., Schiavone, P., Ru, C.-Q. (2010a). The effects of surface elasticity on an elastic solid with mode-III crack: complete solution. Journal of Applied Mechanics 77, 021011.

Kim, C.I., Schiavone, P., Ru, C.-Q. (2010b). Analysis of a mode-III crack in the presence of surface elasticity and a prescribed non-uniform surface traction. Zeitschrift für angewandte Mathematik und Physik 61, 555-564.

Kim, C.I., Schiavone, P., Ru, C.-Q. (2011a). Analysis of plane-strain crack problems (mode-I & mode-II) in the presence of surface elasticity. Journal of Elasticity 104, 397-420.

Kim, C.I., Schiavone, P., Ru, C.Q. (2011b). The effect of surface elasticity on a Mode-III interface crack. Archives of Mechanics 63, 267-286.

Koutsoumaris, C.C., Eptaimeros, K., Tsamasphyros, G. (2017). A different approach to Eringen's nonlocal integral stress model with applications for beams. International Journal of Solids and Structures 112, 222-238.

Lebedev, N., Ufliand, I.S. (1958). Axisymmetric contact problem for an elastic layer. Journal of Applied Mathematics and Mechanics 22, 442-450.

Lei, D.X., Wang, L.Y., Ou, Z.Y. (2012). Elastic Analysis for Nanocontact Problem with Surface Stress Effects under Shear Load. Journal of Nanomaterials 2012, 7.

Li, S., Mear, M.E. (1998). Singularity-reduced integral equations for displacement discontinuities in three-dimensional linear elastic media. International Journal of Fracture 93, 87-114.

Li, X.-F., Zhang, H., Lee, K.Y. (2014). Dependence of Young's modulus of nanowires on surface effect. International Journal of Mechanical Sciences 81, 120-125.

Liu, C., Rajapakse, R. (2010). Continuum models incorporating surface energy for static and dynamic response of nanoscale beams. IEEE Transactions on Nanotechnology 9, 422-431.

Liu, C., Rajapakse, R., Phani, A.S. (2011). Finite element modeling of beams with surface energy effects. Journal of Applied Mechanics 78, 031014.

Liu, J., Mei, Y., Xia, R., Zhu, W. (2012). Large displacement of a static bending nanowire with surface effects. Physica E: Low-dimensional systems and Nanostructures 44, 2050-2055.

Lowe, P.G., Lowe, M.A. (1971). Classical Theory of Structures: Based on the Differential Equation. Cambridge University Press.

Magnus, W., Oberhettinger, F. Formulas and Theorems for the Functions of Mathematical Physics (Chelsea, New York, 1954). 35.

Mahmoud, F., Eltaher, M., Alshorbagy, A., Meletis, E. (2012). Static analysis of nanobeams including surface effects by nonlocal finite element. Journal of Mechanical Science and Technology 26, 3555-3563.

Meyers, M.A., Chawla, K.K. (1999). Mechanical Behavior of Materials. Prentice-Hall, New York.

Mi, C. (2017). Surface mechanics induced stress disturbances in an elastic half-space subjected to tangential surface loads. European Journal of Mechanics - A/Solids 65, 59-69.

Miller, R.E., Shenoy, V.B. (2000). Size-dependent elastic properties of nanosized structural elements. Nanotechnology 11, 139.

Mindlin, R., Tiersten, H. (1962). Effects of couple-stresses in linear elasticity. Archive for Rational Mechanics and analysis 11, 415-448.

Mindlin, R.D. (1964). Micro-structure in linear elasticity. Archive for Rational Mechanics and Analysis 16, 51-78.

Mossakovskii, V.I. (1954). The fundamental mixed problem of the theory of elasticity for a halfspace with a circular line separating the boundary conditions. Journal of Applied Mathematics and Mechanics 18, 187-196 (in Russian).

Mossakovskii, V.I. (1963). Compression of elastic bodies under conditions of adhesion (Axisymmetric case). Journal of Applied Mathematics and Mechanics 27, 630-643.

Murdoch, A.I. (2005). Some Fundamental Aspects of Surface Modelling. Journal of Elasticity 80, 33-52.

Nakayama, T., Yamamoto, K., Satoh, H., Konno, T.J., Clemens, B.M., Sinclair, R. (1995). Structure and corrosion properties of Al/Si and Fe/Zr multilayers. Materials Science and Engineering: A 198, 19-24.

Nan, H., Wang, B. (2012). Effect of residual surface stress on the fracture of nanoscale materials. Mechanics Research Communications 44, 30–34.

Nan, H.S., Wang, B.L. (2013). Effect of crack face residual surface stress on nanoscale fracture of piezoelectric materials. Engineering Fracture Mechanics 110, 68-80.

Nan, H.S., Wang, B.L. (2014). Effect of interface stress on the fracture behavior of a nanoscale linear inclusion along the interface of bimaterials. International Journal of Solids and Structures 51, 4094-4100.

Nguyen, T., Rungamornrat, J., Senjuntichai, T., Wijeyewickrema, A. (2015). FEM-SGBEM coupling for modeling of mode-I planar cracks in three-dimensional elastic media with residual surface tension effects. Engineering Analysis with Boundary Elements 55, 40-51.

Nguyen, T.B., Rungamornrat, J., Senjuntichai, T. (2016). Analysis of planar cracks in 3D elastic media with consideration of surface elasticity. International Journal of Fracture 202, 51-77.

Oliver, W.C., Pharr, G.M. (1992). An improved technique for determining hardness and elastic modulus using load and displacement sensing indentation experiments. Journal of materials research 7, 1564-1583.

On, B.B., Altus, E., Tadmor, E. (2010). Surface effects in non-uniform nanobeams: continuum vs. atomistic modeling. International journal of solids and structures 47, 1243-1252.

Peddieson, J., Buchanan, G.R., McNitt, R.P. (2003). Application of nonlocal continuum models to nanotechnology. International Journal of Engineering Science 41, 305-312.

Perriot, A., Barthel, E. (2004). Elastic contact to a coated half-space: Effective elastic modulus and real penetration. Journal of Materials Research 19, 600-608.

Piessens, R., de Doncker-Kapenga, E., Ueberhuber, C. (1983). Quadpack. A subroutine package for automatic integration. Springer Series in Computational Mathematics, Berlin: Springer, 1983.

Pinyochotiwong, Y., Rungamornrat, J., Senjuntichai, T. (2013). Rigid frictionless indentation on elastic half space with influence of surface stresses. International Journal of Engineering Science 71, 15-35.

Potapov, V. (2013). Stability via nonlocal continuum mechanics. International Journal of Solids and Structures 50, 637-641.

Povstenko, Y.Z. (1993). Theoretical investigation of phenomena caused by heterogeneous surface tension in solids. Journal of the Mechanics and Physics of Solids 41, 1499-1514.

Pradhan, S., Phadikar, J. (2009). Bending, buckling and vibration analyses of nonhomogeneous nanotubes using GDQ and nonlocal elasticity theory. Structural Engineering and Mechanics 33, 193-213.

Preethi, K., Rajagopal, A., Reddy, J.N. (2015). Surface and non-local effects for non-linear analysis of Timoshenko beams. International Journal of Non-Linear Mechanics 76, 100-111.

Rahman, A.A.A., Mahmoud, F.F. (2016). Analysis of nanocontact problems of layered viscoelastic solids with surface energy effects under different loading patterns. Acta Mechanica 227, 527-548.

Rau, I.S., Dhaliwal, R.S. (1972). Further considerations on the axisymmetric Boussinesq problem. International Journal of Engineering Science 10, 659-663.

Reddy, J. (2007). Nonlocal theories for bending, buckling and vibration of beams. International Journal of Engineering Science 45, 288-307.

Reddy, J., El-Borgi, S., Romanoff, J. (2014). Non-linear analysis of functionally graded microbeams using Eringen's non-local differential model. International Journal of Non-Linear Mechanics 67, 308-318.

Reddy, J., Pang, S. (2008). Nonlocal continuum theories of beams for the analysis of carbon nanotubes. Journal of Applied Physics 103, 023511.

Reddy, J.N. (2004). Mechanics of laminated composite plates and shells: theory and analysis. CRC Press, Boca Raton, FL.

Reddy, J.N. (2015). An Introduction to Nonlinear Finite Element Analysis. Oxford University Press, Oxford, UK.

Reddy, J.N. (2018). Energy principles and variational methods in applied mechanics. John Wiley & Sons, New York, NY.

Rungamornrat, J., Mear, M.E. (2008). Weakly-singular, weak-form integral equations for cracks in three-dimensional anisotropic media. International Journal of Solids and Structures 45, 1283-1301.

Rungamornrat, J., Tangnovarad, P. (2011). Analysis of linearly elastic inextensible frames undergoing large displacement and rotation. Mathematical Problems in Engineering 2011.

Rungamornrat, J., Tuttipongsawat, P., Senjuntichai, T. (2016). Elastic layer under axisymmetric surface loads and influence of surface stresses. Applied Mathematical Modelling 40, 1532-1553.

Sapsathiarn, Y., Rajapakse, R. (2012). A model for large deflections of nanobeams and experimental comparison. IEEE Transactions on Nanotechnology 11, 247-254.

Sapsathiarn, Y., Rajapakse, R. (2013). Finite-element modeling of circular nanoplates. Journal of Nanomechanics and Micromechanics 3, 59-66.

Selvadurai, A.P.S. (2000). Partial differential equations in mechanics. Berlin New York: Springer.

Selvadurai, A.P.S., Katebi, A. (2015). An adhesive contact problem for an incompressible non-homogeneous elastic halfspace. Acta Mechanica 226, 249-265.

Sendova, T., Walton, J.R. (2010). A new approach to the modeling and analysis of fracture through extension of continuum mechanics to the nanoscale. Mathematics and Mechanics of Solids 15, 368-413.

Senjuntichai, T., Rajapakse, R.K.N.D. (1995). Exact stiffness method for quasi-statics of a multi-layered poroelastic medium. International Journal of Solids and Structures 32, 1535-1553.

Shenoy, V.B. (2005). Atomistic calculations of elastic properties of metallic fcc crystal surfaces. Physical Review B 71, 094104.

Şimşek, M., Yurtcu, H. (2013). Analytical solutions for bending and buckling of functionally graded nanobeams based on the nonlocal Timoshenko beam theory. Composite Structures 97, 378-386.

Sneddon, I.N. (1946). The distribution of stress in the neighbourhood of a crack in an elastic solid. Proc. R. Soc. Lond. A 187, 229-260.

Sneddon, I.N. (1951). Fourier transforms. McGraw-Hill, New York.

Sneddon, I.N. (1965). The relation between load and penetration in the axisymmetric Boussinesq problem for a punch of arbitrary profile. International journal of engineering science 3, 47-57.

Spence, D.A. (1968a). Self Similar Solutions to Adhesive Contact Problems with Incremental Loading. Proceedings of the Royal Society of London. Series A, Mathematical and Physical Sciences 305, 55-80.

Spence, D.A. (1968b). A Wiener-Hopf Equation Arising in Elastic Contact Problems. Proceedings of the Royal Society of London. Series A, Mathematical and Physical Sciences 305, 81-92.

Tada, H., Paris, P.C., Irwin, G.R. (2000). The Stress Analysis of Cracks Handbook. American Society of Mechanical Engineers, New York.

Tian, L., Rajapakse, R. (2007). Analytical solution for size-dependent elastic field of a nanoscale circular inhomogeneity. Journal of applied mechanics 74, 568-574.

Timoshenko, S.P., Gere, J.M. (1961). Theory of elastic stability. McGraw-Hill, Singapore.

Tirapat, S., Senjuntichai, T., Rungamornrat, J. (2017). Influence of Surface Energy Effects on Elastic Fields of a Layered Elastic Medium under Surface Loading. Advances in Materials Science and Engineering 2017.

Toupin, R.A. (1964). Theories of elasticity with couple-stress. Archive for Rational Mechanics and Analysis 17, 85-112.

Tranter, C.J. (1951). Integral transforms in mathematical physics. John Wiley: New York.

Vila, J., Fernández-Sáez, J., Zaera, R. (2017). Nonlinear continuum models for the dynamic behavior of 1D microstructured solids. International Journal of Solids and Structures 117, 111-122.

Walton, J.R. (2012). A note on fracture models incorporating surface elasticity. Journal of Elasticity 109, 95-102.

Walton, J.R. (2014). Plane-strain fracture with curvature-dependent surface tension: mixed-mode loading. Journal of Elasticity 114, 127-142.

Wang, C., Kitipornchai, S., Lim, C., Eisenberger, M. (2008). Beam bending solutions based on nonlocal Timoshenko beam theory. Journal of Engineering Mechanics 134, 475-481.

Wang, C., Zhang, Y., Ramesh, S.S., Kitipornchai, S. (2006). Buckling analysis of micro-and nanorods/tubes based on nonlocal Timoshenko beam theory. Journal of Physics D: Applied Physics 39, 3904-3909.

Wang, G.-F., Feng, X.-Q. (2009). Surface effects on buckling of nanowires under uniaxial compression. Applied physics letters 94, 141913.

Wang, G.-F., Yang, F. (2011). Postbuckling analysis of nanowires with surface effects. Journal of Applied Physics 109, 063535.

Wang, G.F., Li, Y. (2013). Influence of surface tension on mode-I crack tip field. Engineering Fracture Mechanics 109, 290-301.

Wang, Q., Liew, K. (2007). Application of nonlocal continuum mechanics to static analysis of micro-and nano-structures. Physics Letters A 363, 236-242.

Wang, Y., Rajapakse, R.K.N.D. (1994). An Exact Stiffness Method for Elastodynamics of a Layered Orthotropic Half-Plane. Journal of Applied Mechanics 61, 339-348.

Wang, Z.-Q., Zhao, Y.-P., Huang, Z.-P. (2010). The effects of surface tension on the elastic properties of nano structures. International Journal of Engineering Science 48, 140-150.

Wong, E.W., Sheehan, P.E., Lieber, C.M. (1997). Nanobeam mechanics: elasticity, strength, and toughness of nanorods and nanotubes. science 277, 1971-1975.

Wu, C.H. (1999). The effect of surface stress on the configurational equilibrium of voids and cracks. Journal of the Mechanics and Physics of Solids 47, 2469-2492.

Wu, C.H., Wang, M.L. (2000). The effect of crack-tip point loads on fracture. Journal of the Mechanics and Physics of Solids 48, 2283-2296.

Wu, C.H., Wang, M.L. (2001). Configurational equilibrium of circular-arc cracks with surface stress. International journal of solids and structures 38, 4279-4292.

Wu, Q., Volinsky, A.A., Qiao, L., Su, Y. (2015). Surface effects on static bending of nanowires based on non-local elasticity theory. Progress in Natural Science: Materials International 25, 520-524.

Yakobson, B.I. (2003). Nanomechanics, in: (ends.)., I.W.A.G.D.W.B.S.E.L.a.G.J.I. (Ed.), Handbook of nanoscience, engineering, and technology. CRC Press, Florida.

Yang, F. (2003). Thickness effect on the indentation of an elastic layer. Materials Science and Engineering: A 358, 226-232.

Yang, Y., Lim, C.W. (2011). A variational principle approach for buckling of carbon nanotubes based on nonlocal Timoshenko beam models. Nano 6, 363-377.

Zhao, X. (2009). Surface loading and rigid indentation of an elastic layer with surface energy effects. University of British Columbia.

Zhao, X., Rajapakse, R.K.N.D. (2009). Analytical solutions for a surface-loaded isotropic elastic layer with surface energy effects. International Journal of Engineering Science 47, 1433-1444.

Zhao, X., Rajapakse, R. (2013). Elastic field of a nano-film subjected to tangential surface load: Asymmetric problem. European Journal of Mechanics-A/Solids 39, 69-75.

Zhou, S., Gao, X.-L. (2013). Solutions of half-space and half-plane contact problems based on surface elasticity. Zeitschrift für angewandte Mathematik und Physik 64, 145-166.

Appendix A: OUTPUT

Articles in International Journals:

- [1] Intarit P, Senjuntichai T, Rungamornrat J, Rajapakse RKND. "Penny-shaped crack in elastic medium with surface energy effects." *Acta Mechanica*, February 2017, 228(2): 617-630, DOI: 10.1007/s00707-016-1728-9.
- [2] Tirapat S, Senjuntichai T, Rungamornrat J. "Influence of surface energy effects on elastic fields of a layered elastic medium under surface loading." *Advances in Materials Science and Engineering*, 2017, 2017 Article ID 7530936, 11 pages; https://doi.org/10.1155/2017/7530936.
- [3] Intarit P, Senjuntichai T, Rungamornrat J. "Elastic layer under axisymmetric indentation and surface energy effects." *Zeitschrift für angewandte Mathematik und Physik*, 2018, 69(2), 29
- [4] Senjuntichai T, Keawsawasvong S, Plangmal R. "Vertical vibrations of rigid foundations of arbitrary shape in a multi-layered poroelastic medium." *Computers and Geotechnics*, 2018, 100, 121-134.
- [5] Tirapat S, Senjuntichai T. "Analysis of indentation on layered elastic medium with surface energy effects." *Key Engineering Materials*, 2018, 775, 524-530, https://doi.org/10.4028/www.scientific.net/ KEM.775.524.
- [6] Senjuntichai T, Keawsawasvong S, Plangmal R. "Three-dimensional dynamic response of multi-layered poroelastic media." *Marine Georesources and Geotechnology*, 2018, article in press.
- [7] Keawsawasvong S, Senjuntichai T. "Influence of anisotropic properties on vertical vibrations of circular foundation on saturated elastic layer." *Mechanics Research Communications*, revised manuscript.

[8] Senjuntichai T, Keawsawasvong S, Plangmal R. "Embedded foundation under horizontal and moment loading in multi-layered poroelastic media. *International Journal of Geomechanics-ASCE*, under review.

Articles in Conference Proceedings:

- [1] Senjuntichai T. "Influence of surface energy effects on various contact problems." *Keynote Speaker* at The 4th International Conference on Sustainable Civil Engineering Structures and Construction (SCESCM 2018), Yogyakarta, Indonesia, September 5-7, 2018.
- [2] Tirapat S, Senjuntichai T, Rungamornrat J, Rajapakse RKND. "Variational formulation of interaction between elastic plate and elastic medium under the influence of surface energy." The 3rd International Conference on Civil Engineering and Materials Science (ICCEMS 2018), Chengdu, China, April 13-15, 2018.
- [3] Tarntira K, Senjuntichai T. "A multi-layered elastic medium under surface energy influence." The Thirtieth KKHTCNN Symposium on Civil Engineering, Taiwan, November 2-4, 2017.
- [4] Nguyen BT, Rungamornrat R, Senjuntichai T. "Analysis of non-planar, nano-sized cracks in 3D elastic media by BIEM-FEM coupling." The 15th East Asia-Pacific Conference on Structural Engineering and Construction (EASEC-15), Xi'an, China, October 11-13, 2017.
- [5] Keawsawasvong S, Senjuntichai T. "Dynamic Response of Two Rigid Foundations on Multi-Layered Poroelastic Medium." The 4th International Conference on Advanced Materials, Mechanics and Structural Engineering (AMMSE 2017), Tianjin City, China, September 22-24, 2017.
- [6] Wongthongsiri S, Panupattanapong K, Son NN, Nguyen BT, Rungamornrat J, Senjuntichai T. "FE Solutions of Near-Tip Elastic Field of Mode-I Nano-cracks." The 22nd National Convention on Civil Engineering, Nakhon Ratchasima, July 18-20, 2017.

- [7] Tirapat S, Senjuntichai T, Rungamornrat J. "A Layered Elastic Medium with Surface Stress Influence under Surface Loading." The 28th KKHTCNN Symposium on Civil Engineering, Bangkok, Thailand, November 16-18, 2015.
- [8] Nguyen BT, Rungamornrat J, Senjuntichai T." Applications of Surface Elasticity Theory to Modeling of 3D Cracks with Nano-scaled Influence." The 28th KKHTCNN Symposium on Civil Engineering, Bangkok, Thailand, November 16-18, 2015.

Appendix B: REPRINTS/MANUSCRIPTS